Development of Laser-based Directed Energy Deposition System with Non-Pneumatic Powder Feedstock Handling and Synthesis of Toolpath Strategies

A thesis submitted in partial fulfillment of the requirements for the degree of

Doctor of Philosophy

By

Ambrish Singh

(176103107)

Department of Mechanical Engineering

Indian Institute of Technology Guwahati

Guwahati- 781039

September 2023

Department of Mechanical Engineering
Indian Institute of Technology Guwahati
Guwahati-781039
INDIA

CERTIFICATE

It is certified that the work contained in the thesis titled "**Development of Laser−based Directed Energy Deposition System with Non−Pneumatic Powder Feedstock Handling and Synthesis of Toolpath Strategies**," submitted by **Ambrish Singh**, Roll No. 176103107 to the Indian Institute of Technology Guwahati for the degree of Doctor of Philosophy has been carried out under my supervision in the Department of Mechanical Engineering, Indian Institute of Technology Guwahati. This work has not been submitted elsewhere for the award of any other degree or diploma.

Dr. Sajan Kapil
Department of Mechanical Engineering
Indian Institute of Technology Guwahati
Guwahati-781039, Assam, India
Date:

Dr. Manas Das
Department of Mechanical Engineering
Indian Institute of Technology Guwahati
Guwahati-781039, Assam, India
Date:

Declaration

I declare that this written submission represents my idea in my own words, and where others' ideas or words have been included, I have adequately cited and referenced the original sources. I also declare that I have adhered to all principles of academic honesty and integrity and have not misrepresented or fabricated or falsified any idea/data/fact/source in my submission. I understand that any violation of the above will cause for disciplinary action by the institute and can also evoke penal action from the sources that have thus not been properly cited or from whom proper permission has not been taken where needed.

Singh

Date:

Ambrish Singh
Roll No.: 176103107

Dedicated to My Teachers

ACKNOWLEDGMENT

I would like to express my sincerest thanks and gratitude to my thesis advisors, Dr. Sajan Kapil and Prof. Manas Das, for allowing me to explore the domain of *Additive Manufacturing* under their active and kind supervision. This exploration, with the sterling support of my supervisors, broadened my mindset and provided me with invaluable tools for research and scientific inquiry.

I am also thankful to my doctoral committee members, Prof. U.S. Dixit, Prof. Pankaj Biswas, and Prof. Chandan Das, for their valuable feedback and encouragement of my ideas. Their support helped me maintain an unwavering effort toward accomplishing project objectives. Also, I am thankful to all the faculty members of the Department of Mechanical Engineering at the Indian Insitute of Technology Guwahati, whose support has helped me develop a scientific and research aptitude. I would also like to acknowledge the *Central Instrumentation Facility (CIF)* at IIT Guwahati for their kind assistance in carrying out my research work.

I would also like to thank the *Department for Science and Technology (DST-India)* for their financial support of the project (DST/TDT/DDP-09/2021) 'Design and Development of a Bulk Material Handling Device for Metering, Mixing, and Delivery of Powder Feedstock' under the *Device Development Program (DDP)* and Ace Manufacturing Systems Ltd., Bangalore who are the industry project partner. Furthermore, I express my sincere thanks to GNRC Medical, North Guwahati, for allowing us to use their CT Scanner for scanning the printed part and providing the DICOM file for analysis. Also, my sincere thanks to the machining team at the *Tool Room and Training Center (TRTC, Amingaon)* for their help in the fabrication of a functional nozzle prototype.

A sincere thanks also goes to my lab mates, Mr. Sadaival Singh and Mr. Ritam Samra, for their significant inputs in the development of the TSP-based toolpath and its implementation via *Robotic-Wire Arc Additive Manufacturing(R-WAAM).* I would also like to thank Mr. Atul Singh Rajput for his suggestions on collaborative work for the post-processing of additively fabricated parts through Magnetorheological finishing. I also express my sincere thanks to my seniors and friends Dr. Manjesh Kumar, Dr. Abhinav Kumar, Anand Mohan Pandey, Ranajit Mahanti, Hari Narayan Singh Yadav, Akash Tyagi, Kanak Jindal, Ravi Prakash, who made my time on the campus memorable.

Last, but not least, I am deeply indebted to my parents for their constant support and motivation.

Ambrish Singh

Abstract

Pneumatic methods of powder feedstock handling are prevalent in laser-based *Directed Energy Deposition (DED)*. These methods use inert gases (mostly Argon) to meter, convey, and inject powder feedstock into the melt pool created by the laser on the substrate. Although several variants of pneumatic feedstock handling exist in the literature, the difference is mainly in the mechanism of powder metering and the geometric design of the powder delivery nozzle. This work identifies several shortcomings of such pneumatic-based feedstock handling systems and offers an easy solution that could be more economical. A gravity-based system, proposed herein, has been demonstrated to be a viable replacement for pneumatic methods. The gravity-based non-pneumatic system utilizes a helical-grooved shaft rotating inside a powder-filled hopper to meter the mass flow rate. This metered influx of powder is subsequently delivered to the powder delivery nozzle, which creates a conical and convergent envelope of powder stream around the fusion source before finally injecting it into the melt pool.

The powder delivery nozzle uses a bladed-centrifugal distributor to distribute the powder influx uniformly across its periphery, which is subsequently shaped into a convergent powder stream. The uniformity of powder's spatial distribution around the fusion source is essential to maintain omnidirectionality in the developed setup and to fabricate parts with minimal defects. A novel centrifugal distributor was designed and manufactured in the light of design inputs received via the *Discrete Element Method (DEM)* modeling of granular flow. For accurate process modeling, the inputs to the DEM model were tested for their significance on the behavior of granular media in terms of spatial and temporal uniformity of its distribution. Out of the three input variables selected for the sensitivity analysis, which included *Coefficient of Static Friction (COSF)*, *Coefficient of Rolling Resistance (CORR)*, and *Coefficient of Restitution (COR)*, COSF was found to significantly affect the responses. Consequently, an apparatus was fabricated to accurately evaluate the COSF values of powder samples against their interacting material.

A DED machine tool was developed by interfacing a 1kW fiber-coupled continuous wave laser with a vertical CNC machine to additively fabricate parts. This machine tool is hybrid in nature, with both additive and subtractive capabilities, such that each process (DED and Machining) can be used in tandem or independently without one hampering the other. The interfacing of the laser with the CNC was achieved by mounting the optical head on the housing of the CNC spindle and repurposing the coolant ON/OFF control to initiate/ terminate the laser beam as dictated by the user (provided toolpath). The CNC was also retrofitted with the non-pneumatic powder handling system, wherein the feedstock metering unit was mounted alongside the CNC spindle. Custom mounts were fabricated to accommodate the powder delivery nozzle

parallel to the cutting tool and concentric with the laser beam with a converged powder stream coincident with the melt pool. Through multiple case studies, the developed machine tool was demonstrated to be robust in nature and can be used for part fabrication via DED, followed by machining-based post-processing through milling.

Several toolpath strategies were also studied as part of this work. The selection of a toolpath for the deposition of material has an influence on part properties and process efficiency. *Space-filling Curves (SFCs)* offer a unique opportunity in AM to fabricate parts with a high strength-to-weight ratio and include a density gradient in the final product. However, often, it is desirable for an SFC to have properties such as a common start and stop point, a minimal number of turns, and very few retractions/ lifts. A *Traveling Salesman Problem (TSP)*--based solver is utilized to synthesize a toolpath with the aforementioned properties. The toolpath is generated by first digitizing a domain within a contour via an arrangement of grid points; subsequently, these points (represented by a list of coordinates) are fed to a heuristic-based TSP (Lin-Kernighan) solver to obtain the toolpath. The layout of the grid points within the contour governs the nature of the toolpath. Furthermore, the number of turns and the direction of travel, to a large extent, can be varied by varying the distance between two consecutive grid points in a digitized grid.

A density gradient in the toolpath, synthesized from a TSP approach, can be obtained by appropriately clustering cities or grid points. A region with a high cluster of grid points will result in a densely packed toolpath, consequently depositing more material, whereas regions with a low density of grid points will lead to sparsely deposited material. In this work, the variation of density in a digitized grid is obtained through a force balance amongst the grid points, which are assumed to be connected through a network of springs. Through appropriate consideration of linear and torsional springs, the grid points can be arranged in a rectangular, circular, and contour-adaptive manner. The user input for the gradient in part density can either be an equation or a density map (image). The toolpath conforms to this gradient while preserving its continuous, closed-loop property. The ability of the toolpath to conform to the prescribed gradient with the direction-favoring aspect is one of its unique characteristics. The toolpath was utilized for printing an acetabulum bone with CT scan images as a density map for the respective layer. A CT scan of the printed part validates the conformity of the toolpath to the input density map.

On a final note, this work is an attempt at the conceptualization of a methodology that essentially enables the development of a machine tool of hybrid (i.e., additive and subtractive) capability. The subsystems that enable DED, such as feedstock handling (non-pneumatic system), energy source (laser interfacing), and CNC motion (TSP-based toolpath planning), are brought together in synergistic sync while ensuring both ease of development and ease of use.

Table of Contents

List of Figures

List of Table

Nomenclature

AM	Additive Manufacturing
FGM	Functionally Graded Material
MAM	Metal Additive Manufacturing
PBF	Powder Bed Fusion
BME	Bound Metal Extrusion
SPD	Selective Powder Deposition
MMC	Metal Matix Composite
PID	Particle Intensity Distribution
LBID	Laser Beam Intensity Distribution
DPP	Dry Powder Printing
PZTs	Piezoelectric Transducers
SFC	Space Filling Curve
TSP	Travelling Salesman Problem
DEM	Discrete Element Method
RSM	Response Surface Methodology
COSF	Coefficient of Static Friction
CORR	Coefficient of Rolling Resistance
COR	Coefficient of Restitution
COV	Coefficient of Variation
FFF	Fused Filament Fabrication
FDM	Fused Deposition Modeling
CMT	Cold Metal Transfer
WAAM	Wire Arc Additive Manufacturing
MAT	Medial Axis Transform
CAD	Computer-aided Design
STL	Standard Tessellation Language
TSP	Travelling Salesman Problem
ASTM	American Society for Testing and Materials

Chapter 1

Introduction and Literature Survey

Additive Manufacturing (AM), as the name suggests, is a generative technology where instead of removing material from a workpiece, as in the case of subtractive manufacturing, material(s) is (are) added selectively and strategically layer after layer to get the desired part geometry. AM, which was initially introduced as a method for quick and easy prototyping, has now grown into a full-fledged manufacturing process capable of series production of functional components[1,2]. ASTM lists seven categories of AM techniques; however, these categories are ‘umbrella’ terms, with multiple variants of each technique falling under their general purview. Broadly speaking, the process sequence for AM can be subdivided into pre-processing, processing, and post-processing, as illustrated in Fig. 1.1.

The pre-processing involves the preparation of a CAD model followed by its tessellation and slicing. Following slicing, contour information and toolpath for material deposition can be extracted. This step of pre-processing is followed by processing, where, having selected the AM technique, the part is fabricated each layer at a time. The final step is post-processing, which allows for enhancement of the surface and (or) mechanical properties of the fabricated part.

Apart from part fabrication from scratch, AM is now also recognized for part repair, surface cladding, and realization of Functionally Graded Materials (FGMs). These capabilities are especially prominent in the case of the Directed Energy Deposition (DED) process, which is the subject of discussion for this study.

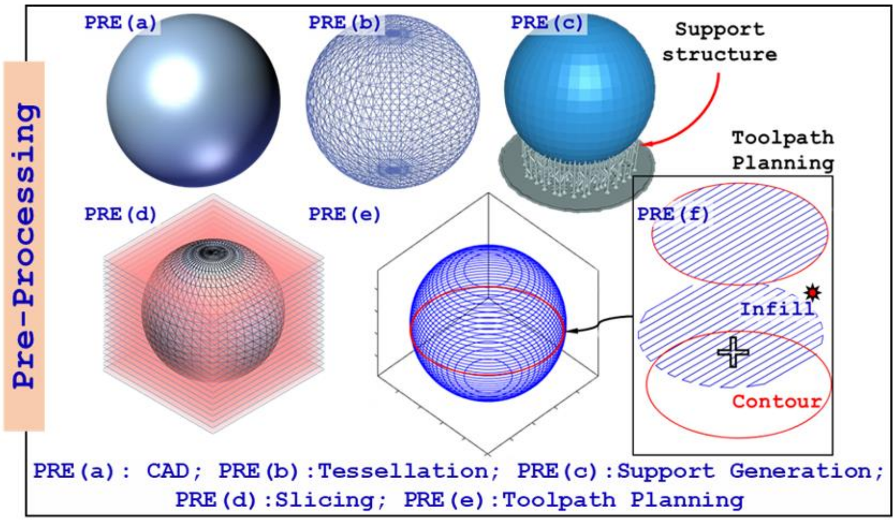

(a)

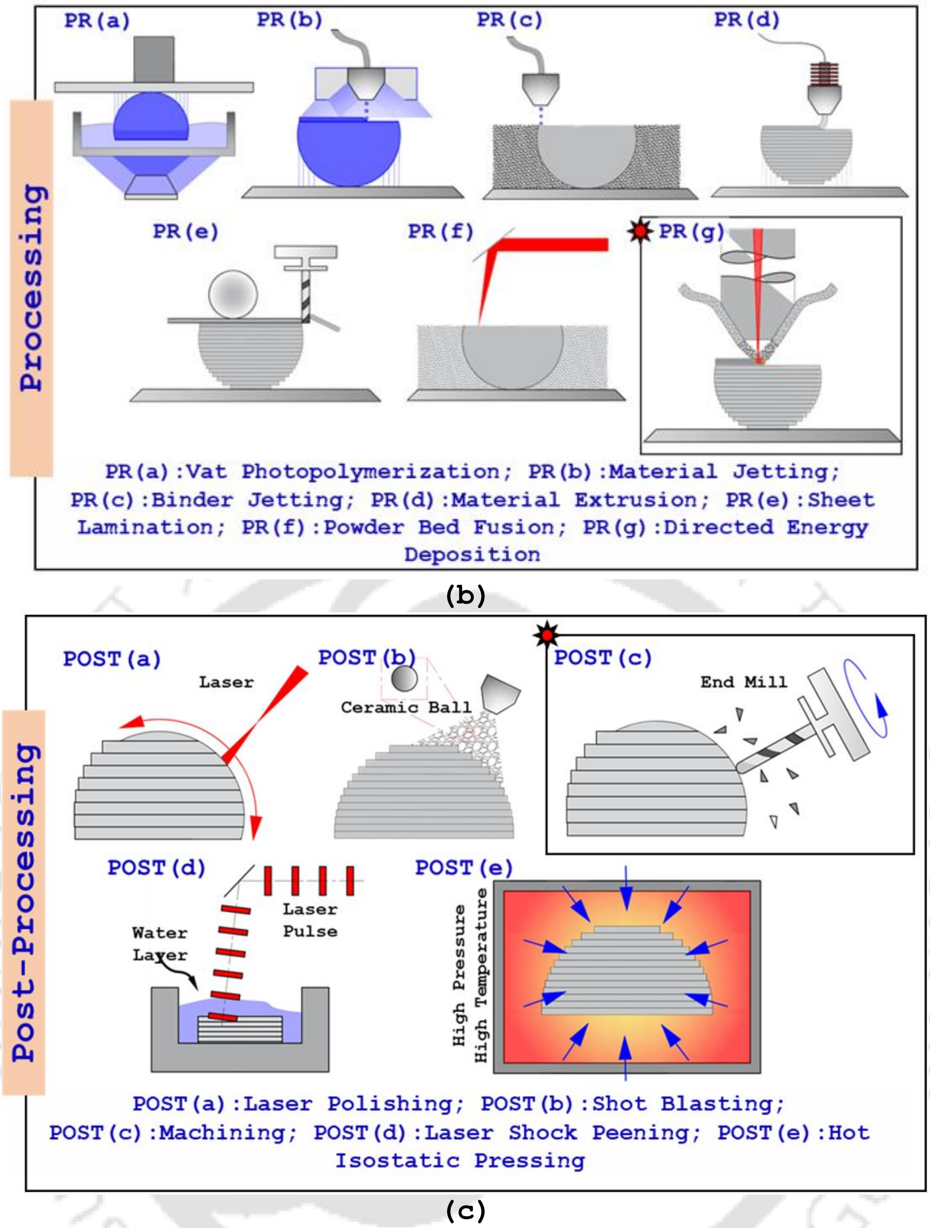

Fig. 1.1: Process sequence for additive manufacturing with (a) pre-processing common to (b) all seven AM processes, as categorized by ASTM, and (c) a few post-processing techniques for quality improvement of AM parts

As far as the historical development of this process is concerned, often, its origin is linked to Sandia National Laboratories (USA) [3]. However, the idea of fabricating structures solely from the deposition of weld metals through the various welding processes is much older [4,5].

Improvement in any technology requires a thorough understanding of its participating sub-systems. An increase in efficiency of each of these sub-systems will translate into increased efficiency of the technology as a whole. AM is perhaps an excellent example of this idea. Conceived in the 1960s [6], the AM has seen immense growth only in the past few decades. One contributing factor to this delayed growth is the lack of peripherals that provide a scaffold for this technology. These supporting technologies (or peripherals) would include high-performance computing, better

CAD handling software, improved economic electronics, etc. [7]. Even though the ideas and compilation thereof presented in this literature review are in the context of DED, with appropriate considerations, they can be extended to other AM technologies as well (such as Dry Powder Printing (DPP) and Selective Powder Deposition (SPD)).

1.1 Metal Additive Manufacturing

Based on the classification put forth by ASTM along with a few additional Metal Additive Manufacturing (MAM) processes, a classification chart is presented in Fig. 1.2. It must be understood that MAM is a highly dynamic field with new and improved processes being introduced at a rapid pace. Therefore, the technology classification, along with its underlying basis, must evolve to keep it comprehensive and relevant.

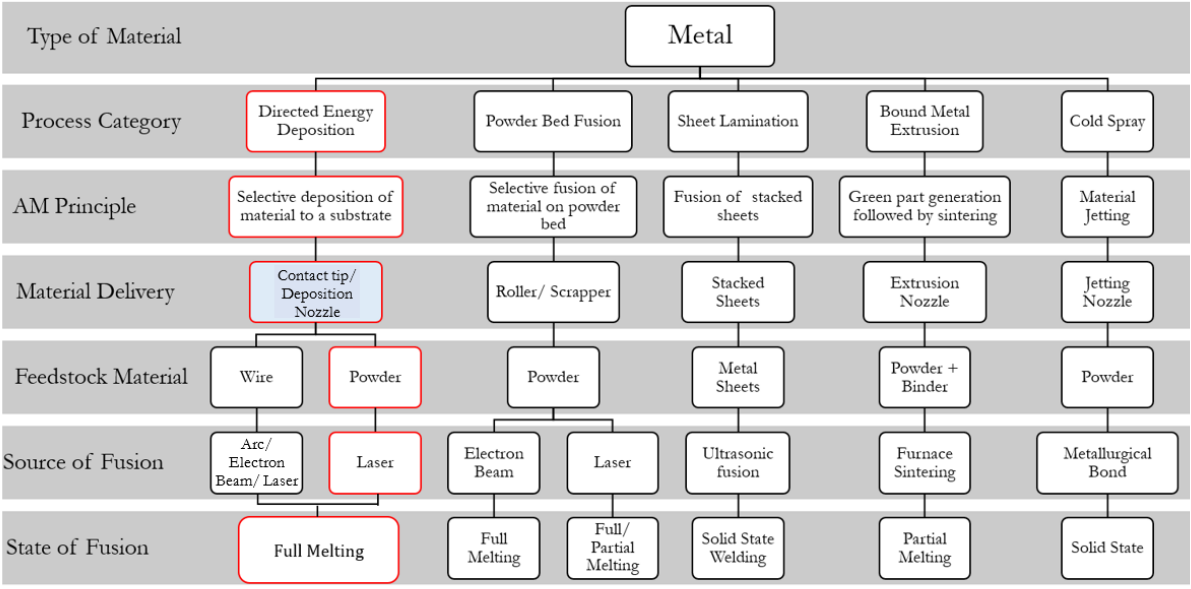

Fig. 1.2: Classification of Metal Additive Manufacturing. Adapted with permission from [8], copyright (2018) Elsevier

Out of all the processes in the classification chart, two laser-based processes are fairly common, namely Directed Energy Deposition (highlighted in red) and Powder Bed Fusion (PBF). Sheet lamination/ Ultrasonic consolidation [9] is a hybrid process that uses a milling head to carve the layer geometry and a rolling sonotrode to join metal sheets. Cold spray [10] is another AM technology in which accelerated powder particles impact the substrate at supersonic speeds and form a metallurgically bonded layer. Bound Metal Extrusion (BME) [11] is a two-stage process where a green part corresponding to the part geometry is built first, followed by furnace sintering to achieve the final strength [12]. Selective Powder Deposition (SPD) [13] is another two-stage metal AM technology where loose powder particles are deposited selectively in a crucible, followed by infusing the structure with an infill material. As the infill melts, it infuses into the loose 'build' powder while avoiding the supporting sand, thus binding them and providing strength to the overall part.

1.1.1 Directed Energy Deposition

DED has three distinct sub-systems; each accomplishes a unique but integral task in the process flow. These sub-systems include a focused heat source (Laser/ electron beam), a feedstock injection unit, and a substrate (print bed) with motion control (CNC table/ robotic arm). Laser/ EB first creates a small melt pool on the substrate, into which feedstock 'build' material (wire or powder or a combination of both) is injected, leading to a growth in the volume and mass of the melt pool. Upon repeating this process for every layer, with geometric inputs provided via a CAD file, the desired part geometry can be achieved. It is important to notice the necessity of a melt pool, without which the powder particles would lack the necessary fusion with the substrate [14,15]. In other words, a melt pool ensures effective layer-to-layer bonding. Reviews by Thompson *et al.*[16,17], and Costa and Vilar [18] give a better appreciation of the complexity involved.

Applications of DED extend from 3D printing of metallic components and part restoration [19] to surface cladding [20] and combinatorial alloy designing [21]. Hip implants[22], blisks [23], large-scale aerospace components [24], conformal cooling channels [25,26], etc., are a few examples of process capability. Fabrication of FGMs with superior mechanical properties is perhaps one of the most significant applications of DED [27,28]. Metal Matrix Composite (MMC) is another budding field of research in DED with a primary focus on feedstock development. Processing of Nickel-based superalloys [29] with relative ease through DED for applications in high-temperature and corrosive environments has further widened the domain of this technology.

Another application of DED is the manufacturing of grid-stiffened structures. Grid-stiffened structures [30,31] are popular in aerospace applications due to their high load-carrying capacity with minimal structural weight. These structures prevent local flutter, absorb vibrations, and possess high bending stiffness while providing convenient mounting points for other structural members and machine components. Essentially, grid-stiffened structures are conventional plate and shell members backed by repetitive patterns of ribs, laid out in a specific geometric configuration, as shown in Fig. 1.3. A special case and popular case of grid-stiffened structures is an isogrid structure formed by repeating ribs in a triangular pattern.

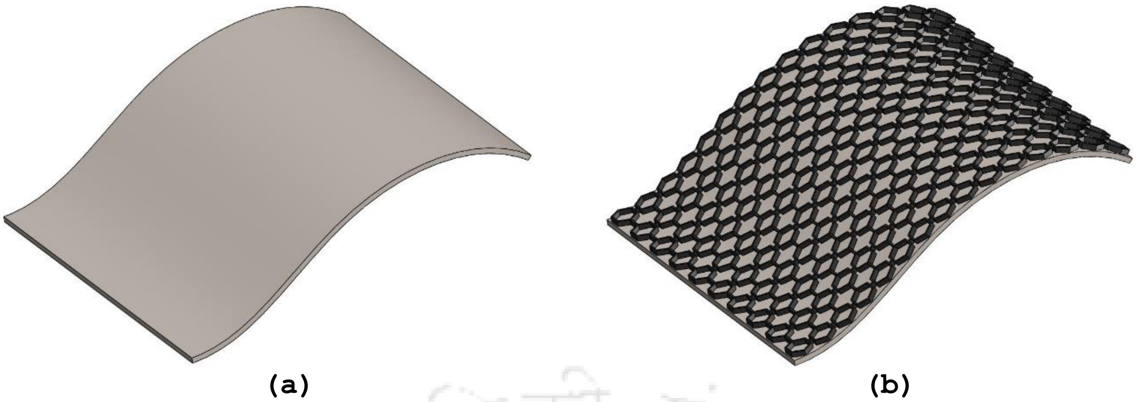

Fig. 1.3: Use of DED to promote high stiffness-to-weight ratio (a) plate structure and (b) grid stiffened structure backed by honeycomb rib pattern promoting high bending stiffness and less weight.

1.2 Feedstock Material

Feedstock for DED can be in the form of a wire or powder. In the case of wires as feedstock and electric arc as a heat source, DED is more commonly referred to as Wire Arc Additive Manufacturing (WAAM). An extension of the welding process, WAAM is capable of fabricating 3D parts at a very high deposition rate. Due to high deposition rates and the use of a non-focused heat source (i.e., an arc instead of a laser), parts generated by WAAM are generally of near-net-shape with poor dimensional accuracy and surface finish ($R_a \approx 200$ μm). Therefore, it is typical of WAAM to be coupled with a CNC mill, which imparts final dimensional accuracy and surface finish to the product, thus forming a hybrid manufacturing system (station) [32,33]. A detailed description of WAAM and a comparative study with powder-feed DED can be found in Refs [34,35]. One advantage of WAAM over DED is high catchment efficiency and deposition rates, thus producing more economical parts at a faster pace. Catchment efficiency is defined as the percentage ratio of the weight of material deposited to the weight of material supplied [36]. Due to the limited availability of materials in wire form, the list of printable materials for WAAM is fairly small. The possibility of powder as feedstock coupled with an electric arc as a heat source has not been extensively explored in the literature[37]. The use of a laser beam with wire feedstock is generally referred to as Wire Laser Additive Manufacturing (WLAM) [38]. Even though some studies have demonstrated the capability of WLAM to achieve high geometrical resolution (700 μm and 300 μm of layer width and height, respectively)[39], the process is often associated with high deposition rates and poor dimensional accuracy. As compared to powder feedstock, wires at the same feed rate and laser power exhibit a higher deposition rate, thus, signifying higher catchment efficiency (≈100%) [40,41]. A comparative study by Syed *et al.* [40] demonstrates 20-

30% higher surface roughness (R_a) values (in the plane of deposition) for powders as compared to wire feedstock. This increase in (R_a) value in the case of powder feedstock is commonly attributed to the loosely adhering powder particles on to the deposited track [40,42]. It must be noted that surface roughness values vary with build orientation and measurement direction [43], thus necessitating further studies in this regard. Generally, WLAM, due to high deposition rates and feedstock size (wire diameter), provides poor dimensional accuracy when compared with powder feed [23]. A similar argument put forth by several studies [39,44] suggests that high dimensional accuracy and small feature size achievable in powder-bed-based processes partially stem from fine feedstock particles, which are employed during the print. Some studies in WLAM have reported the width of the deposited track to be several times the wire diameter resulting in poor resolution of the fine geometric features [39]. However, the dimension of deposited track is highly susceptible of process parameter. A lateral feed of wire feedstock is very common in WLAM systems [38–41], which renders the process monodirectional. Even though the development of coaxial wire feed systems has been suggested in the literature [44], generating a conical, coaxial, and convergent feedstock envelope similar to powder feedstock is a challenging task. The lateral feed of the wire relative to the fusion source makes WLAM systems highly sensitive to feedstock orientation and processing conditions [40,41].

Powders are the most common form of feedstock when it comes to DED. Owing to the mechanism of pneumatic powder metering in most DED setups, powder particle size in DED is much larger as compared to Powder Bed Fusion (PBF). Generally, for PBF, particle diameter ranging from ≈ 10-50 μm [45–47] is preferred, whereas, for DED, it is around ≈50-150 μm [23,48–50]. These particle size ranges should be considered as a general rule of thumb, signifying DED requires larger particle diameters as compared to PBF; however, there are studies conducted beyond these specified size ranges [51,52]. Large particle sizes in DED provide easy flowability and are more likely to break the surface tension of the melt pool upon impact as compared to smaller particles, thus offering higher catchment efficiency [53]. Smaller particles are also susceptible to agglomeration, which decreases their flowability and, consequently, ease of use. Like most process parameters in DED, the selection of powder particle size demands the selection of optimal value. The selection of very small particle sizes leads to decreased catchment efficiency, whereas very big particles result in high surface roughness [54]. From an ease-of-feed perspective, Saboori *et al.*[23] suggests a particle size range of 50-200 μm in DED.

The list of printable materials (in powder form) for DED is quite long. However, there is a clear distinction between powdered alloys and elemental powders. Powdered alloys imply starting with an alloyed billet/ ingot (already alloyed raw material) followed by its atomization (via appropriate means) to obtain the powder fit for DED. On the other hand, the process of DED itself can be used for the manufacturing of alloyed components. Each material constituent, in its elemental (powder) form, is added to the melt pool simultaneously in correct proportions to arrive at the final composition of the alloy, thus leading to the generation of parts with desired material and geometric properties. This method of part production has certain advantages; for example, in the case of Ti-6Al-4V, which is one of the difficult-to-machine materials, DED can be implemented to achieve the desired alloy composition concurrent to the desired part geometry [55,56]. This method of simultaneously achieving material properties and geometric shapes minimizes (or eliminates) the necessary processing of the part through machining.

A combination of both forms of feedstock, wire as well as powder, has been reported in the literature [57–59] and is schematically shown in Fig.1.4. Simultaneous feeding of wire and powder feedstocks leads to higher deposition rates when compared with either of these fed alone. So far, for the same material of wire and powder, no discontinuity in the microstructure of the final deposit has been reported in the literature. However, the feeding of two different materials, one in wire and another in powder form, remains an unexplored field of study.

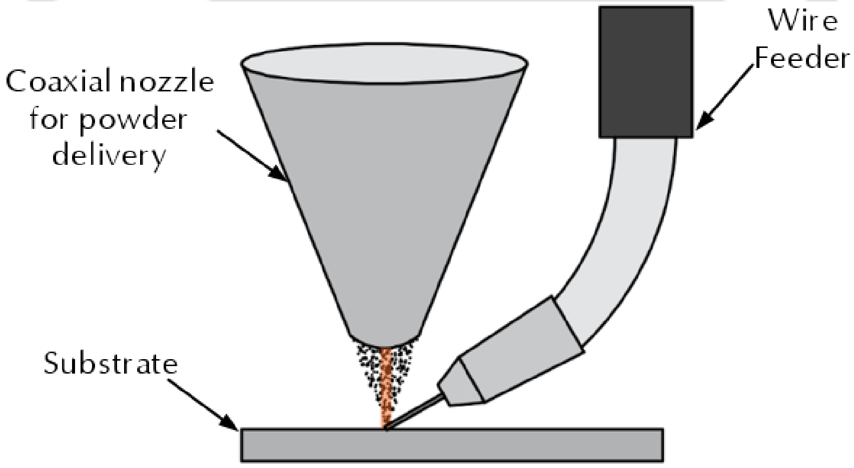

Fig.1.4: Combination of wire and powder forms of feedstocks in DED. Adapted with permission from [60], copyright (2005) Elsevier.

Another form of feedstock is machining chips. Machining is one of the most common manufacturing processes; thus, the utilization of machining waste as feedstock for DED could prove economical when combined as a hybrid manufacturing station. Mahmood *et al.* [61] used a pneumatic method of powder metering and conveyance to deposit machining chips in a DED setup. They also studied the effect of chip size on the mechanical properties of the deposited track. Their results show a successful deposition of machining swarf to produce tracks with very low porosity.

1.3 Powder Feeding System

Powder handling for DED can be categorized into three separate phases: powder metering, powder conveyance, and powder delivery, as shown in Fig. 1.5. The first phase of powder metering involves measuring the right amount of powder from the reservoir (generally a hopper) to be delivered to the melt-pool. Several mechanisms, discussed in the following sections, are used to achieve powder metering. The second phase involves powder transportation from the metering setup to the nozzle, which is most commonly done by an inert carrier gas such as argon. Other conveyance methods include vibration, screw (auger), and gravity chutes. The third phase, which is accomplished via a powder delivery nozzle, is converging the powder stream into a single focal spot.

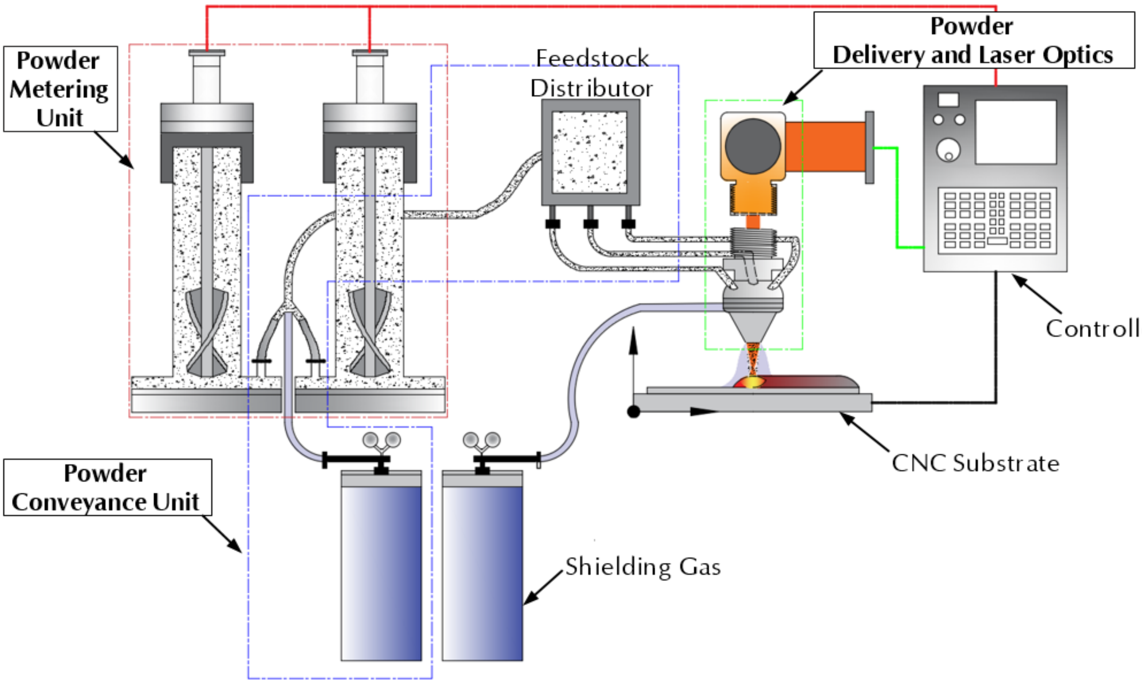

Fig. 1.5: Schematic illustration of Powder-Feed DED setup highlighting phases of powder-feeding

Figure 1.6 outlines these phases for feedstock handling, along with various mechanisms through which they are accomplished. It is important to note that even though a clear distinction between powder metering, conveyance, and delivery is made here but, often, these mechanisms are inter-connected with combined functionalities [62].

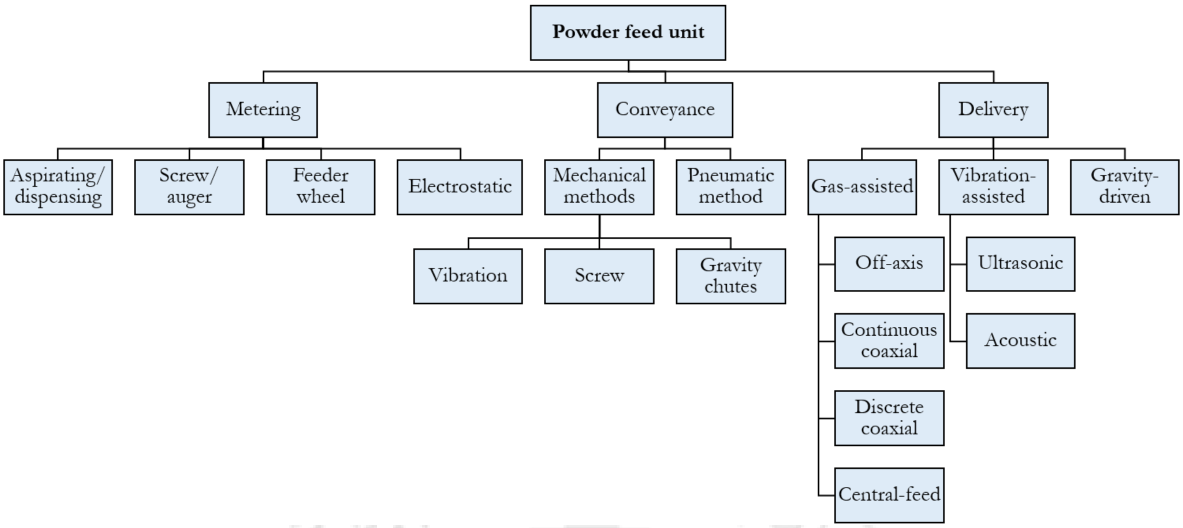

Fig. 1.6: Classification chart of a powder feed mechanism in DED

1.3.1 Powder Metering and Conveyance Systems

Multiple methods can accomplish metering and transport of granular matter; Yang and Evans [63] provide an excellent review on the topic. Each of these methods has several design variants. A few popular ones are discussed here.

A batch of granular matter, when subjected to motion such as vibration or rotation, is susceptible to segregation [50]. This movement-induced segregation of bulk solids often stems from variations in particle sizes, shapes, and densities. Prediction of segregation, given the flow conditions and interacting geometry, is a complex task. Unlike fluid flow, there is no single granular flow equation that fully describes a multi or even a single-component system. Most of the design decisions regarding bulk matter homogeneity for equipment like a mixer and mechanical conveyors are mostly based on small-scale experiments and engineering judgment [64–66]. This problem of particle segregation is exacerbated in the case of fabricating FGMs that require two or more constituents to be mixed in a given ratio before being fed into the melt pool. The motion of granular material, given the localized flow conditions, can operate in multiple flow regions where each of these regions is identified by different normal and tangential particle velocities [64]. Thus, it is possible for a constituent to find itself in a flow region that pushes it faster toward the outlet than the rest of the participating elements [65]. Therefore, a mixer (or distributor) installed down the line from a metering station plays a crucial role in ensuring feedstock homogeneity—however, studies by Prenenkil *et al.*[67] suggests that a powder mixer is as good as the metering station feeding it. A powder mixer can even out small fluctuations induced by a metering station in the feedstock ratio but is mostly ineffective for larger inconsistencies. This places enormous emphasis on accurate and consistent feedstock metering in DED, especially in the context of non-pneumatic systems.

1.3.1.1 Screw/ Auger Method

The Archimedean screw is perhaps the oldest method of metering and transportation for granular matter[68]. One variation of the screw conveyor, developed by Jinping *et al.* [69], involves providing axial vibration to the screw, which assists in the transportation process. The use of a screw conveyor for powder metering and transportation in the DED process was suggested as early as 1988 by Steen and Weerasinghe [70]. The design consists of a motor-driven screw that pushes a specified amount of powder (a function of the screw's rotational speed) into a confined gas chamber. A stream of inert gas picks up the metered powder from the gas chamber and carries it forward to the delivery nozzle. Figure 1.7(b) schematically shows the setup.

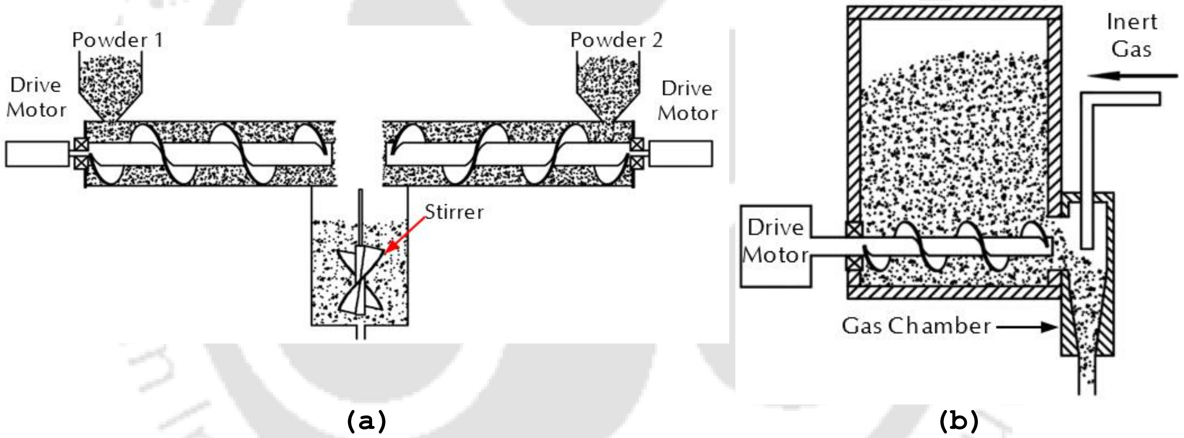

Fig. 1.7: Screw conveyor design for (a) multi-material feed and (b) handling of powder through an auger-based systems in DED. Adapted with permission from [71], copyright (2022) Elsevier.

The setup can be easily fabricated with a twist drill acting as a screw conveyor. Other embodiments, as suggested by the authors, include screws with flanged helix and gas-agitated powder hopper to assist in the handling of cohesive powders. For the creation of FGMs, Jepson *et al.* [72] suggest the use of two independently driven screw conveyors, where each conveyer handles a different powder material, as shown in Fig. 1.7(a). Varying the rotational speed of the screws can meter the ratio of mix.

1.3.1.2 Vibration–assisted Powder Metering and Conveyance

The use of mechanical vibrations to meter and transport granular material is very common in agriculture and food processing industries; however, it is rarely used in MAM. Guo *et al.* [73]

implemented a vibratory feeder in Electron Beam Selective Melting (EBSM) for the fabrication of an FGM comprising Ti6Al4V and Ti47Al2Cr2Nb, Fig. 1.8 shows the setup. Vibratory conveyors, as suggested by Wilkler [74], operate based on either of two mechanisms, "Sealskin" or "Jerk." The "Sealskin" mechanism employs two different friction coefficients for a forward and backward motion of the conveyor platform. The "Jerk" mechanism, on the other hand, implements a slow forward motion followed by a quick return motion (hence the term "Jerk") to achieve material transport.

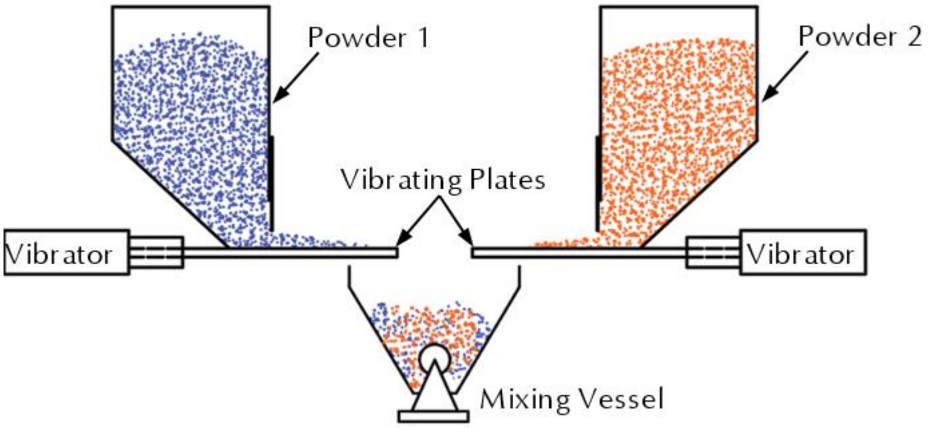

Fig. 1.8: Schematic setup depicting the application of vibration for powder metering and conveyance. Adapted from [73] under Creative Commons CC BY 4.0 license.

Dunst *et al.* [75] suggested a combination of axial (along the transport direction) and radial (perpendicular to the transport direction) vibration for the transportation of fine granular matter, as illustrated in Fig. 1.9.

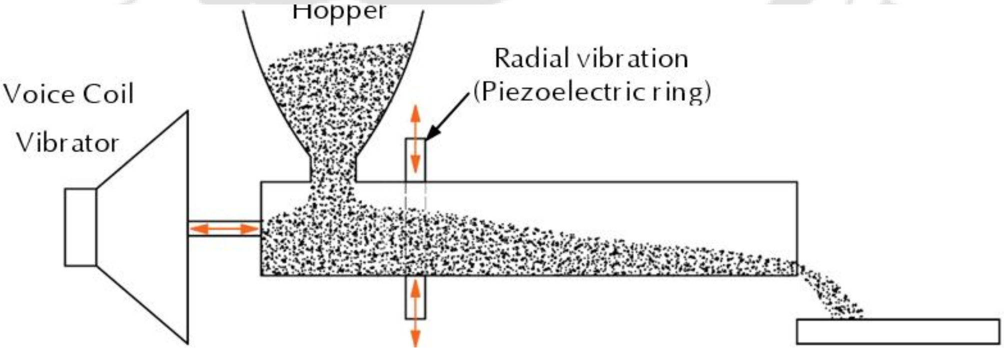

Fig. 1.9: Synchronized axial and radial vibration for metering and conveyance of powder material. Adapted from [75] under Creative Commons CC BY 4.0 license.

During the forward stroke of a vibration cycle, the material is pushed forward. In the backward stroke, however, radial vibration (essentially) lifts the powder particle off the conveyor surface, thereby achieving material transport in one single direction.

1.3.1.3 Gravity-driven Systems

Similar to vibration-based systems, the use of gravity as a method of powder handling in DED setups is very rare. The two systems [76,77], which employ gravity for feedstock handling, are illustrated in Fig. 1.10. For gravity chutes with narrow passageways, intermittent powder flow is observed, i.e., during the flow, granular material separates into a dense (with high particle density) and a dilute region (with low particle density, typically filled with air) thus, giving rise to flow instabilities, Fig. 1.11(a) schematically shows these regions [78].

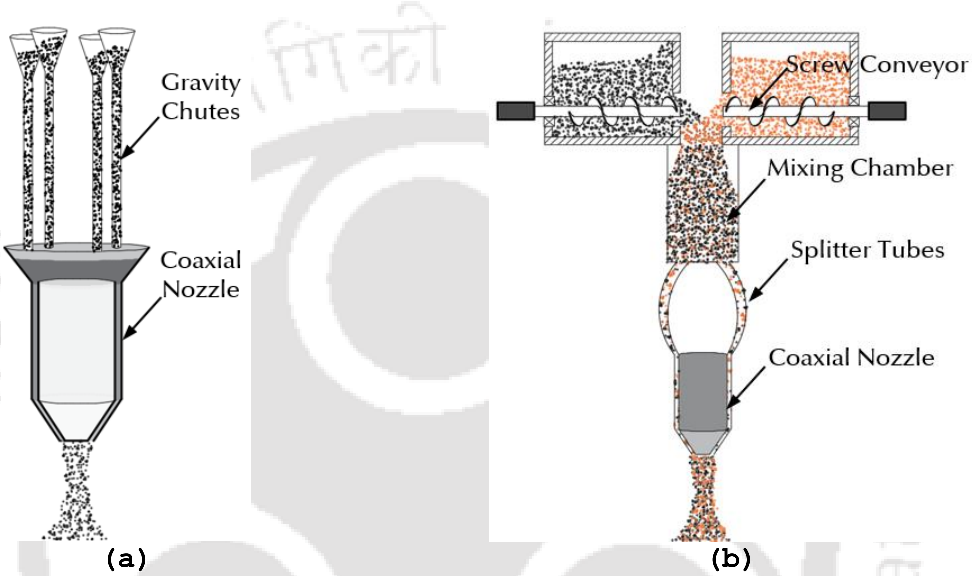

Fig. 1.10: Gravity–driven powder conveyance systems for DED setups with (a) simple gravity chutes attached to a hopper and (b) screw for powder metering, followed by splitter tubes for feeding of powder into a coaxial nozzle. Adapted with permission from [76], copyright (2006) Elsevier.

Another challenge associated with the gravity-based system is the phenomenon of 'Jamming,' shown in Fig. 1.11(b). Jamming stops the granular flow by forming an arch-like structure with the particles butting against each other and the walls of the flow channel (this phenomenon is often observed in salt and pepper shakers). Zuriguel *et al.* [79,80] conducted experiments to understand the process of Jamming. It was found that jamming is highly susceptible to particle morphology; material properties, however, do not play a significant role. With data from multiple experiments, a critical value of $R_C = 4.94 \pm 0.03$ was determined where R_C is the ratio of the orifice radius to the grain radius. Above this critical value of R_C, the probability of a jamming event becomes negligible. Apart from the jamming, control of mass flow rate for the gravity-based system, even though feasible [81], is difficult.

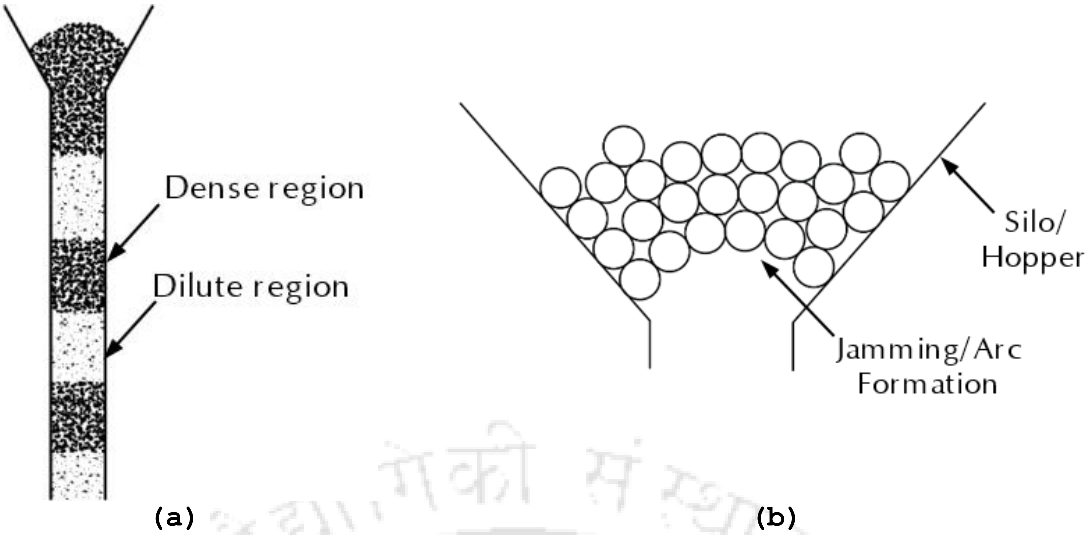

Fig. 1.11: Challenges associated with gravity-driven granular flows (a) intermittent dispensing (b) Particle jamming at the outlet

1.3.1.4 Pneumatic Method

Out of all the methods presented in this article, pneumatic powder feeders are the most popular ones for feedstock handling in DED. Many commercial DED systems [82–84] employ this method for powder metering, conveyance, and delivery. Pneumatic methods, in principle, work by creating a pressure difference within an elaborate system of interconnected tubes and conduits that facilitates the metering and conveyance of powder feedstock. Many mechanisms exist through which one can exploit pressure differences for the transport of granular matter. One such mechanism, developed exclusively for powder delivery in DED setups by Jeantette *et al.*[83] is shown in Fig. 1.12.

The system features an index plate rotating against a stationary base plate. This rotating index has holes at regular intervals. A passageway for the powder outlet is created when the hole of the base plate, one of the holes of the index plate, and an inlet port for compressed gas align with the outlet port of the system. At this configuration, high-velocity inert gas rushes inside the system, and by virtue of the Venturi effect, powder from the hopper is drawn into this stream through appropriate provisions in the design; Fig. 1.12(exaggerated view) shows these provisions. It is to be noticed that powder transfer takes place only when all the holes and ports are aligned. Thus, depending on how long the alignment has been, one can meter powder flow.

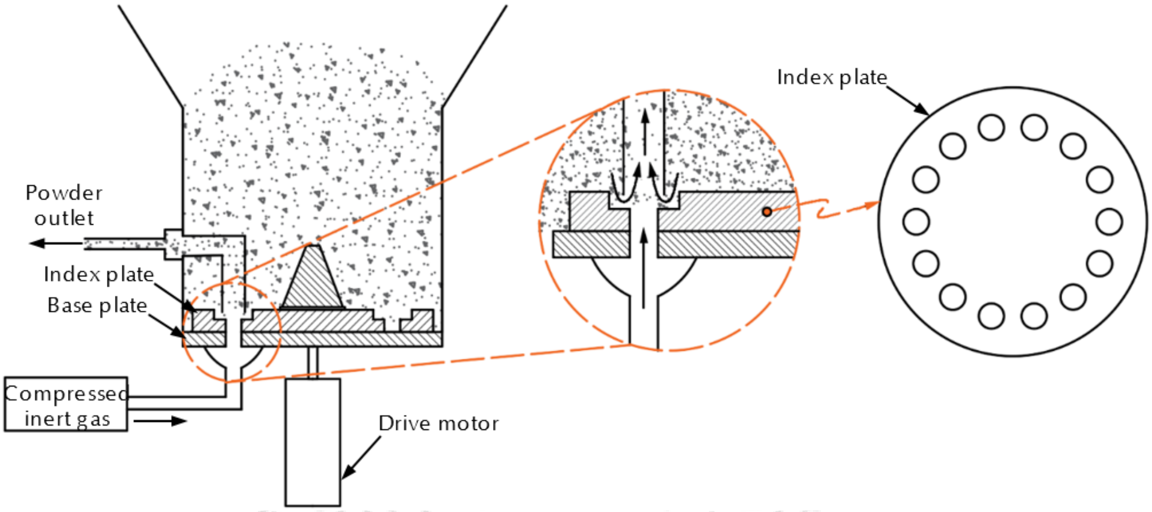

Fig. 1.12: Feeder wheel design for powder metering and conveyance using an inert carrier gas [71,83]. Adapted with permission from [71], copyright (2022) Elsevier.

Similar to the one described above, many such mechanisms exist; Fig. 1.13(a) shows perhaps the most popular of them all. Developed by Douche *et al.* [85] in 1992, the system contains a rotating disk with a groove for powder deposition on its top face. On one end, the groove/ slot is in continuous contact with the hopper, while on the other, a vacuum line is attached. Powder from the hopper, under gravity, falls in the groove, which is then subsequently drawn up into the vacuum line and is transported for further processing. Variation in the rotational speed of the disk varies the amount of powder deposited in the groove, thus, metering powder mass. Another mechanism [86], shown in Fig. 1.13(b), features a metering wheel, the geometry of which forms a pocket for the powder to drop into, which is subsequently ejected by the use of pressurized inert gas. The powder ejected from this pocket is conveyed down the line using an inert carrier gas. Variation in the rotational speed of the metering wheel varies the amount of powder accumulated in the pocket, thus metering powder flow.

Apart from the ones mentioned above, many other pneumatic-based mechanisms for powder metering and transport are reported in the literature [87,88]; some are more popular than others. These systems, depending on the manufacturer, are calibrated such that the rotational speed of the metering disk reflects the powder mass flow rate at the exit. Each of these mechanisms, depending upon their characteristic attributes, has found applications in the pharmaceutical industry, additive manufacturing, agricultural and food processing, etc.

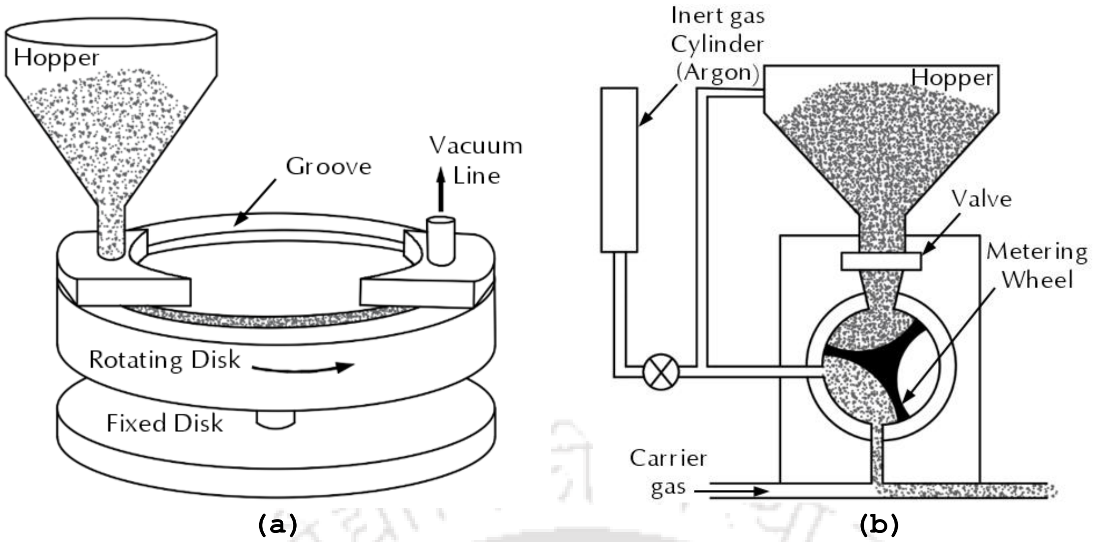

Fig. 1.13: Pneumatic methods for powder metering and conveyance (a) rotating grooved disk (b) rotating metering wheel. Adapted with permission from [71], copyright (2022) Elsevier.

1.3.1.5 Electrostatic Method

The use of the electric field to meter granular flow has been studied in the past. Chen *et al.* [89] demonstrated that for voltage ranging within 1.4 –1.8 kV, granular flow (nickel particles) under the effect of gravity, in the presence of an electric field, separates into dense and dilute regions. However, for voltage values above 2kV (defined as critical voltage), a reduction in mass flow rate with the absence of the dilute region was observed. In another experiment by Balachandran *et al.* [90], a reduction in mass flow rate down to as low as 3% of the free flow was observed. The setup of Balachandran *et al.* [90], shown in Fig. 1.14(b), is drastically different from Chen *et al.* [89](Fig. 1.14 (a)), as the position of electrodes, instead of being perpendicular to the flow direction, is along (or parallel) the flow direction. Two separate theories have been put forward in the literature to explain the retardation of flow under the effect of the electric field.

In the first case (with electrodes perpendicular to the flow direction, Fig. 1.14(a)), a high electric field polarizes the neutral powder particles (i.e., one end becomes slightly positive while the other becomes slightly negative), creating a charge imbalance. This charge imbalance causes powder particles to adhere to the glass walls, especially near the electrodes of the flow channel. These adhering powder particles further narrow the exit opening, thus resulting in a reduced mass flow rate.

As for the second case (Fig. 1.14(b)), no clear explanation of the phenomenon exists. However, an electrical clamping mechanism seems to be a common justification for the effect [91–94]. For the device to be operational, continuous inter-particle contact is essential. Under the effect of a high electric field, when two fairly resistive particles contact each other, a tiny amount of current (of the order of microampere) flows through them. Given the narrow area of contact, the current flowing through the contact point is highly constricted in nature resulting in its local electric fields. This local electric field acting in the nearby regions of the contact point results in the clamping of two particles together, thus retarding powder flow.

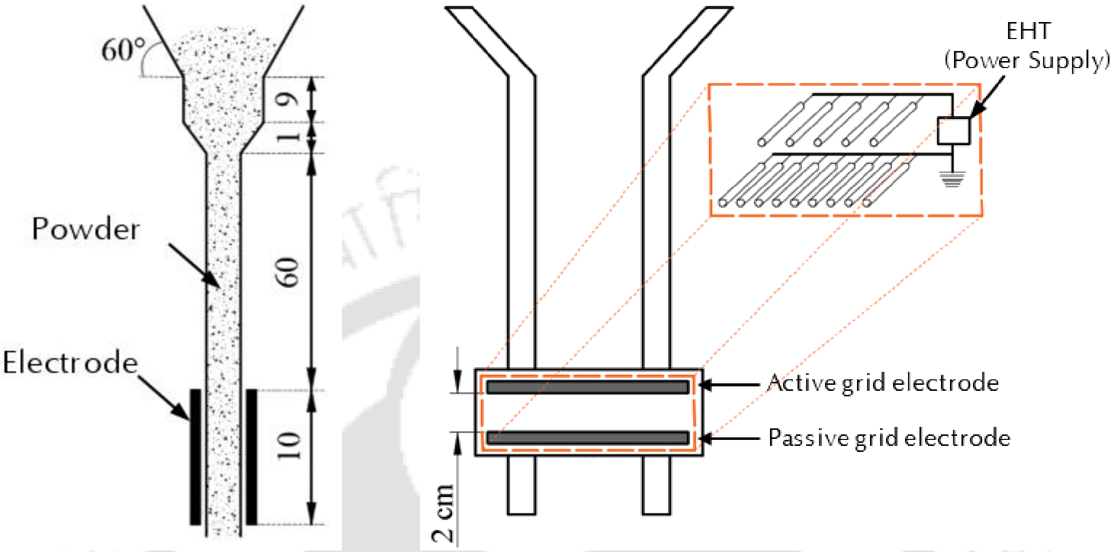

(a) (b)

Fig. 1.14: Electrostatic method of powder metering (a) parallel (adapted with permission from [89], copyright (2001) American Physical Society) and (b) perpendicular electrode configuration (adapted with permission from [90], copyright (1997) IEEE)

Kumar *et al.* [62,95], based on the electrostatic method of feedstock handling, developed a powder bed-based AM process that closely resembles a photocopy machine. The setup uses a corona device to appropriately alter positive and negative polarities between powder particles and their interacting components. This change in polarity pushes and pulls the particles wherever desired (either on a photoreceptive belt or on a print bed), thus generating the part geometry layer-by-layer. The final strength of the part is achieved through furnace sintering. This Powder-Bed AM technology has been given the name 'Electrophotographic Printing' by the authors.

Other methods of powder metering using electric fields are also reported in the literature [96], but most of them are avoided in DED systems due to their inconsistency in mass flow rate and high susceptibility to electrical conductivity.

1.3.2 Powder Delivery Nozzles

Based on feed orientation relative to the heat source, powder delivery nozzles for DED can be of four types, namely, off-axis, discrete coaxial, continuous coaxial, and central feed with an annular heat source. Fig. 1.15 schematically shows these powder delivery nozzles. Apart from an off-axis nozzle (which is typically used for surface cladding of rotary components), the other three types (i.e., continuous coaxial, discrete coaxial, and central feed) possess omnidirectional capabilities making them suitable for the generation of 3D parts and component repair [97]. Omnidirectionality implies invariance of material and geometric properties of the deposited track (unless intended otherwise by the user) irrespective of the travel direction of either the substrate or the deposition head. Lamikiz *et al.* [98] present a review of the various patented nozzle designs.

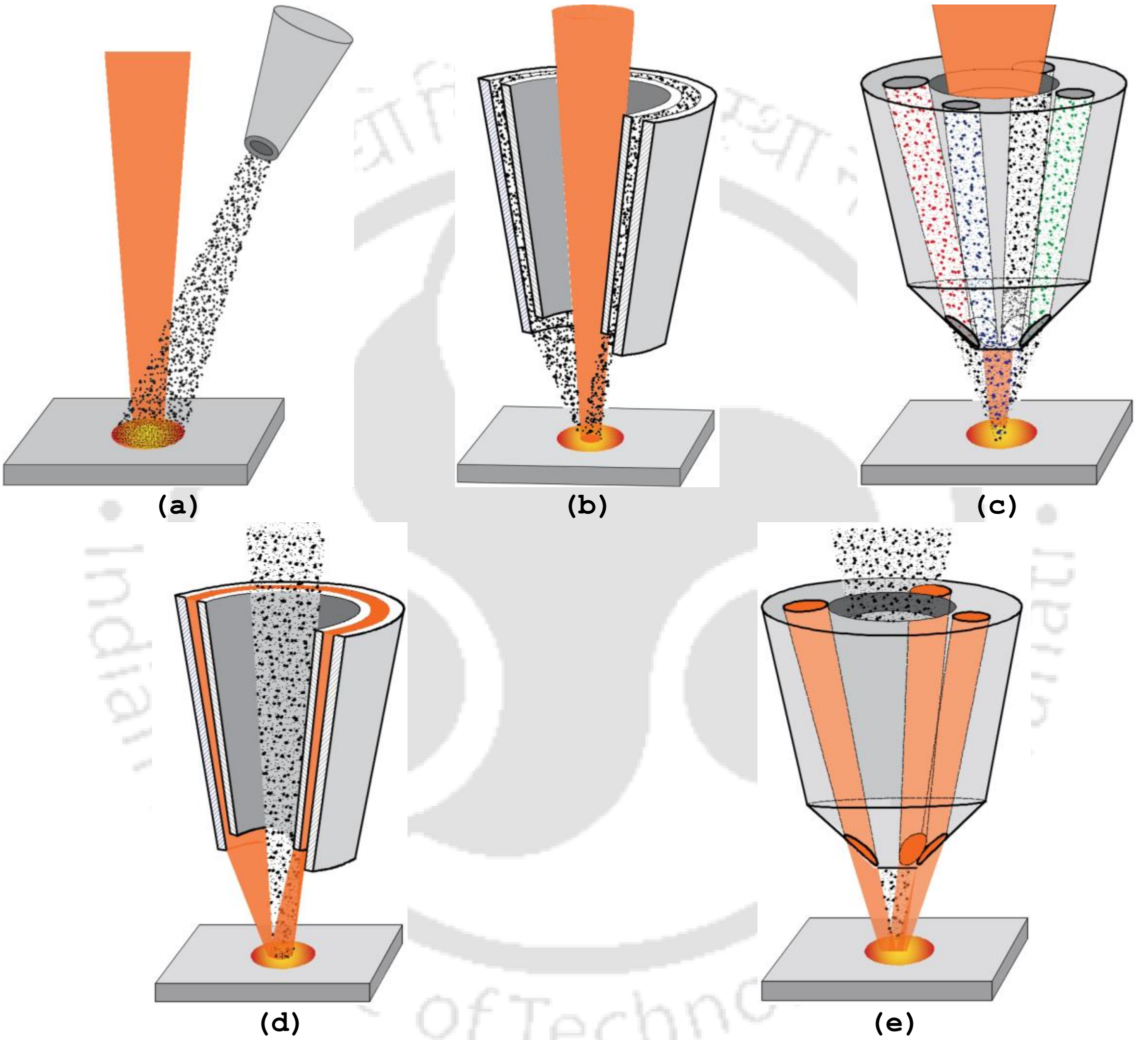

Fig. 1.15: Spatial orientation of powder feedstock with respect to the laser beam for (a) off-axis, (b) discrete coaxial, (c) continuous coaxial and central feed nozzle with (d) annular laser beam, and (e) discrete converging laser beams (Position of laser and powder stream marked by red and grey color, respectively).

1.3.2.1 Off-axis/ Lateral Feed Nozzle

Feeding of powder oblique to the heat source facilitates easy setup design with some limitations. Silva *et al.* [99] present a comparative study between the off-axis and coaxial nozzle for laser cladding of a cylindrical aluminum substrate with aluminum bronze powder. The study reveals a higher catchment efficiency of the coaxial nozzle than the off-axis nozzle, especially at higher powder feed rates. Li *et al.* [100] presented an interesting case of forward and backward scanning direction, each with three possibilities of feed orientation, as shown in Fig. 1.16. Figure 1.16(a, b, and c) represents three possible cases of feed orientation for positive scanning direction (i.e., nozzle ahead of the heat source), while Fig. 1.16(d, e, and f) represents cases of negative scanning direction (i.e., nozzle trailing the heat source).

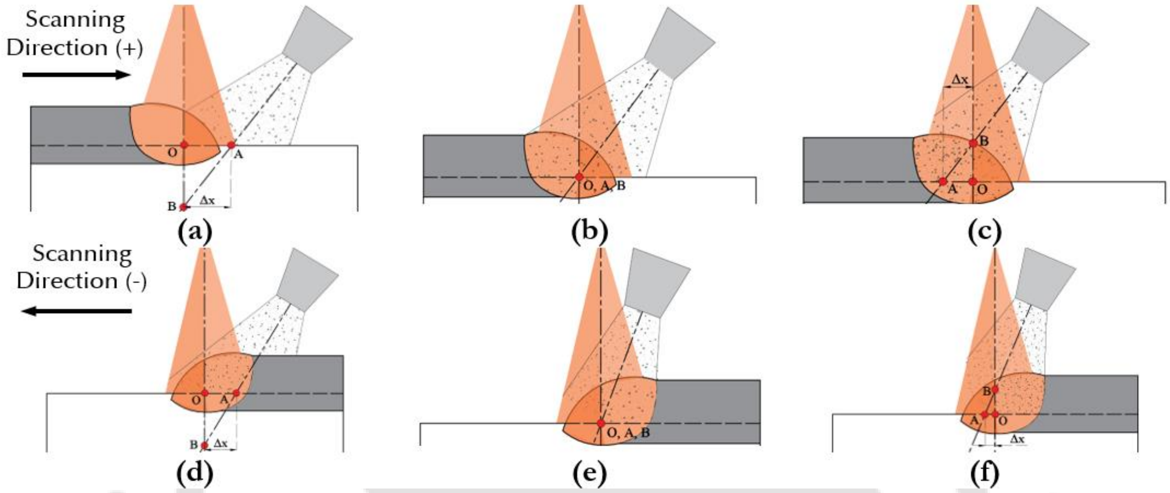

Fig. 1.16: Relative positions of laser and powder stream for an off-axis nozzle, with (a), (b), and (c) showing positive scanning direction and (d), (e), and (f) representing negative scanning direction. Adapted with permission from [100], copyright (2003) Elsevier.

Point 'O' marks the intersection of the laser axis with the substrate surface, whereas point 'A' marks the intersection of the powder feed axis (which is diverging in nature) with the substrate surface. Point 'B' is the intersection point of the axis of the powder feed stream and laser. The horizontal distance between point 'B' and point 'A'' is represented by 'Δx,' which is positive when B is below O; otherwise, it is negative. Part of the melt pool ahead of the laser axis, towards the travel direction, is termed as 'head' while the part behind the laser axis, opposite to the travel direction, is called as 'tail' of the melt pool. Due to the nature of the heat flux coupled with higher thermal conductivity in the trailing part of the laser, a spatially asymmetric melt pool is generated, because of which the head of the melt pool exhibits a lower area as opposed to the tail part. For positive scanning velocity with $\Delta x \geq 0$ (Fig. 1.16(a)), the nozzle injects powder into the head part, which itself is a small area, thus, resulting in poor catchment efficiency. But for the case when $\Delta x \leq 0$ (Fig. 1.16(b, c)), more powder is injected into the tail part resulting in higher catchment efficiency. For negative scanning velocity with $\Delta x \geq 0$ (Fig. 1.16(d)), even though the injected powder's trajectory is towards the tail part of the melt pool, the majority of the particles bounce off of the raised clad layer before reaching the melt-pool thus, resulting in poor catchment efficiency. However, for the case of $\Delta x < 0$ (Fig. 1.16(f)) with negative scanning direction, the catchment is highest, attributed to the fact that a higher percentage of powder particles are being injected into the tail part of the melt pool.

From the above discussion, it is clear that to obtain a higher catchment efficiency, negative scanning velocity with $\Delta x < 0$ should be preferred. This configuration, however, results in a poor surface finish due to the particle adhering to the freshly deposited clad layer. Thus, in order to achieve a good surface finish while at the same time maintaining a reasonable powder catchment efficiency, the authors suggest a positive scanning direction with the nozzle as close to the melt pool head as possible [100].

Lateral feed nozzles create an asymmetry in powder temperature, laser beam intensity, and the resulting melt pool shape. Attempts have been made by researchers to avoid these asymmetries while preserving the simplicity of the setup. Kapil *et al.* [101] developed a wire feed system with an appropriate mechanism to keep the wire always front-feeding to the heat source irrespective of the travel direction. Such systems require on-the-fly calculation of feed orientation and quick adjustment to match the travel direction of the heat source. Similar systems for powder feed have not been reported in the literature.

In order to avoid anisotropy in DED parts and achieve higher dimensional accuracy of the builds, coaxial nozzles are preferred over lateral feed nozzles. Coaxial nozzles, owing to their capability of generating uniform powder distribution (a conical envelope) around the fusion source, also facilitate higher degrees of freedom for the motion of the substrate, thus producing more complex objects.

1.3.2.2 Coaxial Nozzles

Given the limitation of lateral feed nozzles in producing complex parts with homogeneous properties, coaxial nozzles (as shown in Fig. 1.17) are more commonly used in the DED process. In the case of the cladding of cylindrical components, lateral feed nozzles are more relevant. Coaxial deposition nozzles follow a generic design layout for powder dispensing. It includes provisions for shield gas for the protection of laser optics from metal fumes and dust, passageways for a convergent powder stream, and shroud gas for melt pool protection, as shown in Fig. 1.17

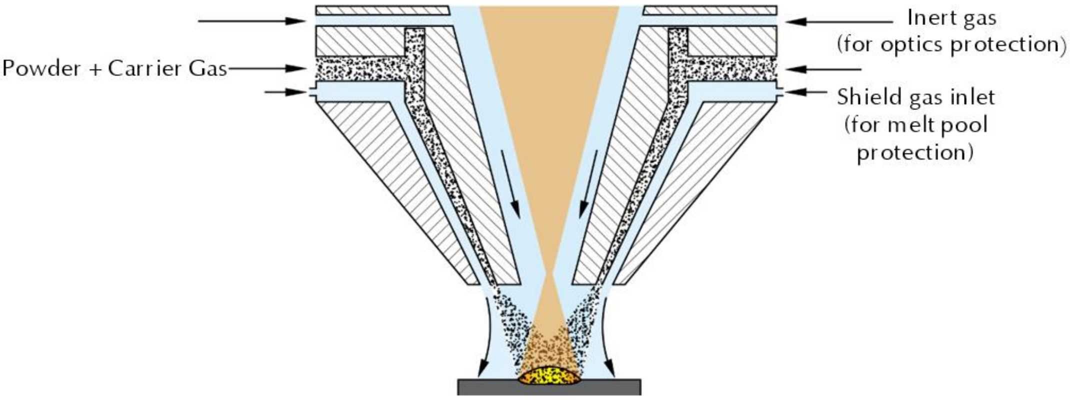

Fig. 1.17: Generic design layout for coaxial nozzles in DED

1.3.2.3 Continuous Coaxial Nozzle

Except for the off-axis, all other types of powder feed nozzles shown in Fig. 1.15(b-e) possess omnidirectional capabilities, with continuous coaxial nozzles being the most popular one. Continuous coaxial nozzles are identified by their annular outlet, formed by two coaxial cones, which are spaced apart by a specified amount, as shown in Fig. 1.17. The cones converge the incoming powder stream to a focal point, the location of which matches that of the melt pool. Ideally, the size of the powder stream focal spot should not exceed that of the melt pool to ensure high catchment efficiency [102]. The location of the powder stream focal spot along the Z-direction (direction of laser beam travel) can be varied by varying the cone angles of the inner and outer cones.

A design feature that seems to be widely popular, especially in filed patents of continuous coaxial nozzles [84,103], is the addition of channels or passageways in the space between two cones. A CFD study by Arrizubieta *et al.* [104] reveals that the nozzles equipped with these passageways gave rise to a convergent powder stream, whereas the ones without these channels generated a divergent powder stream (like a spray) without any clear focal point. Fabrication of such inter-conical channels is accomplished by machining grooves on the outer periphery of the inner cone. After machining these grooves, the two cones (inner and outer) are press-fitted to each other, thus providing a confined passageway for powder delivery [84,103]; Fig. 1.18 schematically shows these cones. A further search of literature into the dimensions of these channels, especially in relation to other process parameters such as particle size, velocity, the position of the focal point, and pressure at the nozzle outlet, highlighted a major gap with little to no studies conducted so far. The presence of inter-cone channels, even though common, are not universal. Ju *et al.* [105] identified key geometric parameters and carried out a design optimization to achieve a higher powder catchment efficiency with maximum Depth of Focus (distance up to which the powder stream remains convergent after having converged at the focal plane). Through CFD analysis, the optimum structural dimension for the given laser power was obtained. It is noteworthy that the nozzle design featured in the study did not include any inter-cone channels.

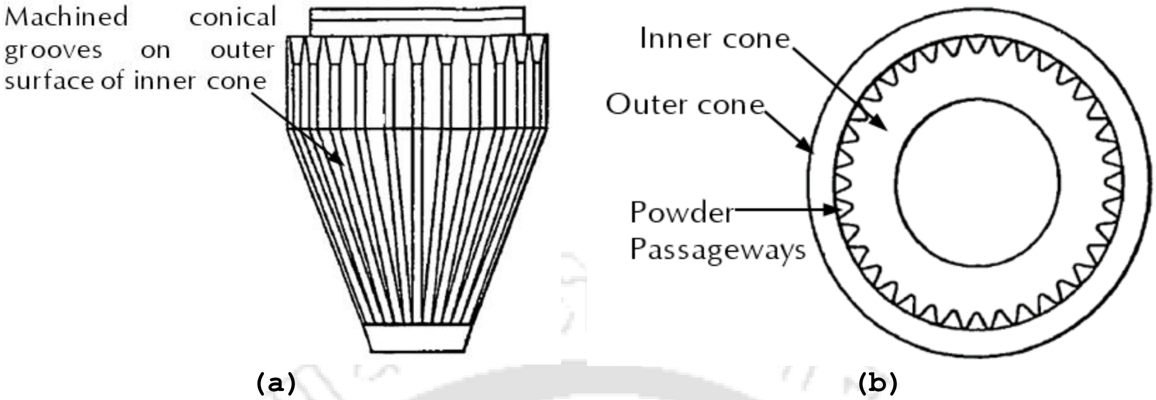

Fig. 1.18: Passageways created by the press-fit assembly of grooved inner cone and smooth outer cone [84]

From the above discussion of lateral feed and coaxial nozzles, two important points emerge. One, the coaxial nozzle should converge the powder stream into a tight focal spot, preferably of the order of laser beam dimension, and second, it should distribute the powder uniformly across its periphery at the exit. Both these conditions ensure invariance of track properties irrespective of the travel direction. Several patents for continuous coaxial nozzles claim such abilities[82–84,106,107]. A design feature that runs common to all continuous coaxial nozzles is a powder holding space similar to a manifold (or an accumulation space), shown in Fig. 1.19. The powder stream coming from the metering station first enters this chamber before entering the annular region between the inner and outer cones. This design feature acts as a mixing chamber for multiple feed materials (either uniformly or creating a gradient) before being dispensed into the melt pool. As a consequence of this feature, FGMs can be realized via continuous coaxial nozzles [108].

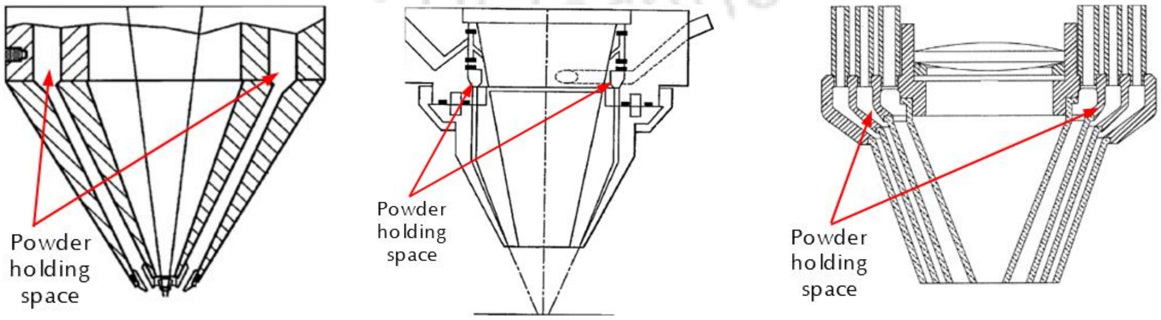

(a) [83] **(b)** [84] **(c)** [106]

Fig. 1.19: Powder holding space for powder accumulation and subsequent dispensing, a feature common to all continuous coaxial nozzles

For most designs, the cone angle (often assisted by a shroud gas cover [109]) converges the powder stream into a focal point. However, Whitfield and Hageniers [106] present an alternative design. This novel design features a vacuum port that not only converges the powder stream but also partially captures carrier and shield gases for reuse.

1.3.2.4 Discrete Coaxial Nozzle

Discrete coaxial nozzles, shown in Fig. 1.15(c), use multiple (usually, but not limited to, 3-4) jets of powder stream, delivering feedstock directly to the melt pool via separate and distinct powder delivery channels. These channels are spatially oriented in such a way that a convergent powder stream can be generated. The inclination of these channels with respect to each other affects powder flow characteristics and shifts the location of the powder stream's focal point relative to the laser beam both across and along the plane of deposition [42,102].

Key geometric parameters for the design of discrete coaxial nozzles, as identified by Wu *et al.*[110] is schematically shown in Fig. 1.20(a). Similar to continuous coaxial nozzles discussed in the previous section, discrete coaxial nozzles also have a few design variations. Figure 1.20(a) shows a generic layout that is common in all variants. Here, R_{in} and φ are the injection radius and injection angle respectively, D_n is the powder channel's exit diameter and S_D is the stand-off distance.

Apart from channel geometry, the spatial orientation of powder jets with respect to deposited clad can also be varied for discrete coaxial nozzles. This variation is brought about by providing rotation to the deposition head (as shown in Fig. 1.20(b, c)), which, even though changes the feed position of powder delivery streams but maintains their concentricity with the laser.

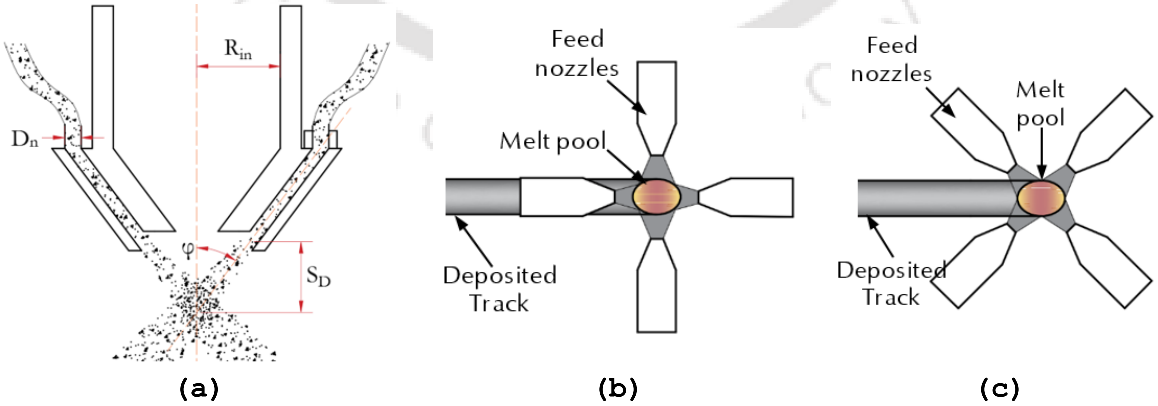

Fig. 1.20: Discrete coaxial nozzle (a) generic design layout (adapted with permission from [110], copyright (2023) Elsevier) stream orientation relative to the clad track at (b) 90° and (c) 45° (adapted with permission from [111], copyright (2018) Elsevier)

For a successful nozzle design, it is imperative to understand the correlation between geometric parameters and their effect on the powder stream generated. The following is the correlation between powder stream behavior and nozzle geometry [110].

- Powder mass concentration, which signifies the number of particles per unit area of the focal spot (in other words, how tight/ small is the focal spot), is negatively correlated to nozzle exit diameter and injection radius. An increase in either of these parameters (D_n and R_{in}) leads to an increase in focal spot size and reduces the powder mass concentration. Injection angle (φ), on the other hand, seems to have a positive effect on spot size. The correlation, even though not linear, suggests that with an increased injection angle, focal spot size reduces, consequently increasing the powder mass concentration at the focal point.
- Standoff distance (S_D) shows a negative correlation with injection angle (φ) and nozzle exit diameter (D_n). An increase in either of these quantities (φ / D_n) decreases the standoff distance and moves the focal plane closer to the nozzle exit plane. Injection radius (R_{in}) on the other hand, is positively related to standoff distance, i.e., an increase in R_{in} increases the standoff distance.

The spatial orientation of the powder stream relative to the deposited clad seems to have no significant impact on flow characteristics. According to the experiments conducted by Tan *et al.* [111], the nozzle's spatial orientation has little to no influence on powder mass concentration at the focal point and standoff distance. This observation was also reflected in the geometry of the deposited clad, which showed no significant changes when nozzle tip orientation was changed from $90°$ (Fig. 1.20(b)) to $45°$ (Fig. 1.20(c)) to the deposited track.

The number of powder streams/ channels that are participating in the deposition has a significant influence on stream characteristics and, consequently, on catchment efficiency. Studies by Kovalenko *et al.* [112] demonstrate that with the increase in powder channels (from 3 to 6), particle velocity in each of the delivery streams reduces. Just by reducing the particle velocity, the catchment efficiency (indicated by the clad area) can be increased.

In the context of discrete coaxial nozzles, consider two cases shown in Fig. 1.21. For the first case, Fig. 1.21(a), powder streams from 4 outlets merge to give a high powder mass concentration at the center. This position is marked as the focal point of the nozzle. An overlapping red spot represents the laser beam. In this configuration, the travel of the cladding head in the direction marked as "A" will yield different track properties as compared with the travel direction marked "B." This disparity arises because, in the travel direction "A" as the laser moves forward it encounters a region of high particle density (formed due to overlapping of powder streams 1 and 2) whereas, in travel direction "*B*" a low particle density region is encountered by the laser.

Ensuring the area of overlapping powder streams is more than the laser spot size (shown in Fig. 1.21(b)) ensures uniformity of the deposited tracks. This analysis also highlights the importance of achieving the correct standoff distance from the substrate, as any change in standoff distance induces a corresponding change in the overlapping area of the powder streams [110]. Thus, improper stand-off distance can not only lead to reduced catchment efficiency but can also affect the track properties.

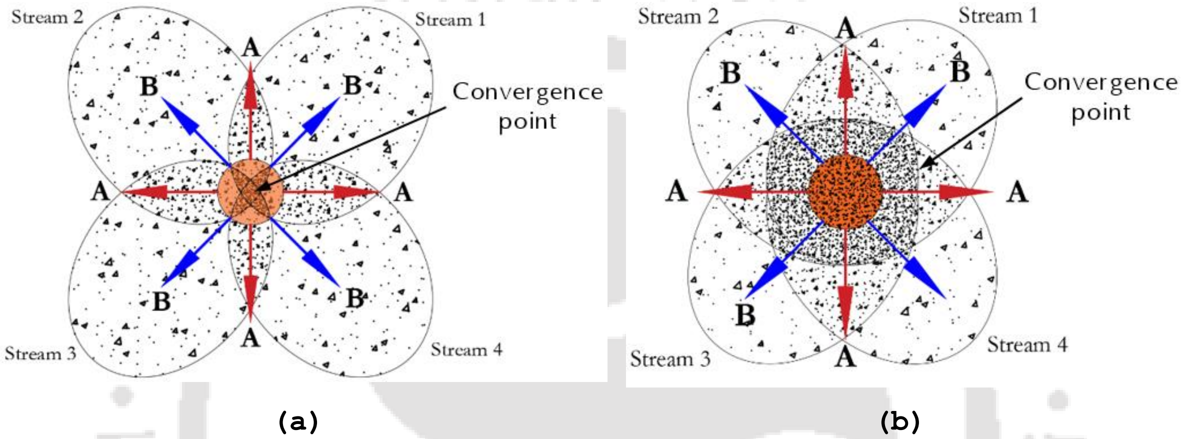

Fig. 1.21: Effect of standoff distance on the degree of overlap of individual powder stream at the focal plane in a discrete coaxial nozzle.

1.3.2.5 Comparison between the continuous and the discrete coaxial nozzle

Very few studies [113] in the literature exist comparing continuous and discrete coaxial nozzles, making it difficult for the end-user to select the one that best suits their application. The study by Zhong *et al.* [113], comparing discrete (3-jet) and continuous coaxial nozzle, takes into account six different performance metrics and compares both the nozzle types against each other. The term dilution signifies the amount of substrate (or previous layer/ track) that gets melted during the deposition process and mixes with the fresh incoming material.

As far as Particle Intensity Distribution (PID) is concerned, both the nozzles exhibit a very similar trend, i.e., a high number of particles at the center of a focal point and a rapid decline in the radial direction. The continuous coaxial nozzle, in the work of Zhong *et al.* [113], shows higher catchment efficiency (indirectly reflected through the clad area) than the 3-jet (discrete) one. Authors attribute this observation to high particle velocity (also reflected in the particle's depth of penetration into the melt pool) achieved in the case of a continuous coaxial nozzle enabling powder particles to pierce through the surface tension of the melt pool instead of rebounding from it.

1.3.2.6 Creation of FGMs and Head Orientation

A gradient in material and geometric properties can be achieved along and across the build direction. The amount of literature on FGMs across the build direction (in the deposition plane) is far more limited than along the build direction (perpendicular to the deposition plane). Consider Fig. 1.22, four powder streams named 1, 2, 3, and 4 are part of a discrete coaxial nozzle, with streams 1 and 2 delivering copper to the left side of the pool and 3 and 4 delivering tool steel to the right. Arrows marked in yellow show the melt pool circulation due to Marangoni convection, which governs the degree of mixing in the melt pool. Such a setup is difficult to accomplish with continuous coaxial nozzles due to an annular outlet.

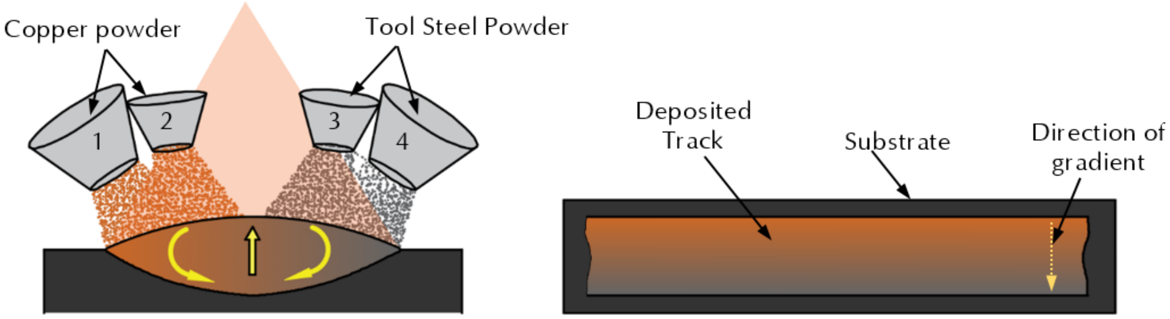

Fig. 1.22: Formation of material gradient constituting Cu and tool steel within a single deposited track, an advantage of the discrete coaxial nozzle over the continuous coaxial one

Another advantage of the discrete coaxial nozzle over a continuous one is the ability to manipulate carrier gas flow rates and flow velocities for individual powder streams. A head tilt of a continuous coaxial nozzle over an angle of 45° renders it non-omnidirectional with increased density of the powder on the bottom than on the top, Fig. 1.23(a).

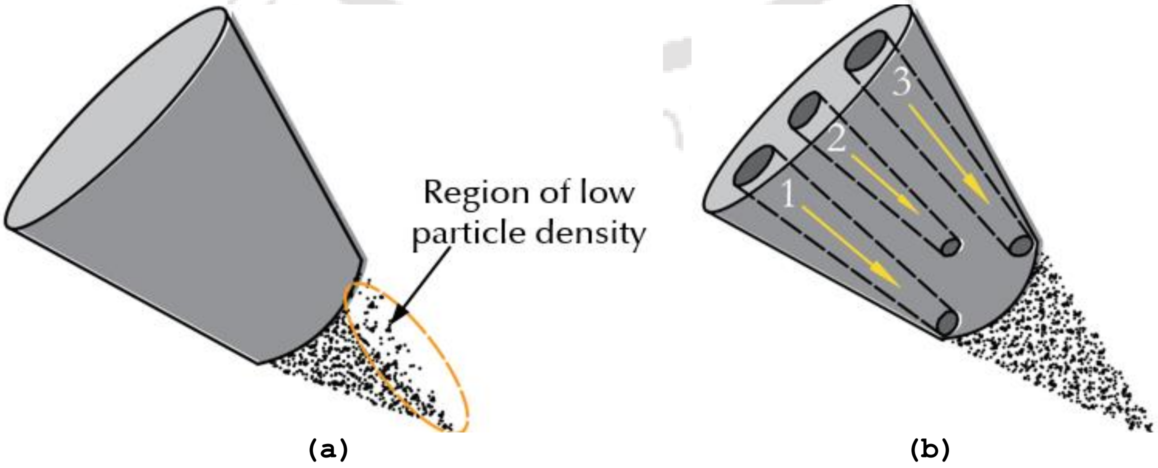

Fig. 1.23: (a) Continuous and (b) discrete coaxial nozzles at an inclination of 45° to the substrate

With discrete coaxial nozzles, omnidirectionality beyond 45° can be easily restored by simply increasing the drag velocity of carrier gas for the upper powder streams (3) as compared to the bottom ones (1, 2), shown in Fig. 1.23(b).

1.3.2.7 Central Feed Nozzles

The spatial orientation of feedstock relative to the energy source plays an important role in the fabrication, repair, and cladding processes. It not only affects the part properties but also has a significant role in process efficiency and, consequently, process economics. So far, in our previous discussions of powder feed nozzles, the laser (the energy source) remained central (almost perpendicular) to the melt pool while powder was injected at an inclination to the laser. Central feed nozzles, as the name suggests, feed powder perpendicular to the melt pool while the energy source is introduced at an inclination to the powder stream, Fig. 1.15(d and e). In other words, the powder stream and the laser beam simply switch their respective positions for central feed nozzle design.

Such configuration has its own advantages and limitations. Govekar *et al.* [114] in their study have demonstrated that central feed nozzles exhibit a higher catchment efficiency than their coaxial counterparts. In the case of coaxial nozzles, the recorded efficiency can be as low as 30% [26,115]**,** whereas, for central feed nozzles, the efficiency is above 80% [114], which is significantly better.

Another common design flaw of angular feed coaxial nozzles can be exposed by tracking the trajectory of a particle from the nozzle exit plane into the melt pool. Consider Fig. 1.24; a particle marked A on its path toward the center of the melt pool interacts with the laser beam at location X. From X onwards, particle A strips a portion of the laser beam's energy and directs it toward the center of the melt pool where it is headed. This, combined with the Gaussian heat intensity profile of the laser beam, results in insufficient heating at the edge of the melt pool and excessive heating at the center. Consequently, the track so generated shows a lack of fusion with the substrate at the edges and excessive dilution at the center [116]. The central feed powder delivery nozzle addresses this challenge by ensuring minimal laser-powder interaction outside the melt pool. As for the laser beam intensity distribution, TEM 10 + TEM 01 mode is preferred over TEM 00 mode for central feed nozzles, thus ensuring sufficient heating of the edges and minimal dilution at the center [114,117]. Fig. 1.25 shows the deposited clad's cross-section with different laser beam intensity profiles.

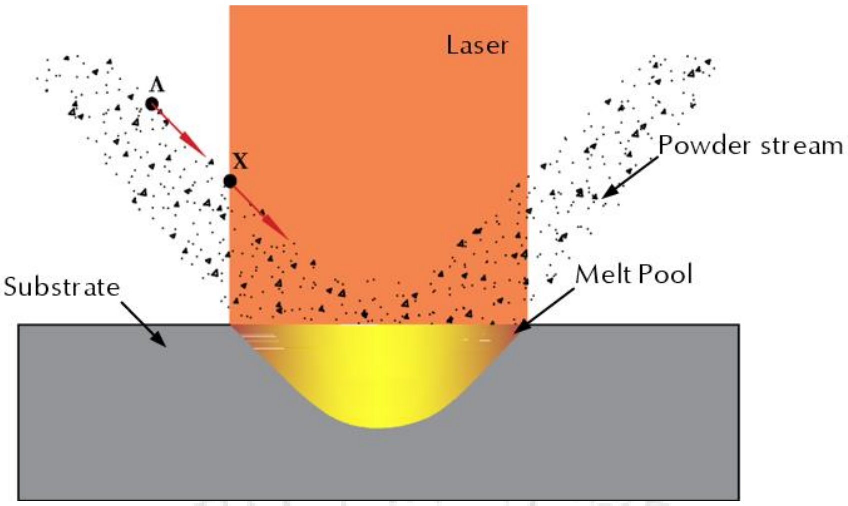

Fig. 1.24: Interaction of powder particles with a laser beam for angular powder feed (coaxial) nozzles

Another advantage of using a central feed powder delivery nozzle is the minimal divergence of the powder stream. As is the case with angular feed nozzles (off-axis and discrete coaxial nozzles), even though the powder stream emerges from a circular outlet, due to the inclination of the powder stream, the profile of injected powder on a horizontal plane (perpendicular to the laser beam) becomes an ellipse. Such a profile is difficult to converge into one tight focal point, thus resulting in decreased catchment efficiency.

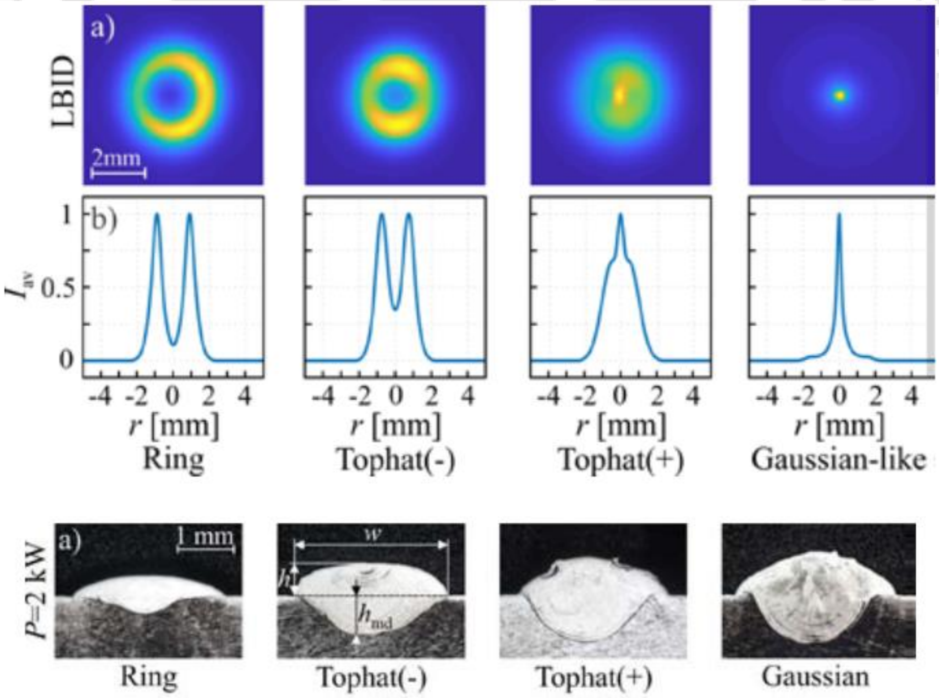

Fig. 1.25: Cross-section of deposited clad track corresponding to various *Laser Beam Intensity Distributions (LBIDs)*. Reproduced from [114] under Creative Commons (CC BY 4.0) license.

Unlike other coaxial nozzles, central feed nozzles, despite their advantages, are very rare in DED setups, partially due to the difficulty in their fabrication. Even though some researchers have come up with different variants of central feed nozzles [118], these designs are still not common.

1.4 Drawbacks of Carrier Gas and Other Alternatives

The use of conveyance gas is widely popular in DED setups; however, they do suffer from certain limitations. Some of these limitations, along with possible alternatives, are highlighted in the following section.

Several studies have suggested that high particle velocity leads to a decrease in powder catchment efficiency along with a deteriorated surface finish of the deposited clad [112,119]. The particles rebounding off of the substrate or due to interparticle collision tend to stick either to the trailing part of the clad track or to the heated nozzle surface [42,119]. This results in the decreased service life of the nozzle and poor surface finish of the deposited track.

According to some researchers [119], the use of conveyance and shield gases increases the convective cooling of the melt pool, thus creating high energy dispersion. Elimination of shield and carrier gasses could have the effect of higher heat intensity for the same laser power, which would make the process more energy-efficient. This theory, however, requires a rigorous theoretical and experimental study which seems to be lacking in the literature.

A proper aspect ratio of a deposited track is crucial in the DED process [116]. It ensures sufficient bonding of the track to the substrate (especially at the edges) with minimum dilution (especially at the center). This criterion, however, is not easy to accomplish when a carrier gas is used for powder handling. Powder particles traveling with high velocities upon impacting the free surface of the melt pool generate a force of sufficiently high magnitude due to momentum transfer. This force acts along the trajectory of the particles. Since a majority of them are routed toward the center of the melt pool, the resulting track often shows high dilution at the center and a lack of fusion at the edges [120]. Along with powder particles, carrier and shield gases often exacerbate the problem by imparting an additional force to the melt pool. The same is the reason for the asymmetrical burn-in shape in the case of off-axis nozzles, signifying a shift in the location of maximum dilution from the melt pool center to its side, as shown in Fig. 1.26[120]. The higher the particle velocity and mass flow rate, the more pronounced the problem [121]. Some studies have also suggested entrapment of carrier gas into the melt pool [122], which leads to increased porosity and, consequently, a decline in the mechanical properties of as-built parts [119,122,123].

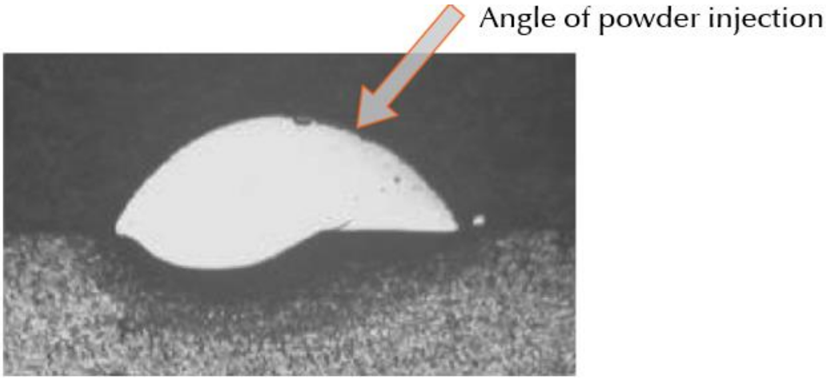

Fig. 1.26: Asymmetric burn-in shape observed in depositions made by off-axis nozzles. Reproduced from [120] under Creative Commons CC BY 4.0 license.

Results of a comparative study by Wang *et al.* [124], summarized in Table 1.1, show better performance of gas-free powder delivery systems as opposed to gas-assisted ones.

Table 1.1: Comparison between vibration-assisted and gas-assisted powder delivery nozzles [119]

Sl. No	Performance Metric	Vibration-Assisted	Gas-Assisted
1.	Sample cross-section	8.60 mm^2	8.09 mm^2
2.	Total Porosity	0.015 mm^2	0.040 mm^2
3.	Surface Roughness	2.14 μm	14.25 μm

Given the limitations discussed so far, it is imperative to improve powder delivery systems for the DED process. Vibration-assisted powder delivery nozzles, discussed briefly in the next section, have been shown by some researchers [119] to be a viable alternative.

1.4.1 Vibration-assisted Powder Delivery Nozzles

Vibrations-assisted powder delivery systems, in principle, exploit the phenomenon of "Jamming" in granular flows within confined channels to initiate, meter and terminate powder flow. Jamming, as discussed briefly in section 1.3.1.3, refers to a self-induced blockage in granular flows under the effect of gravity in confined spaces (or channels). A successful design of such systems requires the dimensions of the flow channel to be less than or equal to four times the particle diameter [79,80]. This criterion ensures a system's natural state of blockage unless acted on by an external agency, which, in this case, is vibration. Variations in frequency, amplitude, and duration of application (pulsed/ continuous) can be used to manipulate the flow properties of granular media [125].

Similar to gas-assisted nozzles, vibration-assisted powder delivery systems have a few variants. Table 1.2 illustrates some of these variants with key setup details and process parameters. It is important to note here that most of these methods do not maintain a concentric laser beam (although such a configuration can be devised). Often, they are employed for *Dry Powder Printing (DPP)*[126], which typically involves dispensing the powder first in a given contour, followed by laser-sintering of the same. An advantage of such an approach is the freedom to change the laser parameters such that it optimally fits the material currently being processed. For example, in the case of SS316L and soda-lime glass [127], two powder hoppers with *Piezoelectric Transducers (PZTs)* dispense each of these materials separately as per the geometry and gradient required. The use of PZTs for vibration-based powder metering can also be found in the works of Zhang *et al.* [127]. Following this step, a laser with appropriate parameters (spot diameter, scanning speed, intensity, etc.) scans the contour matching the pre-placed powder, thus sintering it.

Wang and Li [119] developed a 4-jet discrete coaxial nozzle, schematically shown in Table 1.2(f), that maintains powder-feed concentric to the laser beam. A centrally placed PZT vibrates the powder hopper relative to the flow channels, while a central conduit is kept free for laser beam travel. This design allows for powder injection directly into the melt pool, unlike DPP. The authors report a catchment efficiency greater than 95% with improved as-built track properties for the setup. Wolff *et al.* [128] employ nothing more than a medical syringe with an embedded piezoelectric element to act as an off-axis delivery nozzle. Even though the study was primarily focused on capturing melt pool dynamics during deposition using X-rays and high-speed imaging, the setup itself is extraordinarily simple yet effective.

1.5 Process Parameters and Stream Characteristics

Table 1.3 and Table 1.4 highlight typical values for these geometric dimensions and process parameters. The mass flow rate of powder is critical in the DED process. Contrary to one's intuition, a high mass flow rate to achieve high deposition rates and thus build products faster is not always desirable [121,129]. Haley *et al.* [130], in their study, presented new ideas and observations regarding the "Residence Time" of a particle on the melt pool surface before submerging in it. Through high-speed imaging, it was observed that incoming particles would often rebound from the ones already floating on top of the melt pool. This creates an upper limit on the maximum feed rate achievable for a given melt pool size. This phenomenon of particle rebound was termed the "Self–Shielding Effect" by the authors [130].

Particle velocity is another parameter that plays a significant role in the DED process. Very high particle velocity, as mentioned earlier, is detrimental to the catchment efficiency of the system and results in the poor surface finish of the clad. Also, high velocities often decrease the flight time (time between particle exit from the nozzle and impact on the melt pool) of powder particles, which leads to a decrease in radiative heating by the laser beam [116]. Consequently, the higher the particle velocity, the more laser power is required to melt the particles [116].

Some studies [113,131] have also suggested that too low of a particle velocity is also detrimental to catchment efficiency and surface finish, as particles do require a certain amount of kinetic energy to break the surface tension of the melt pool upon impact and thus achieve penetration. The problem of optimum particle velocity, given the melt pool size, thus becomes a problem of great importance and immediate attention.

The angle of powder injection in the melt pool has been shown to have a significant influence on melt pool stability. An increase in the number of in-flight powder particles that are directly in the path of the laser beam increases the melt pool volatility, which in turn increases the melt pool spatter [128]. Similar observations have also been reported in the case of laser welding in keyhole mode [132]. Given the importance of this parameter, the existing literature in this regard is surprisingly limited.

Table 1.2: Schematic illustration of various vibration-assisted powder delivery setups

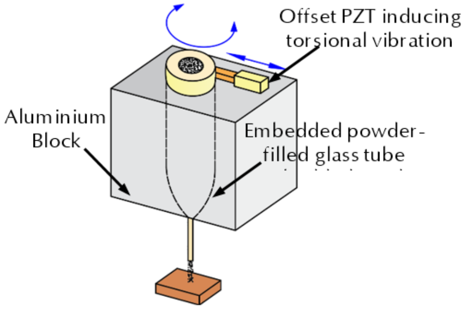

(a) Torsional vibration applied through an offset PZT. Adapted with permission from [133], copyright(2003) IOP Publishing, Ltd.

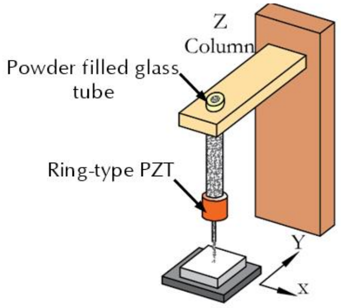

(b) Powder flow actuated by a ring-type PZT for DPP. Adapted with permission from [134], copyright(1996) Elsevier.

Setup Description	Setup Details	Setup Description	Setup Details
A powder-filled glass tube embedded inside an aluminum block vibrated torsionally through an offset PZT.	ϕ_T: 50 and 125 μm ϕ_P: 3-22 μm (Cu, Fe, Invar) ν: 49 kHz $\dot{m}$: 0.005-0.3 mg/s	Powder-filled glass tube vibrated with a ring-type PZT employed for Dry Powder Printing (DPP).	ϕ_T: 110-400 μm ϕ_P: 14 -72 μm (Assorted) ν: - $\dot{m}$: 10-30 mg/s

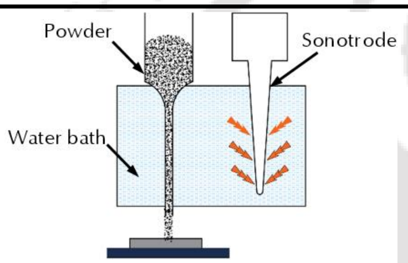

(c) Vibration applied through a water bath. Adapted with permission from [135], copyright(1996) IOP Publishing, Ltd.

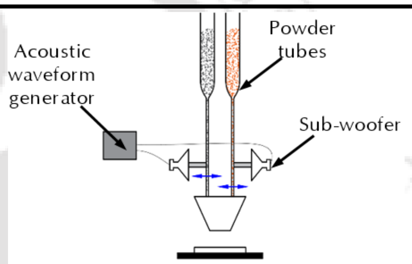

(d) Acoustic vibration through subwoofers. Adapted with permission from [136], copyright(2005) Elsevier.

Setup Description	Setup Details	Setup Description	Setup Details
Uniform pulsed ultrasonic vibration was applied to the capillary tube filled with powder through a water bath.	ϕ_T: 280 μm ϕ_P: 12 μm (WC) ν: 20 kHz (Pulsed) $\dot{m}$: 0.05 mg/pulse	Acoustic vibration is imparted by sub-woofers to the capillary tubes via a rigid connection.	ϕ_T: 380-600 μm ϕ_P: 63-212 μm (Cu and H13) ν: 50-300 Hz (Threshold Amplitude:15 μm) $\dot{m}$: 5.8-35 mg/s

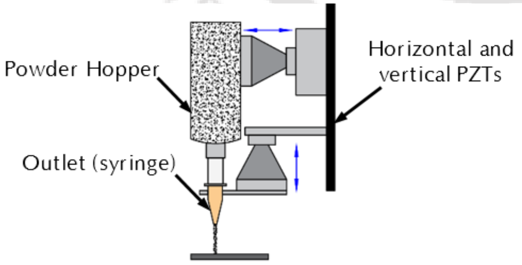

(e) Horizontal and vertical PZTs on a single mount. Adapted with permission from [137], copyright(2020) Elsevier.

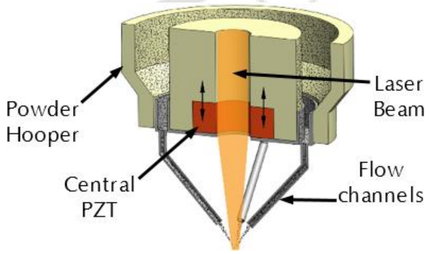

(f) Concentric laser beam and powder feed. Adapted with permission from [119], copyright(2011) Sage Publication.

Setup Description	Setup Details	Setup Description	Setup Details
Two PZTs provide horizontal and vertical vibration to the powder dispenser. A surgical hypodermic needle acts as a nozzle.	ϕ_T: 200 and 350 μm ϕ_P: 10-90 μm (SS316L, Soda Lime) ν: 20 kHz $\dot{m}$: 1.25- 5.80 mg/s	Centrally placed PZT vibrates the flow channel relative to the hopper while maintaining a concentric laser beam.	ϕ_T: 600 μm ϕ_P: 45-150 μm (SS316L, IN718) ν: 20 kHz $\dot{m}$: 120 mg/s

$\boldsymbol{\phi_T}$: Inner diameter of the outlet orifice; $\boldsymbol{\phi_P}$: Particle Diameter; $\boldsymbol{\nu}$: Vibrational Frequency; $\boldsymbol{\dot{m}}$: Mass flow rate

Table 1.3: Geometric dimensions and process parameters for a typical DED system

Sl. No.	Laser Power (W)	Nozzle type	Geometric Specification $\boldsymbol{\phi_T}$ (mm) $\boldsymbol{\alpha}$ $\boldsymbol{F}$ (mm)	Powder Mass flow rate (g/min)	Carrier gas flow rate (l/min)	Scanning speed (mm/s)	Track Dimension (mm)	Ref
1.	500	4-Jet Discrete coaxial	1.19 18.25° 9.27	6.5 (Inconel 718)	4	10.58	Height: 0.1-0.4 Width: 1-1.4	[138]
2.	2100	4-Jet Discrete coaxial	2 ≈25-30° ≈10	21-31 (EuTroLoy)	-	8-15	Height: 0.87 Width: 3.32	[102]
3.	2100	Continuous Coaxial	1-0.50 ≈26-30° ≈13 ± 2	8-15 (EuTroLoy)	-	8-15	Height: 1.06 Width: 3.48	[102]
4.	1000	Continuous Coaxial	4 ≈30° 20	3 (Stainless Steel)	2-8 m/s (flow velocity)	10	--	[139]
5.	325	4-Jet Discrete coaxial	1.12 25° 8.76	30 (SS316L)	3.78	16.9	Dimension of the order of 0.50	[130]
6.	2.4	Continuous coaxial nozzle	1 27° 30	3.6 (SS304)	15	15	Height: ≈1 Width: ≈ 3	[105]
7.	2100	4-Jet Discrete coaxial	1.5 25° 13	6.17 (SS316L)	9	3-8	Height: ≈0.2-0.6 Width: ≈ 2-4	[111]
8.	4500	Single jet off-axis	3 45° 15	20-40 (SS316L)	20-40	-	Track area: 0.48-7.82 mm2	[120]

$\boldsymbol{\phi_T}$: Outlet Diameter; $\boldsymbol{\alpha}$: Powder injection angle from vertical; $\boldsymbol{F}$: Powder stream focal point from the nozzle outlet

1.5.1 Stream Characteristics

Powder delivery nozzles at the focal plane show a Gaussian distribution of powder particles [140,141]. Such a distribution implies the validity of $(1/e^2)$ rule to determine focal radius of powder stream. The rule states that the powder stream's spot radius at the focal (convergence) plane is determined by the location at which the particle density is $(1/e^2)$ of the maximum. Variation of particle density along the horizontal plane (perpendicular to the laser beam's travel direction) can be experimentally measured using the setup proposed by Tabernero *et al.* [141]. The setup contains multiple concentric cylinders, which are placed at the location of measurement in a horizontal plane (perpendicular to the build direction). The amount of powder (by weight) collected by each of these cylinders gives a rough particle distribution at any given plane of measurement.

Table 1.4: Typical process parameters for Directed Energy Deposition

Sl. No	Ref.	Cladding Head								Work Material (Feedstock)			Motion Control		
		Power Source (Laser)			Feed Nozzle										
		Make	Power (W)	Beam Character a. Beam Profile b. Wavelength(nm) c. Spot Dia. (mm)	Make	Injection Angle (From Vertical)	Type	Gas Flow (l/min)	Mass Flow (g/min)	Make	Material	Particle Diameter (μm)	Make	Scan Rate (mm/s)	Working Distance (mm)
1	[130]	IPG Photonics (Fibre Laser)	325 (CW)	**a.** Top Hat **b.** 1064 **c.** 0.94	Optomec 750 LENS®	25°	4-Discrete Coax	3.78	30	Carpenter Inc.	GA SS316L	45-105	Siemens	16.9	8.76
2	[116]	Rofin Sinar (Nd:YAG)	2000 (CW)	**a.** Top Hat **b.** N.A. **c.**3.2	N.A.	20°	Continuous (Coax)	N.A.	4-10	Sulzer Metco	Nickel Chromium Alloy	≈60	N.A.	1.6-5.6	13
3	[142]	LaserLine (Fibre Coupled Diode)	2000 (CW)	**a.** Gaussian **b.** 900-1030 **c.** 4.0	In House	N.A.	4-6 Discrete Coax	5.9	5-40	Sulzer Metco	Co-based Alloy	40-105	N.A.	2-6	5* Defocused
4	[143]	DMG MORI (Fibre Coupled Diode)	2000 (CW)	**a.** Top Hat **b.** 1020 **c.** 3.0	DMG MORI	N.A.	Continuous Coax	4-10	16-20	N.A.	Inconel 625	45-125	Siemens	13-16	N.A.
5	[108]	Trumpf (Yb:YAG Disk)	4000 (CW)	**a.** Gaussian **b.** 1064 **c.** 3.5	In House	N.A.	Continuous Coax	10	15-30	Praxair (USA)	Iron and STS316	44-150	KR 100-3 Kuka Six-Axis Robot	1-10	5-15
6	[144]	IPG Photonics (Nd:YAG Fiber)	645 (CW)	**a.** N.A. **b.** 1064 **c.** N.A.	Optomec 850M LENS®	N.A.	Continuous Coax	N.A.	0.9-28.8	N.A.	SS316L	44-105	Siemens	2-20	N.A.
7	[138]	IPG Photonics (Yb Doped Fiber)	500 (CW)	**a.** N.A. **b.** 1064 **c.** 0.79-0.93	Optomec MR-7 LENS®	18.25°	4-Discrete Coax	4	6.5	N.A.	Inconel 178	44-125	Siemens	8.5-16.9	7.87-12.06
8	[145]	IPG Photonics	500 (CW)	**a.** N.A. **b.** N.A. **c.** N.A.	Optomec MR-7 LENS®	25°	4-Discrete Coax	4	3	N.A.	Ti-6Al-4V	44-149	Siemens	8.5	11.4
9	[114]	N.A.*** (Diode)	2000 (CW)	**a.** Varied between Gaussian, Top hat, Annular **b.** 900-1100 **c.** 3	In House	N.A.	Central Feed	N.A.	8-17	N.A.	SS316L	53-125	N.A.	5-10	≈7
10	[146]	Rofin-Sinar (CO_2)	1200 (CW)	**a.** Annular **b.** 10600 **c.** 1.1 and 2.2	In House (Custom)	N.A.	Continuous Coax	12	8-20	N.A.	SS316L, H13** (GA & WA)	≈100-110	Unimatic CNC	2	N.A. (Constant)

*Defocused distance refers to the amount of substrate offset from the focal plane

**GA and WA particles exhibit different DED characteristics.

*** N.A. (The authors failed to find the corresponding data)

1.6 Toolpath Planning

Toolpath planning is an important aspect of Additive Manufacturing. The motion of the deposition head/fusion source has a significant role to play in both the geometric and material properties of the printed parts. The cost of the printed part, energy consumption, print speeds, thermal distortions, surface roughness, part stiffness, etc., are greatly influenced by the toolpath (deposition) strategy implemented during the print. Several toolpath strategies exist in the literature; some are generic in nature, while others cater to specific outcomes. A review by Jiang *et al.* [147], based on the objective of the path planning strategy, proposes three categories: (a) improvement in print quality, (b) increase in material yield, and (c) achieve special material or geometric properties (such as Functionally Graded Materials (FGMs), Topologically Optimized Prints (TOP), Porous Prints, etc.). The selection of a toolpath strategy is a multi-faceted task, taking inputs from users, analyzing the desired output, and selecting the optimum toolpath that best fits the outcome.

1.6.1 Toolpaths Planning for Uniform Density Parts

Several space-filling algorithms exist in the literature; a few common ones are raster [148], zigzag [149], and spiral [150]. Apart from these generic strategies, the contour offset toolpath [151], fractal space-filling [152], and island scanning [153], as illustrated in Fig. 1.27, are a few other methods of toolpath generation for space-filling in AM. Table 1.5 presents a summary of several toolpath algorithms that have been previously studied in the literature. As previously mentioned, most of the toolpaths cater to one or more specific objectives. Studies have suggested that reducing the length of the scan lines promotes isotropy and minimizes thermal distortion [154,155]. This can be achieved using the island and fractal-based scan strategy [153]. However, the part isotropy through these strategies comes at the expense of part accuracy. Material deposition through a toolpath featuring a high number of turns, such as Hilbert and paintbrush, without any corrective measures (through closed-loop feedback control), could distort the part through over-deposition at the corners [156–159].

In a study carried out by Comminal *et al.*[159], three possible causes of corner over-deposition were proposed for polymer-based FFF, namely, corner rounding, corner swelling, and corner ringing. Corner rounding originates from the local smoothing of a deposition path at corners, whereas corner swelling is attributed to continuous material extrusion with a reduced printing speed while negotiating a sharp turn. Corner ringing, on the other hand, arises from vibrations induced at the corners due to variations in traction forces at a corner. For the case of powder-based Directed Energy Deposition(DED) systems, instantaneous regulation of powder inflow as the deposition approaches a corner is proposed by Arrizubieta *et al.* [156] for uniform material deposition. In the case of Powder Bed Fusion (PBF), studies have shown protruding material at the edges and corners of the fabricated parts; however, studies of this phenomenon within the context of an infill strategy are limited [160,161].

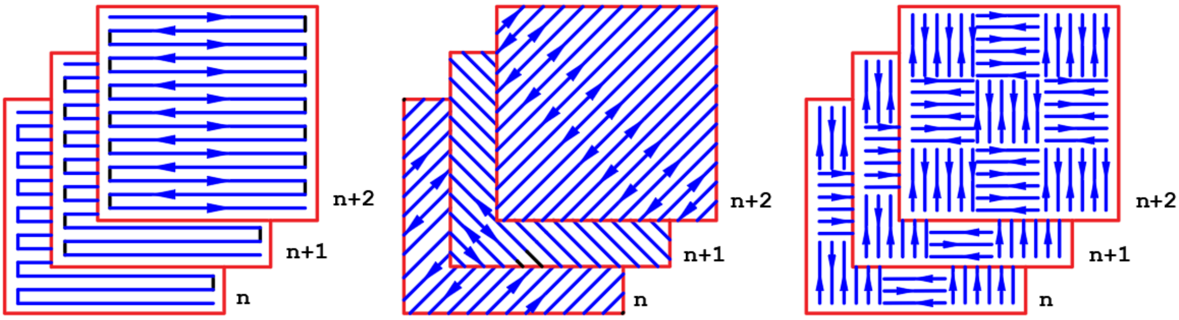

Raster Scan

Inclined Raster Scan
(90°layer rotation)

Island Scan

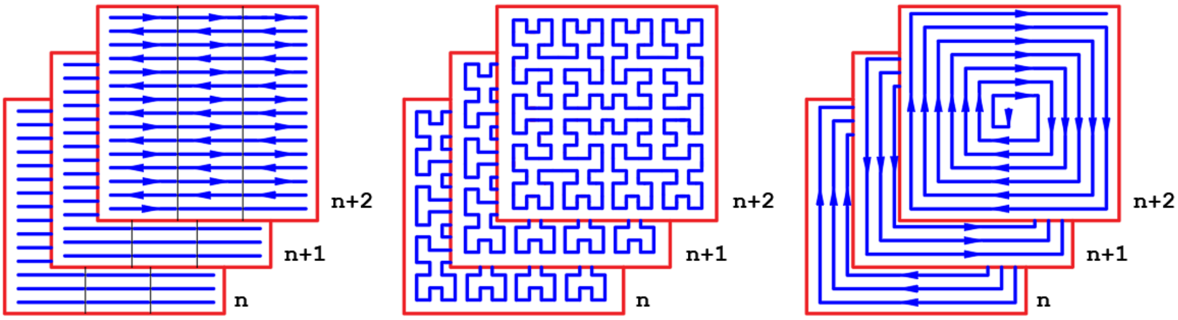

Paintbrush Scan

Hilbert Scan

Spiral Scan
(Alternating inside
out and outside in)

Fig. 1.27: Layerwise scanning strategy for area filling in Additive Manufacturing

Studies have suggested that direction parallel algorithms promote part anisotropy [162,163]. Lin *et al.* [164] suggest a Maze-like toolpath that first discretizes the printing area into a series of regions, followed by the generation of a Space-Filling Curve (SFC). The SFC generation comprises generating a set of grid points that are connected through a recursive backtracking algorithm. The toolpath demonstrates relatively low part anisotropy with high deposition efficiency. Work by Zhai *et al.* [165] implements the Travelling Salesman Problem (TSP) scheme to obtain a toolpath for porous structures. The toolpath generation primarily consists of dividing the print region into subregions, which are then traversed based on a TSP scheme. The subregions are later merged and filled with the Fermat Spiral curve to further increase the process efficiency.

Table 1.5: Methods of Toolpath Generation for Area Filling in AM

Ref	Toolpath Strategy	Underlying Working Principle and Characteristics
Hybrid	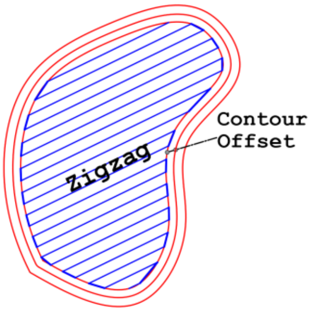 Image adapted with permission from [166], copyright(2013) Elsevier	• For each sliced layer, use the NURBS curve for an accurate representation of the boundary. • Offset NURBS to generate a contour-parallel toolpath for geometrical accuracy. • Use a zigzag-based toolpath scheme for interior area filling for higher build efficiency and reduced computational time.
(MAT)	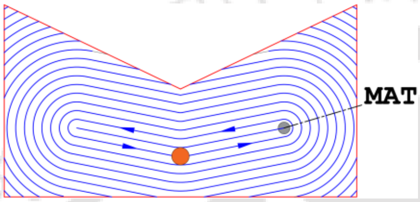 Image adapted with permission from [167], copyright(2015) Elsevier	• Compute Medial Axis Transform (MAT) for a given geometry. • Categories computed MAT into branches and sub-branches. • Use the computed branches to form various branch loops. • Recursively offset the loops to generate the toolpath.
Hilbert Curve	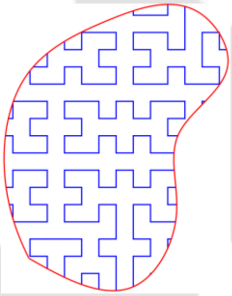 Image adapted with permission from [171], copyright(2018) Elsevier	• The 'Hilbert Curve' can be assumed to be a composition of a set of unit shapes. • Several algorithms for curve generation exist [168–170]; however, the placement of multiple unit cells in the correct orientation (achieved through rotation), which is then connected to produce a 'single curve,' provides a simple and elegant solution[170].
Water-Pouring	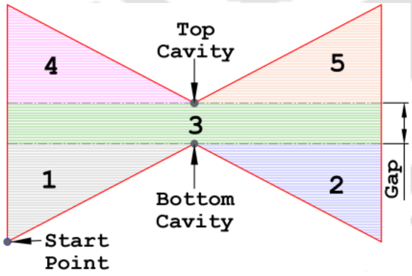 Image adapted with permission from [172], copyright(2019) Elsevier	• This strategy termed the water-pouring path-planning method, starts tool motion by first defining a start point and deposition direction. • Upon encountering a gap (marked 3), the valley area (marked 2) is filled first, followed by the gap area. • Upon encountering the 'top cavity,' one side of the cavity (marked 4) is filled, followed by another side (marked 5).
Bézier Curve	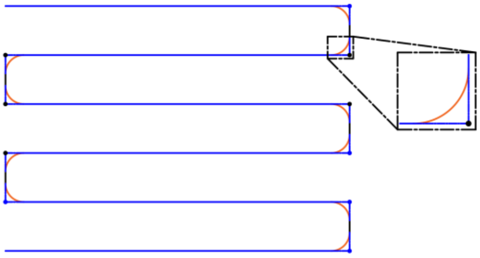 Image adapted with permission from [158], copyright(2017) Elsevier	• The toolpath is obtained by merging straight lines and parabolas in a sequential manner. • This strategy can be implemented for a 'jerk-free' tool motion, ensuring a constant velocity and uniform deposition.

It is often the case that, the deposition toolpaths are borrowed from machining and partly adapted to suit AM [173]. However, the concerns in machining with regards to part quality are significantly different from AM. It is to be highlighted that the process of machining, as it imparts geometry to the raw stock, does not alter the mechanical properties of the material it started with. A variation in the surface properties due to cutting forces in machining is to be expected, but the underlying mechanical and microstructural properties remain the same. This is not the case with AM, as the part, during fabrication, goes through severe thermal gradients leading to internal stresses[173–175]. Moreover, the material deposition, owing to minor variations in material feed and the deposition strategy, is not always uniform. For instance, consider the work of Thanumoorth *et. al.*[176], which investigates the effect of rotation in raster deposition between two successive layers. The study shows that an infill rotation of $45°$ exibits optimum strength and ductility. Furthermore, samples fabricated without and with infill rotation showed larger and finer grain size, respectively. A difference in the cooling rates were also observed with the studied infill strategies. A similar study for thin substrates by Soffel *et. al.* [177] showed that deposition strategy with long longitudinal cladding tracks produces significantly smaller cantilever distortion when compared to short transverse tracks. An interesting study by Woo *et. al.* [178] on FGM fabricated through DED revealed that an island scanning strategy significantly reduces that residual stress values as compared to bidirectional scanning. However, island scanning strategy showed several internal defects along the corner junction of the interfacing island. Another interesting view put forth by Wirth *et al.* [179] and Soffel *et. al.* [177] relates laser interaction time to part porosities observed in DED. Higher the laser interaction the longer the fluid motion in the melt pool, which in turn, supports the escape of entrapped gases thereby increasing part density. Although the toolpath strategy avoids variations in interaction time during deposition, however, while negotiation sharp corners/ turns in a toolpath, often adjustments are made to the depositions speed with may inadvertently change the interaction time. The amount of literature directly addressing this possible phenomenon is limited and further studies are necessary to arrive at a conclusive result.

Generally speaking, CNC machine tool platforms, irrespective of whether they come from the additive or the subtractive side of manufacturing, move sequentially from one point to the next. In the case of machining, it is the cutting tool that moves, whereas, in the case of AM, it is the deposition head or the fusion source. Moving from one point to the next involves interpolation, which could either be linear or circular in nature. Rapid changes in the direction of movement, specifically when taking a sharp turn, induce high accelerations. A detailed account of these accelerations can be found in the work of Jozwik *et al.* [180]. Rapid accelerations in a CNC platform are detrimental to both the machine tools and the part being fabricated. On the one hand, high accelerations induce vibrations in the machine tool, which could excite the natural frequencies of the structure, thereby compromising machine rigidity [181]. On the other hand, these accelerations inadvertently vary the processing parameter (such as deposition speed and travel velocity), which could lead to over or under-deposition of material [156]. Several approaches exist in the literature to minimize the accelerations in a CNC platform [182–184]. One such approach [158] of using a Bézier curve is presented in Table 1.5. The work presented here addresses the question of uniform CNC motion and, consequently, that of uniform deposit through minimizing the 'number of turns' in an area filling toolpath.

The underlying idea of the toolpath strategy, proposed as part of this work, exploits the fact that the toolpath of the deposition head (or the analogous unit as dictated by the AM process) can be treated as a salesman with an objective to visit specified grid points (analogous to cities). The navigation of the grid points can be carried out with a preset objective, such as minimizing the total distance traveled with a constraint to mandatorily visit each grid point once and only once. Even though such ideas have been explored in the past [185,186](mostly in the context of machining), the present work explores the effect of grid points, their relative position with each other, and the outer boundary on the resulting toolpath. The area-filling strategy proposed here offers a minimal number of retractions and turns and is a closed-loop path, having a common start and stop point.

1.6.2 Toolpath Planning for Functional Graded Materials

Functionally graded materials can be broadly categorized into two varieties: material-based and density-based FGM. An FGM can also be a combination of both. A material-based FGM uses multiple print materials, each of which is integral to the fabricated part; however, the percentage of each species varies as dictated by the user[187–189]. A density-based FGM primarily focuses on achieving tailored part density through selective material deposition over the input space. This spatial variation of density is a consequence of path planning and not the property of the material (as would have been the case for the material-based FGM). Spatial variation in density can be achieved by considering either the entire 3D space or a layer at a time. Since *Additive Manufacturing (AM)* uses layerwise deposition, an algorithm for density gradient in each layer (2D) can generate spatial variation in 3D space. In the work of Prevost *et al.*[190], the spatial variation of density within the part considers the part volume(3D), which is then redistributed to achieve the desired gradient. This variation in density causes a shift in the *Center of Gravity (CG)* of the part, consequently balancing the object (models, figurines, etc.) in a desired pose, schematically shown in Fig. 1.28(a). The algorithm uses a voxel-based approach jointly modifying (carving and/or deforming) the interior and the surface of the model to achieve the spatial gradient. Another implementation of a voxel-based approach was proposed by Telea *et al.* [191], which detected the local thickness of the part being printed and compared it to the printer's print resolution for printability assessment. An interesting application of spatial density variation can be found in the works of Stava *et al.* [192], wherein the proposed algorithm first identifies the localized regions in part with high-stress values, which is subsequently reinforced with either thickening the part or by means of strut insertion. Open-cell foam structures typically consist of interconnected struts dividing the 3D space into regions. These structures exhibit high irregularity or an aperiodic lattice. The work of Martinez *et al.* [193] exploits this property using Voronoi open-cell foam to generate objects with gradient elasticity. Figure 1.28(c) schematically shows the density variation using Voronoi-based regions(cells) for a planar part.

Bates *et al.*[194], showed the variation in density of a honeycomb structure significantly affects its energy-absorbing properties. The gradation in honeycombs, as shown in Fig. 1.28(e), was achieved by printing infill between the two lines for honeycomb for thicker regions and printing single lines (bead width equal to nozzle diameter) for thinner regions. A similar study by Choy *et al.*[195] showed higher specific energy absorption of graded samples of cubic and honeycomb lattice structures as compared to uniform ones. However, gradation of density, as illustrated in Fig. 1.28(g), was achieved by varying the amount of material deposited, thereby altering the thickness of the struts along the graded direction. The spatial density variation has been extensively studied within the context of part topology optimization [196]. In the works of Wu [197], a quadtree-based toolpath was suggested, which was refined (further discretized) in accordance with the structural information derived from topology optimization. The resulting infill structure, for a given mechanical load, provided optimal stiffness when compared with uniform density, schematically shown in Fig. 1.28(f). Liu *et al.*[198] analyzed the shell-graded infill from a geometric perspective, describing both the shell and infill in a parameter-based explicit way. The authors consider a uniform lattice which, when subjected to a deformation gradient field, acquires a non-uniform structure. Thus, a coordinate transformation matrix can be constructed in accordance with the deformation gradient field that, when imposed upon the uniform parent lattice, generates an optimized graded infill (Fig. 1.28(b)).

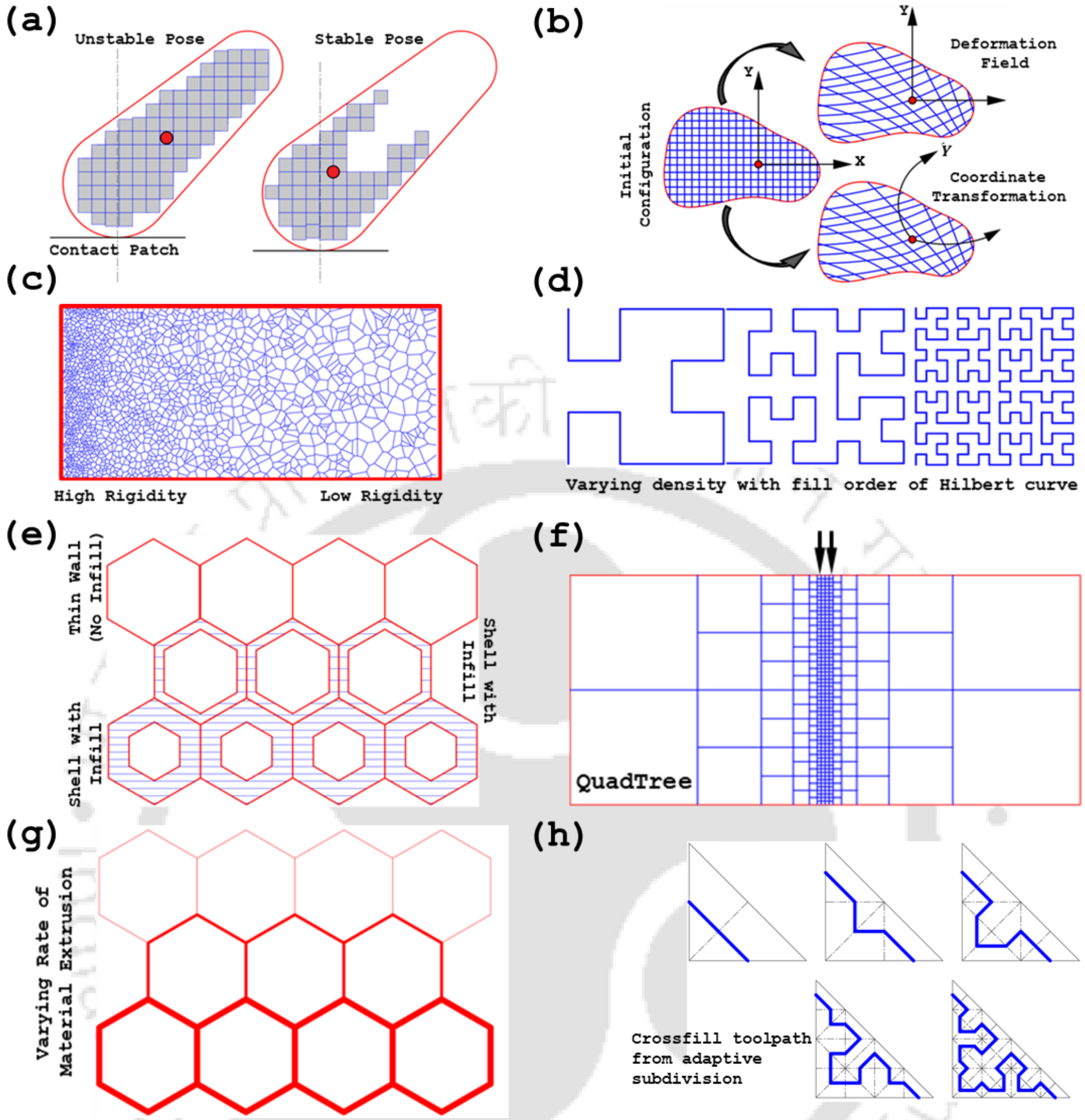

Fig. 1.28: Schematic representation of user-defined gradient toolpath achieved through (a) modifying print surface and interior (adapted with permission from [190], copyright 2016, Elsevier), (b) deformation-based coordinate transformation matrix (adapted with permission from [198], copyright 2020, Elsevier), (c) Voronoi open-cell foam[193], (d) varying order fractal-based (adapted with permission from [199], copyright 2020, Elsevier), (e) shell with infill (adapted with permission from [194], copyright 2018, Elsevier) (f) adaptive quadtree (adapted with permission from [197], copyright 2018, Elsevier) (g) varying extrusion rate (adapted with permission from [195], copyright 2018, Elsevier) (h) crossfill (adapted with permission from [200], copyright 2019, Elsevier)

Several fractal-based algorithms also exist in the literature [152,199,201,202]; one methodology to achieve gradient with fractal structures is through variation of the order of the curve, as illustrated in Fig. 1.28(d). An effective algorithm to generate a graded infill with a continuous toolpath, termed ‘Cross-fill,’ was proposed by Kuiper *et al.* [200]. The algorithm is based on the adaptive subdivision of a cube encapsulating the input model. This cube is divided into prismshaped cells, which can be further subdivided as defined by the density map. A data structure constructed from a combination of a graph and a tree representing connectivity and hierarchy, respectively, is used to generate a continuous toolpath. Fig. 1.28(h) schematically shows the graded infill using 'Crossfill' for a planar layer.

1.7 Literature Summary

The selection of toolpath, process parameters, and design considerations for feedstock handling systems in DED involves a trade-off between desired outputs. These trade-offs are performed such that the resulting processing condition favors an optimal case of part fabrication. A summary of some key process variables, their interplay with each other, and their impact on the deposition process as a whole are highlighted in this section.

- *Powder Injection Angle (PIA):* High inflight (particles between nozzle outlet and melt pool) laser-powder interaction leads to melt-pool instability, low catchment efficiency (due to inflight particle vaporization), and poor deposition characteristics [128]. Therefore, a PIA (defined as the angle of inclination of the powder stream relative to the axis of the laser beam) should be chosen such that it minimizes inflight laser-powder interaction while promoting sufficient radiative heating and desired powder stream characteristics. A low PIA supports a longer depth of focus [105] (signifying decreased interparticle collision), consequently promoting an increased range of passive stability and high deposition efficiency [115]. Conversely, a high PIA is linked with reduced size of the focal spot, decreased focal length, and a high particle concentration at the focal spot [110].
- *Mass Flow Rate:* High mass flow rate is often associated with increased surface roughness [203] and track porosity [204]. In the case of coaxial nozzles, a high mass flow rate attenuates the laser beam, often resulting in high substrate dilution at the track center and a lack of fusion at the edges [116]. For a given melt pool size, studies have suggested a limiting value of mass flow rate beyond which no particle absorption is possible into the melt pool [48].
- *Particle Velocity:* The velocity of particles entering the melt pool, to a large extent, affects the substrate dilution [120]. The higher the particle velocity, the more dilution, thus making particle velocity an important consideration in achieving overall geometric accuracy.
- *Omnidirectionality and Positional Deposition*: Invariance in track properties irrespective of the deposition direction or orientation (termed omnidirectionality) ensures dimensional accuracy and improved part performance. Lateral feed nozzles are non-omnidirectional

and primarily find application in the cladding of rotary components, whereas coaxial nozzles are omnidirectional and are employed for part fabrication through AM. A detailed account of omnidirectionality, as a property of various AM machine tools, is presented in Appendix 1.

- *Toolpath Synthesis*: The start and stop of deposition to achieve area filling in DED-based processes should be avoided as it induces defects in the fabricated parts, thereby necessitating a need for a continuous toolpath that can be tailored to favor one direction of deposition over another. Although such toolpaths exist in the literature, such as fractal-based toolpaths, they are often associated with a high number of turns, consequently increasing the tendency of over-deposition at the corners. This necessitates the development of a toolpath that accomplishes continuous deposition with a minimal number of turns.
- *Gradient Toolpath*: Selective material deposition to produce a user-defined gradient in the density of the fabricated parts can enable the production of objects that mimic nature, such as a bone or a plant stem. While this can be accomplished using a curated toolpath, ensuring ease of printing to prevent defects is challenging. This ease of printing mandates a toolpath to have properties such as being Heuristic, minimal lifts, minimal number of turns, etc., while preserving the user-specified gradient input.

1.8 Motivation and Objectives of Presented Work

Figure 1.29 highlights a few common limitations of pneumatic powder delivery. Section 1.4 discussed these limitations in detail. Fig. 1.29(a) shows the porosity in the deposited track, and Fig. 1.29(b)highlights the oxidation of the deposit due to the pneumatic powder feeding method. Further, Fig. 1.29(c) shows high dilution of the track at the center and lack of fusion at the edges, and Fig. 1.29(d) shows the powder particles ejected from the nozzle that could not be injected into the melt pool, sticking to solidified layer due to partial melting. This partial melting leads to a deteriorated surface finish of the fabricated part.

The primary objective of the project is to address the limitations of a pneumatic powder delivery system and develop a toolpath strategy that facilitates sparse and close-loop continuous deposition with a minimal number of turns. As part of this work, an indigenously developed laser-based DED platform was utilized to test the viability of the proposed non-pneumatic method of powder feedstock handling.

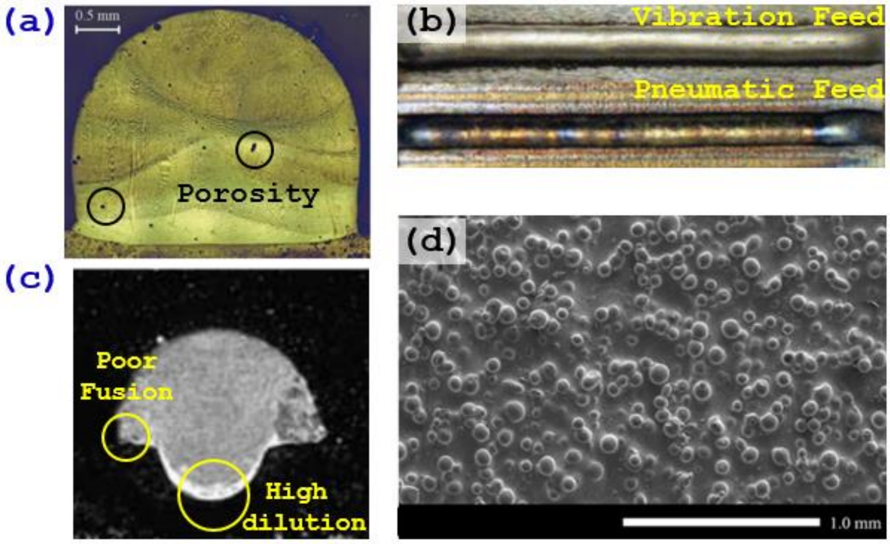

Fig. 1.29: Pneumatic powder feed system leading to (a) porosity, (b) poor protection against oxidation (as evident from track discoloration, reproduced with permission from [119], copyright(2011) Sage publication), (c) improper aspect ratio of the deposited track (reproduced with permission from [116], copyright ()), and (d) poor surface properties due to sticking of the unmelted particle (reproduced with permission from [205], copyright (2022), Elsevier)

The following methodology was adopted to accomplish the project objective.

1. Conceptualization of nozzle design and CAD modeling.
2. Simulation of powder delivery through the designed nozzle to understand and visualize bulk material behavior.
3. Identification and analysis of key process parameters through iteration of the previous two steps.
4. Prototype development and small-scale testing.
5. Fabrication of the functional nozzle prototype.
6. Integration of powder delivery system with the laser optical head and CNC build platform, which would enable part fabrication through Additive Manufacturing (AM).
7. Toolpath planning for area filling using continuous and closed-loop deposition through heuristic-based Travelling Salesman Problem (TSP) solver.

1.9 Organization of Thesis

The thesis titled 'Development of Laser-based Directed Energy Deposition System with Non-Pneumatic Powder Feedstock Handling and Synthesis of Toolpath Strategies' is categorized into seven chapters; the following is a brief outline of their respective content.

1. *Chapter 1* contains an introduction to the DED process with a detailed account of the literature review pertinent to the development of the setup, powder feedstock handling, and toolpath planning.
2. *Chapter 2* highlights the results from the DEM analysis detailing the methodology for the selection of simulation parameters and providing inputs for various design decisions.
3. *Chapter 3* outlines the experimental setup describing the method and mechanism of non-pneumatic powder feedstock metering, conveyance, and delivery to the melt pool.
4. *Chapter 4* details the retrofit process of a 1kW Continuous Wave (CW) laser unit with the existing CNC vertical milling center.
5. *Chapter 5* outlines the methodology for continuous toolpath generation using a TSP solver for uniform density.
6. *Chapter 6* describes the fabrication of density-based FGMs through continuous deposition using inputs either in the form of density functions or density maps.
7. *Chapter 7* provides a conclusion to the thesis emphasizing key findings, advantages, limitations, and a brief account of future work.

Chapter 2

Discrete Element Method Simulations and Evaluation of Material Properties for Investigation of Bulk Material Behavior

With an objective to develop a non-pneumatic feedstock handling system for DED, the initial design that was pursued is illustrated in Fig. 2.1. The metering part of the feedstock handling unit features a rotating auger that varies the mass flow rate through rotational speed. Although similar designs exist in the literature, both in the context of AM and otherwise [70,206], an auger-based system delivers powder in pulses instead of a continuous stream; Chapter 3 further addresses the shortcomings of this design and its alternative. The metered powder from the hopper enters the powder delivery nozzle from four (or more) inlet ports, as shown in Fig. 2.1, which is then guided to the center of a rotating bladed-centrifugal disk (spreader). The centrifugal spreader scatters the powder influx across its periphery, which subsequently falls into an annular section. This annular section is formed by placing two cones, inner cone $'a'$ and outer cone $'b'$, as shown in Fig. 2.1. The emerging powder stream exiting the nozzle, is conical and convergent in nature, with a distinct focal point that, by design, matches the location of the melt pool.

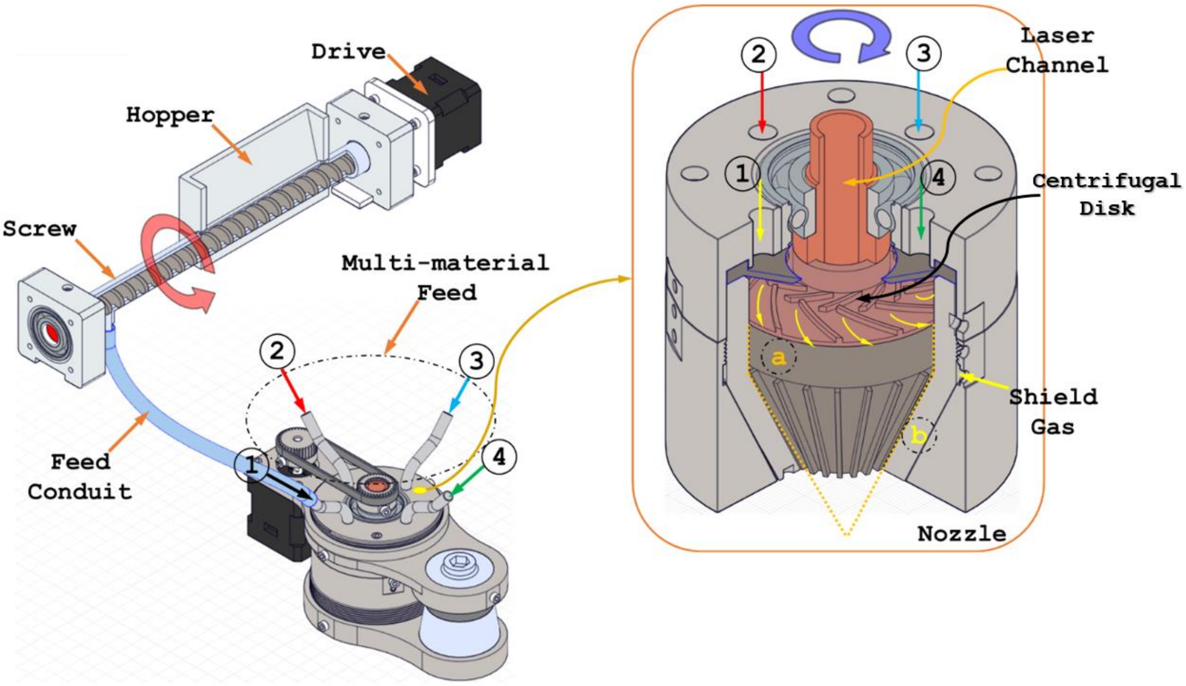

Fig. 2.1: Layout of a gravity-based feedstock handling unit

The bladed centrifugal spreader is a crucial component of the proposed design, and to ascertain its viability in the present application, Discrete Element Method (DEM) simulations were performed. This chapter provides insight into the selection of input parameters for the DEM model and the sensitivity of these parameters on the performance of the centrifugal disk. The following chapter (Chapter 3) presents the rationale behind the design choices made during the conception and later fabrication of this centrifugal disk.

The rotation of a bladed disk to scatter bulk materials has applications in several domains. Spreading of fertilizer in an agricultural field [207,208], maintenance of horticultural grounds[209], maintenance of roadways (and other similar infrastructures)[210], and design of mining equipment[211] are a few examples. The motivation for the use of a centrifugal distributor disk for particle distribution in DED was derived from the domain of agriculture, where such equipment is utilized for particle (seeds, fertilizers, etc.) spreading, as illustrated in Fig. 2.2(a). The analysis of particle spread, as produced by the rotating bladed disk, is often performed through the collection of particles in marked bins placed at specific locations within the field of distribution, as illustrated in Fig. 2.2(b). A similar methodology is employed in this study for the performance evaluation of various designs of centrifugal disks.

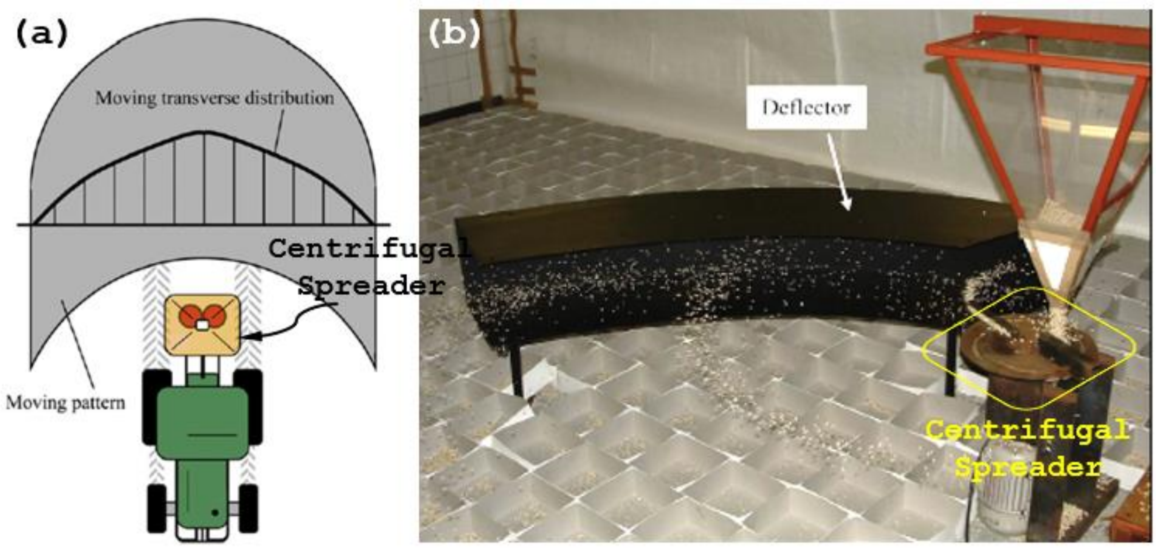

Fig. 2.2: Use of centrifugal spreaders for particle distribution in agricultural fields (a) centrifugal spreader mounted on a tractor and (b) analysis of particle spread through particle collection in marked bins. Reproduced with permission from [207], copyright(2011) Elsevier

Modeling such processes provides valuable insight into process dynamics that help design new and improved bulk handling systems and equipment. DEM-based modeling of bulk material is commonly used to study and predict granular flow behaviors under various operating conditions. Typically, the accepted performance of a centrifugal spreader is spatial uniformity of particle distribution for a given area of spread. Parameter sensitivity analysis for centrifugal spreaders by Liedekerke *et al.* [212] and Coetzee *et al.* [213] shows friction coefficient as the most dominant factor in DEM simulations.

In the investigations made within the context of the Powder Bed Fusion (PBF) process by Nan *et al.*[214], authors considered a straight blade recoater moving with a constant velocity that makes contact with the bulk material for powder recoating. The study analyzed design parameters for a recoating system, such as the gap between the recoater blade and the powder layer underneath, revealing a linear increase in particle volume for a given layer with an increase in gap height. In a similar study by Wang *et al.* [215] for the PBF process, several designs of powder recoater blades were considered concluding that a round-shaped blade can provide higher particle density for a given layer thickness with better powder compaction. Furthermore, in a study of cylindrical rotating recoaters by Zhang *et al.* [216], the effect of the recoater blade's rotational and translational velocity and diameter of the cylindrical recoater on powder-bed density was analyzed.

Modeling such granular phenomena requires several user inputs; these inputs need to be experimentally measured or calibrated through various methods. Given the complexity of obtaining the material properties for granular media, a parameter sensitivity analysis becomes essential. The parameter sensitivity study, as presented here, is from the perspective of a centrifugal spreader dispersing the granular media, which is the central idea of the proposed nozzle design. The rotation of the disk scatters the powder particles across its periphery, thus resulting in a uniform spatial distribution of the powder particles. The sensitivity analysis is performed by implementing Response Surface Methodology (RSM) to identify the dominant factors and factor interactions. The three common inputs for particle contact(interaction) modeling in a DEM simulation, namely, Coefficient of Static Friction (COSF), Coefficient of Rolling Friction (CORF), and Coefficient of Restitution (COR), are taken as factors, whereas spatial and temporal variation is taken as a response. Also, given the importance of the COSF in DEM simulations, a simple setup for its accurate measurement is proposed. The experimental setup is tested for a variety of powder samples, and their corresponding values of COSF are reported. These COSF values for the selected powder-equipment pair can aid in the calibration of material interaction parameters for a given DEM simulation.

2.1 Discrete Element Method

The continuum approach assumes that the working media (solid or liquid) completely fills the space it occupies. For example, most CFD analyses generally ignore the motion of individual fluid molecules and their interaction with the neighboring molecule within a fluid domain. In contrast to the continuum approach, a discrete approach emphasizes individual particles, which, when assembled, gives the macroscopic (or overall) outlook. In other words, in a discrete approach, the macroscopic behavior of a system results from microscopic interactions within the constituent particles. The discrete approach is especially helpful in studying phenomena occurring at length scales comparable to particle diameter. Thus, given the advantages of the DEM in studying granular flow and other bulk material phenomena, Altair EDEM™ (version 2021) was used for granular flow simulation. A gravity-based cladding nozzle was devised through multiple simulations with various geometries of participating components. With each simulation, changes were made in the geometry for the next iteration to achieve favorable conditions of laser metal cladding.

2.1.1 DEM Simulation Approach

The collision of granular material, both between particles and particle to geometry, can be modeled using a hard and soft-sphere approximation. The hard-sphere model is based on an advanced prediction of a collision based on particle trajectory [217]. In the hard-sphere model, the particle collisions are treated as instantaneous, occurring at a single point of contact on the particle surface. However, this approximation results in poor prediction of granular flow behavior. Experimental observations suggest that particle collision involves surface contact (due to elastic deformation) that happens over a short period of time. Also, hard-sphere models are difficult to implement for complex part geometries, multi-particle collisions, and non-spherical particles. Moreover, the effect of complex contact forces, such as friction for dense granular flows, is further difficult to investigate using hard-sphere models [217,218].

The soft-sphere model is most commonly used in DEM simulations [219]. The soft-sphere model, even though it assumes particles to be geometrically rigid, accounts for non-instantaneous contact through a parameter $'\delta'$ called as overlap, as illustrated in Fig. 2.3[220]. This 'long-lasting' particle collision allows for the calculation of contact forces and dissipative effects using an appropriate provision in the mathematical model. Generally, soft-sphere models are implemented through the following steps.

- Setting up equipment and particle properties along with a computational domain
- Inserting particles into the computational domain by defining position and inlet velocity
- Detecting particle-to-particle and particle-to-geometry contact
- Calculating forces on each particle using an appropriate particle contact model

- Determining particle accelerations using Newton's second law, which subsequently results in new particle states

2.1.2 Contact Force Model

The interaction of particles is the most important consideration in any DEM simulation. As mentioned earlier, contact between granular matter, attributing to particle deformation, occurs over a finite area and is non-instantaneous. The contact force can be categorized into two components: normal (F_N) and tangential (F_T) [221]. The amount of overlap (δ) can be expressed as $\delta = (R_1 + R_2) - d$ where, R_1 and R_2 are the particle radii, and d is the distance between the particle centers (C_1 and C_2), illustrated in Fig. 2.3.

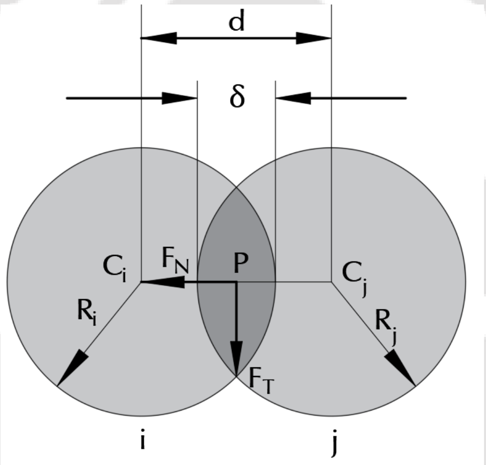

Fig. 2.3: Normal and tangential force on particles during contact

According to Hertz's theory, as described by Horabik *et al.* [221], for two spheres contacting over a finite circular area with a radius $'a'$, the normal contact force is given by equation 2.1, where E^* and $R^*$are effective young's modulus and particle radius, and are expressed through equations 2.2 and 2.3, respectively.

$$F_N = \frac{4E^*}{3R^*} a^3 \tag{2.1}$$

$$E^* = \frac{E_i E_j}{E_i(1 - \nu_j{}^2) + E_j(1 - \nu_i{}^2)} \tag{2.2}$$

$$R^* = \frac{R_i R_j}{R_i + R_j} \tag{2.3}$$

E_i, E_j denotes Young's moduli and ν_i, ν_j denotes Poisson's ratio of the two contacting spheres of radii R_i and R_j, respectively. The normal contact force is related to the degree of particle overlap (δ) through equation 2.4.

$$F_N = k_N \delta_N^{3/2} \tag{2.4}$$

where the spring stiffness (k_N) is expressed in terms of effective Young's modulus (E^*) and effective particle radius (R^*) through equation 2.5

$$k_N = \frac{4}{3} E^* R^{*1/2} \tag{2.5}$$

The radius of the circular contact area is related to overlap (δ_N) by the expression 2.6

$$a = \sqrt{R^* \delta_N} \tag{2.6}$$

In addition to the normal force, a normal damping force (F_N^d) is also considered, given by equation 2.7

$$F_N^d = -2\beta \sqrt{\frac{5}{6}} \cdot V_N^{Rel} \sqrt{S_N m^*} \tag{2.7}$$

where $m^* = \left(\frac{1}{m_i} + \frac{1}{m_j}\right)^{-1}$ is the equivalent mass of two contacting particles $'i'$ and $'j'$. V_N^{Rel} is the normal component of the relative velocity and β (depends on the coefficient of restitution 'e'), and S_N are expressed through equations 2.8 and 2.9, respectively.

$$\beta = \frac{\ln e}{\sqrt{(\ln(e))^2 + \pi^2}} \tag{2.8}$$

$$S_N = 2E^* \sqrt{R^* \delta_N} \tag{2.9}$$

Similar to the above expressions, which consider the normal force component, the tangential force component (F_T), as formulated by Mindlin and Deresiewicz [222], is given by equation 2.10.

$$F_T = -k_T\delta_T \tag{2.10}$$

$$k_T = 8G^*\sqrt{R^*\delta_N} \tag{2.11}$$

where k_T and δ_T are the tangential stiffness and overlap, respectively, and G^* is the equivalent shear modulus. Additionally, tangential damping is given by (F_T^d) expressed through equation 2.12

$$F_T^d = -2\beta\sqrt{\frac{5}{6}}\cdot V_T^{Rel}\sqrt{S_T m^*} \tag{2.12}$$

$$S_T = 8G^*\sqrt{R^*\delta_n} \tag{2.13}$$

Tangential contact force models, generally, are implemented through incremental steps, wherein the force at each time step is computed and added to the force value from the previous time step. This accounts for changes in the normal force that affect tangential force. The magnitude of the tangential force at time-step $'n'$ is given by equation 2.14

$$F_T^n = \begin{cases} F_T^{n-1} + k_T^n\Delta\delta_t, & \Delta F_n \geq 0 \\ F_T^{n-1}\left(\dfrac{k_T^n}{k_T^{n-1}}\right) + k_t^n\Delta\delta_t, & \Delta F_n < 0 \end{cases} \tag{2.14}$$

The tangential force, as expressed through equation 2.14, suggests that when the normal force between the previous and current time step decreases (ΔF_n), then, it must be rescaled prior to computing the next time step. This is to account for the fact that upon a decrease in normal force, the contact area decreases; consequently, the old value of tangential force cannot be sustained by the updated reduced area [223–225]. Also, the tangential force in the Mindlin no-slip model is limited by Coulomb's friction, where if $F_T > \mu F_n$, then $F_T = \mu F_n$.

The Hertz-Mindlin no-slip model does not account for particle cohesivity in granular media. The use of Johnson-Kendall-Robert's (JKR) contact force model for particle cohesion considers the effect of Van der Waals forces and allows for modeling adhesive dry or wet granular media[214,221,226,227]. The JKR normal force and the relation between contact radius $'a'$ and particle overlap $'\delta'$ is given by equations 2.15 and 2.16, respectively. The parameter $'\gamma'$ represents the surface energy for two contacting bodies.

$$F_{JKR} = -4a^{\frac{3}{2}}\sqrt{\pi\gamma E^*} + \frac{4E^*}{3R^*}a^3 \tag{2.15}$$

$$\delta = \frac{a^2}{R^*} - \sqrt{\frac{4\pi\gamma a}{E^*}} \tag{2.16}$$

The JKR model, in conjunction with Hertz-Mindlin's no-slip theory, introduces cohesive forces even if the particles are not in contact. The minimum particle distance for this cohesive force to be active is given by equation 2.17. The maximum value of cohesive force, also referred to as pull-out force, is given by equation 2.19.

$$\delta_c = -\sqrt{\frac{4\pi\gamma a_c}{E^*}} + \frac{a_c^2}{R^*} \tag{2.17}$$

$$a_c = \left[\frac{9\pi\gamma {R^*}^2}{2E^*}\left(\frac{3}{4} - \frac{1}{\sqrt{2}}\right)\right]^{\frac{1}{3}} \tag{2.18}$$

$$F_p = -\frac{3}{2}\pi\gamma R^* \tag{2.19}$$

2.2 Input Parameter Sensitivity Analysis

The contact force model in DEM typically requires three user-input parameters for particle simulation: Coefficient of Static Friction (COSF), Coefficient of Rolling Resistance(CORR), and Coefficient of Restitution(COR). These parameters are considered for a material pair, i.e., particle-particle and particle-geometry interaction.

2.2.1 Simulation Setup

The powder particles are introduced on the rotating disk off-axis, as illustrated in Fig. 2.4(a). The rotation of the disk spreads/ scatters the powder particles across its periphery. The parameters taken for the simulation are listed in Table 2.1. Underneath the rotating disk, thirty-six equally spaced mass sensors(bins) are placed. The powder mass received by each of these bins provides insight into the spatial distribution of the powder dispersion. Variation in the recorded mass by each of these bins represents particle uniformity (or, conversely, non-uniformity). The height of the computational domain was chosen to accommodate virtual powder mass sensors for quantifying spatial distribution while maintaining a reasonable computational time.

The residence time, representing the time period a particle stays in the simulation, is used to quantify the temporal variation in the mass flow rate. Monitoring the residence time tracks the time period from the generation of a particle at the injection surface to its exit from the computational domain, as illustrated in Fig. 2.4. Since the centrifugal spreader is a continuously operating system, i.e., particles are fed at a specified rate and drained, not all particles will stay within the computational domain for the same time duration. However, the percentage Coefficient of Variation (%CoV) for the residence time during the set simulation period can be used to quantify the temporal variation of the given system.

Table 2.1: Parameters for DEM simulation

Simulation Parameter	
Simulation Run Time	1 s
Simulation Time Step	1e-08 s (0.95% of Rayleigh time step)
Cell Size (for contact detection)	$4\left(\frac{D}{2}\right)$
Particle Shape	Spherical
Particle Diameter (D)	100 µm
Material Density	7980 kg/m^3
Poisson's Ratio	0.3
Young's modulus	2.1e+09 Pa
Distributor rotational speed	200 RPM
Particle Insertion Rate	10 g/min

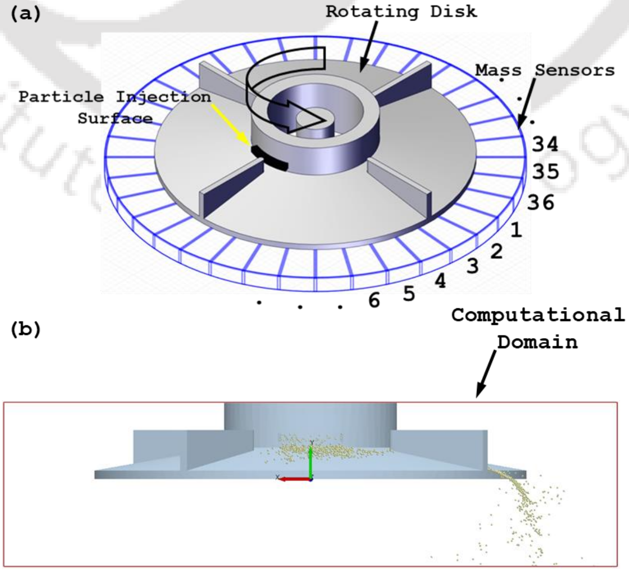

Fig. 2.4: Schematic representation of (a) problem formulation and (b) modeling step in the DEM environment

2.2.2 Modeling Spherical as Non-Spherical Particle

The static and rolling friction coefficients are the two key user inputs for particle contact modeling in DEM simulations. However, for a given phenomenon, under specific conditions of granular flow, these parameters can be selected such that the resulting flow behavior reasonably approximates the particle shape[228]. Furthermore, these parameters can also be altered to accurately capture the surface roughness of the interacting equipment material [214]. Consider a case where a spherical particle with identical values of COSF and CORF is allowed to move freely on a tilting platform, as illustrated in Fig. 2.5(a). Also, under identical conditions, a non-spherical particle with the same value of COSF but negligible CORF is modeled, as shown in Fig. 2.5(b). Comparing the angle at which the two particles start to slide (the tangent of which is the coefficient of static friction) suggests no significant difference, as illustrated in Fig. 2.5. From this observation, it can be inferred that, under specific conditions for a given phenomenon, through an appropriate selection of identical COSF and CORF values, a spherical particle can be approximated as a non-spherical particle. The selection of rolling friction with torque-based rolling resistance models to approximate non-spherical particles with spherical ones has also been studied in the works of Wensrich *et al.*[228] A similar observation can be made from the results of Geer *et al.* [229]; such approximation can have advantages in terms of model simplification and reduced computational load. However, it is to be understood that approximating a powder batch of non-spherical particles with spherical ones cannot be treated as a general rule of thumb, and such an assumption induces considerable discrepancy between the observed and simulated values[228]. For instance, the bulk material behavior arising from centrifugal spreading (the subject of the current study) does not constrict the particles in narrow passageways, and centrifugal force is the primary driving force for the flow. In cases where the granular flow takes place in constricted passageways under the effect of gravity, a spherical particle assumption may induce a more significant error when compared with centrifugal spreading [230,231]. Furthermore, studies have suggested an influence (of various levels of significance) of particle shape and surface roughness of the interacting components on the response of granular flow behavior [232,233]. In the case of the AM powders, which are formed through gas atomization, SEM images, as shown in Fig. 2.7, reveal an approximate spherical particle morphology.

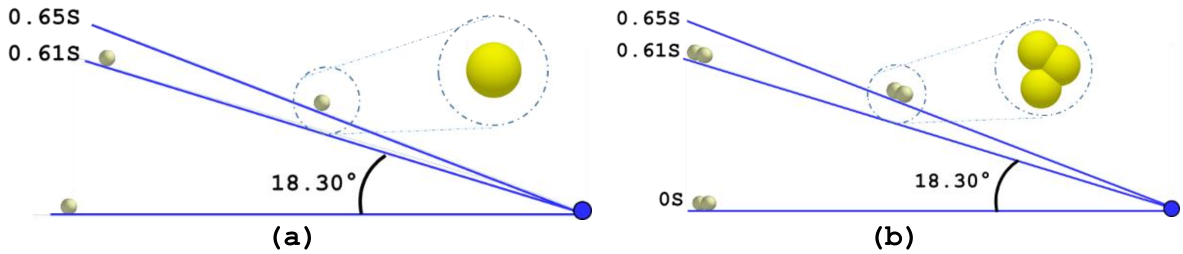

Fig. 2.5:(a) Spherical particle with COSF=CORF=0.3 and (b) non-spherical particle with COSF=0.3 and negligible CORF

2.2.3 Response Surface Methodology

Response Surface Methodology (RSM) is a statistics-based mathematical modeling technique to determine the effect of multiple input parameters on one or several responses (or outputs). RSM is also widely employed for computing operating parameters within which an optimal (minima or maxima) response can be achieved. This study, however, aims to find the input parameter(s) that has the most significant effect on a selected response. As previously discussed, through RSM, a sensitivity analysis of three input variables, namely, COSF, CORF, and COR, is evaluated for two responses (or outputs), namely, 'Spatial Distribution' and 'Temporal Distribution.' A similar approach, combining DEM simulation with RSM and other statistical tools for material calibration, sensitivity analysis, and process parameter optimization, can be found in the literature[234–239]. To implement RSM, a suitable experimental design should be selected to generate a dataset containing a set of values of input variables and their corresponding responses. In this study, *Central Composite Design (CCD)* was implemented for an experimental design[240,241]; other methods of experiment design include Box-Behnken Design (BBD)[240], Doehlert Design[242], etc.

Table 2.2 shows the selected upper and lower limit of the three input variables, and Table 2.3 shows the response values corresponding to each set of input parameters having implemented the CCD. The selection of upper and lower limits in the Design of Experiments (DOE) is based on preliminary experiments (outlined in section 2.2.4.2) and a literature survey.

Table 2.2: Upper and lower limit of the input variables used during the simulation

Variable	Low Level	Middle Level	High Level
COR	0.3	0.47	0.65
COSF	0.1	0.30	0.50
CORF	0.1	0.30	0.50

Table 2.3: Experimental design with input values and corresponding responses

Run	Variable 1: COR	Variable 2: COSF	Variable 3: CORF	Response 1: Spatial Variation	Response 2: Temporal Variation
1	0.47	0.3	0.5	181.81	29.45
2	0.65	0.1	0.5	190.68	28.62
3	0.30	0.5	0.5	130.57	37.51
4	0.65	0.1	0.1	190.52	28.63
5	0.65	0.5	0.1	141.12	31.13
6	0.30	0.3	0.3	187.80	29.64
7	0.47	0.3	0.3	180.30	29.56
8	0.30	0.1	0.1	202.53	27.90
9	0.47	0.1	0.3	200.94	27.82
10	0.47	0.3	0.3	180.87	29.53
11	0.30	0.5	0.1	140.17	30.51
12	0.47	0.3	0.3	181.65	29.56
13	0.47	0.3	0.3	186.03	28.58
14	0.47	0.3	0.3	186.52	29.45
15	0.65	0.3	0.3	181.92	30.51
16	0.65	0.5	0.5	128.50	32.49
17	0.47	0.3	0.3	182.81	28.47
18	0.47	0.5	0.3	150.04	33.08
19	0.47	0.3	0.1	185.58	28.22
20	0.30	0.1	0.5	192.99	28.90

Minor variations in the selected responses can be observed for the simulations performed at identical input conditions. These input conditions correspond to the simulation runs at the 'middle level' (mean values) of input values. These variations, shown in Fig. 2.6 for the average mass received by each bin, can be attributed to the stochastic nature of particle injection into the system and the particle-particle and particle equipment contact [243].

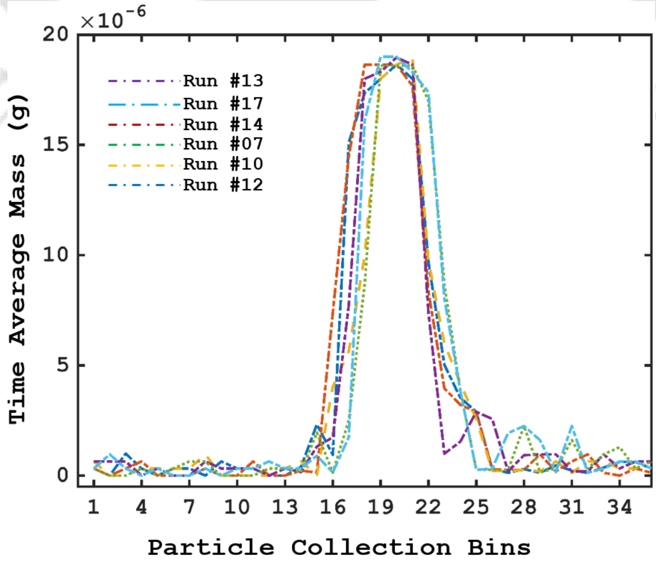

Fig. 2.6: Variations in the average particle mass recorded by each bin across six simulation runs corresponding to the middle level of input parameters

2.2.4 Evaluation of Material Interaction Properties

An experimental setup was designed to accurately evaluate the value of COSF for various powder materials used in AM. These values can be further implemented in DEM simulations and analysis and can serve as preliminary values to guide the process of material calibration. The measurement of COSF for a material pair (powder-equipment material) is carried out by measuring the angle of inclination at which relative sliding between the material pair starts to occur. This method is fundamental and has been applied by Nan *et al.* [214] in a similar context of powders sliding on a substrate. Other studies [244] have also employed this method of tilting substrate to evaluate the COSF and CORF values, and it is, therefore, not novel. However, the experimental setup proposed here emphasizes avoiding human-induced errors and promoting automation, thereby enhancing reliability, ease of use, and adaptability. The experimental setup is generic and can be used to measure COSF for any given material pair.

2.2.4.1 Sample Preparation and Particle Granulometric

The particles were characterized using multiple SEM image analyses of a sample batch. The results from image analysis of 1500 individual particles show powder batch with D_{10}, D_{50}, and D_{100} values of 54 μm. 76 μm, and 101 μm, respectively. Gas-atomized particles are used as part of this study, which are mostly spherical, with non-sphericity primarily arising from smaller satellite particles adhering to larger ones, as shown in Fig. 2.7.

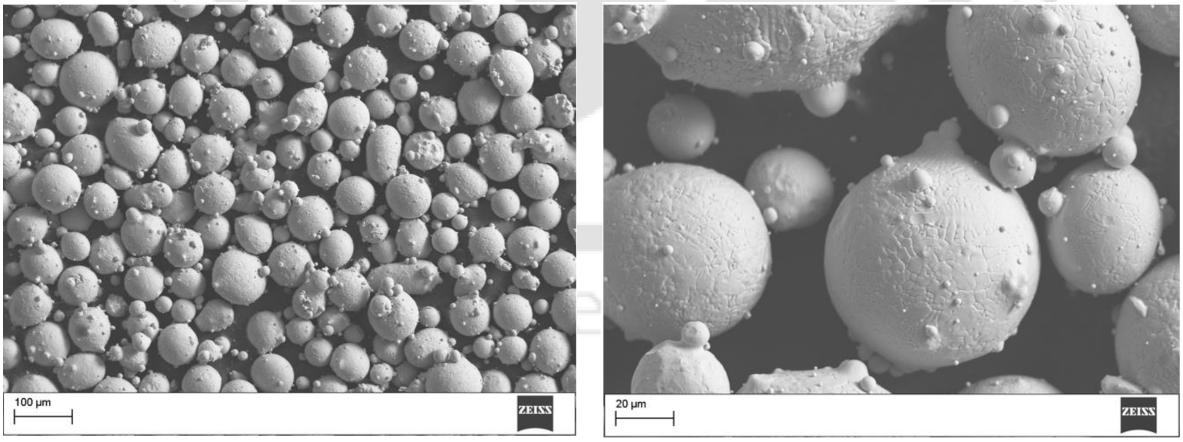

(a) (b)

Fig. 2.7: SEM image of a powder sample (a) mostly spherical morphology of powder particles (b) small satellite particles adhering to larger ones

For sample preparation, a small steel plate is covered with a layer of quick-drying glue, which is then lowered (glue side down) in the batch of powder material, as illustrated in Fig. 2.8(a). Use of a low viscous cyanoacrylate adhesive is recommended. This coats one side of the steel plate with the granular media (as illustrated in Fig. 2.8(b)), whose friction coefficient will be evaluated. Also, this method of powder coating the test sample ensures that the interacting surface of the powder particles remains free from any adhesive. This test sample is then placed on the substrate, thus forming a material pair, which is the subject for the determination of the COSF. Initially, the substrate is horizontal, then inclined continuously and smoothly until the test sample begins to slide. This sliding angle $'\theta'$ is recorded for the computation of μ_s through the expression 2.20.

$$\mu_s = \tan\theta \tag{2.20}$$

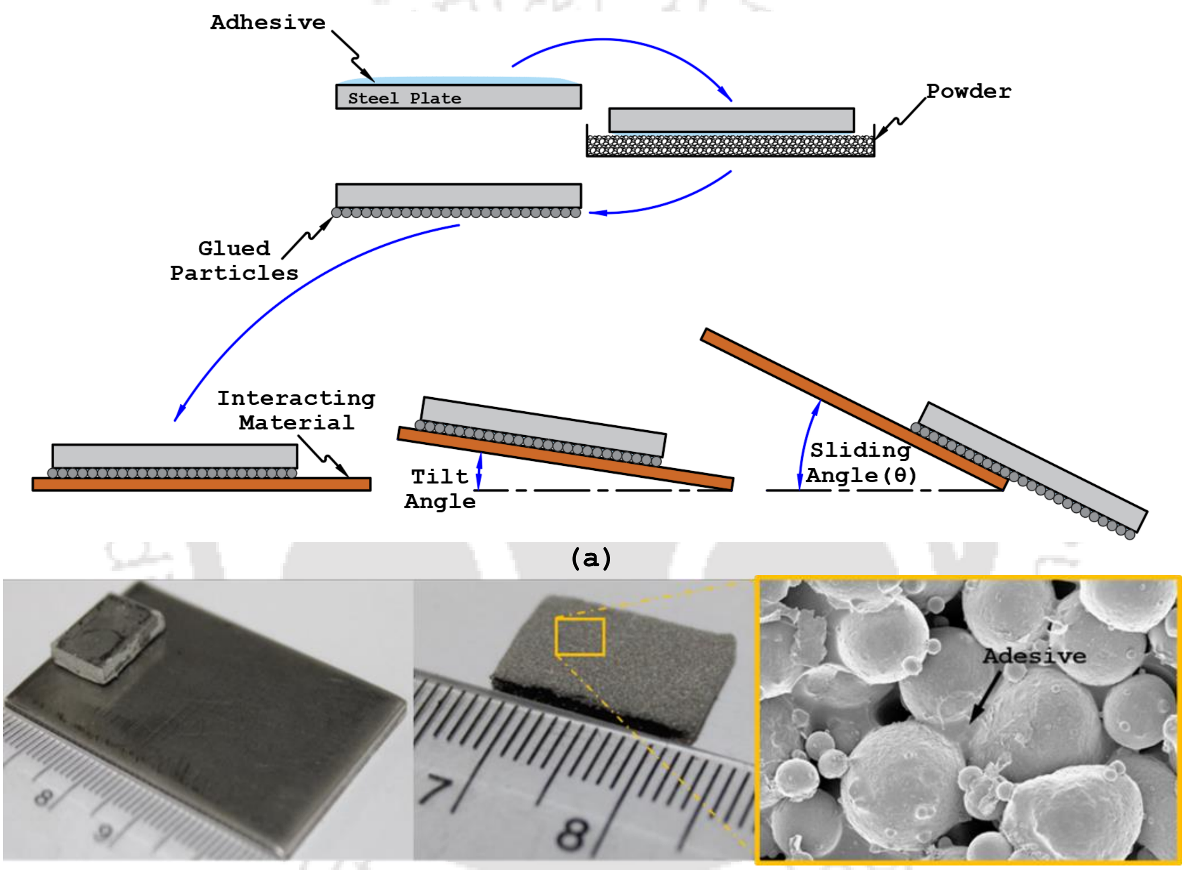

(a)

(b)

Fig. 2.8: (a)Schematic representation of the proposed method of test sample preparation and (b) SEM image of a prepared test sample

To ensure the repeatability of the proposed sample preparation method and to evaluate COSF values of commonly available metallic powders, nine test samples of different materials were prepared and tested against the SS316L test platform, as illustrated in Fig. 2.9. The elemental composition of each of these test samples is listed in Appendix 2.

Fig. 2.9: Metal powders that are considered subjects for the calculation of COSF against the SS316L test platform

2.2.4.2 Setup for Evaluation of COSF

Figure. 2.10 shows the experimental setup developed for measuring the friction coefficient values for various test samples. With reference to Fig. 2.10, the test setup comprises a motor (1), whose RPM is reduced through a series of timing belts and pulleys (2) connected to the base of the test platform (4). The rotation of the motor inclines the test platform relative to the horizontal. The angle of inclination is tracked with the help of an encoder (6). A DC motor is preferred over a stepper motor to avoid jerks encountered between each step, which may force the test sample to slide prematurely before the frictional force reaches its maximum. An accelerometer (3) is also attached to the build platform that acts as a leveling sensor for the system, thus ensuring each experimental run starts with an inclination angle of zero degrees relative to the horizontal. As the angle of inclination approaches its critical value, the displacement (sliding) of the test sample (7) from its initial position is sensed through a Distance Ranging Sensor (DRS) (5). The input from the DRS triggers the motor to stop, thus providing the sliding angle, which can subsequently be used to calculate the friction coefficient value.

The proposed experimental setup has provisions for mounting the test platform of various materials. This allows flexibility as any material pair can be used as the experiment's subjects. Furthermore, placing the test sample on the platform is the only user interaction with the setup; consequently, the human-induced error in recording the data (or in other similar aspects) is kept to a minimum.

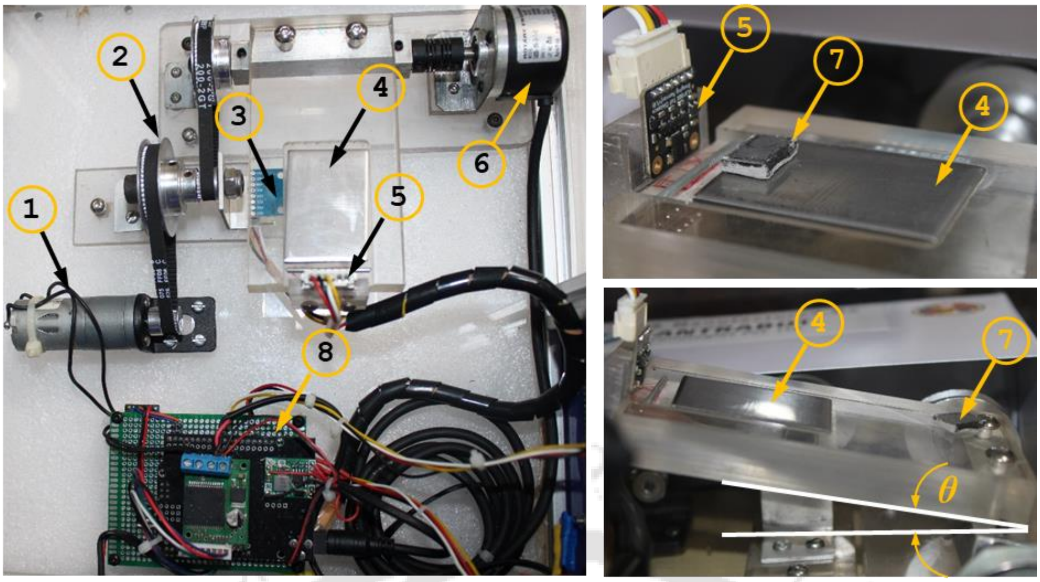

Fig. 2.10: Experimental setup for measuring static friction coefficient constituting a DC motor(1), timing belt and pulley arrangement (2), accelerometer (3), test platform (4), ranging sensor (5), rotary encoder (6), test sample (7) and machine control board (8).

Various test samples of different powder materials, as shown in Fig. 2.9, were tested against the SS316L test platform using the developed experimental setup and the sample preparation technique (described in section 2.2.4.2). Figure 2.11 shows the average recorded values of the critical sliding angle $'\theta'$ for each test sample; correspondingly, the COSF values are listed in Table 2.4.

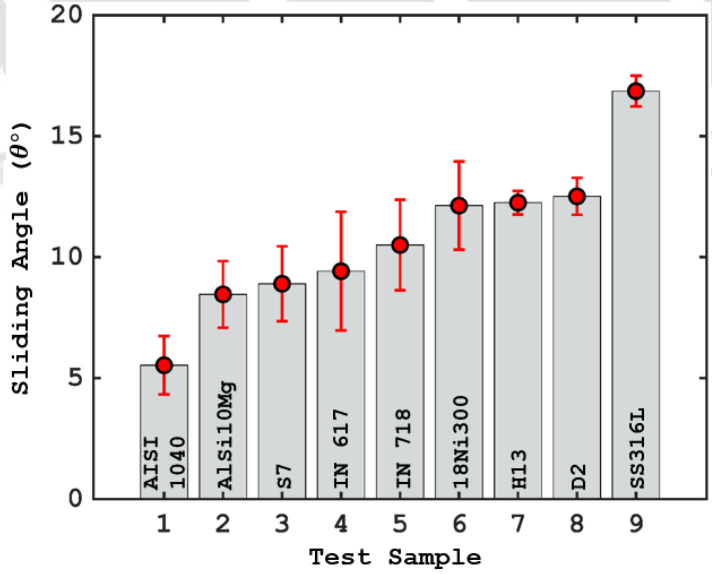

Fig. 2.11: Recorded values of the critical sliding angle $'\theta'$ for each test sample

Table 2.4: Coefficient of Static friction for the tested powder samples against SS316L steel base plate

Test Sample	COSF
AISI 1040	0.10
AlSi10Mg	0.14
S7	0.15
IN 617	0.16
IN 718	0.18
18Ni300	0.21
H13	0.21
D2	0.22
SS316L	0.30

The variation in the recorded values of COSF for various powder test samples is expected to stem from the surface roughness of the test platform and the morphology of the powder particles. The test platform used as part of this study had a R_a value of 1.6 μm. It is worth noting the study by Nan *et al.* [214], where an appropriate selection of COSF value exclusively modeled the incorporation of surface roughness of an AM part. Other surface properties of the test platform, such as scratches, dents, waviness, surface contaminants, etc., are also expected to influence the recorded COSF values. Furthermore, the effect of these parameters will be more pronounced for smaller particle sizes, typically of the order of surface roughness of the test platform. However, further studies are required to quantify these effects conclusively.

2.3 Results and Discussion

From the sensitivity analysis done using the RSM, single factors influencing the studied response are discussed first, followed by interaction terms. The possible reasons for the observed behavior during the experiments and post-analysis of the results from similar studies in the literature are also presented.

2.3.1 ANOVA Results

Following the experimental design shown in Table 2.3, twenty numerical simulations were performed at set values of input variables. The corresponding responses were analyzed using the RSM method, the results of which are summarized in Table 2.5. The statistical significance of the model was determined by observing the P-values for each response. A quadratic model was selected to analyze spatial and temporal particle variation, which displayed a normal distribution of the residuals, thereby signifying sufficient reliability of the model. The model equation was significant for all the selected models, accompanied by a non-significant 'Lack of Fit.' Table 2.5

also highlights key statistical parameters for establishing the quality of the ANOVA study. These parameters include a Coefficient of Determination *(COD)*(R^2), adjusted COD ($R^2_{Adjusted}$) and Adequate Precision (*Ade Pre*). While $R^2_{Adjusted}$ points to the amount of variation about the mean explained by the model; adequate precision reflects the signal-to-noise ratio[245,246].

Table 2.5: Analysis of Variance (ANOVA) for selected responses and inputs

Fit Model	**Source**	**Sum of Squares**	**df**	**Mean Square**	**F-Value**	**p-Value**
Response: Spatial Variation						
Quadratic	**Model**	**9984.04**	**9**	**1109.34**	**65.78**	**< 0.0001**
	A-COR	45.44	1	45.44	2.69	0.1317
	B-COSF	**8251.89**	**1**	**8251.89**	**489.32**	**< 0.0001**
	C-CORR	**125.11**	**1**	**125.11**	**7.42**	**0.0214**
	AB	21.75	1	21.75	1.29	0.2826
	AC	5.57	1	5.57	0.3306	0.5780
	BC	20.67	1	20.67	1.23	0.2941
	A^2	25.92	1	25.17	1.49	0.2498
	B^2	**422.41**	**1**	**422.40**	**25.05**	**0.0005**
	C^2	48.55	1	48.19	2.86	0.1218
	Residual	168.32	10	16.86		
	Cor Total	10152.87	19			
R^2=0.9834, $R^2_{Adjusted}$=0.9684, *Ade Pre*=24.1615						
Response: Temporal Variation						
Quadratic	**Model**	**90.71**	**9**	**10.08**	**16.09**	**< 0.0001**
	A-COR	0.9442	1	0.9442	1.51	0.2477
	B-COSF	**52.26**	**1**	**52.26**	**83.41**	**< 0.0001**
	C-CORF	**11.22**	**1**	**11.22**	**17.91**	**0.0017**
	AB	2.94	1	2.94	4.70	0.0554
	AC	**5.53**	**1**	**5.53**	**8.83**	**0.0140**
	BC	**6.78**	**1**	**6.78**	**10.83**	**0.0081**
	A^2	1.70	1	1.70	2.71	0.1307
	B^2	**3.70**	**1**	**3.70**	**5.90**	**0.0355**
	C^2	0.5583	1	0.5583	0.8912	0.3674
	Residual	6.26	10	0.6265		
	Cor Total	96.98	19			
R^2=0.9354, $R^2_{Adjusted}$=0.8773, *Ade Pre*=17.0941						

2.3.1.1 Influence of Individual Parameters

The influence of each of the selected variables on the studied responses is highlighted in Fig. 2.12. The effect of individual factors (variables/ input) on any given response is examined by keeping the values of other participating factors at their central level. Figure 2.12(a) shows the COSF is strongly but negatively correlated to spatial variation. An increase in COSF decreases the spatial variation, thus promoting uniformity in the powder particle distribution around the rotating spreader/ disk. The other two factors, i.e., COR and CORF, statistically have a non-significant influence on spatial variation. The temporal variation, as shown in Fig. 2.12(b), is significantly influenced by the static friction coefficient; higher values of COSF suggest a non-uniform temporal particle distribution. In other words, the mass flow rate, as discharged by the rotating disk, becomes more erratic with increased COSF. A similar observation can be made for the case of CORF and COR. However, the correlation between CORF and temporal variation is statistically significant compared to COR.

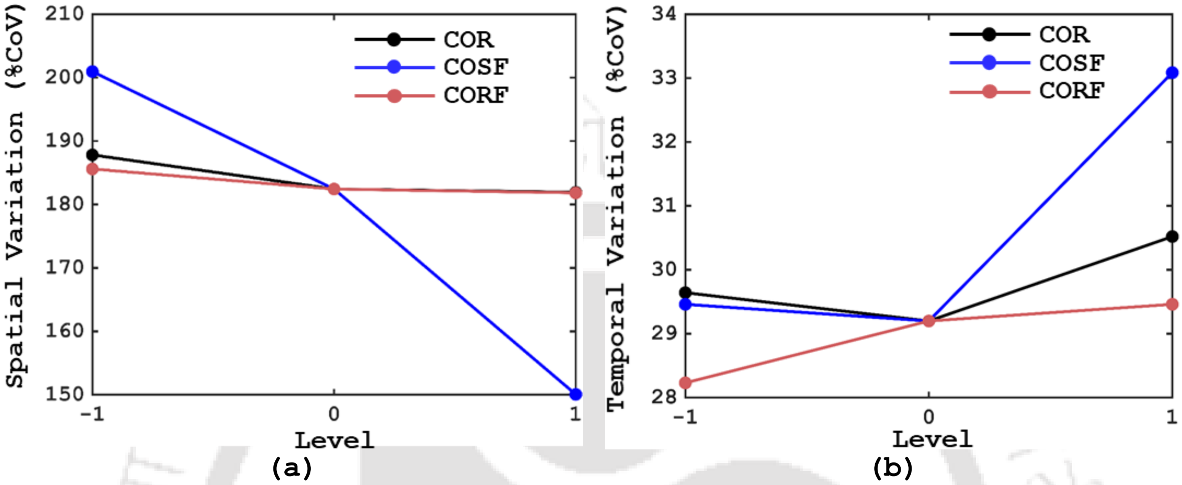

Fig. 2.12: Effect of individual factors on the selected responses (a) spatial variation, and (b) temporal variation

2.3.1.2 Influence of Quadratic and Interaction Parameters

Table 2.6 shows the interaction parameters that significantly influence the selected responses. CORF and COR have minimal influence on spatial distribution. Figure 2.13(a) and (b) show the influence of COSF interaction with CORF and COR, respectively. The interplay of CORF with COSF and COR values strongly influences the temporal variation, as illustrated in Fig. 2.13(c) and (d).

Table 2.6: Significant quadratic and interaction parameters

Spatial variation	Temporal Variation
-	AC
-	BC
B^2	B^2

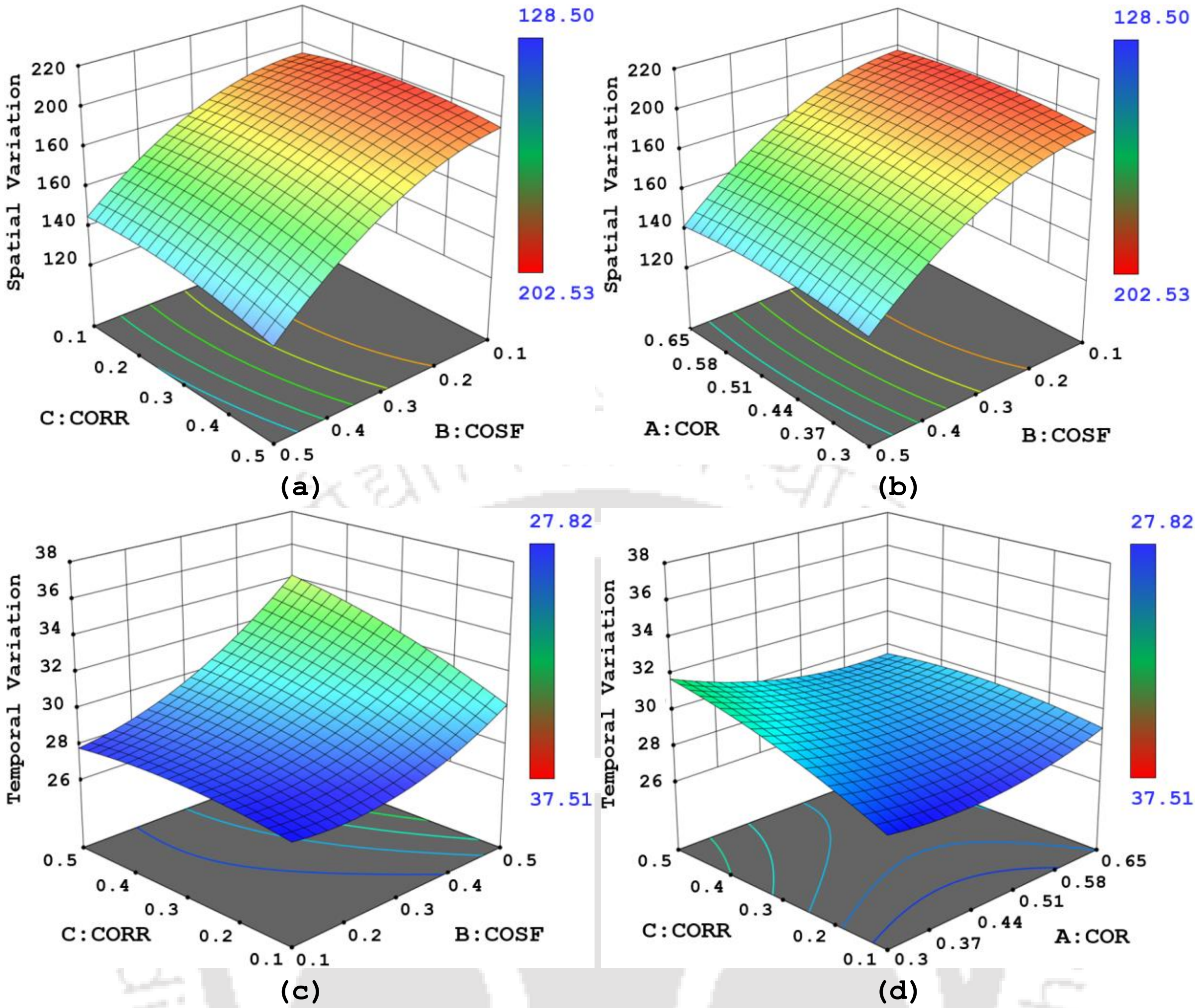

Fig. 2.13: Response surface for interaction parameters for (a, b) spatial variation and (c, d) temporal variation of the particle distribution

2.3.1.3 Remarks on Temporal Variation

From the ANOVA observations of single and multifactor interactions, it can be inferred that an increase in COSF and CORF restricts the flow of particles across the spreader disk's surface, increasing the interparticle collision and, thus, randomizing the particle discharge rate. Figure 2.14(a) and (b) show the number of contacts that occur as the simulation progresses for both high and low values of friction coefficients (sliding and rolling), respectively. For the cases where the friction coefficient values are low, the particles move uniformly and coherently (almost resembling a block), which reduces the temporal variations in mass flow rate.

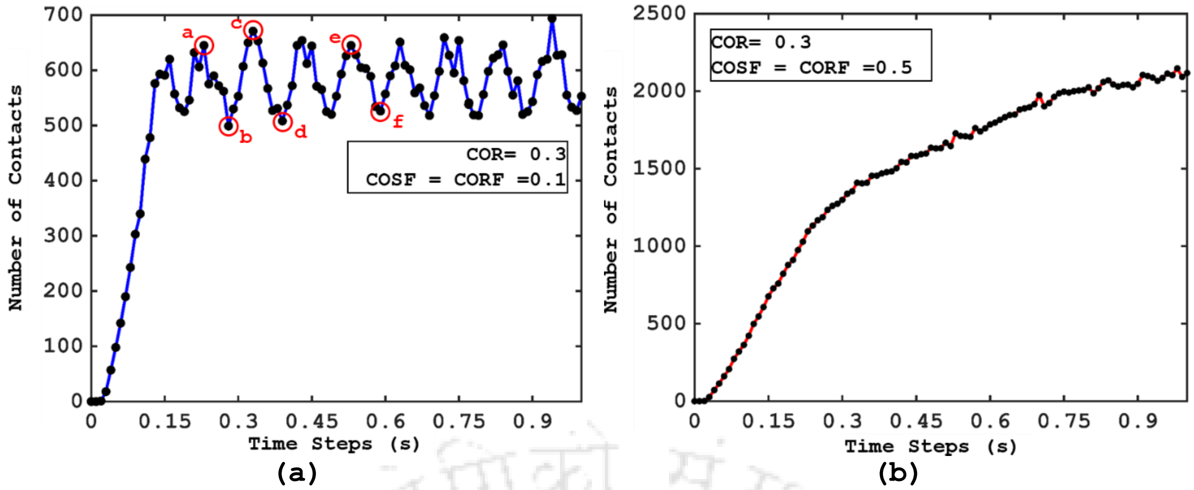

Fig. 2.14: Number of contacts observed for the case of (a) low and (b) high COSF and CORF values

This phenomenon of particles moving in a block can also be qualitatively visualized in Fig. 2.15. Figure 2.15(a-f) shows the simulation at time steps corresponding to the data points a, b, c, d, e, and f marked by red circles in Fig. 2.14(a).

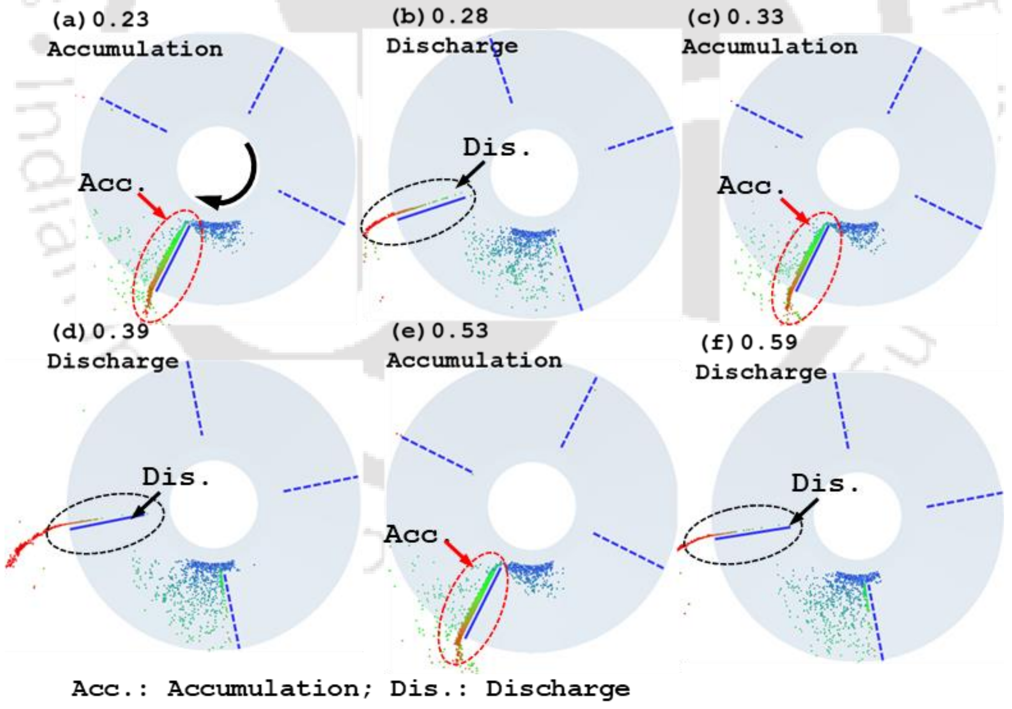

Fig. 2.15: Discharge of particles as 'blocks' with (a), (c), and (e) showing particle accumulation in front of the blade and (b), (d), and (f) showing particle discharge

With reference to Fig. 2.14(a), the periodic sawtooth variation of particle contact, i.e., the peaks (marked by a, c, and e) followed by the valleys (marked by b, d, and f), corresponds to particle accumulation and discharge cycles, respectively. As shown in Fig. 2.15, the solid blue line represents the blade for which these cycles were observed. During accumulation, the particles pile up in front of the blade, increasing the number of contacts, followed by discharge of the powder pile, thus decreasing the number of contacts. A similar observation was made for the remaining (unmarked) peaks and valleys.

Although qualitatively speaking, a similar observation can be made for the case with high COSF and CORF values; however, the phenomenon is not as pronounced, as illustrated in Fig. 2.16. Also, from Fig. 2.16(a-f), it can be observed that for high values of COSF and CORF, the number of contacts is significantly high with no distinct periodicity. Another perspective on the phenomenon can be obtained by considering the following. For the case with high friction coefficient values, the particles, as they land on the disk surface, are dragged along the rotational direction, thus preventing pile-up. Conversely, in the case with low friction values, the particles are pushed along the rotational direction primarily by the disk blades. In other words, the particles can be considered as if they are 'slipping' on the rotating disk unless a blade is encountered, thus promoting pile-up and granular motion as a 'block.'

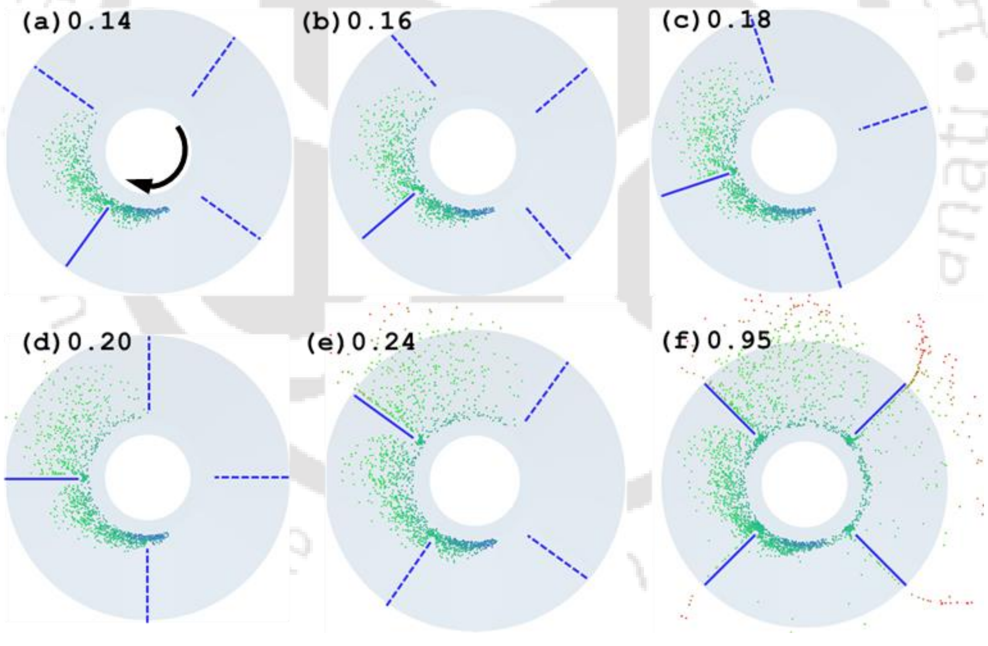

Fig. 2.16: Nature of granular flow observed for high values of COSF and CORF

2.3.1.4 Remarks on Spatial Variation

Following the method described in section 2.2.1, the spatial variation was quantified using the statistical parameter Coefficient of Variation(%CoV). As previously mentioned, thirty-six equally spaced mass sensors are placed underneath the rotating disk. The %CoV for the average mass recorded by these sensors/ bins represents the spatial distribution of the powder particles. A high

%CoV shows poor (or non-uniform) particle distribution, while a low %CoV signifies uniformity in the particle distribution. Figure 2.17(a) & Fig. 2.17(b) show two cases with low and high values of friction coefficients, respectively. It can be observed that for very low values of friction coefficients, the spatial uniformity of particle distribution is very poor, as signified by high %CoV, where some of the sensors receive zero powder particles within their domain, and others receive a very high value. The opposite is true of higher values of friction coefficients.

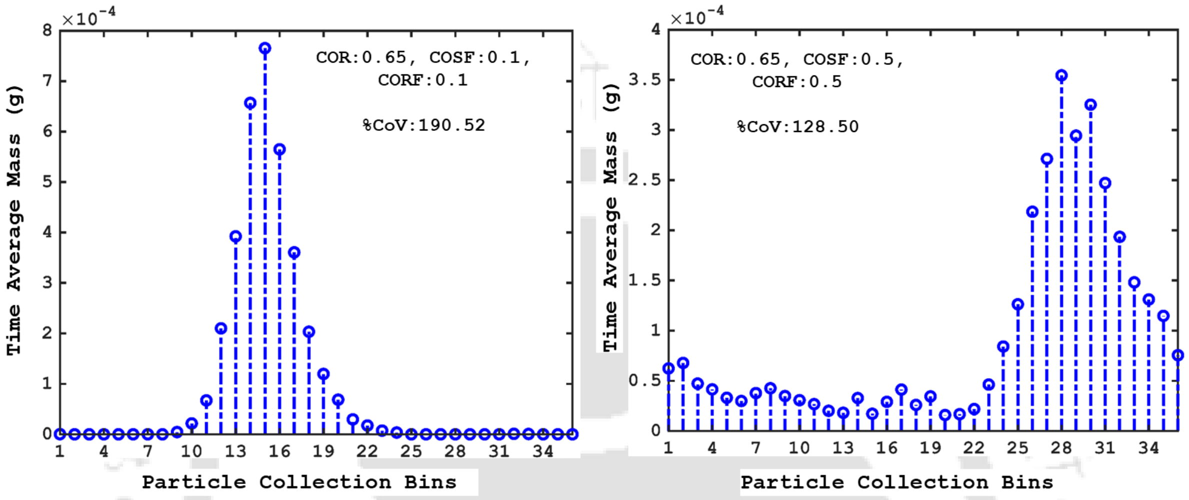

(a) **(b)**

Fig. 2.17: Spatial distribution observed for the case of distributor disk with (a) low and (b) high values of COSF and CORF

One probable cause for this behavior can be deduced qualitatively by observing Fig. 2.16(a-f). Attributing to high friction coefficient values, the region covered by the powder particles on the disk even before the blade makes contact (Fig. 2.16(a)) is fairly large. Subsequently, when the blades contact these powder particles, the 'region-of-spread' across the disk circumference is further enhanced. Furthermore, the particles were found to avoid accumulation and motion as a block, thus improving the spatial distribution across the disk circumference.

2.3.2 Experimental Validation

Experimental validation of the numerical study was carried out by considering a distributor disk of sufficiently complex geometry fabricated from SS316L, spreading powder particles of the same material across its periphery. As shown in Fig. 2.18(a), the distributor disk contains two sets of blade rows, where the first row of blade curves in the direction of rotation and the second row curves against it. The COSF value was obtained through experimentation using the test setup detailed in section 2.2.4.2. Given that the interacting material pair (bulk and equipment material) are of the same grade of stainless steel (SS316L), the values of interaction parameters remain the same for both powder-powder and powder-equipment interaction. The value of the rolling friction coefficient was kept equal to that of static friction, while a coefficient of restitution of 0.64 was obtained from the works of Nan *et al.* [214]. To ensure similar simulation and experimental conditions, thirty-six equally spaced bins were fabricated from Fused Filament Fabrication (FFF) and were kept underneath the distributor disk, as shown in Fig. 2.18(b). Table 2.7 lists the relevant simulation parameters.

Table 2.7: Parameters for DEM simulation used for experimental validation

Simulation Parameter	
Particle-particle Static Friction Coefficient	0.3
Particle-distributor Static Friction Coefficient	0.3
Particle-particle Rolling Friction Coefficient	0.3
Particle-distributor Rolling Friction Coefficient	0.3
Particle-particle Coefficient of Restitution	0.64 [214]
Particle-distributor Coefficient of Restitution	0.64 [214]

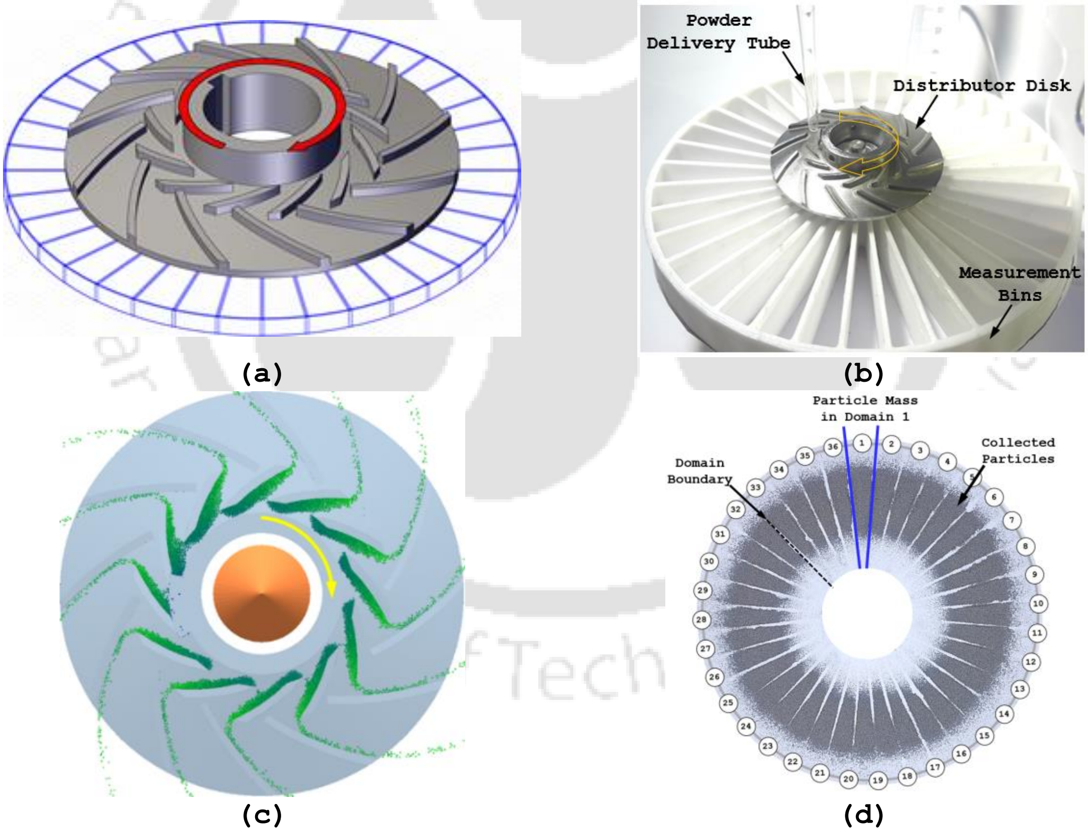

Fig. 2.18: The two-stage distributor geometry used for experimental validation (a) distributor disk and setup of measurement bins, (b) experimental setup, (c) spread pattern generated using the disk in DEM environment, and (d) particle spread pattern as generated during the experiment

After conducting the experiments, the powder mass within each bin could be distinctly observed and later collected using a fine brush. Subsequently, the total weight of powder particles within the individual compartments was measured to obtain the spatial particle distribution.

Figure 2.19 shows the variation in total powder mass received by each bin during the simulation and experiment. As previously discussed, the %CoV of the powder mass recorded by each of the bins within their domain is used to quantify the spatial distribution of the powder particles. The %CoV for the simulation and experiment was observed to be 13.01% and 15.50%, respectively, thereby suggesting a percentage error of 17.46% between the two.

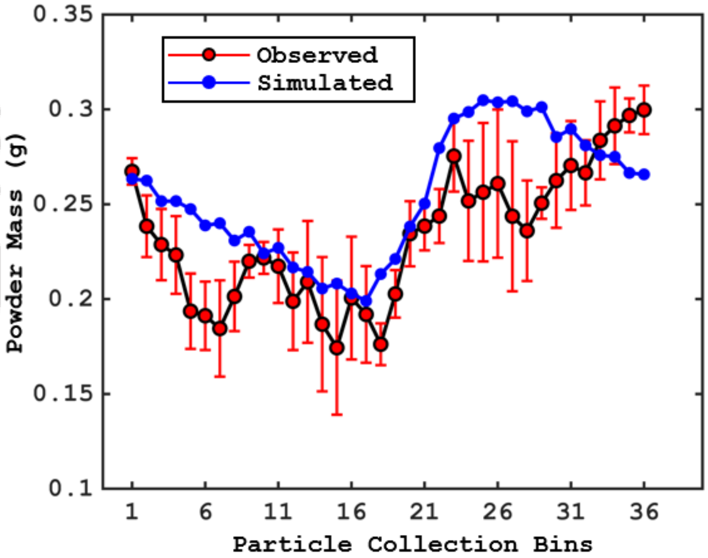

Fig. 2.19: Comparision between the simulated and the observed spatial distribution of the powder particles for a two-stage distributor disk

The results from the experimental validation of the simulation results, as shown in Fig. 2.19, exhibit a discrepancy. Local comparison of results at each data point, i.e., a side-by-side comparison of recorded mass by each of the thirty-six bins in simulation and experimentation, would suggest a higher discrepancy of results for some bins over others. The %CoV establishes a global comparison metric, considering the recorded data's local variations. A possible cause of the discrepancy observed in the simulated and experimental results may stem from the stochastic nature of the centrifugal spreading process. The process of centrifugal spreading is generally applied for distributing large-sized particles with a considerable spread area. The nature of the process in this study involved smaller particles spread over a relatively smaller area. Therefore, the effect of particle size on the percentage error observed between the experiment and simulated results requires further in-depth investigation. Furthermore, the particle interaction parameters can be exclusively calibrated to the distributor disk geometry such that the discrepancy in the observed results is minimized.

The surface roughness of the distributor disk provides another possible reason for the observed difference between the modeled and experimental results. Variations in the R_a value across the surface of the distributor disk adds an additional factor of randomness in the distribution of powder particles. The effect of surface defects (machining marks, deviation in part dimensions, dents, and scratches) and variations in the R_a is more likely to affect the response of the system for smaller particles as compared to larger ones. Accurately capturing the equipment geometry along with its surface properties thus becomes essential for more reliable modeling of the granular flows.

2.4 Summary

This chapter outlined the work carried out for the study of centrifugal spreaders, focusing on the sensitivity analysis of DEM input parameters on the spatial and temporal distribution of the particle spread. The following key observations were made under the conditions and the range of process variables used in this study.

- The coefficient of static friction significantly influences the uniformity in the spatial distribution of the powder particles and is positively correlated. For the case of temporal variation, the coefficient of static and rolling friction, independently as well as their interaction, was found to be dominant. Furthermore, the interaction between the coefficient of restitution and rolling friction was statistically significant in temporal variation.
- Parameters associated with restricted granular flow conditions, such as higher values of coefficient of static and rolling friction and lower values of coefficient of restitution, promote uniformity in spatial distribution, whereas the opposite is the case for temporal distribution. Through observing the overarching effect of material interaction parameters on selected responses, it can be inferred that achieving uniformity in the spatial and temporal distribution involves a tradeoff. For the presented case of the centrifugal spreader, spatial uniformity is achieved at the expense of temporal uniformity, thus implying a problem of optimization between the two responses.
- The experimental setup developed for the measurement of COSF promotes the ease of material property evaluation and is cost-effective. This setup is easily fabricated and, when combined with the outlined methodology of sample preparation, can be reliably used for various types of powder-equipment material pairs.

The percentage error in the simulated and observed values of spatial distribution is relatively high. This can be partially attributed to the negligence of particle cohesivity in the contact model. Several other contact force models that consider the cohesivity of particles exist in the literature; however, additional terms, such as surface energy, are often used to factor in the effect. These additional terms should be included in the design space of ANOVA to further the understanding of parameter sensitivity. Also, the rotational speed of the distributor and particle size distribution were not considered as part of the sensitivity analysis and required further investigation. Additionally, techniques for reducing computational time, such as coarse-graining and appropriate selection of time steps, need further study to establish a valid range of simulation parameters in a reasonable computational time. Given the importance of accurately capturing the surface properties of interacting parts to develop more reliable models of granular behavior, further studies in this regard are essential.

Chapter 3

Development of Non-pneumatic Method of Powder Feedstock Handling

As discussed in Chapter 1, the feedstock handling in DED, for simplicity, can be categorized into three phases: powder metering, conveyance, and delivery. In the initial iterations of the proposed non-pneumatic design for feedstock handling, a screw conveyor (auger) was selected as the means for powder metering. This metered powder is delivered to the powder delivery nozzle under gravity, thus accomplishing conveyance. Finally, for the third phase, the influx of powder received by the delivery nozzle will be shaped into a conical and a convergent envelope of powder stream around the laser beam. These three phases of the proposed feedstock handling unit are illustrated in Fig. 3.1.

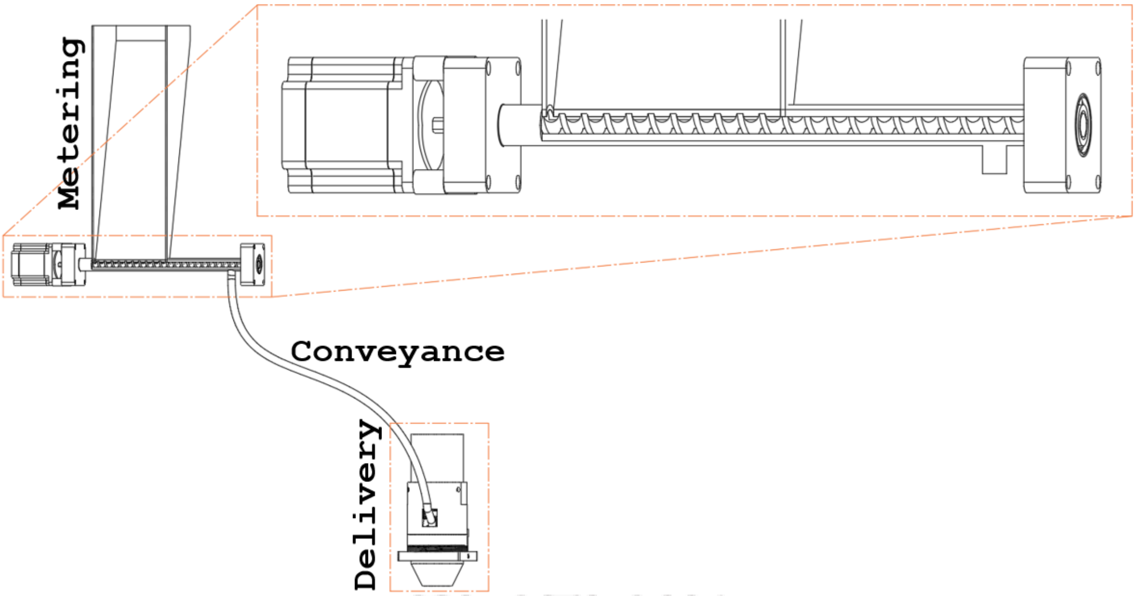

Fig. 3.1: Initial design for non-pneumatic powder handling system showing three phases of powder metering, conveyance, and delivery

The objective of this chapter is to present the challenges faced during various phases of gravity-based feedstock handling and present their possible solution. These solutions were derived from the design inputs received through multiple DEM simulations and preliminary experiments.

3.1 Powder Metering

Even though accurate, the auger-based powder metering suffers from pulsed powder discharge, an observation also made by Bitragunta *et al.* [247] and is schematically illustrated in Fig. 3.2. The design of the screw conveyor consists of a screw flight, with a thickness (say) t_f and in between the gap of two consequtive screw flights is a packet of powder (say) t_g. The powder is delivered to the delivery nozzle when the powder packet is over the opening; otherwise, the opening is blocked by the screw flight. Thus, a pulsed discharge is observed. This pulsation is more pronounced when the auger is rotated at slower rotational speeds for small mass flow rates, as is the case in DED. Therefore, an alternative design is proposed to address the pulsation of the powder discharge.

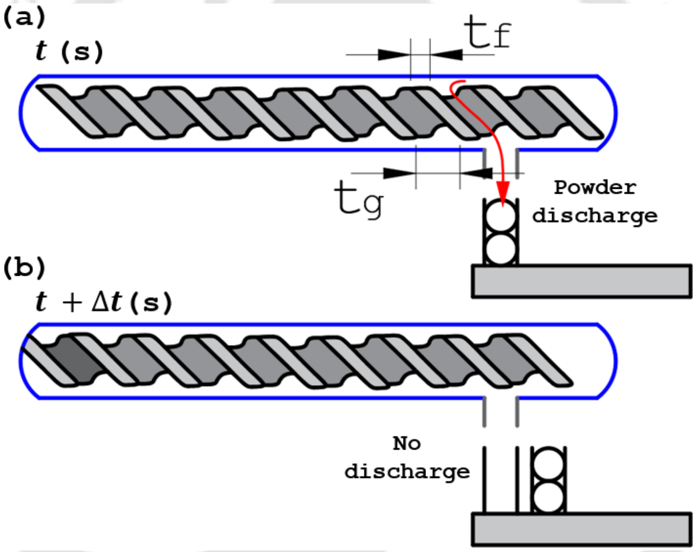

Fig. 3.2: Two states of auger configuration at the time (a) t the powder pocket is delivered to the substrate and (b) $t + \Delta t$ screw flight over the discharge opening and thus blocking the powder flow

Consider the setup shown in Fig. 3.3. A cylindrical rod (12) with a helical groove along its periphery, termed a metering rod, is rotated within a powder-filled encasement (10). The pitch of the helical groove is equal to the length of the encasement, an essential condition for continuous powder metering. The upper part of the encasement is fitted with a powder hopper (2), whereas the lower part has three openings for powder discharge. These openings, $14a$, $14b$, and $14c$, termed powder outlet, have respective outlet widths b_1, b_2, and b_3, as shown in Fig. 3.3(a) and Fig. 3.3(b). The outlet width can be used to vary the powder mass discharged for each of the three outlets, or conversely, it can be adjusted to tune the system for equal powder discharge. The hopper (2), using baffles(16), has provision for partitioning its volume into two or more sections for multi-material feed, as shown in Fig. 3.3(c). The position of the baffle(s)(16), along with bulk material properties, governs the 'ratio-of-mix' amongst the powder species at discharge. The rotational speed of the metering rod(12) and the volume and number of helical grooves determine the powder mass flow rate.

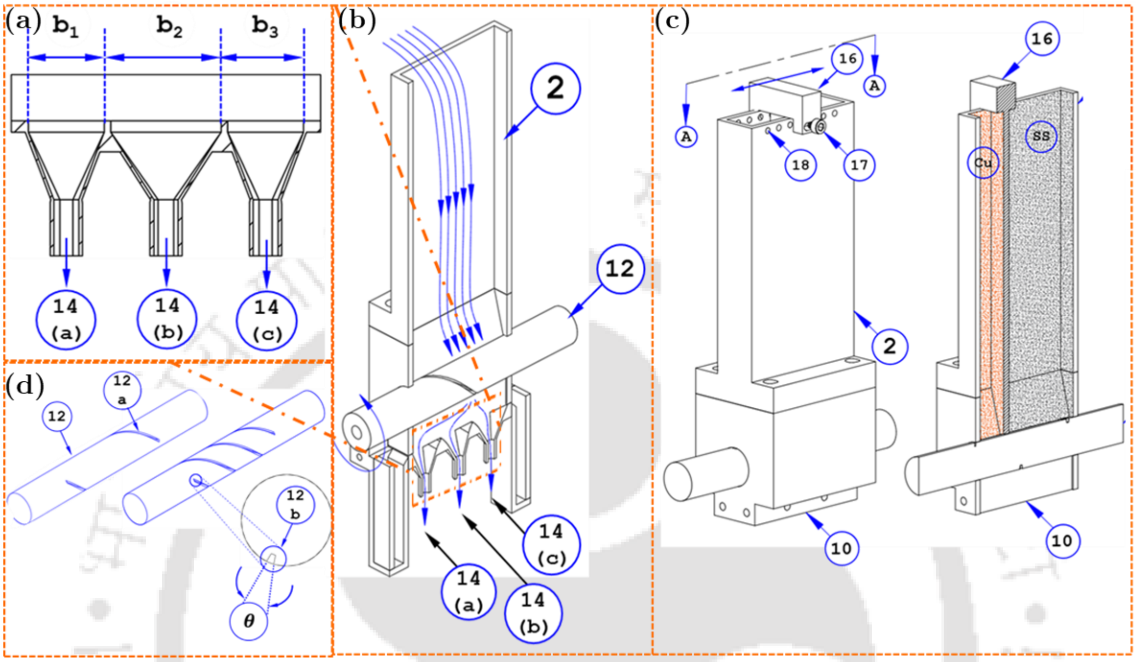

Fig. 3.3: Groove-based powder metering apparatus (a) adjustable powder hopper slot (b) powder metering through rotating metering shaft (c) provision for multi-material input and (d) draft angle of the helical groove on the metering rod to prevent powder clogging

Consider a case of free-flowing particles where the particle size is large and is non-cohesive. For such a case, a segmented helical groove (12c) on the metering shaft, as shown in Fig. 3.4, is proposed. These segments restrict the powder particles from adjusting themselves within the helical groove, consequently improving the uniformity of the powder discharge from each of the three hopper outlets (14). The addition of segments in the helical groove of the metering shaft (12) prevents powder particles from accumulating at the preferred region within the groove (a region marked $'a'$ in Fig. 3.4(a)) and subsequently disproportionately discharging from the hopper outlets.

The clearance between the metering shaft and the encasement allows for the rotation of the metering shaft; however, attributing to this clearance, the powder mass discharged will be higher than the predicted values. Therefore, as shown in Fig. 3.5, a calibration curve becomes essential. Furthermore, as is noted from Fig. 3.5(a), a higher value of standard deviation is observed at higher mass flow rates, and the calibration curve is not linear, thus further signifying the need for calibration of the setup. The powder mass discharged from each of the three outlets was analyzed for consistency in powder delivery, as shown in Fig. 3.5(b).

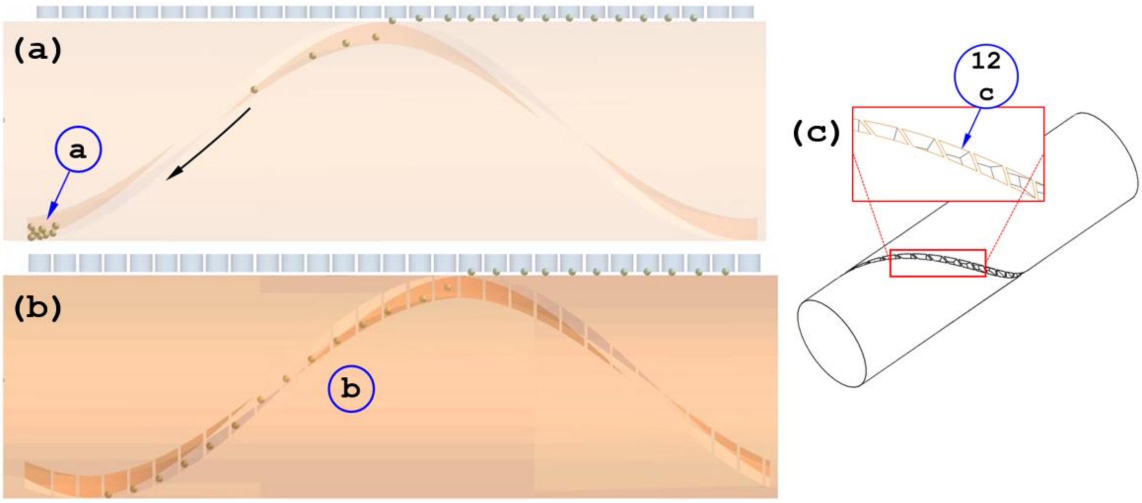

Fig. 3.4: A metering rod with (a) non-segmented helical groove where powder particles accumulate in a region marked a, (b) segmented helical groove promoting uniform discharge of powder during operation, and (c) exaggerated view of the segments

The straight-line nature of the plot suggests a continuous and steady increment in the powder weight from each of the three outlets. Therefore, it can be concluded that the metering unit can sustain a steady powder delivery during a deposition without any clogging or unmetered (free) powder flow.

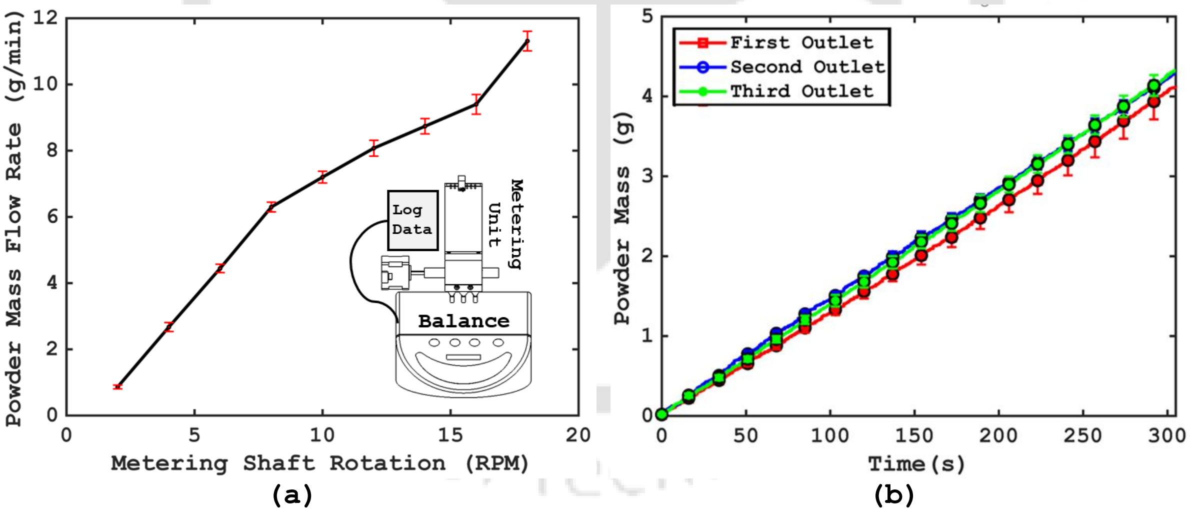

Fig. 3.5: (a) Calibration curve of powder flow rate with metering shaft rotation (b) rate of powder mass accumulation (for a fixed RPM) for 300s from each of the three powder delivery outlets

3.2 Design Consideration for Distributor

The rotating distributor is a crucial component of the proposed powder delivery unit. Its performance is dictated by its ability to provide spatial uniformity in the generated granular dispersion while maintaining a constant mass flow rate, as illustrated schematically in Fig. 3.6(a).

This spatial uniformity of powder distribution around the melt pool imparts omnidirectional capability to the proposed design. Figure 3.6(b) schematically shows a non-uniform distribution that induces geometric deviations (error) in deposited bead, which is dependent on the direction of travel. As illustrated in Fig. 3.7, several variations of distributor design were tested through DEM simulations for their ability to generate a spatially uniform powder spread. While some of the tested variants were able to provide a relatively uniform powder spread, but were difficult to produce through machining, and others provided a poor spatial distribution.

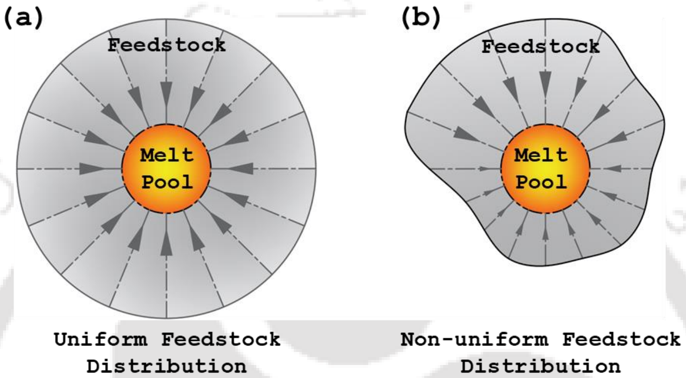

Fig. 3.6: Distribution of powder particles around the fusion source (a) uniform spatial distribution and (b) non-uniform distribution

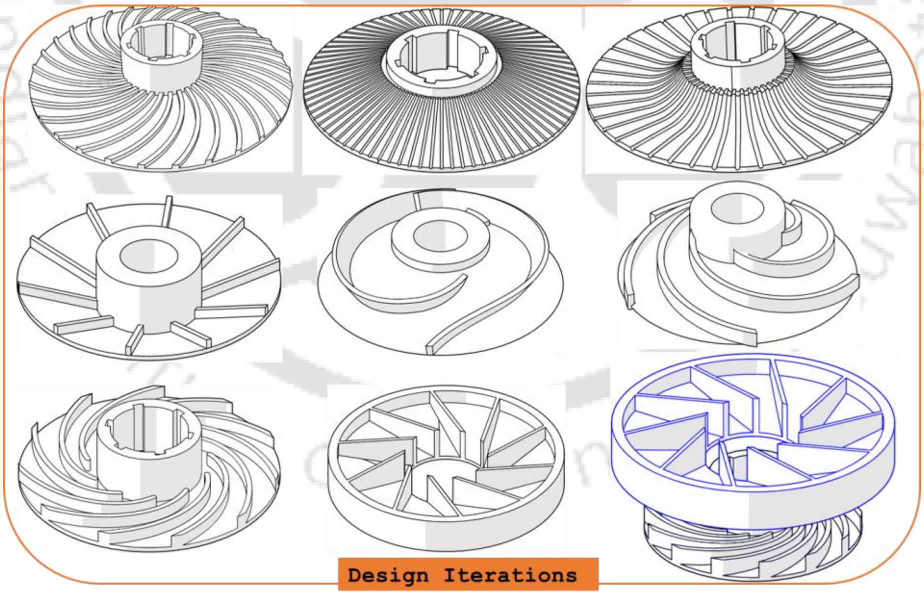

Fig. 3.7: Various design iterations evaluated for feedstock spatial distribution

As described previously in section 2.2.1, quantifying the spatial distribution of the powder particles around the fusion source was made through virtual mass sensors placed in a circular array underneath the rotating distributor, as illustrated in Fig. 3.8. For the study presented here, thirty-six equally spaced sensors record the total powder mass received within their respective domains at fixed intervals during the simulation. These values can then be averaged over the simulation time to reveal the powder particles' spatial distribution (uniformity of particle scatter). The Coefficient of Variation (COV) in the recorded mass amongst the sensors provides a means to quantify the spatial uniformity of particle distribution.

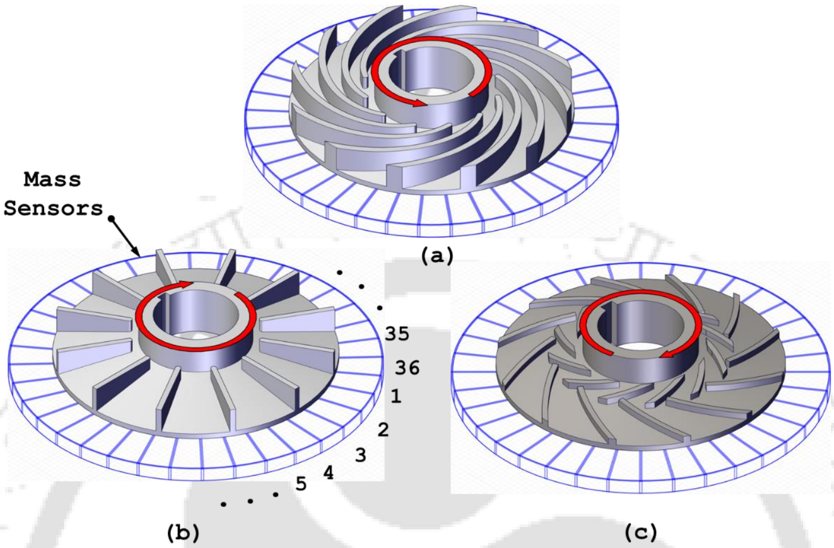

Fig. 3.8: Arrangement of virtual sensors (or bins) to quantify spatial uniformity of particle distribution for (a) curved blade, (b) straight blade, and (c) two-stage distributor

3.2.1 Performance Evaluation of Distributor Designs

A vital performance trait of a distributor is its ability to scatter the incoming bulk matter across its periphery uniformly, thus ensuring uniformity in the feedstock's spatial distribution and consequently making the nozzle omnidirectional. However, ensuring uniform spatial distribution of the granular media is a challenging task, primarily due to its discrete and random nature. A distributor with a large number of blades can offer ordered granular flow due to the confinement of the powder particles within the narrow channels formed by the blade. However, this uniformity comes at the expense of decreased mass flow rate and increased manufacturing difficulty.

Consider the three types of distributor designs with a curved blade, a straight blade, and a two-staged blade, as previously illustrated in Fig. 3.8 (a), (b), and (c), respectively. The following section discusses critical findings and key observations concerning these distributor designs.

3.2.1.1 Straight Blade Distributor

As the name suggests, a straight blade distributor features a rotating disk fed off-axially with granular media at a constant flow rate and uses a radially straight set of blades for its dispersion. Multiple design iterations with the number of blades ranging from 0 to 50 (incrementing in steps of 2) were analyzed for the degree of spatial uniformity and mass flow rate. The spatial uniformity of the granular media, as offered by these designs, can be observed in Fig. 3.9(a)-(l). Figure 3.10 (a)-(f) provides the average powder mass received by each sensor for the simulation time of 1s.

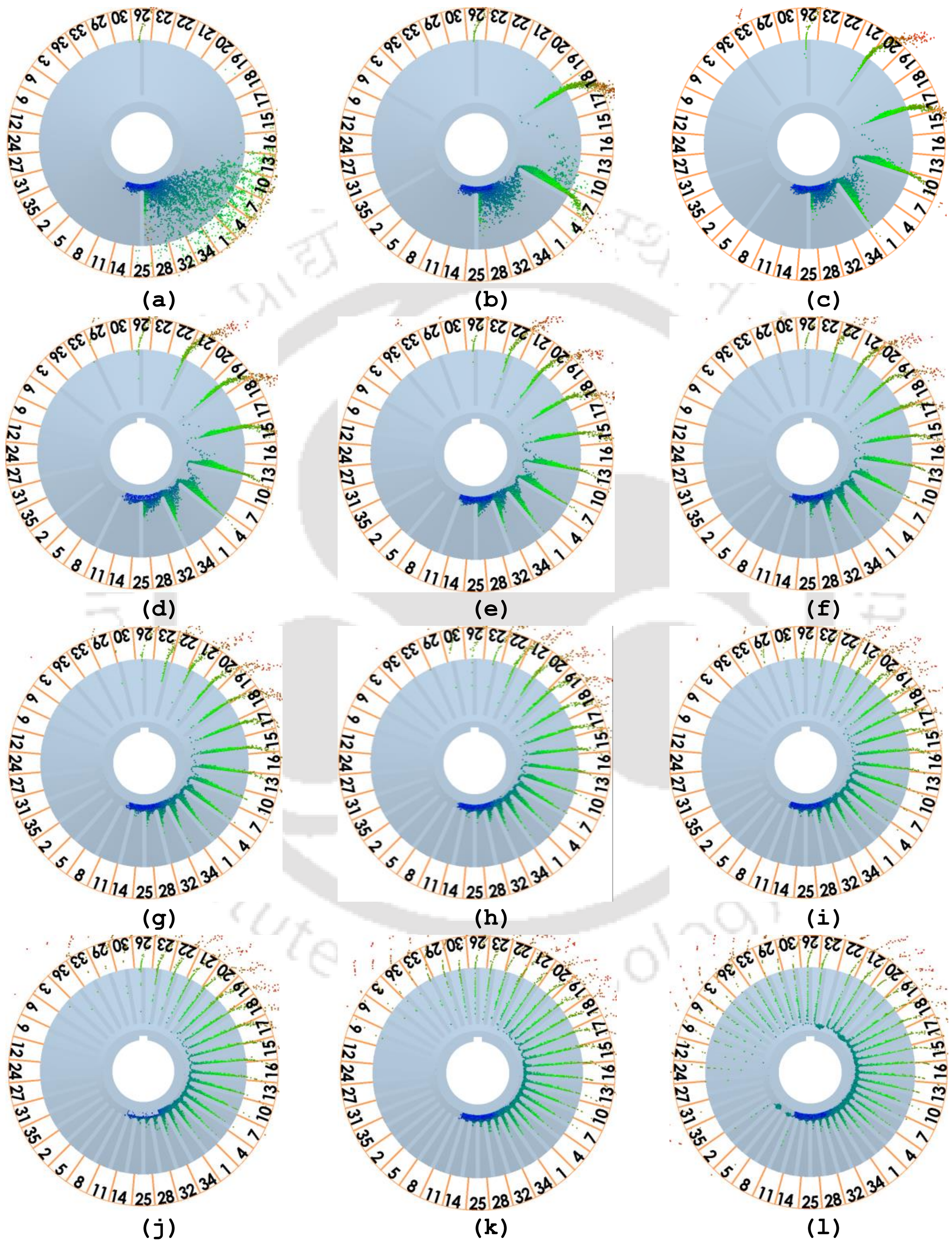

Fig. 3.9: Variation in the spatial distribution of powder particles with the number of blades for a straight-bladed distributor with (a)2, (b)6, (c)10, (d)14, (e)18, (f)22, (g)26, (h)30, (i)34, (j)38, (k)42, and (l)46 blades

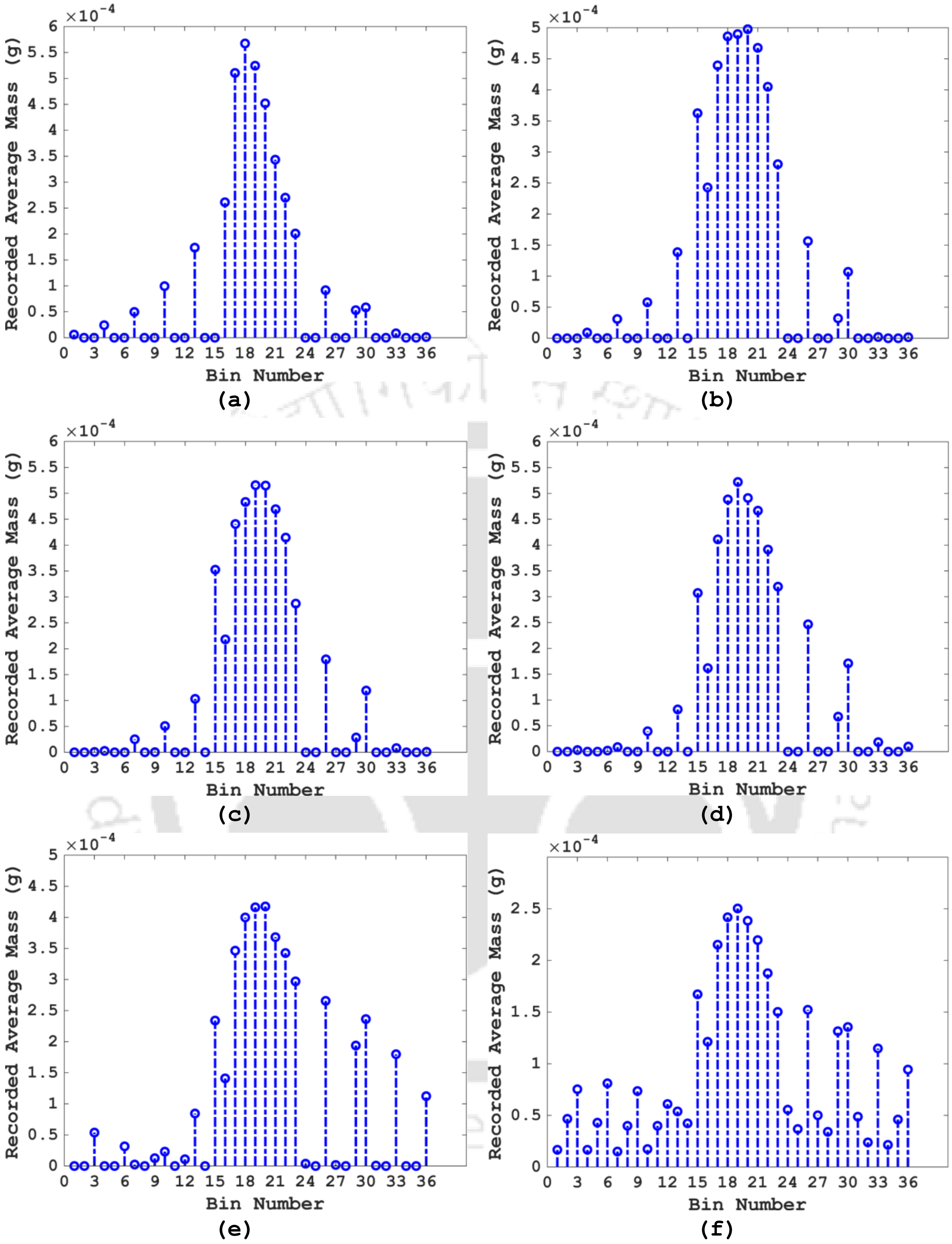

Fig. 3.10: Time-averaged mass recorded by each bin for a straight-bladed distributor with (a)10, (b)18, (c)26, (d)34, (e)42, and (f)50 blades

The %COV in the recorded mass amongst the sensors showed a marginal decline as the number of blades increased. Also, with a significantly high number of blades, even though %COV showed a moderate reduction, but was accompanied by a decrease in the mass flow rate, as shown in Fig. 3.11.

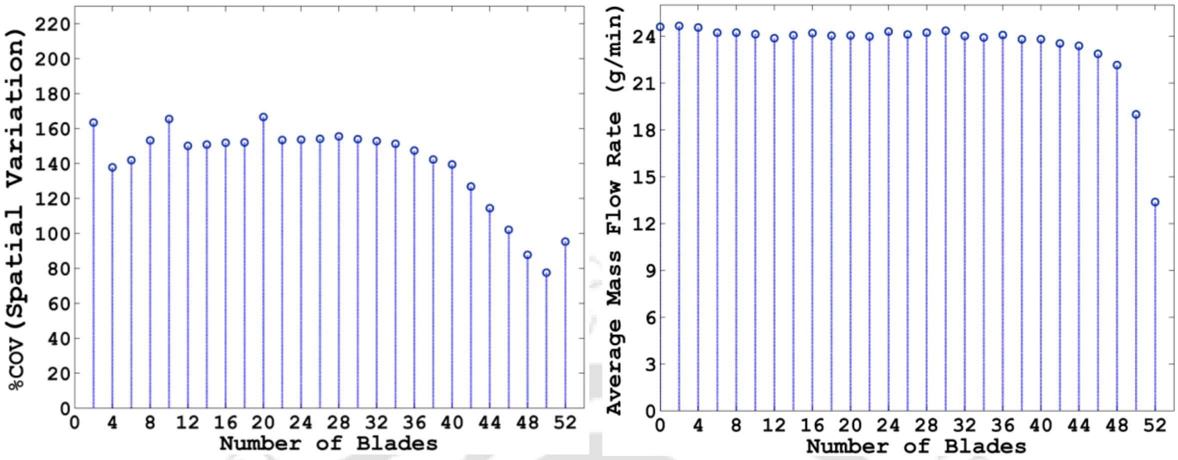

(a) (b)

Fig. 3.11: Particle distribution observed in a straight blade distributor with an increasing number of blades showing (a) marginal improvement in spatial uniformity and (b) variation in mass flow rate

3.2.1.2 Curved Blade Distributor

Figure 3.12 (a)-(l) illustrates the results from the analysis of a curved blade distributor. The design iterations consist of the number of blades starting from 2 and going up to 27 in increments of 2. Compared to the straight blade, a curved blade distributor shows a significant decrease in %COV values for the recorded average mass amongst the mass sensors as the number of blades on the disk increases, as illustrated in Fig. 3.12(a-l). This is also evident from Fig. 3.13(a-f), which depicts increased uniformity amongst the sensor data as the number of blades increases.

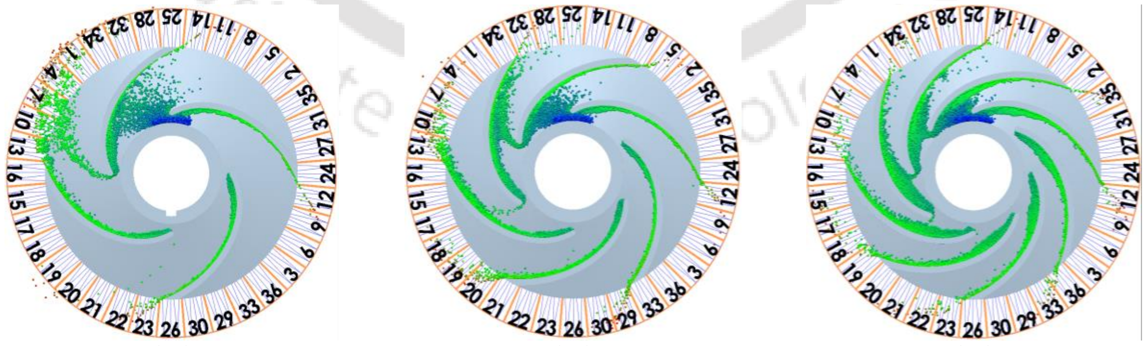

(a) (b) (c)

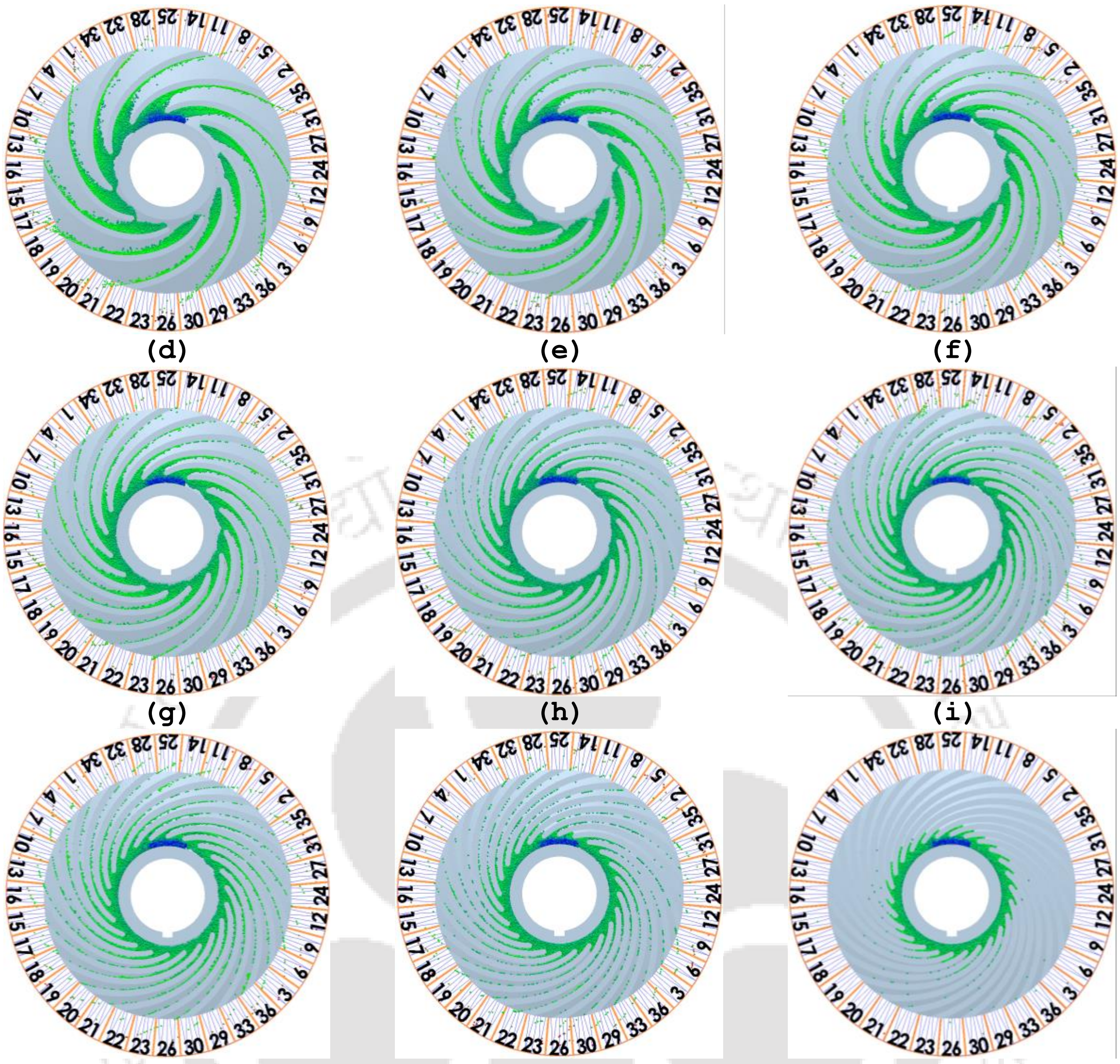

(d) (e) (f)

(g) (h) (i)

(j) (k) (l)

Fig. 3.12: Variation in the spatial distribution of powder particles with the number of blades for a straight-bladed distributor with (a)4, (b) 6, (c)8, (d)10, (e)12, (f)14, (g)16, (h)18, (i)20, (j)22, (k)24, and (l)26 blades

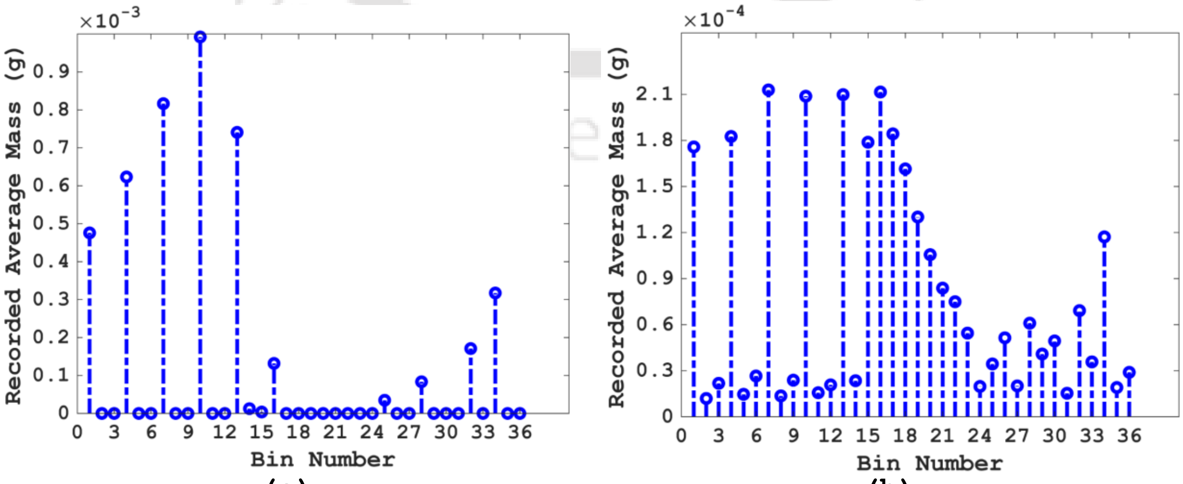

(a) (b)

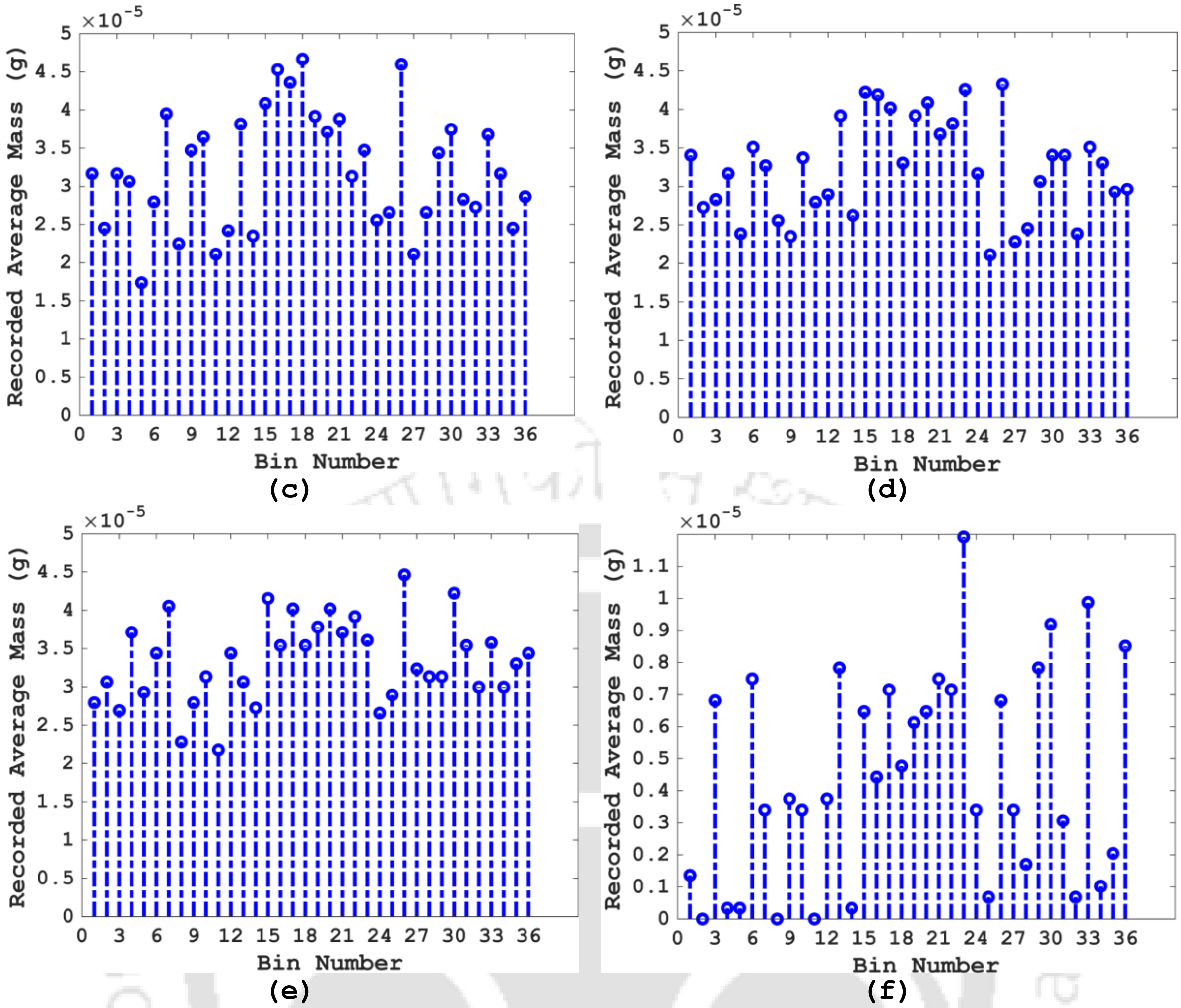

Fig. 3.13: Time-averaged mass recorded by each bin for a straight-bladed distributor with (a)0, (b)6, (c)14, (d)18, (e)22, and (f)26 blades

Although it is desired to have a uniform spatial particle distribution, the tradeoff with the mass flow rate for a curved blade distributor is severe. As the number of blades increases, the powder mass flow rate falls, as shown in Fig. 3.14(b). This decline can be attributed to the narrowed passageways on the disk due to the increased number of blades. With a distributor disk having a number of blades higher than 26, a complete clogging of the particle flow was observed at the inflow section. Furthermore, it can also be argued that the curved blade profile increases the blade length, which in turn increases frictional losses, thereby resulting in a decreased mass flow rate.

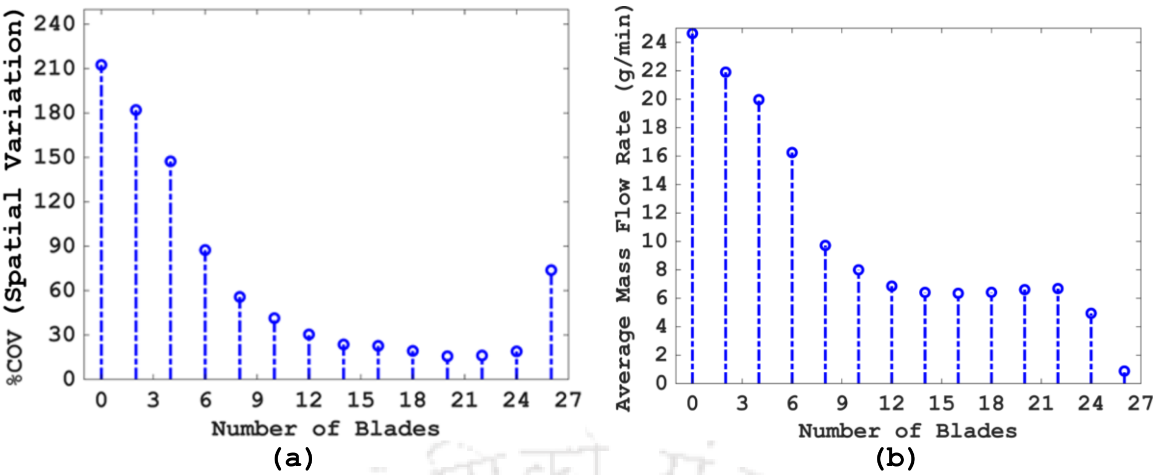

Fig. 3.14: Particle distribution observed in a curved blade distributor with an increasing number of blades showing (a) marginal improvement in spatial uniformity and (b) variation in mass flow rate

3.2.1.3 Design of Two-Stage Distributor

From the analysis of the previous two distributor designs, a conclusion can be made that the curvature of the blade is essential for achieving spatial uniformity in particle distribution. However, higher blade curvature also produces a poor mass flow rate due to frictional losses. A two-stage distributor design features two rows of curved blades rotating opposite to each other on a single disk. Simulation results from a two-stage distributor design show improved spatial uniformity in particle dispersion with a recorded %COV amongst the mass sensors of 11.29 along with a relatively high mass flow rate averaging at 27 g/min, as illustrated in Fig.3.8(b) and Fig.3.8(c), respectively.

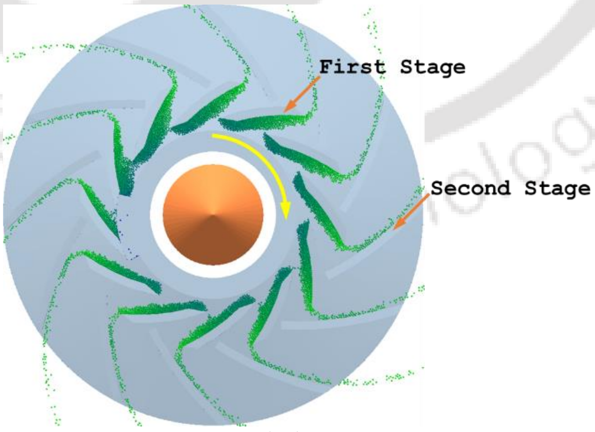

(a)

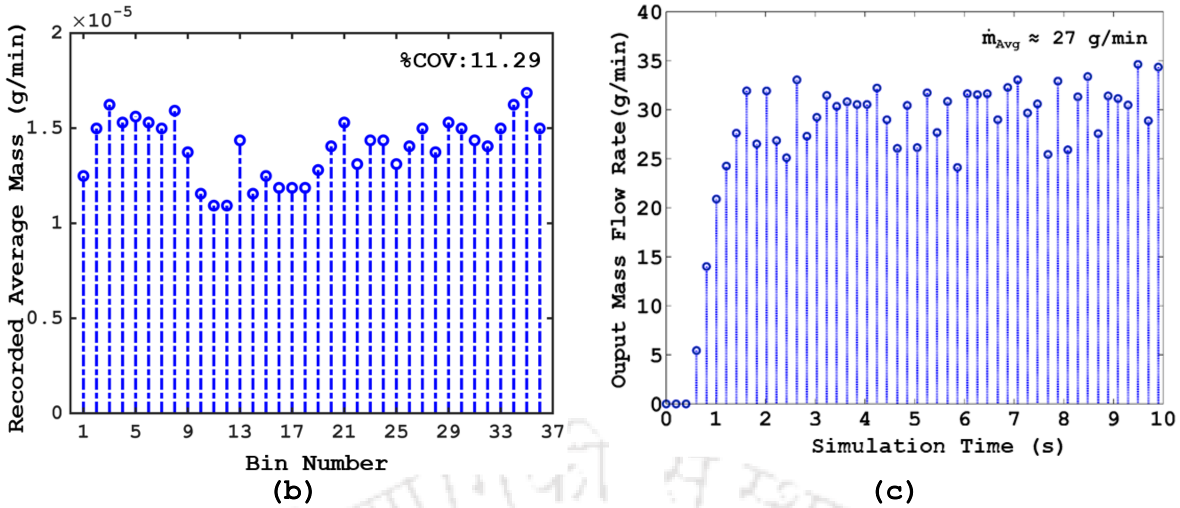

Fig. 3.8: Performance evaluation of a two-stage distributor design showing (a) spatial distribution of powder particles, (b) average mass recorded by mass flow sensors, and (c) mass flow rate over the total simulation time

The rationale behind the design choice for a two-stage distributor can be explained as follows. Consider a straight-blade distributor with two blades on the disk, as illustrated in Fig. 3.15. The process of bulk material dispersion through a rotating disk can be decomposed into three separate and distinct phases.

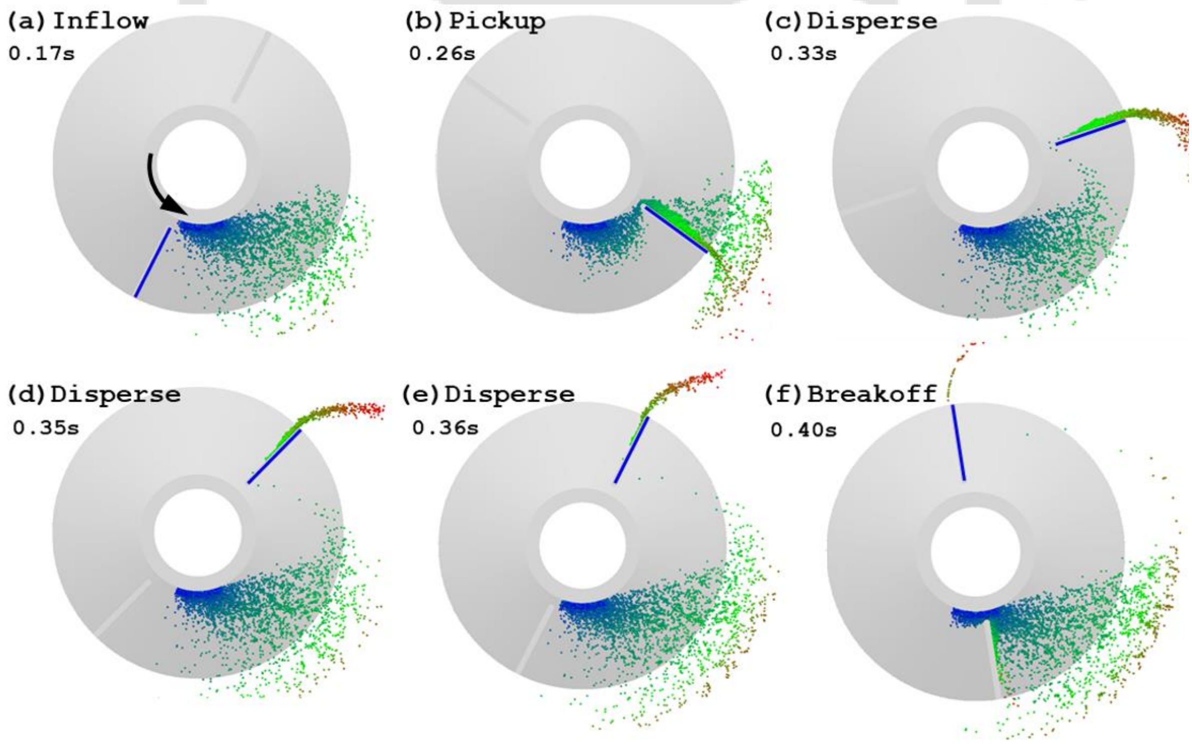

Fig. 3.15: Phase of particle dispersion through a rotating disk (a) inflow, (b) pickup (c,d, and e) dispersion, and (f) breakoff

The first phase is material inflow (Fig. 3.15(a)). During inflow, the particles are on the disk; however, their motion is solely dictated by the rotation of the disk, i.e., the blades of the disk do not interact with the particles. In the second phase, termed pickup (Fig. 3.15(b)), the disk blades collect the particles in front of it, consequently forming particle piles. These piles increase the interparticle and particle geometry interaction due to accumulation (increased bulk material density). In the third phase of dispersion(Fig. 3.15 (c)-(e)), attributing to the centrifugal force, the accumulated particle piles are pushed radially outwards and are dispersed off from the disk. Figure 3.15(f) marks the end of the dispersion phase and is termed a breakoff. A breakoff is identified by the localized absence of bulk material on the disk corresponding to a specified (unique) blade for further dispersion.

After 'breakoff,' the blade enters an idle region (illustrated in Fig. 3.16) where its rotation does not account for any particle dispersion. It is evident from Fig. 3.16 that the longer the idle region, the higher the non-uniformity in spatial distribution. Furthermore, the underlying cause of a prolonged idle phase can be primarily attributed to the absence of bulk matter available to any given blade for dispersion. In other words, shorter idle time and, consequently, better spatial uniformity can be achieved by ensuring that each blade on the disk maintains a constant inflow of bulk material.

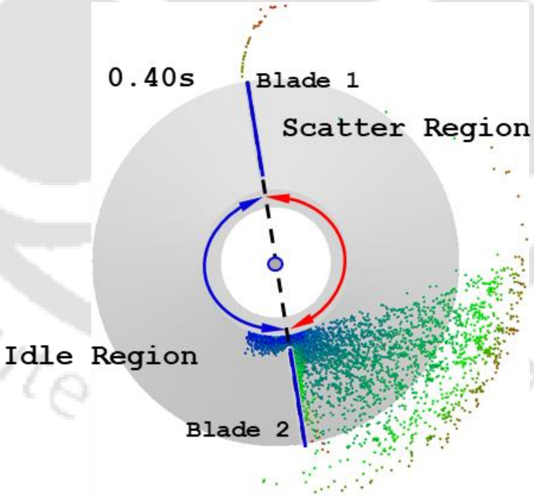

Fig. 3.16: Scatter and idle regions observed during particle dispersion through a distributor

Consider a curved blade distributor, as shown in Fig. 3.17. The direction of distributor rotation relative to a curved blade can be categorized into forward-swept and backward-swept. A forward-swept distributor rotates in the direction of blade curvature, whereas a backward-swept one rotates against it, as illustrated in Fig. 3.17(a) and Fig. 3.17(b), respectively. A forward-swept distributor provides increased spatial uniformity but a decreased mass flow rate, whereas the opposite is true for a backward-swept distributor.

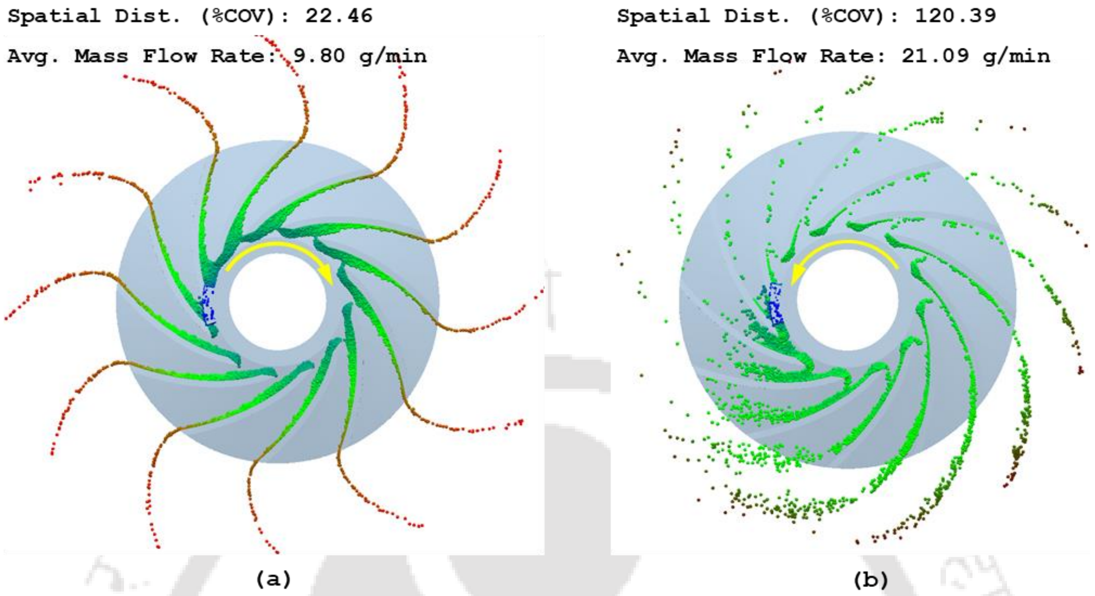

Fig. 3.17: Orientation of blades relative to the direction of rotation for (a) forward-swept and (b) backward-swept distributor design

Results from the simulations performed under identical conditions of the blade geometry, inlet mass flow rate (30 g/min), and rotational speed are shown in Fig. 3.17. A forward-swept distributor (Fig. 3.17 (a)) registered an average exit mass flow rate of 9.80 g/min with high spatial uniformity of powder particles. On the other hand, a backward-swept distributor shows a higher mass flow rate (21.09 g/min) with poor spatial uniformity. Also, it is evident from the results that a forward-swept distributor retains powder particles for its entire rotation, thereby significantly increasing its scatter region with little to no idle region. Thus, from the discussion on phases of bulk material dispersion presented earlier and the results from these comparative studies on backward versus forward-swept blade designs, it can be inferred that a forward-swept blade can be used for particle retention, followed by a row of the backward-swept blade for particle dispersion. Such a design can establish a uniform feed of bulk material to each of the blades of the distributor disk that are responsible for particle dispersion, which would increase the scatter region and consequently improve the spatial uniformity of powder dispersion.

To understand the reason behind the high retention/ accumulation of powder particles in the case of a forward-swept distributor, consider the following argument. In the case of a forward-swept blade, the blade curvature is negative, i.e., the blade curves towards the particle and into the direction of rotation, as illustrated in Fig. 3.18(a). This increases the contact length between the particle and the blade, thereby increasing frictional resistance and restricting particle motion. In the case of a backward-swept blade, the blade curvature is positive, i.e., the blade curves away from the particle and the direction of rotation, as illustrated in Fig. 3.18(b). This positive curvature reduces the contact length (ideally, with no deformation, the contact reduces to a point), thereby reducing frictional resistance and promoting ease of motion.

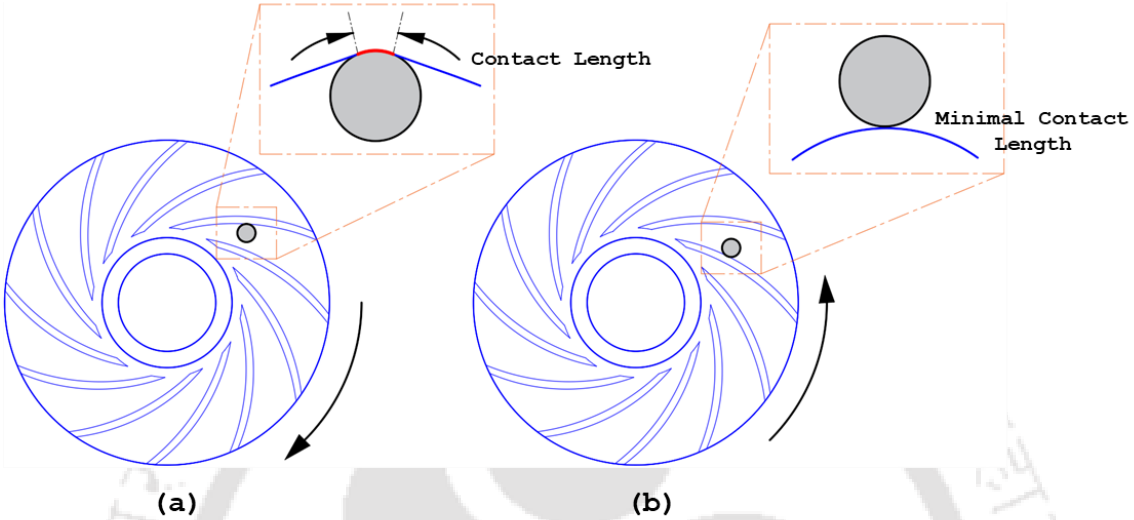

Fig. 3.18: Negative blade curvature for (a) a forward swept blade resulting in increased contact length and (b) positive blade curvature for a backward swept blade, thus reducing contact length

The observations above and the analysis suggest using a two-stage distributor design for better performance in particle dispersion without significantly compromising the mass flow rate. The first stage of the distributor, which is forward-swept, primarily acts as a buffer that maintains a constant feed of powder particles to the second stage for dispersion. The length of the first-stage blades is shorter than the backward-swept second stage, thus avoiding the loss of mass flow rate. Improved spatial uniformity and mass flow rate make the two-stage blade design ideal for the proposed powder feed nozzle in DED.

3.3 Power Stream Analysis

After exiting the nozzle, the powder stream travels toward the melt pool on the substrate. A powder stream analysis is crucial to determine the focal length and the deposition plane. In the subsequent sections, using novel virtual mass sensor methods, an effort is made to quantify the powder stream with parameters pertinent to the DED process.

3.3.1 Evaluation of Focal Length

Qualitatively speaking, the powder stream after exiting the nozzle is of conical and convergent nature, an attribute desirable for DED. A linear array of virtual mass sensors ascertain the focal length of the powder stream relative to the nozzle outlet. This array consists of 46 sensors, each with a cubical domain of side length 0.5 mm, as illustrated in Fig. 3.19(a). During the simulation, these sensors record the total particle mass at specified intervals within their domain. The linear array of 46 sensors was incrementally moved downwards along the flow stream, maintaining symmetry with the nozzle axis. Figure 3.19 shows the conical nature of the powder flow stream as deduced from the data recorded by the mass sensor array. Close to the nozzle outlet, the sensors at the extreme ends of the array register powder particles, whereas the sensors located in the middle did not receive any particles. As the sensor array was moved downwards towards the focal point of the powder stream, a change in trend was noticed, such that the extreme sensors recorded no powder flow, and the middle ones recorded the highest values. In other words, close to the nozzle outlet, a near bimodal distribution of powder particles was observed with two distinct peaks. Moving downstream towards the focal point shows the particle distribution shifting from bimodal to unimodal, with the two peaks progressively coming closer, as illustrated in Fig. 3.19(b)-(g). Moving further downstream, beyond the focused region, the particle distribution shifts to an almost bimodal pattern again. Using this methodology, the analysis of the powder stream suggests a focal length of ≈24.0 mm, i.e., at 24 mm (and onwards) from the nozzle outlet, the middle sensors (at and around the nozzle axis) start to register powder particles within their domain consistently.

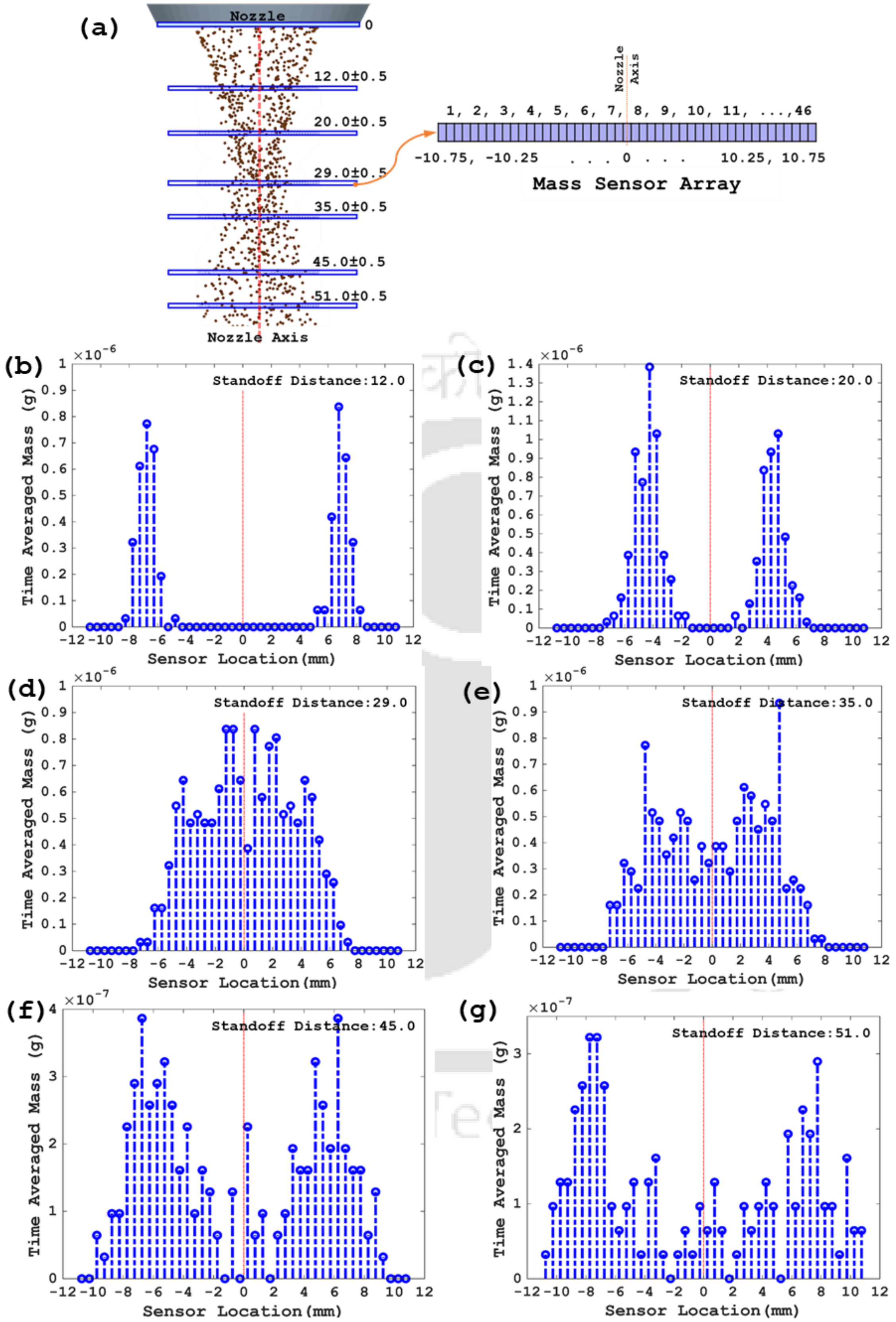

Fig. 3.19: (a) Arrangement of mass sensors for particle stream analysis with subsequent plots showing particle distribution at a standoff distance of (b)12.0, (c)20.0, (d)29.0, (e)35.0, (f)45.0, and (g)51.0 mm

The particle distribution at the focal plane of the converged powder steam was also visualized using an array of linear mass sensors. Each array element was a cube with a side length of 0.5 mm, which was rotated about the vertical (along the nozzle axis) from 0° to 180° with an increment of 20° at each iteration. Figure 3.20 shows the powder collected by each bin, thereby revealing the powder stream focal spot diameter (spot size) of ≈10 mm recorded at 28 mm from the nozzle outlet with a gradual decline in the powder mass downstream of flow.

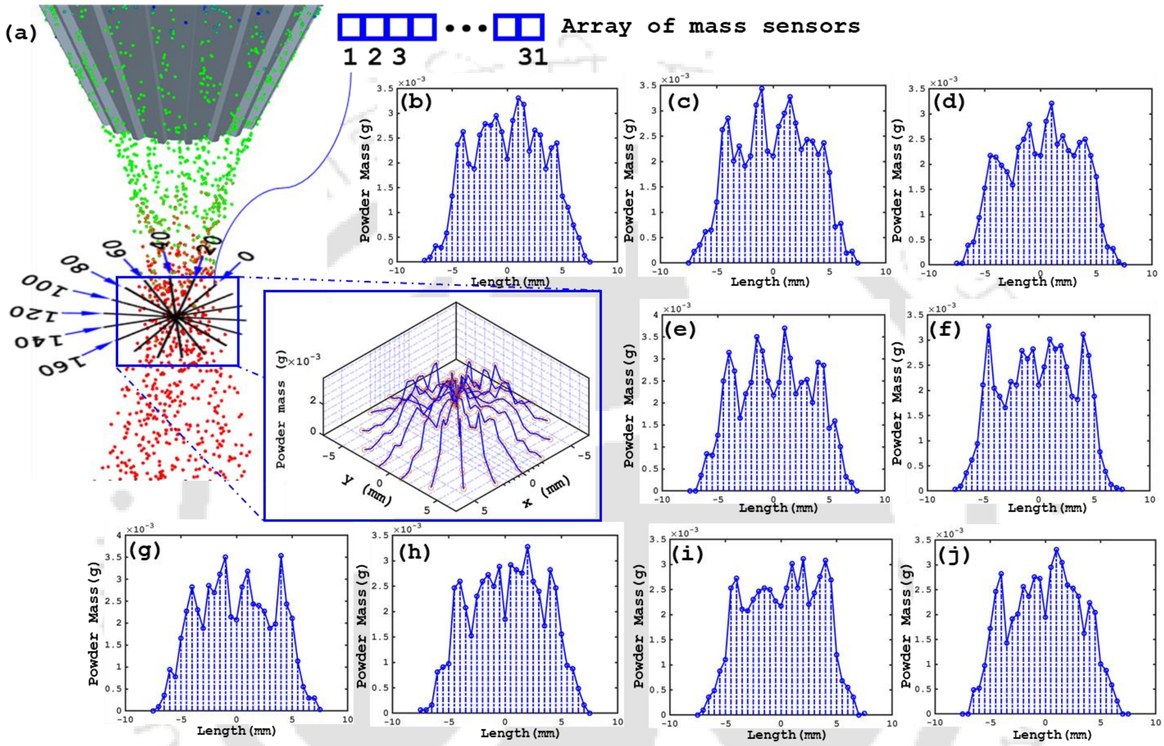

Fig. 3.20: (a)Arrangement of virtual mass sensors and recorded values for (b)0°, (c)20°, (d)30°, (e)40°, (f) 60°, (g) 80°, (h) 100°, (i) 120°, (j) 140°, (k)160°, of bin rotation about the vertical axis, respectively

The 'depth of convergence' determines the distance until which a powder stream remains focused, having converged at the focal plane. Within the DEM environment, a vertical array of circular 'stacked' mass sensors, each with a diameter of spot size, was placed at the focal plane, as illustrated in Fig. 3.21. It can be observed from Fig. 3.21 that the powder stream converges at ≈ 24 mm from the nozzle outlet and maintains a reasonable powder flux till ≈ 30 mm, beyond which a gradual decline in its value is observed.

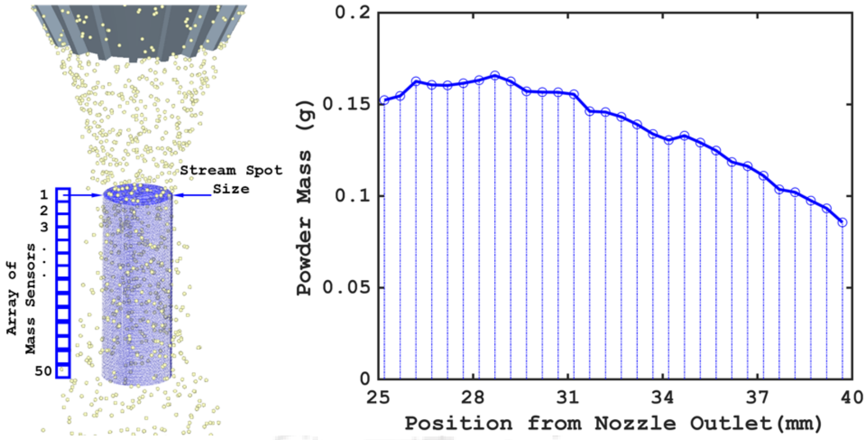

Fig. 3.21: Measurement of 'depth-of-convergence' of powder stream using virtual mass sensors showing a gradual decline in powder influx along the flow stream

3.3.2 Powder Mixing

A DEM simulation to observe the mixing capabilities of the powder delivery nozzle was also carried out as part of the performance evaluation. Powder influx, instead of entering the nozzle from one inlet, was divided into three individual streams, each entering the nozzle at a different inlet location. Separate colors were assigned to the respective streams for identification at the outlet. The method of virtual sensors (described previously) was implemented to determine the contribution of each of the individual powder streams toward the overall powder mass.

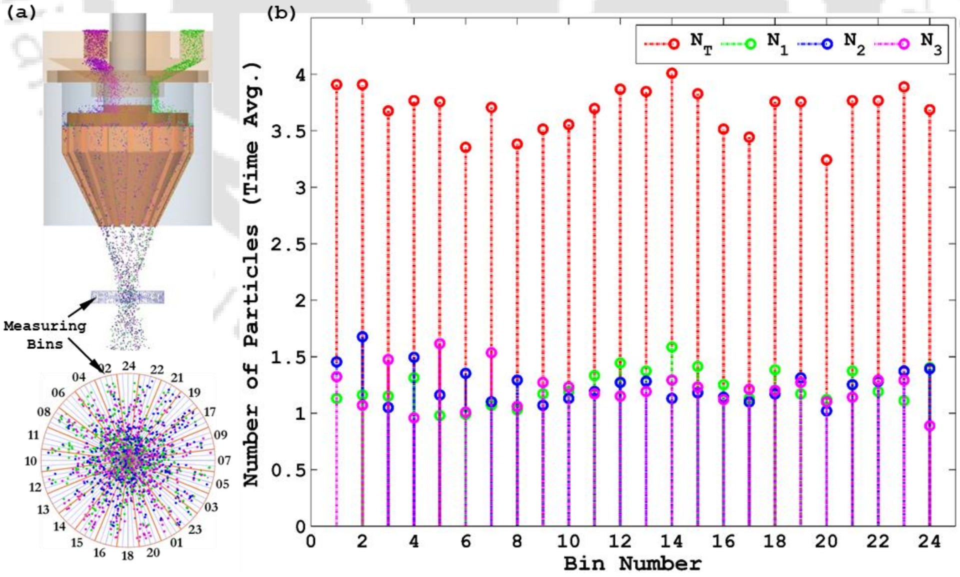

Fig. 3.22: Evaluation of mixing capability of the nozzle (a) arrangement of the virtual particle sensor, and (b) contribution of individual particle stream towards the total powder mass at the focal point

Refering to Fig. 3.22, N_T shows the average number of particles received by the virtual mass sensors at the focal point. N_1, N_2, and N_3 represents the contribution of each particle variety toward the total amount (N_T). Qualitatively, as illustrated in Fig. 3.22, the contribution of each particle variety, making up the total amount of powder mass at the focal point, does not differ significantly. This points to the good mixing capabilities of the proposed design. However, quantifying the results and performing simulations with multiple materials with different densities and particle sizes needs further analysis. Powder particles of different materials vary in material density which could lead to particle segregation during metering and centrifugal spreading. The particle segregation is also affected by particle size distribution, particle shape, and the mixing process[248]. Yao *et. al.* [249] have explored the effects of particle segregation in powder bed fusion process. The analysis of particle segregation is even more complex in non-binary systems with more than two particle mixtures. Pneumatics systems have also reported particle segregation due to material properties. Studies by Li *et. al.* [250] have shown small and lightweight particles travelling faster in the feedlines as compared to heavy ones thus, leading to unexpected properties of the FGM. It is important to note that, if a material based FGM is to be fabricated, then, the variation in material composition must reflect the intended user input. However, due to particle segregation, the fabricated parts may display unexpected material composition that deviates from the specified ratio of material mixture.

The study presented here, even though prima facie, shows good mixing capabilities, however, this is within the context of identical material with same bulk material properties. A detailed analysis of particle segregation with different bulk materials is necessary to conclusively state the capabilities of the current design in handling multi-material feed.

3.3.3 Effect of Nozzle Tilt

Several combinations of machine tool kinematics exist in the literature for layerwise fabrication of complex geometries. For the proposed design, the realization of complex features could not be achieved by tilting the nozzle head. Unlike Wire Arc Additive Manufacturing (WAAM), where the deposition head can be mounted on a robotic arm and can be appropriately moved without any distortion in metal deposition, the proposed nozzle design can accommodate vertical motion only. The tilt of the nozzle, for a magnitude as small as 2°, results in a distorted focal point, as illustrated in Fig. 3.23, which would reduce the catchment efficiency and lead to poor deposition characteristics. In order to implement head tilt in the simulation, the direction of the gravity force vector was manipulated while keeping the orientation of the powder delivery nozzle fixed.

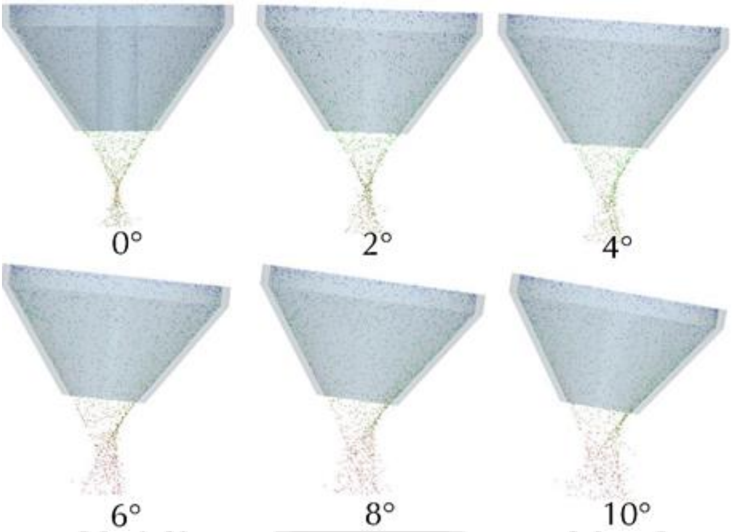

Fig. 3.23: Effect of nozzle tilt angle on powder stream focal point

3.4 Fabrication of Powder Delivery Nozzle

With the inputs from DEM simulations, the powder delivery nozzle was designed (as illustrated in Fig. 3.24(a, b)) and fabricated (Fig. 3.24(c, d)). Given the high focal spot size of the powder stream at the focal plane, an attempt was made to reduce the spot size through a cone extension, as shown in Fig. 3.24(b) and Fig. 3.24(d). The high spot diameter of the converged focal stream, which was observed during the simulation and in experiments, can be attributed to the centrifugal spreader, which essentially disrupts the streamlined particle influx to accomplish spatial uniformity. An extended nozzle cone offered a longer passageway to re-establish the coherence in the direction of particle movement toward the melt pool. However, the length of the cone extension was restricted by the limited focal length of the laser beam. Also, under the condition of powder clog, a provision for inducing vibration through Piezoelectric Transducer(PZT), as illustrated in Fig. 3.24(a, c), is provided with the system. Further geometric details of the fabricated nozzle can be found in Appendix 3.

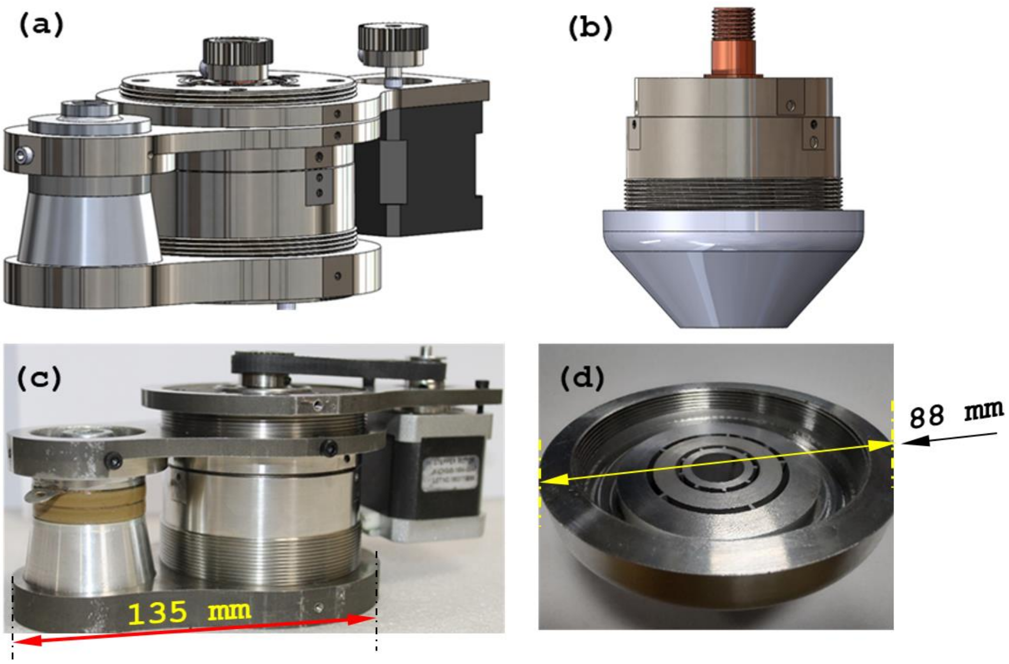

Fig. 3.24: CAD model of indigenously developed powder delivery nozzle (a) without and (b) with extension cone, fabricated (c) nozzle, and (d) nozzle extension

The extension to the nozzle cone decreased the focal spot size from ≈10 mm to ≈7 mm and increased the depth of focus, as shown in Fig. 3.25(e). The powder stream behavior of the delivery nozzle with and without the extension cone was quantified through image analysis using the setup shown in Fig. 3.25(a). The image acquisition setup consists of a wide-beam laser mounted on the CNC that illuminates a cross-section of the powder stream. The acquired images were analyzed using the Mathworks Matlab® image processing toolbox, wherein each image was read and cropped to retain the region of interest, followed by adjusting the image contrast, conversion to grayscale, complementing the image, and resizing using a scale factor.

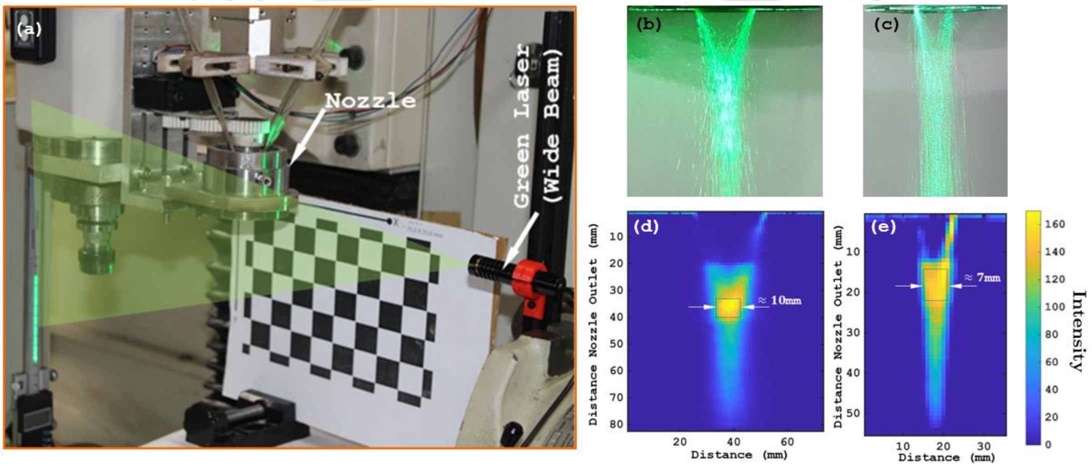

Fig. 3.25: (a)Setup of image acquisition for evaluation of the powder stream focal spot size, evaluation of powder stream focal spot size using acquired and processed images of the nozzle (b, d) without and (c, e) with cone extension, respectively

3.5 Discrete Coaxial Nozzle

The use of the centrifugal spreader in the study outlined above was primarily for developing a continuous coaxial nozzle. These nozzles create a conical envelope of powder surrounding the central laser beam. However, as mentioned previously, using a spreader disk enlarges the spot diameter of the converged powder stream. An alternative to a continuous coaxial nozzle is a discrete coaxial nozzle. A discrete coaxial nozzle, as the name suggests, has multiple distinct powder feed channels that deliver powder to the melt pool. In the current design this was accomplished through direct coupling of the powder feed tubes to the outlets of the metering station. This section presents a numerical study of a discrete coaxial nozzle with the primary objective of reducing the focal spot of the powder stream at the plane of deposition.

3.5.1 DEM Simulation Parameters

The study of the discrete coaxial nozzle is formulated as follows. Consider three powder delivery tubes, as shown in Fig. 3.27, inclined at an angle from the vertical, injecting powder into the melt pool. The particles are considered non-spherical, with particle shapes constructed from combining spheres, as illustrated in Fig. 3.26. These 'formed' particle shapes are approximate representations of the particles observed in Fig. 3.26. Hertz-Mindlin with JKR model is used to evaluate contact forces between particles and particles and equipment (delivery tube). Table 3.1 shows the relevant simulation parameters used in this study.

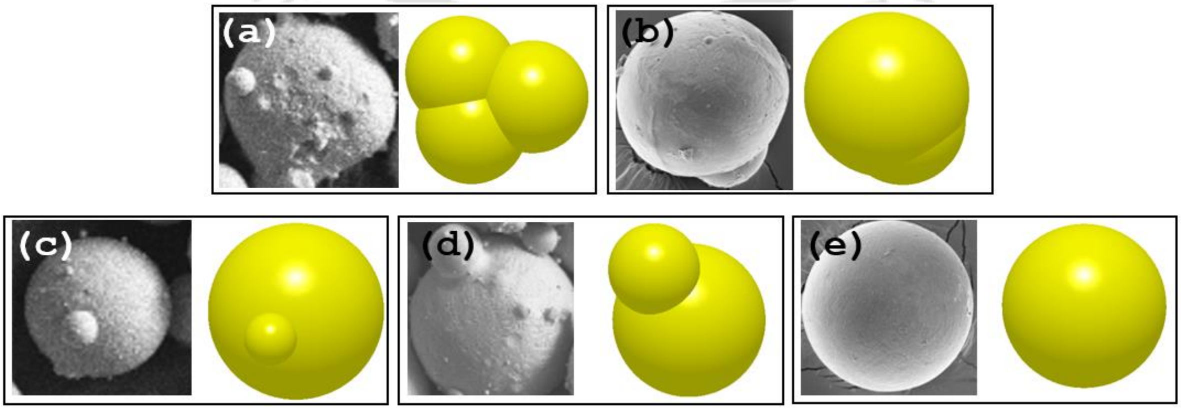

Fig. 3.26: Construction of particle shape through combining spheres (a) trigonal, (b) elongated particle, a particle with (c) small and (d) larger satellite particle, and (e) spherical particle

Table 3.1: Parameters for DEM simulation

Simulation Parameter	
Simulation Run Time	1 s
Simulation Time Step	1e-08 s (0.95% of Rayleigh time step)
Cell Size (for contact detection)	$4\left(\frac{D}{2}\right)$
Particle Shape	Non-Spherical
Particle Diameter (D)	100 μm
Material Density	7980 kg/m^3
Poisson's Ratio	0.3
Material Stiffness	2.1e+09 Pa
Particle Insertion Rate	12 g/min
Interaction Parameters	
Contact force model	Hertz-Mindlin with JKR
Particle-Tube Static Friction Coefficient	0.3
Particle-Particle Static Friction Coefficient	0.3
Particle-Particle Rolling Friction Coefficient	0.3
Particle- Tube Rolling Friction Coefficient	0.3
Particle-Particle Coefficient of Restitution	0.64 [214]
Particle- Tube Coefficient of Restitution	0.64 [214]
Surface energy, γ (mJ/m2)	1.4 [214]

3.5.2 Nozzle Geometry and Mount

The discrete coaxial nozzle is mounted on the laser optical head concentric to the laser beam. The setup consists of three equally spaced feed tubes, adjusted in inclination to the laser axis, to feed powder into the melt pool. The metered powder from the metering station is provided directly to these feed tubes through flexible pneumatic hoses, as illustrated in Fig. 3.27. The absence of a centrifugal spreader and, consequently, the conical envelope of powder is noteworthy here.

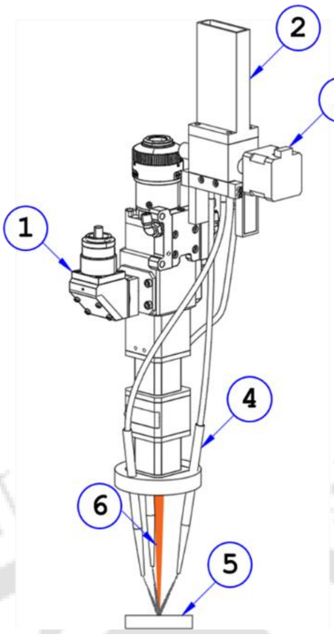

Fig. 3.27: Concentric mount of the discrete coaxial nozzle relative to the laser beam (1) optical head, (2) metering hopper, (3) metering motor, (4) powder feed tubes, (5) substrate, and (6) laser beam

The point of intersection of the axes for each of the three inclined feed tubes marked A in Fig. 3.28(a) is a reference point that is contained within a horizontal plane termed a 'reference plane.' Also, the center of circular outlets of all three feed tubes is kept in the same plane for each of the tested cases. The angle of inclination of the powder feed tubes relative to the plane of deposition (horizontal) is termed the Powder Injection Angle (PIA). As proposed in Fig. 3.27, the discrete coaxial nozzle can have four possible configurations relative to the melt pool. These configurations are listed in Fig. 3.28, wherein cases 1 and 2 considers a higher PIA, whereas case 3 and 4 considers a lower PIA. For each of these PIA values, the nozzles are tested for a lower (cases 2 and 4) and higher standoff distance (cases 1 and 3) from the 'assumed' melt pool at the deposition plane. The results of the simulations are studied for the powder stream's focal spot size and the *Depth of Focus (DOF)*. The DOF, as described previously, shows the distance up till which the powder stream remains focused (within the acceptable value of the degree of spread), having converged at the focal plane.

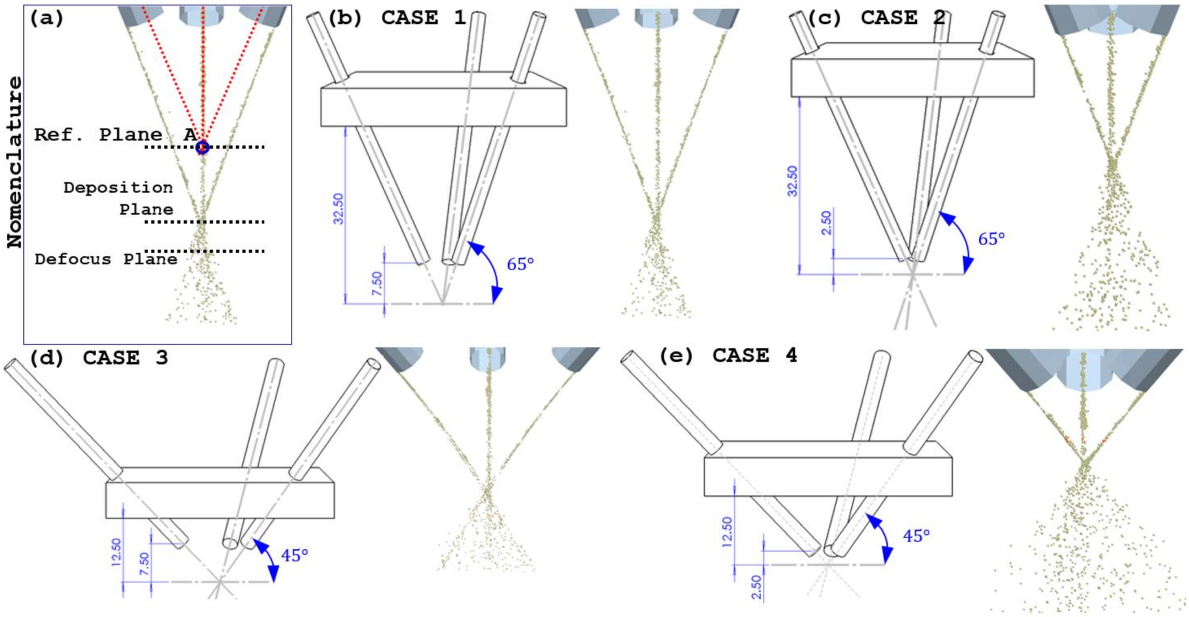

Fig. 3.28: (a) Nomenclature for configuration of feed tubes relative to the reference plane (a) case 1; high PIA and standoff distance, (c) case 2; high PIA with low standoff distance, (d) case 3; low PIA and high standoff distance, and (e) case 4; low PIA and standoff distance

3.5.3 Results and Discussion

Figure 3.29 shows the particle distribution at the focal plane and at a specified distance below the focal plane, termed the defocus plane (the defocus plane is illustrated in Fig. 3.28(a)). The defocus plane is considered at 1.25 mm below the deposition plane. For each of the four cases, the particle distribution is analyzed at the focal and defocus plane, as shown in Fig. 3.29. The following observation can be made from the numerical study. For cases 1 and 2, the powder stream converges at 11.25 mm and 5.67 mm from the nozzle outlet, represented by higher powder density at the focal plane, as shown in Fig. 3.29(a, b) and Fig. 3.29(e, f), respectively. Also, the observation of the degree of powder spread at the defocus plane for cases 1 and 2 is made at a distance of 12.50 mm and 6.92 mm, respectively, as shown in Fig. 3.29(c, d) and Fig. 3.29(g, h), respectively. Similarly, cases 3 and 4 show powder convergence at 10.10 mm and 3.36 mm, with a degree of spread observed at 11.35 mm and 4.61 mm from the nozzle outlet, as shown in Fig. 3.29(i-l) and Fig. 3.29(m-p), respectively. Table 3.2 summarizes these observations, with reference to Fig. 3.29.

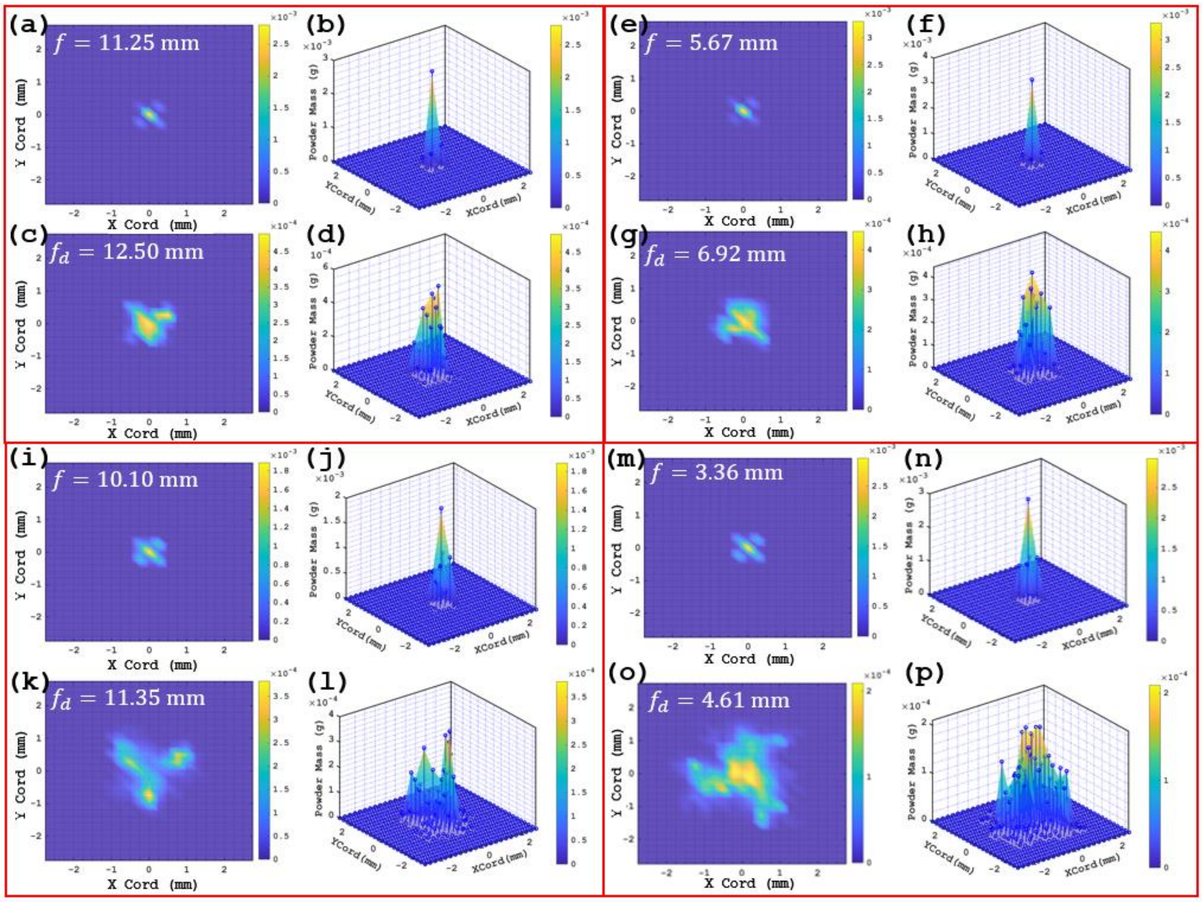

Fig. 3.29: Powder distribution for (a-d) case 1, (e-h) case 2, (i-l) case 3, and (m-p) case 4

Table 3.2: Locations at which observations were made for powder stream analysis

	A. Deposition plane (mm)	**B. Defocus plane (mm)**	**Depth of Focus $(A - B)$(mm)**	**PIA**	**Ref**
Case 1	11.25	12.50	1.25	65°	Fig. 3.29(a-d)
Case 2	5.67	6.92	1.25	65°	Fig. 3.29(e-h)
Case 3	10.10	11.35	1.25	45°	Fig. 3.29(i-l)
Case 4	3.36	4.61	1.25	45°	Fig. 3.29(m-p)

The distances of the planes are measured from the delivery tube outlet.

Through Fig. 3.29, it can be seen that for all the observed cases, the PIA and the standoff distance have no significant influence on the powder stream focal spot size, which was evaluated to be ≈1 mm. However, the DOF is affected by the PIA, where a high PIA suggests a longer DOF (as shown in Fig. 3.29 for cases 1 and 2), and a lower PIA shows smaller DOF values (as shown in Fig. 3.29 for cases 3 and 4). This conclusion on DOF is derived from the observations made on the degree of powder spread at the defocal plane; a higher powder spread suggests lower DOF and vice-versa.

3.6 Summary

This chapter detailed the effect of the number of blades and blade shape on the centrifugal spreader's ability to generate a uniform spatial distribution. The design and fabrication of the powder metering and delivery nozzle with design input from the DEM simulations were also outlined. The following key conclusions can be drawn from the presented study.

- The proposed helical groove design of the powder metering shaft can be used to consistently meter the powder mass flow rate. The helical groove continuously delivers the power mass while avoiding pulsations observed in the case of a screw conveyor.
- A curved blade distributor design with a sufficiently high number of blades, in terms of spatial uniformity, performs better than a straight blade design; however, this increased spatial uniformity comes at the expense of a decreased mass flow rate.
- A two-stage distributor should be preferred over a single-stage distributor for achieving uniformity in the spatial distribution of powder particles around the fusion source. This ensures the omnidirectional capabilities of the nozzle.
- Testing with the fabricated prototypes, along with the results from the DEM simulation, suggests a high spot diameter of around 10 mm of the converged powder stream at the focal point. A longer cone, to a certain extent, can reduce the powder stream focal spot size; however, the cone length is primarily restricted by the focal length of the laser beam.
- The tilting of the nozzle distorts the focal point of the powder stream; thus, it is preferable to use the motion of the substrate underneath the nozzle for part fabrication. The deposition nozzle can be provided with linear (vertical) up-and-down motion equivalent to the layer thickness during part fabrication.
- As suggested by DEM simulation, a smaller focal diameter of the powder stream can be obtained through a discrete coaxial nozzle with powder influx received directly from the metering station. A high powder injection angle relative to the horizontal plane of deposition is suggested for a higher DOF with a smaller converged powder spot size.

Chapter 4

Interfacing Laser with the CNC Milling Machine and Installation of Powder Feeding System for Part Fabrication through DED

Modern manufacturing requires process efficiency, flexibility, and quality of the produced parts. Given that the said 'part' often involves a sequence of manufacturing operations to achieve its final fit and finish, achieving all three objectives under the purview of a single manufacturing station becomes essential. Machine hybridization is a methodology aimed toward developing the above-stated 'single manufacturing station.' Machine hybridization, through automation, addresses challenges associated with the part transfer within each manufacturing operation, which, otherwise, is time-consuming, inefficient, and prone to errors. Apart from part transfers between manufacturing setups/ stations, machine hybridization offers a multitude of significant advantages over conventional manufacturing concepts [251–254].

Although machine hybridization can be achieved with various objectives in consideration [4–6], this study aims to combine laser-based Directed Energy Deposition (L-DED) with conventional CNC milling to obtain an additive-subtractive hybrid system. Table 4.1 presents a summary of machine hybridization carried out by several researchers to accomplish various objectives.

Table 4.1: Previous attempts at machine hybridization using the method of component retrofit

Sl.No.	Process Name	Machine Configuration	Nature of Hybridization	Ref
1	*Control Metal Build (CMB)*	2.5D Vertical CNC Milling Machine	L-DED and Machining	[255]
2	*Laser-Aided Manufacturing Process (LAMP)*	5Axis Vertical Milling Machine	L-DED, Machining, Laser-based process monitoring, and temperature control	[256]
3	Laser-integrated CNC milling	5Axis Vertical Milling Machine	Integration of milling, laser cladding, and plasma welding on a single platform	[257]
4	Laser cladding on cylindrical systems	5Axis Milling Machine	L-DED and Machining	[258]
5	ArcHLM	3Axis CNC Machine	MIG-based Wire Arc Additive Manufacturing and Machining	[252]
6	*Hybrid-Layer Machining (HLM)*	5 and 3Axis CNC Machine	TIG-based Wire Arc Additive Manufacturing and Machining	[32]
7	High-speed laser cladding	Traditional Lathe Machine with 6Axis Industrial Robot	Laser cladding and Machining	[259]

4.1 Laser and CNC Machining Unit

The relevant details and specifications of the laser used in this study are provided in Table 4.2. The device can be configured to operate in two modes: Local Control (LC) and Remote Control (RC). Through Human Machine Interface (HMI), local control allows the user to set the laser operating parameters manually. Conversely, the RC mode allows for process automation wherein the operating parameters can be preset or varied in situ through the appropriate application of activation (or deactivation) signal. Figure. 4.1 shows the key parameters of the laser optic. These parameters guide the design of mounting arrangements for the powder delivery unit.

Table 4.2: Relevant details and specifications of the laser unit [260]

Particulars	Typical Values
Type : Ytterbium Fiber Laser **Model** : YLR-1000-MM-WC **Make** : IPG Photonics	
Laser Power	1000 W
Operation Mode	CW/ Modulated
Emission Wavelength	1070 nm
Beam Quality (BPP)	6.7 mm·mrad
Optical fiber core diameter	200 µm
Power Consumption	2.7—3.2 kW
Beam Optics	
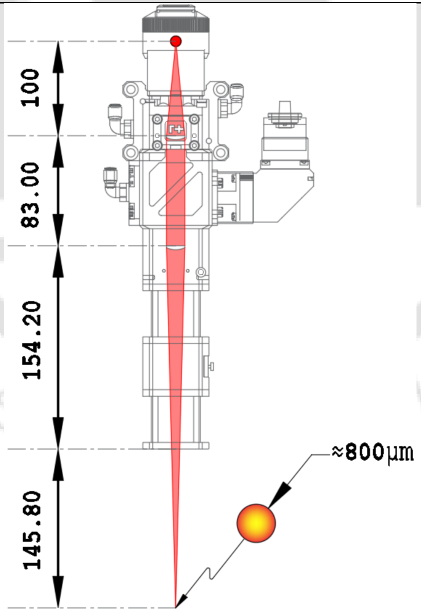	

Fig. 4.1: Laser optics specification [260]

Operating the laser unit follows a sequence of steps before the emission of the beam at a preset power can be enabled. This sequence, listed below, can be triggered manually in LC mode or through low voltage (5–24 V) electrical signals while operating in RC mode.

- Closure of contact pins assigned to set the laser unit to remote mode.
- A dwell time of 2 S (set in accordance with the response time of the system [261])
- Momentary closure of assigned pins (10 and 11) to activate the main power supply
- Set laser power before emission.

Selection of laser power in RC mode can be made with the help of 'control voltage.' Control voltage acts as an electrical signal, the magnitude of which sets the laser output power. The laser unit used in this study allows for varying the control voltage from 1.3 V to 10.0 V; correspondingly, the power of the emitted beam can be varied from 51 W to 1000 W. Figure 4.2 shows the calibration plot for control voltage relative to the laser power.

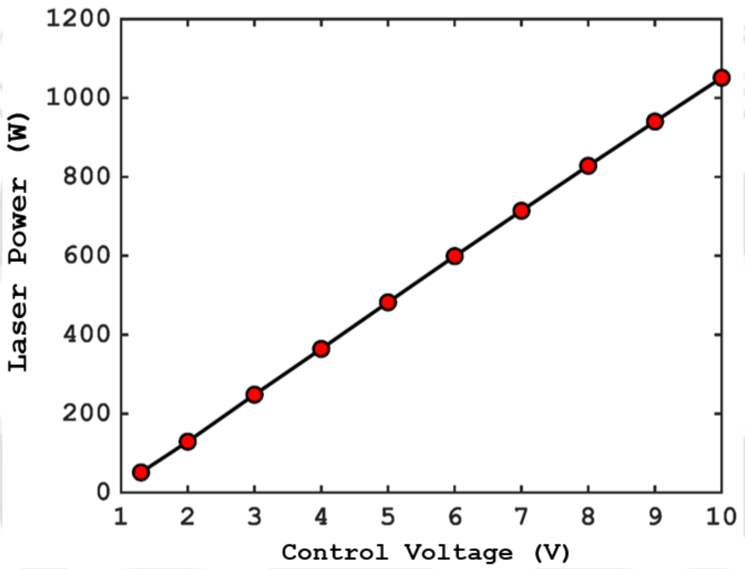

Fig. 4.2: Calibration curve for control voltage against laser output power [261]

The specifications of the CNC machine used in this study are listed in Table 4.3. The machine controller, 'Mach3®', uses a parallel port connector to interface with stepper drivers through the *Machine Control Board (MCB).*

Table 4.3: Relevant details and specifications of the CNC unit [262]

Particulars	Typical Values
Type : 3Axis Vertical CNC Milling Machine **Model** : PCNC 1100 **Make** : Tormach	
Machine configuration	3Axis Vertical Milling Machine
CNC controller	Mach3 Mill
Discrete position move (Machine Resolution)	0.00254 mm
Electrical requirements	200—250 VAC (Single Phase)
Auxillary Coolant	115 VAC

4.2 Interfacing of CNC with Laser Unit

The retrofit of the laser on the CNC vertical milling machine can be categorized into mechanical and electrical interfaces. The mechanical interfacing addresses the challenge associated with mounting laser optics and the feedstock handling unit on the CNC machine. The electrical interfacing provides access to the laser's operating parameters and beam emission/ termination via electrical signals accessed with Mcodes through the CNC controller.

4.2.1 Mounting of Laser Optics and Powder Handling Unit

In order to gain a kinematic advantage, the laser optic was mounted parallel to the spindle axis of the milling machine. Special care was taken to avoid orthogonality of the laser beam with the substrate surface, as illustrated in Fig. 4.3(b).

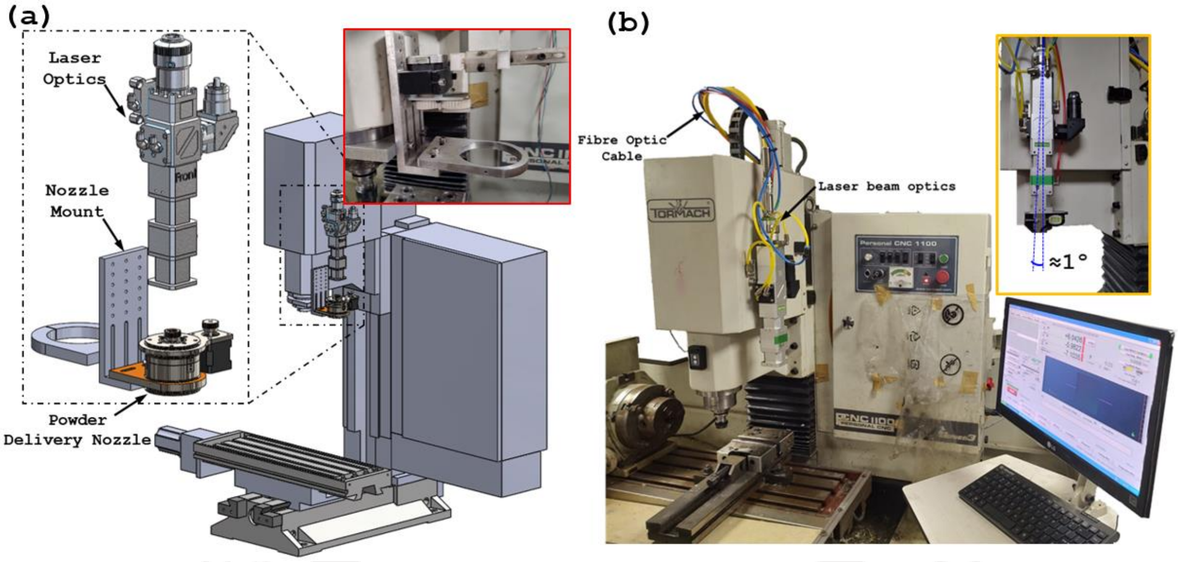

Fig. 4.3: Mounting of laser optic on the CNC Mill (a) CAD model and (b) optics mounted on the CNC mill with a small inclination with the vertical

An additional feature of the mounting arrangement for the powder delivery nozzle is the provision to adjust the position of the powder stream relative to the laser beam. Figure 4.4 schematically shows this arrangement. The powder stream's focal spot relative to the laser beam should have both planar (XY) and vertical spatial adjustment mechanisms. These mechanisms are used to ensure the concentricity of the conical powder stream with the laser beam and the coincidence of the powder stream focal point with the melt pool on the substrate. Figure. 4.4 (a) shows the fabricated mounting bracket for the powder delivery nozzle with provision for appropriate spatial adjustments.

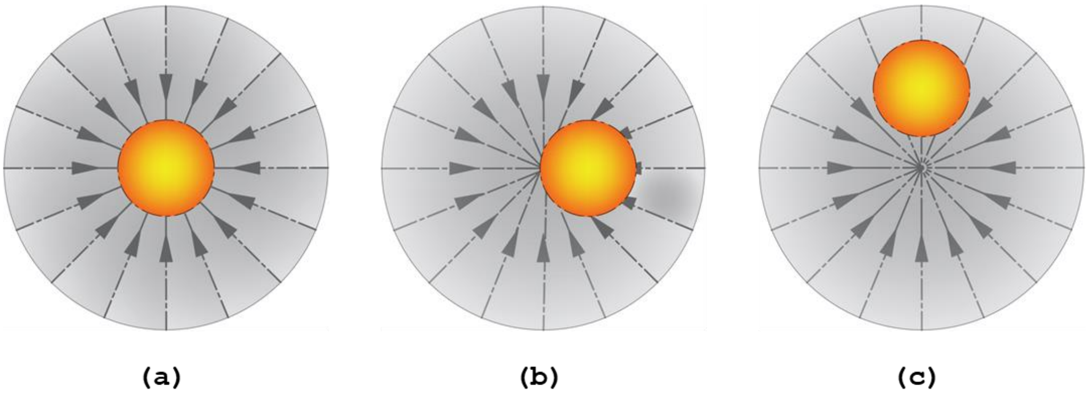

Fig. 4.4: Provision for the powder stream adjustment relative to the laser beam (a) ideal configuration, minor adjustments required in (b) horizontal, along X, and (c) vertical, along the Y direction

4.2.2 Electrical Interfacing of Laser with CNC Unit

Operating the laser through control signals from the CNC controller has the following sequence. First, the laser is turned to RC mode, followed by a dwell time of 2S. Subsequently, the power source to the laser is turned on by momentary closure of appropriate pins. The dwell time for the momentary closure was maintained at 1S. Finally, the power of the emission can be specified, which sets the laser unit in a ready position to emit the beam. With the execution of the above-mentioned 'laser-firing' sequence, the final electrical signal from the controller of the CNC machine can be provided to enable beam emission.

Since the laser beam emission sequence requires several output signals from the CNC controller to the laser unit, it was found that the make and model of the CNC milling machine lacked these necessary provisions. This necessitates auxiliary electrical arrangements, as shown in Fig. 4.5, to generate and communicate key output signals to the laser.

4.2.2.1 Auxillary Electrical Interface

To provide the output signals to the laser unit, a separate Ethernet Smooth Stepper (ESS) control card, coupled with a breakout board, was used. The EES control board was connected to a dedicated computer, and Mach3® software was used to establish necessary communication through an ethernet port. Since both the CNC and the ESS card require Mach3® as control software, two dedicated computers were used for each. This prevents any version clash and avoids complexity. Through the use of this ESS card, several outputs can be generated using custom-assigned M-Codes in the Mach3® environment. The outputs from the ESS control board are fed to an array of relays, which subsequently trigger a particular step in the laser-firing sequence. Thus, it is through these custom-assigned M-codes each step in a given order is executed, thereby completing the laser firing sequence. Table 4.4 details these M codes used for laser control.

The spindle RPM in the Mach3 environment for the ESS control computer can be used to vary the laser output power. Typically, the spindle speed value, which is set through an M04 command, is passed to the Variable Frequency Drive (VFD), which, in turn, adjusts the spindle RPM. However, for the case of laser, an intermediate 'frequency-to-voltage' converter is required to interpret the M04 command as a control voltage for laser output power. Through the calibration curve shown in Fig. 4.2, the magnitude of the control voltage (0-10V) can be set to trigger a corresponding output voltage to the laser unit, which emits the laser beam of set power.

The final output signal that enables the emission of the laser beam is provided through the controller of the CNC machine, using the M codes for coolant control. Using the M08 command in the console of the CNC controller, the emission can be started, and M09 terminates the laser emission. Thus, including these M Codes at appropriate locations in the programmed toolpath can start and terminate the deposition process. Figure 4.5(a) & (b) shows the Tormach machine control board and the auxiliary arrangement interfacing CNC with the laser unit. The output of the pins, marked as J5-1 and J5-5, generates 110V between them when M08 is active. M09 returns the output to 0V. Using a rated contactor across these pins enables and disables the laser beam emission.

Table 4.4: Laser firing sequence executed through a series of control signal

Code	**Description**
Entered from the ESS control computer	
`M107`	Laser set to RC mode
`G04 P2`	Dwell time of 2S
`M110`	Enable power to the laser source Momentary Contact: **ON**
`G04 P1`	Dwell time of 1S
`M111`	Momentary Contact: **OFF**
`M03 S<OUT.POWER>`	Set the laser beam output power
`M30`	End Program
Entered from the CNC Controller	
`M08`	Laser beam emission enabled
`<TOOLPATH GCODE>`	Deposition tool path
`M09`	Laser beam emission disabled

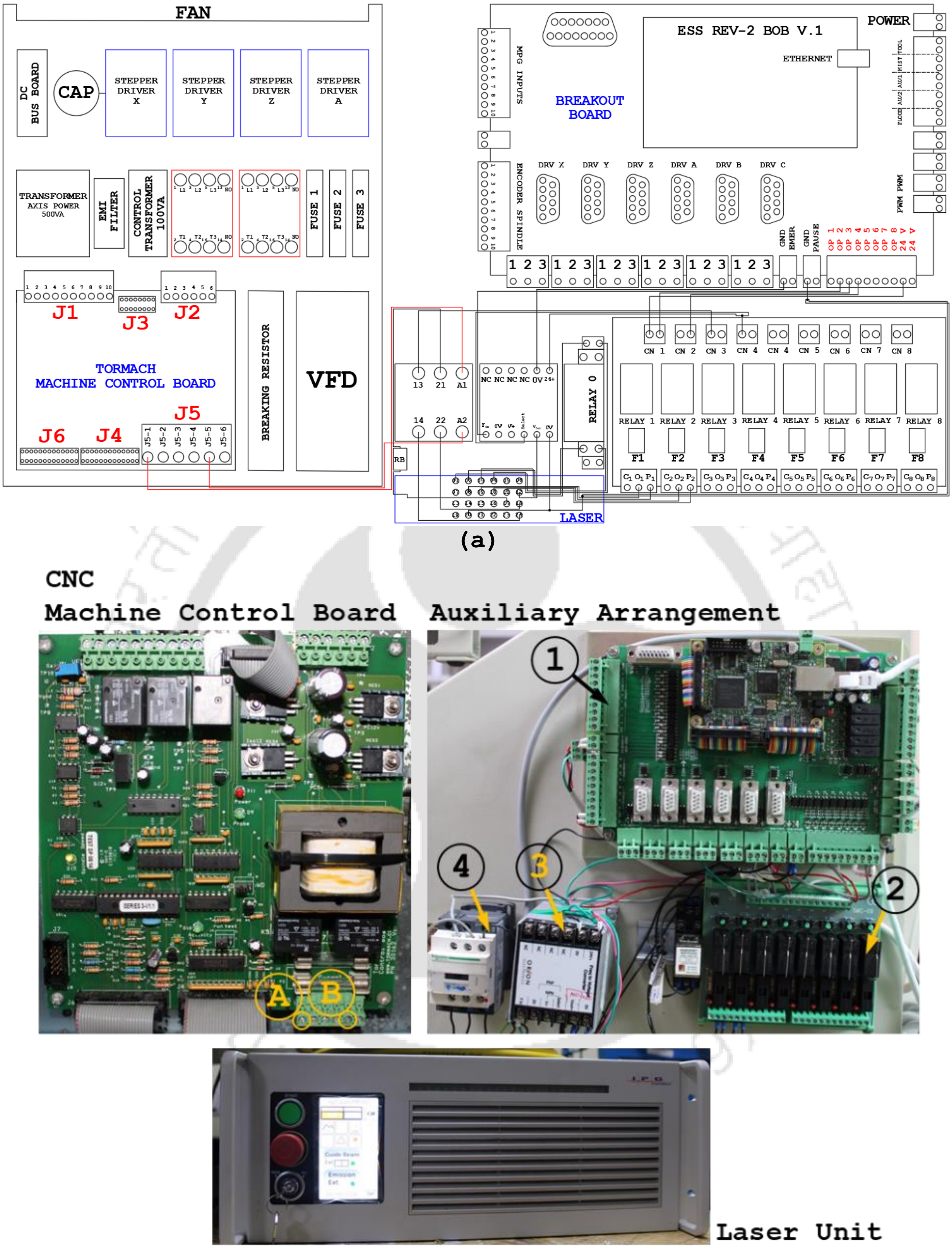

(a)

(b)

Fig. 4.5: Auxiliary arrangement for remotely executing the laser firing sequence (a) electrical schematic and (b) components of the auxiliary arrangement used interfacing the laser unit with the CNC controller, (1) ESS card, (2) relay array, (3) frequency to voltage converter and (4) contactor

4.3 Case Studies

Figure. 4.6 shows a selection of sample parts that were fabricated using the developed setup. Figure 4.6(a) and (b) are examples of thin wall deposition, followed by Fig. 4.6(c) and (d), which are iso grids deposited on a thin sheet of flat and circular substrate. Figure 4.6(e) and (f) are some examples of infill structures, and Fig. 4.6(g) shows a continuous thin wall deposition of a circular cross-section. Figure. 4.6(h) shows the fabrication of a propeller-like component deposited through the programming of the fourth (rotary) axis. Figure 4.6(j) is an example of the feature addition capability of the developed setup, where a flange was deposited on a round stock. Figure 4.6(i) shows the deposition of a thick wall through the use of a trochoidal toolpath, and finally, Fig. 4.6(k) shows a topologically optimized bone plate deposited and later machined on the same machine tool, thus highlighting its hybrid capabilities.

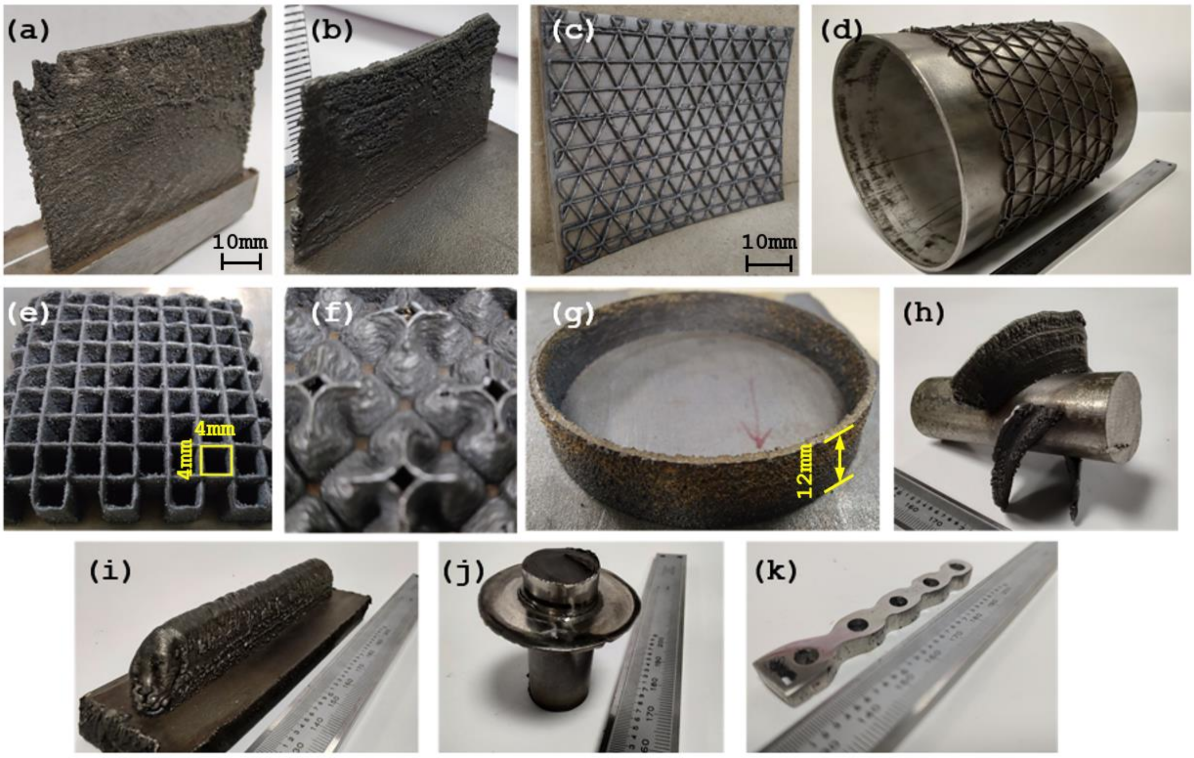

Fig. 4.6: A selection of sample parts fabricated on the developed DED setup showing (a, b) thin wall parts, iso-grid deposited on (c) flat and (d) circular substrate, (e, f) infill structures, (g) continuous deposition of circular cross-section, (h, j) feature addition on a circular substrate (i) trochoidal toolpath for thick wall deposition, and (k) deposition followed by machining of a topologically optimized bone plate

An observation of the cross-section of the deposited cylinder, as shown in Fig. 4.7, reveals minimal variations in the wall thickness of the part. This suggests that, given the conditions of deposition, the developed nozzle is omnidirectional in nature.

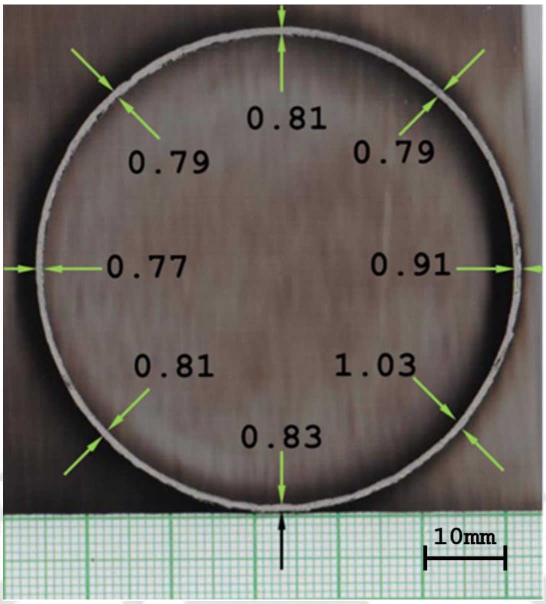

Fig. 4.7: Uniform dimensions observed for the deposited part, signifying omnidirectional behavior

4.4 Summary

This chapter outlined a method for retrofitting a 1kW fiber laser to a CNC machine using an auxiliary electrical interface. The process is based on repurposing coolant control and the associated M-code to trigger the laser on and off. Following are a few highlights from this study.

- Mounting arrangements for installing a powder feed nozzle with provisions to adjust the powder stream's focal point relative to the laser beam were designed and fabricated.
- The method of interfacing laser-CNC-feedstock handling units demonstrated reliability with stable material deposition characteristics.
- The developed setup was tested through several test prints and was found to be omnidirectional.

Chapter 5

Utilization of a TSP Solver for Generating Non-Retractable, Direction Favouring Toolpath for Additive Manufacturing

A complex part, through additive manufacturing, is fabricated via selective deposition/ addition of material. This selective material addition is governed by the CAD input to the AM machine tool. Observing a slice/ layer from the stack of layers in a sliced STL file, two regions of interest can be outlined. One corresponds to the outer contour of the cross-section, and the other is the space bounded within this contour. This work focuses on filling the space bounded by the outer contour of a given cross-section. The curves or toolpaths that are used to fill this bounded space are termed a Space Filling Curve (SFC). Through the appropriate selection of such SFCs, the mechanical properties of the fabricated parts can be influenced.

The variation in nominal dimensions of the deposited track at the start and end of a deposited bead is shown in Fig. 5.1(a). This variation stems from lack of control over the laser power, scanning speed, and material feed rate. Also, the deposited bead at the corners, without any process control, results in the over-deposition of the material, as illustrated in Fig. 5.1(b). To limit such defects, one possible solution is to reduce the number of turns and start/ stop points in a given toolpath. This work attempts to implement this solution through a TSP toolpath with appropriate placement of grid points.

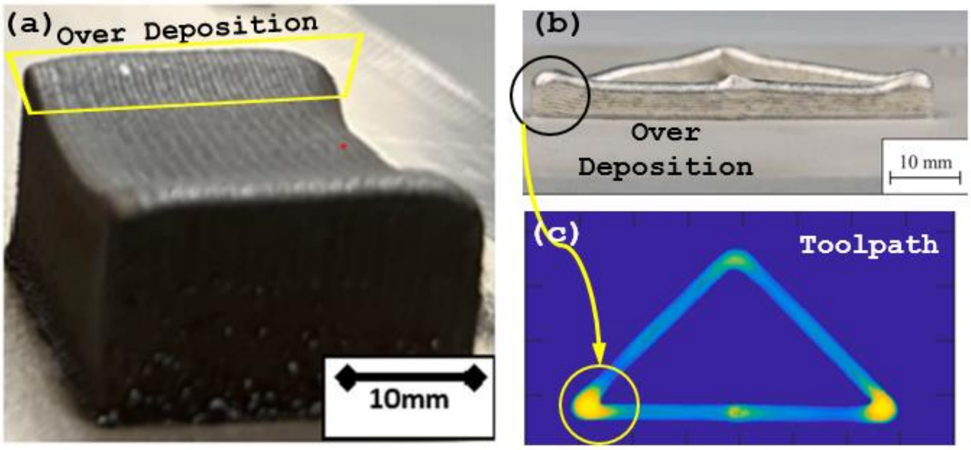

Fig. 5.1: Geometric defects observed at (a) start and stop of deposition (reproduced with permission from [263], copyright(2023) Springer Nature) and (b) corners of the toolpath (reproduced with permission from [264], copyright(2023) Elsevier)

The conventional toolpath strategies, such as spiral, contour offset, Medial Axis Transform (MAT), and raster, represented in Fig. 5.2(a), (b), (c), and (d), respectively, exhibit tool lifts or retractions. These tool lifts/ retractions are characterized by the intermediate termination of material deposition at a specified point, which is subsequently reinitiated at another point during part fabrication. Even though the number of retractions associated with a particular toolpath strategy varies, generally speaking, some toolpaths offer more retractions than others. These lifts or discontinuities in a toolpath for area filling in various AM processes are detrimental to part quality and overall process efficiency.

For instance, in some cases of Wire Arc Additive Manufacturing (WAAM), the weld bead geometry at the start and end maybe different when compared with the middle. This primarily stems from poor process control resulting in variations in heat input and material feed. Multiple starts and stop points in the material deposition for processes such as DED increase the number of unstable regions, which promotes defects in the as-built parts due to accumulated error for each layer [172,265,266]. Furthermore, the conventional toolpaths do not share the same start and endpoint, thus generating open-end curves for material deposition. A continuous toolpath, as illustrated in this study, facilitates material deposition with little to no tool retraction, thus limiting the aforementioned errors in part fabrication. Moreover, another benefit of the TSP algorithm is its closed-loop nature, i.e., the toolpath has a common start and a finish point, which can be selected by the user. This characteristic feature reduces the possibilities of internal defects, which otherwise could incur in toolpath strategies with multiple and different starts and stop points. Also, having a common start and finish point restricts the defects in deposition (such as over and under deposition) caused due to acceleration in CNC motion to a common location, which facilitates the easy implementation of corrective measures. Furthermore, the toolpath strategy, as proposed here, offers versatility and, to some extent, allows the user to dictate the direction in which the deposition should be carried out.

Generally speaking, CNC machine tool platforms, irrespective of whether they come from the additive or the subtractive side of manufacturing, move sequentially from one point to the next. In the case of machining, it is the cutting tool that moves, whereas, in the case of AM, it is the deposition head or the fusion source. Moving from one point to the next involves interpolation, which could either be linear or circular in nature. Rapid changes in the direction of movement, specifically when taking a sharp turn, induce high accelerations. A detailed account of these accelerations can be found in the work of Jozwik *et al.* [180]. Rapid accelerations in a CNC platform are detrimental to both the machine tools and the part being fabricated. High accelerations induce vibrations in the machine tool, which could excite the natural frequencies of the structure, thereby compromising machine rigidity [181]. Further, these accelerations inadvertently vary the processing parameter (such as deposition speed and travel velocity), which could lead to over or under-deposition of material [156]. Several approaches exist in the literature to minimize the accelerations in a CNC platform [182–184]. The work presented here addresses the question of uniform CNC motion and, consequently, that of uniform deposit through minimizing the 'number of turns' in an area filling toolpath.

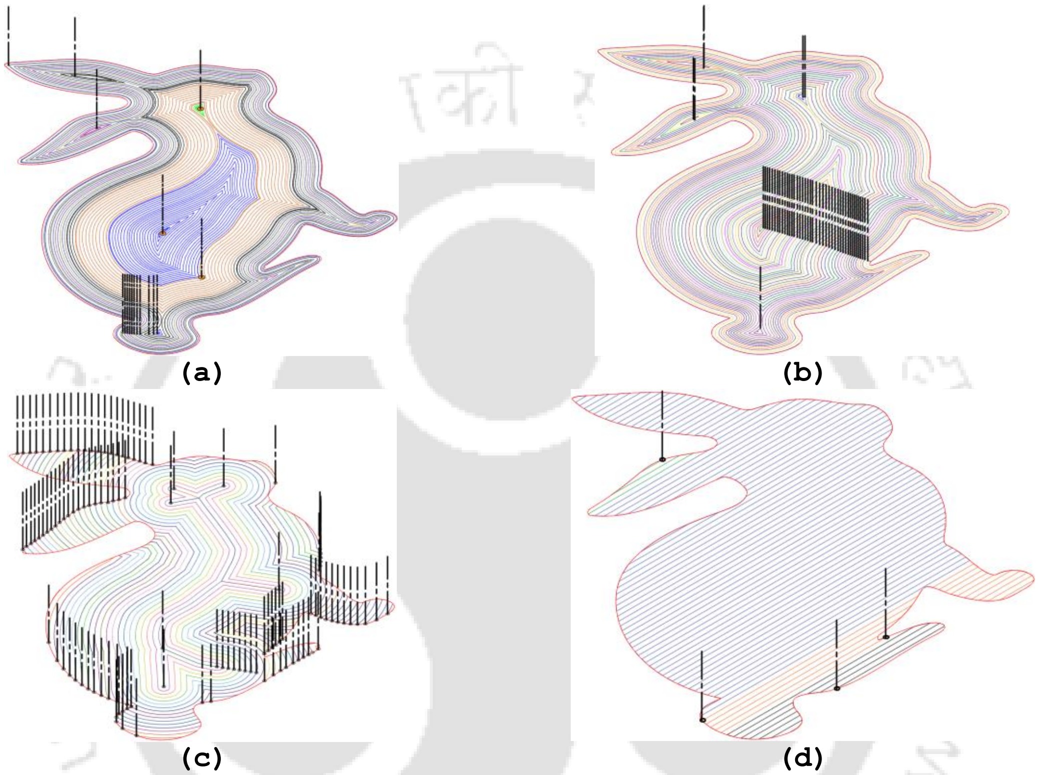

Fig. 5.2: Various toolpath strategies highlighting the number of lifts/ retractions associated with (a) spiral toolpath, 17 lifts, (b) contour parallel, 58 lifts, (c) MAT, 124 lifts, and (d) raster with four lifts

The underlying idea of the toolpath strategy proposed here exploits the fact that the toolpath of the deposition head (or the analogous unit as dictated by the AM process) can be treated as a salesman with an objective to visit specified grid points (analogous to cities). The navigation of the grid points can be carried out with a preset objective, such as minimizing the total distance traveled with a constraint to mandatorily visit each grid point once and only once. Even though such ideas have been explored in the past [185,186](mostly in the context of machining), the present work explores the effect of grid points, their relative position with each other, and the outer boundary on the resulting toolpath. The area-filling strategy proposed here offers a minimal number of retractions and turns and is a closed-loop path, having a common start and stop point.

5.1 Methodology

The *Travelling Salesman Problem (TSP)* is a combinatorial optimization technique with the following problem statement. Consider Graph $G = (V, A)$ where V represents a collection of 'n' vertices, and A is a set of arcs and edges, $C = (c_{ij})$ is an $n \times n$ matrix, typically called a distance (or cost) matrix, associated with A. The TSP aims to obtain a traverse path through each vertex, such that; every vertex in $'G'$ is mandatorily visited once and only once without crossovers (such a traverse path is also called a Hamiltonian Circuit). Furthermore, another noteworthy property of a Hamiltonian Circuit (or path) is its closed-loop nature, implying a common vertex of start and stop.

The solutions to a TSP problem are complex and are categorized into two segments. One set of algorithms focuses on achieving an exact solution, whereas another set provides an approximate or heuristic answer. The heuristic algorithms offer an elegant solution; however, they do not guarantee an optimal tour. The Lin-Kernighan (LK) algorithm used in this study for toolpath planning falls under the category of a heuristic algorithm. The LK algorithm can be understood by a comparison with $\lambda - opt$ algorithm, a much simpler local-optimization counterpart. A $\lambda - opt$ algorithm states, "A tour is $'\lambda - opt'$ (or optimal) if there does not exist a shorter tour that can be obtained by replacing (or reconfiguring) any set of λ links (edges) with any other set of λ links." For example, in the case of a $2 - opt$ algorithm, which is a special case of $\lambda - opt$ algorithm, in each iteration, two edges of the graph are replaced such that the resulting tour is shorter than its predecessor [267]. The algorithm terminates if no such replacements can be found. In the case of the LK algorithm, however, no predefined value of λ is specified. In a study by Helsgaun [267], this property was termed '$variable\ \lambda - opt'$ algorithm. The LK algorithm varies the value of λ during iterations. With each iteration a decision is made whether an increasing value of λ (or reconfiguration of edge) would result in a shorter tour. If a shorter tour is possible, the reconfiguration is made; otherwise, the algorithm terminates. The LK solver used in this study is part of an extensive open-source 'Concorde' solver by the University of Waterloo, Canada [268].

Given the generic nature of the problem and the solution it seeks, TSP has been applied in several contexts, such as job shop sequencing [269], computer wiring [270], search algorithms [271,272], etc. This article explores TSP as a method of generating a space-filling curve in Additive Manufacturing (AM) that is continuous, with constant step-over and minimal turns, and is computationally efficient. The application of TSP for the purpose of toolpath generation, generally, is broken down into two steps. First, given a contour, approximate its interior by a discrete (and well-defined) set of points. This process is referred to as digitization. Second, having digitized the area, determine a travel sequence that achieves the set objectives of the optimization problem. This work explores the effect of digitization on the toolpath and other associated performance parameters. Figure 5.3 schematically outlines the algorithm implemented in the study.

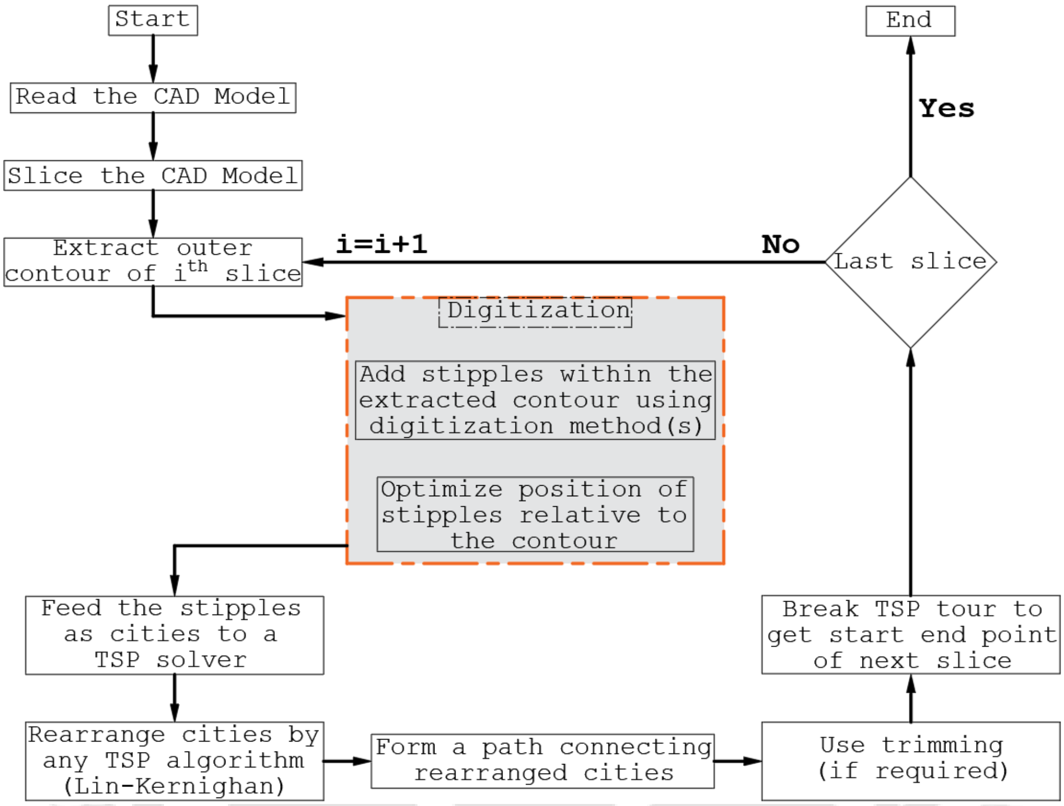

Fig. 5.3: Algorithm of toolpath generation for space-filling using a TSP-based scheme

Figure 5.4 schematically illustrates the process sequence for the toolpath generation. Initially, the imported CAD model (in STL file format) is sliced into multiple layers, as illustrated in Fig. 5.4(a). The next step, referred to as digitization, illustrated in Fig. 5.4(b), generates a set of grid points. The geometric contour extracted from the CAD model, corresponding to a particular layer, is overlayed on the digitized grid, as illustrated in Fig. 5.4(c). The grid points lying inside and close to the boundary are kept while the rest are eliminated, as shown in Fig. 5.4(d). The retained grid points are subsequently used by a TSP solver as cities (or stipples) to generate the toolpath in accordance with preset rules, Fig. 5.4(e). The following step, illustrated in Fig. 5.4(f), trims the generated toolpath relative to the original contour, resulting in a sharp and well-defined boundary. This sequence is repeated for subsequent layers until the final layer is processed.

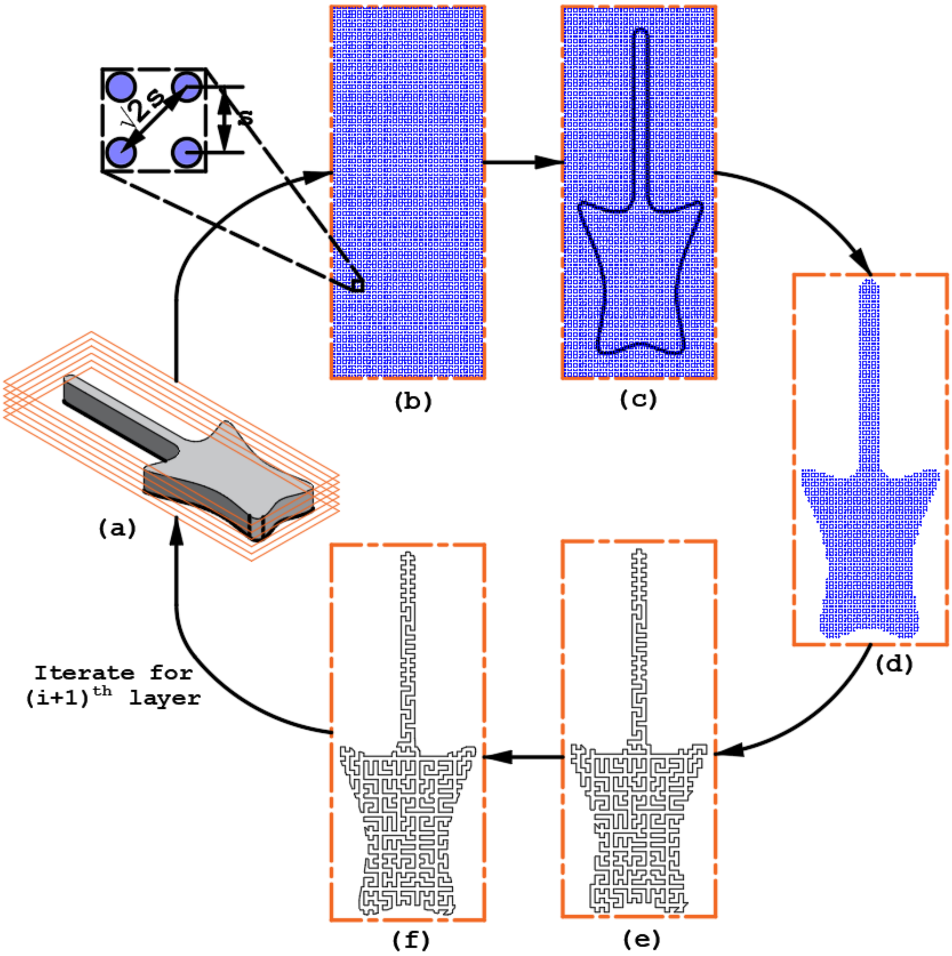

Fig. 5.4: Process sequence for toolpath generation using TSP

Consider the rectangular nature of the grid points, illustrated in Fig. 5.4(b) (exaggerated view), where $'s'$ denotes the step-over of deposited tracks. The toolpath always prefers traveling along the sides rather than the diagonal. This is due to the fact that the sides of a square are shorter when compared to its diagonals. This result is a constant step-over without any intersection of the tracks.

5.2 Investigation on Digitization

The layout of cities (in this context, grid points) plays a crucial role in the overall nature of the toolpath. Two different versions of grid point arrangements were explored in the study. In the first case, a rectangular array of grid points was considered, whereas in the second case, the grid points were arranged in a circular manner, as highlighted in Fig. 5.5(a) and (b), respectively. The resulting toolpaths, as illustrated in Fig. 5.5 for a square and circular geometric contour, were significantly different.

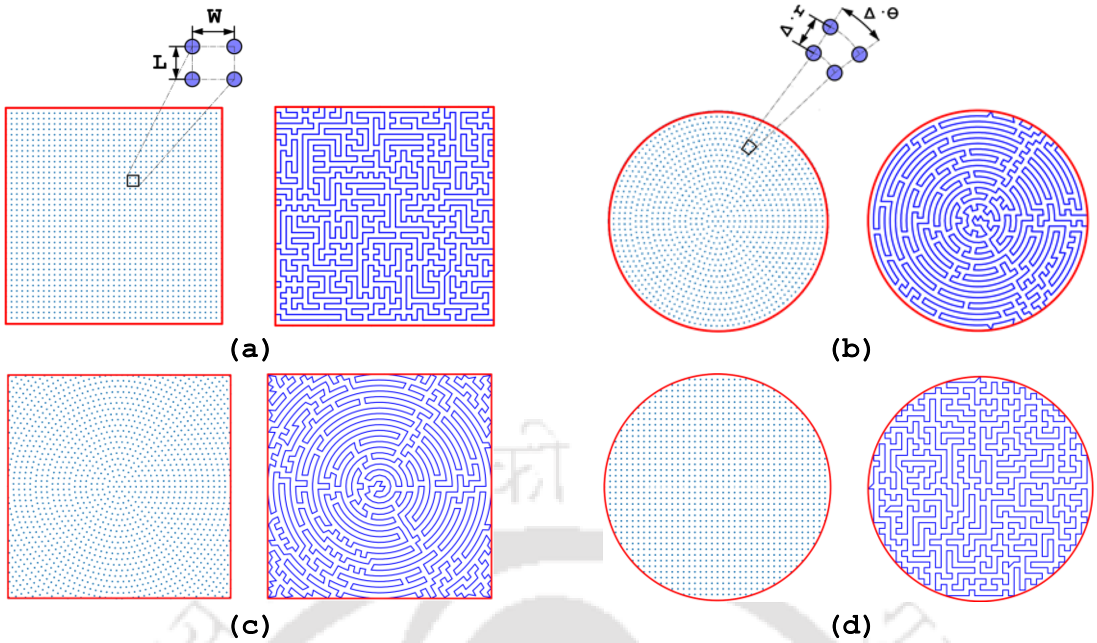

Fig. 5.5: Rectangular grid point array for (a) rectangular, (d) circular geometric contour, and circular grid point array for (b) circular, and (c) rectangular geometric contour.

An observation that can be made from the above-presented illustrations (Fig. 5.5 (a-d)) is the high number of turns while following this TSP-based area-filling toolpath. Turns in CNC motion, as discussed previously, are generally avoided as they induce unnecessary acceleration during an otherwise constant velocity motion [156]. In order to counteract this issue, the toolpath must favor one direction over the other, resulting in a decreased number of turns. Favoring direction can be accomplished in a TSP scheme by simple manipulation of the grid points (or cities). In the case of a rectangular grid, a reduction in width between two immediate points while keeping constant length biases the toolpath to favor motion in the 'width' direction, as illustrated in Fig. 5.6 and Fig. 5.7. The dimension between two consecutive grid points is expressed as a multiple of stepover s.

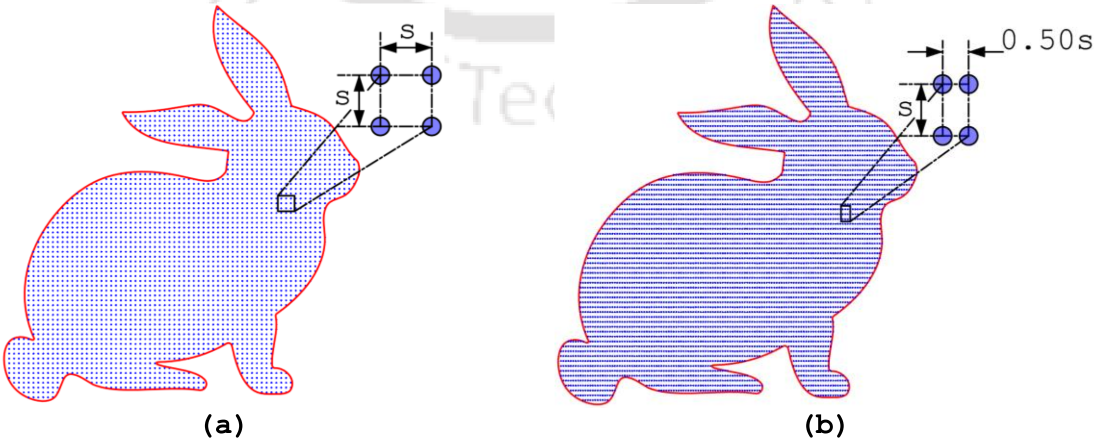

Fig. 5.6: Grid points placed in (a) square format and (b) rectangular format, with the width of the cell half of the length

Figure 5.7 illustrates the effect of grid point placement on the number of turns 'N' for a given contour. As the width between two immediate grid points decreases, attributing to direction favoring, the number of turns associated with a given toolpath also decreases.

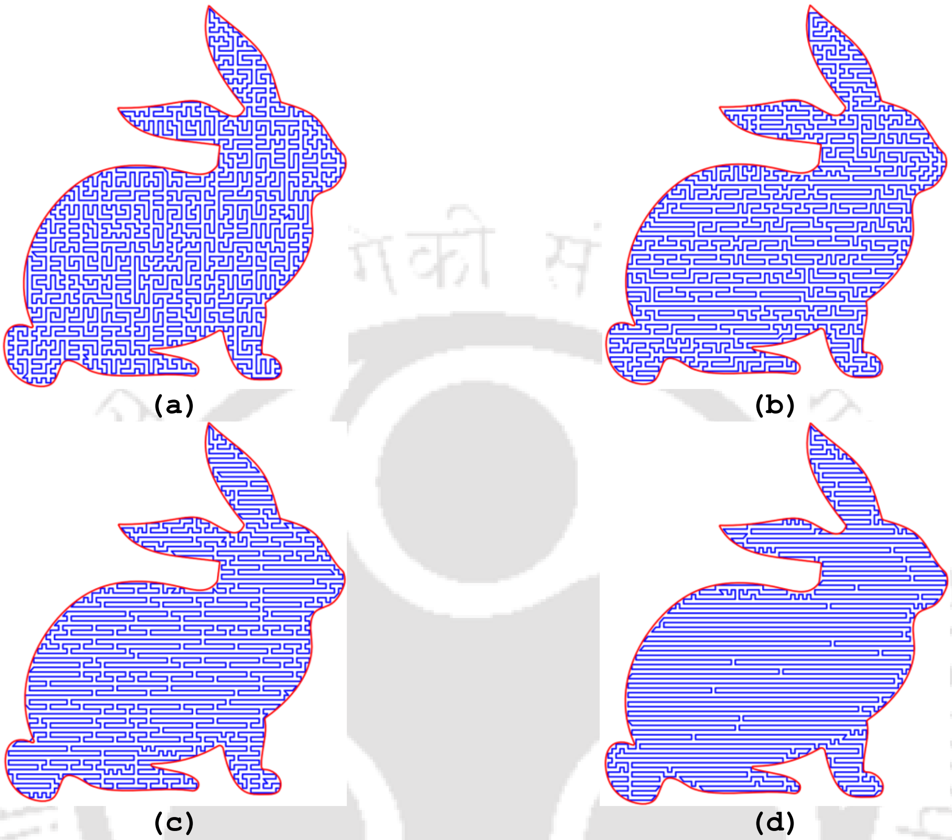

(a) (b) (c) (d)

Fig. 5.7: Reduction in 'Number of Turns (N),' from (a) to (d), as a result of direction favoring, attributed to decreased 'Cell Width (W).' (a) $W = s; N = 1916$, (b) $W = 0.95s; N = 1494$, (c) $W = 0.90s; N = 1132$, (d) $W = 0.85s; N = 543$.

Similar to a rectangular grid, manipulating cell dimensions in a circular grid also results in a toolpath favoring one direction over another. The cell dimensions in the case of a circular grid can be specified using radial and azimuthal distances between two successive radii and two consecutive grid points at the same radius, respectively. The radial distance and the number of points along the azimuth direction (for a given radius) denoted by Δr and a, respectively, can be expressed as

$$\Delta r \approx s\beta \tag{5.1}$$

$$a = \left[\frac{2\pi r}{2r sin^{-1}\left(\frac{s\alpha}{2r}\right)} \right] \tag{5.2}$$

where s denotes the step-over, r is the radius, β, and α can be treated as control variables such that change in their values varies the distance between grid points in radial r and azimuth directions ϕ, respectively, as illustrated in Fig. 5.8. The denominator in equation 5.2 can be viewed as the arc length between two successive grid points placed s distance apart. As the value of r is increased, for a constant step-over, the number of points along ϕ must also increase, thus ensuring a constant distance between two points in ϕ for any given r. The ceiling function associated with equation 5.2 approximates the number of points to its nearest greater integer value.

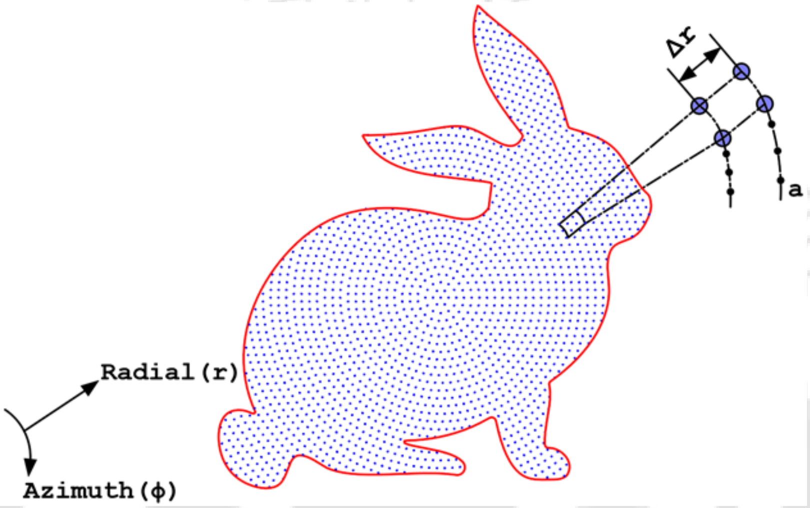

Fig. 5.8: Orientation of circular grid for the digitization of a geometric contour

It can be observed from equations (5.1) and (5.2) that as the value of β decreases, the distance between two consecutive grid points along the radial direction (r) decreases; consequently, the TSP-based toolpath favors radial travel (along r). Conversely, if the value of α decreases, the number of points (a) along ϕ increases, leading to a decrease in distance between two consecutive points. As a result, the toolpath prefers azimuth (along ϕ) over the radial direction of travel. Figure. 5.9 illustrates the variations in the toolpath as a result of direction favoring the case of a circular grid.

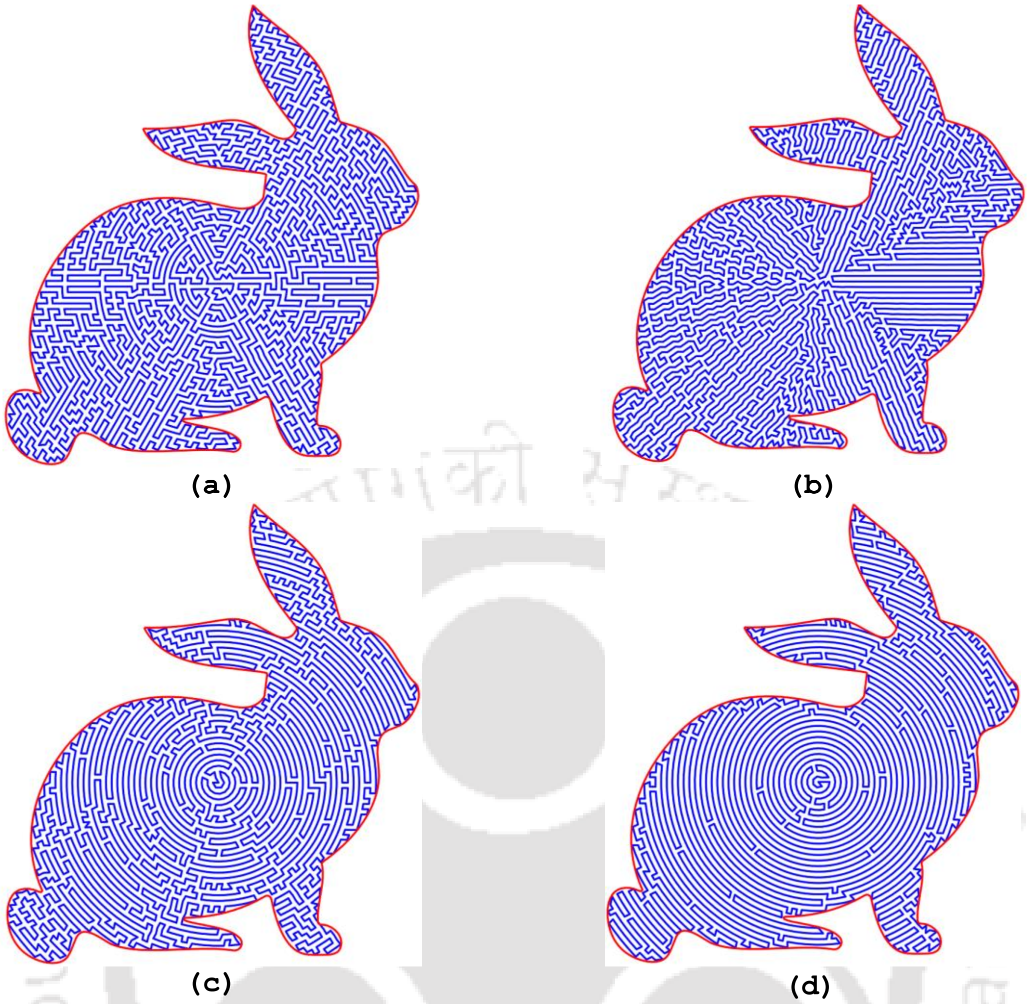

(a) (b) (c) (d)

Fig. 5.9: Favoring of radial and azimuthal directions as a result of decreasing β and α, respectively (a) $\alpha = 1.00; \beta = 0.95; N = 2410$ (b) $\alpha = 1.00; \beta = 0.85; N = 1653$ (c) $\alpha = 0.95; \beta = 1.00; N = 1488$ (d) $\alpha = 0.85; \beta = 1.00; B; N = 734$

5.3 Toolpath Optimization: Grid Fit

The position of the geometric contour relative to the grid points significantly affects the space-filling efficiency of a TSP-based area-filling toolpath. Consider Fig. 5.10, schematically showing a circular geometric contour (outlined in red) positioned relative to square grid points with cell dimensions equal to step-over. The shortest distance between a point on the boundary (red circle) and the nearest adjacent (inside) grid point, marked as '1…5', is represented by $b_1 \dots b_5$, respectively. A 'spillage' parameter $'d'$, representing the total distance by which a deposited track exceeds the boundary, can be defined as

$$d = (s - b_1)^2 + (s - b_2)^2 + (s - b_3)^2 + (s - b_4)^2 + (s - b_5)^2 \tag{5.3}$$

It is to be noted that distances b and d are variables dependent on the chosen grid points, which are inside and immediately adjacent to the boundary. For every point inside the boundary, its minimum normal distance from the boundary is measured. If this distance comes out to be less than stepover, the points are considered for the calculation of d. Within the Python environment, the calculation of distances was made using the library 'Shapely" [273]. These special grid points, collectively represented as P, can be treated as a subset of all the grid points considered for the implementation of a TSP algorithm.

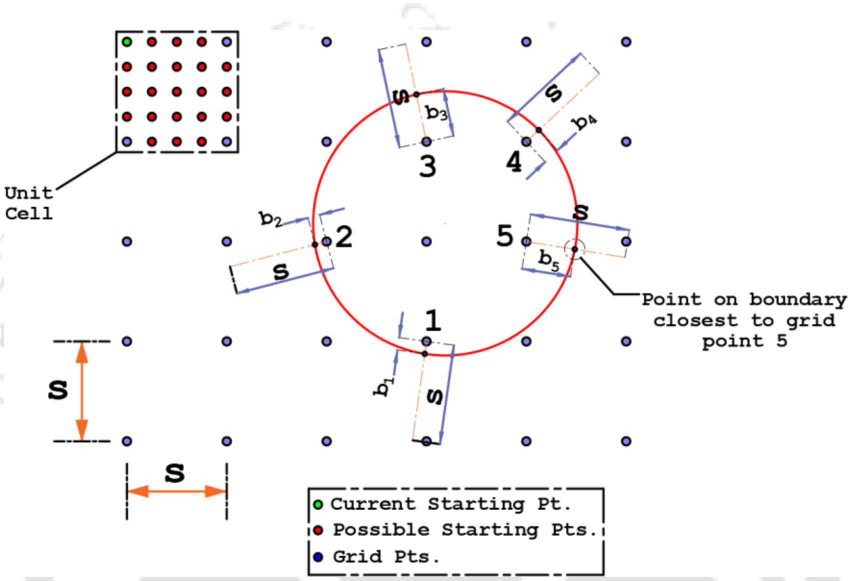

Fig. 5.10: Arrangement of grid points relative to the geometric contour

The example presented in Fig. 5.10 illustrates a simple case of a circular geometric contour with a rectangular grid orientation. For a complex contour with an irregular arrangement of grid points, equation 5.3 can be generalized as

$$d = \sum_{all\ P} (s - b_{1\ldots P})^2 \qquad (5.4)$$

The position of the gridpoint array relative to the geometric contour should be selected such that it minimizes $'d'$ ('spillage') in equation 5.4. Minimizing d not only results in higher geometric accuracy of the deposited track but also positions the grid points for a more uniform deposit, as illustrated in Fig. 5.11. The positioning of the grid points relative to the geometric contour such that an optimum state of digitization is achieved can be accomplished by treating the two entities (i.e., Grid point array and the geometric contour) as separate and independent layers. The layer containing the boundary is overlayed on the layer containing a set of grid points.

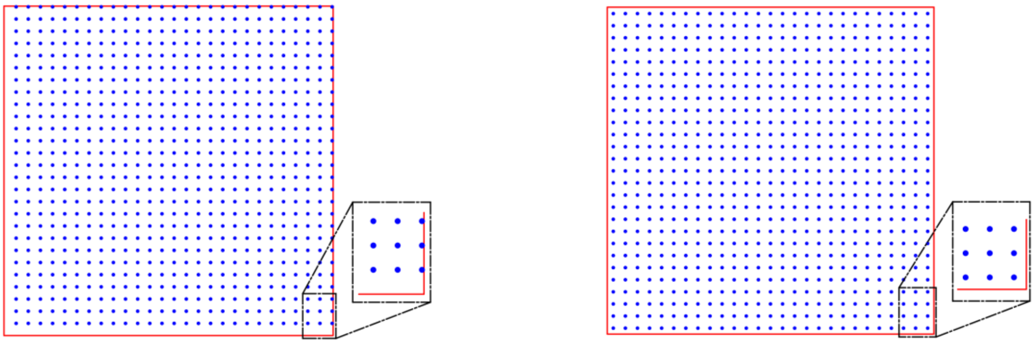

(a) (b)

Fig. 5.11: Grid point position relative to the geometric contour for (a) un-optimized digitization and (b) optimized digitization (minimized $'d'$)

The optimal position of the grid points can be obtained simply by stating the start point of the array. Consider Fig. 5.10 above; the unit cell has 21 different points (marked in red) that can offer possible start points for an equal step-over rectangular grid; the point in green marks the current start point—keeping the position of the geometric contour fixed, choosing a different start point (out of 21) for digitization shifts the entire grid relative to the boundary. Thus, the objective of the optimization can be defined as ‘select a start point within the unit cell that minimizes the spillage parameter (d)’. Enforcing this optimization sequence adjusts the grid such that the resulting toolpath is not just efficient, i.e., requiring minimum post-processing (finishing and/or machining), but, in some cases, also leads to symmetric and uniform deposit. Figure 5.12 schematically illustrates the optimization scheme implemented through the optimal positioning of grid points relative to the contour.

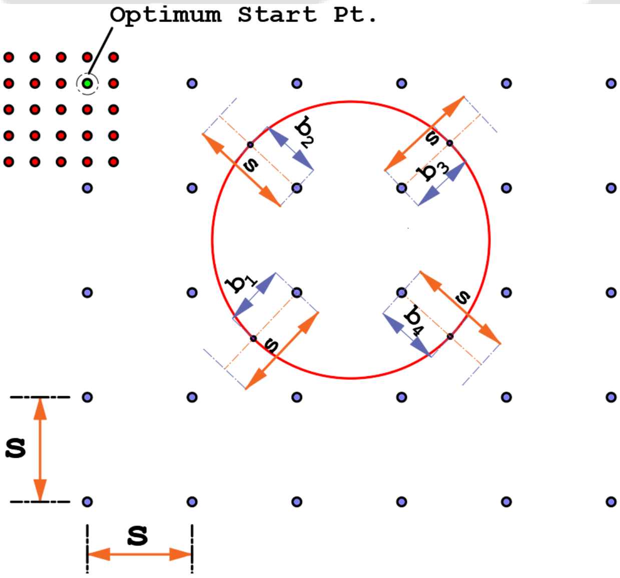

Fig. 5.12: Optimized grid positioning relative to the geometric contour

5.4 Toolpath Optimization: Boundary Trim

The method of using boundary trim to generate accurate and precise space-filling curves has been explored in the past by Kapil *et al.* [152]. Figure 5.13 highlights the effect of the trim algorithm for a given geometry.

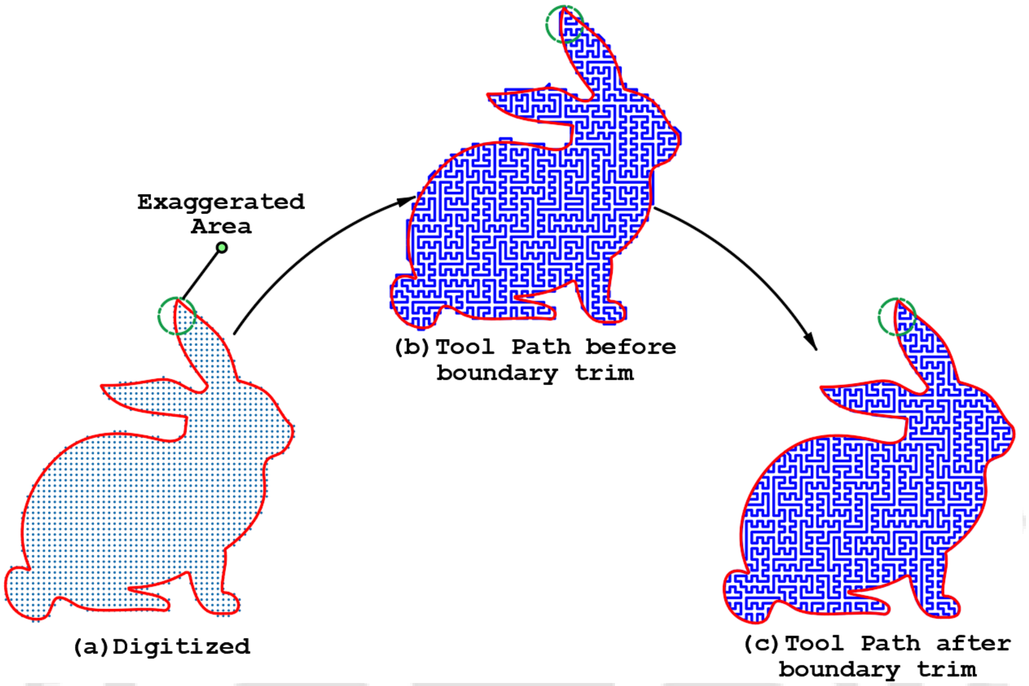

Fig. 5.13: Effect of 'boundary trim' on toolpath for previously considered geometric contour

The implementation of the **'Boundary Trim'** follows a sequence of steps, as listed below.

- Overlay the geometric contour on the grid points and eliminate outside points, retaining those that are within a distance of '$0.5 \times s$' from the boundary. This enforces several grid points outside the boundary, highlighted in red (illustrated in Fig. 5.14(a)), to be considered for a TSP-based toolpath.
- Run the TSP algorithm to obtain the toolpath, as illustrated in Fig. 5.14(b). As expected, attributing to the criteria above, the toolpath extends beyond the contour.
- Identify the intersection points with the boundary as the toolpath exits the geometric contour (marked as '1' in Fig. 5.14(b)) and re-enters (marked as '2' in Fig. 5.14(b)) to make the subsequent connection between other grid points. These two intersection points are inserted both into the boundary data file as well as the grid points for the toolpath.
- Replace the outside grid points in the toolpath with the boundary points between the two (marked as '1' and '2' in the example) intersection points. The resulting toolpath is illustrated in Fig. 5.14(c).

The boundary trim algorithm, in conjunction with the TSP-based toolpath strategy, promotes high-resolution prints, which require very little (if any) post-processing.

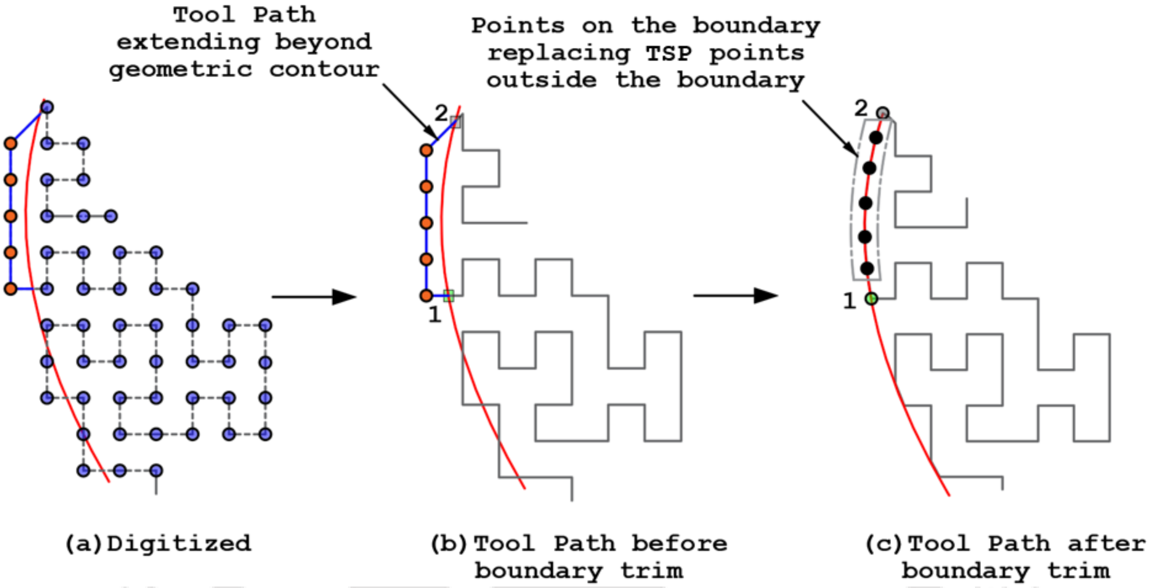

Fig. 5.14: Implementation of the 'Boundary Trim' algorithm, illustrated for the exaggerated section (circled in green) of Fig. 5.13

5.5 Selection of Start and End Points

Fabrication of parts with continuous deposition of material without any 'lifts or retractions' has advantages, both in terms of part quality and process efficiency [274]. These advantages become even more apparent in AM processes such as DED. Frequent arc ignition and extinguishment lead to under and over-deposition of material, thereby causing part defects and geometrical inaccuracies[275–278]. A TSP-based toolpath offers a possible solution to this problem through a common start and endpoint, as illustrated in Fig. 5.15. The material deposition starts at a point marked '*A*' and returns to the same point, having filled the area inside the given contour, thus forming a closed loop. This sequence of material deposition can be repeated for each layer, ensuring a common point of start and stop throughout the fabrication process. The point designated for the start and stop of the deposition is selected such that it lies outside the part contour and can be eliminated by machining, as shown in Fig. 5.15. This limits the defect in the deposited part caused due to the unstable nature of material deposition during start and stop.

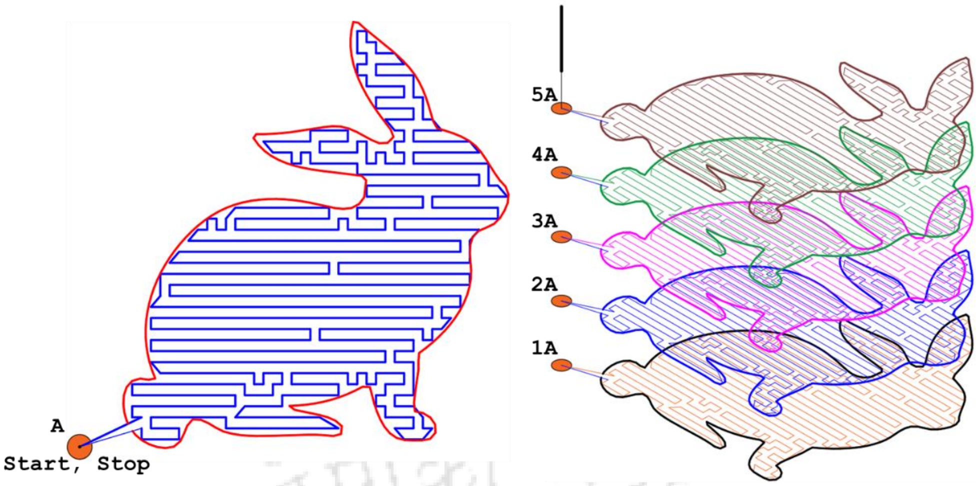

Fig. 5.15: Common start and stop point ('*A*') for material deposition lying outside the part contour for easy machining; 1A-5A marks the location of this point for five layers of deposition, each shown with different color

Apart from the geometric deviations, instabilities in material deposition and heat input at the start and end positions also affect the part properties [279]. Studies by Köhler *et al.* [277] suggest the presence of porosities in the parts deposited by DED at the start/ stop locations. Furthermore, these start/ stop locations also revealed specific local residual stresses resulting in stress peaks. The proposed toolpath attempts to eliminate these defects by appropriately selecting the start/ stop locations such that they are easily machined off during post-processing. Removal of start/ stop instabilities in the material deposition through machining has also been suggested in the works of Köhler *et al.*[277].

Another application exploiting the closed-loop attribute of a TSP-based algorithm is the ability to implement passive corrections. Deposition-based processes like DED and FFF suffer from deposition instabilities during the start and end of the deposition. These instabilities lead to the under-deposition of material at the start and over-deposition at the end. Consequently, material deposition along a line segment, as shown in Fig. 5.16, to build a layered wall will exacerbate the problem attributing to error accumulation. On the other hand, a closed-loop deposition can passively counteract the error, where the under-deposition during the start is compensated by over-deposition at the end, as is evident from the deposited circle shown in Fig. 5.16. The proposed closed-loop, TSP-based toolpath strategy conveniently incorporates this correction for material deposition.

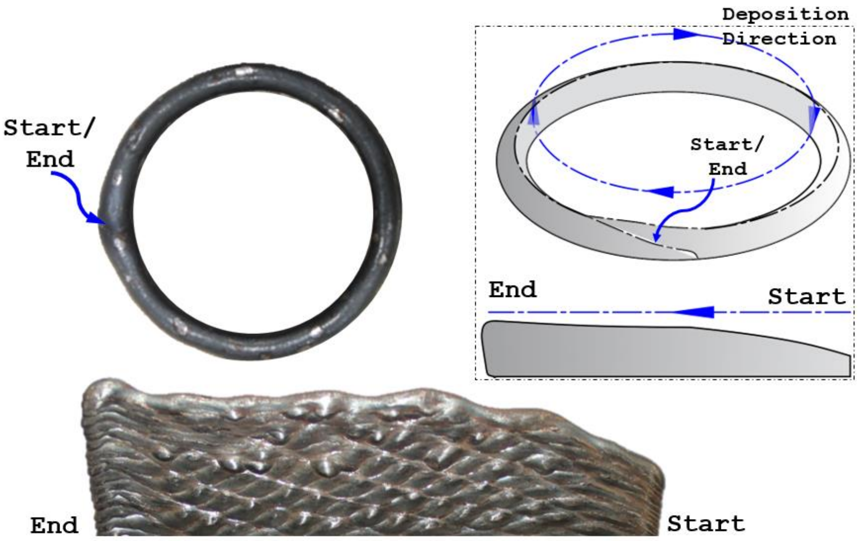

Fig. 5.16: Closed-loop toolpath with a common start and end point compensating for errors due to material instabilities during the beginning and at the end of a deposition

5.6 Results and Discussion

The toolpath strategy was implemented for five selected geometries, as illustrated in Fig. 5.17. The selected geometries are fairly complex in nature, which validates the generic nature of the algorithm and highlights its ease of implementation. Through tests using FFF and CMT-based WAAM printers, the toolpath strategy validates its effectiveness in accurate and efficient material deposition.

5.6.1 Effect of Step-Over on Deposition Efficiency

The efficiency of material deposition (η) for a given toolpath is expressed as the ratio of the area enclosed by the geometric contour A_c to the area of material deposited A_m. The area of the material deposited can be expressed as the product of the toolpath length L and the stepover s. Mathematically it can be expressed as,

$$\eta = \frac{A_c}{A_m} \tag{5.5}$$

$$A_m = L \cdot s; \tag{5.6}$$

The percentage overlap is dependent on the AM processes and the process parameters; for example, in the case of WAAM, studies have suggested an overlap of 73.8% of the bead width [167,280]. It can be observed from the above equations that an increase in the total area of deposited material decreases the deposition efficiency of the toolpath, thus signifying increased post-processing, such as finishing and machining operations. On the contrary, for stock machining, with a toolpath limited to planar motion, the material removal efficiency can be defined as the ratio of the area of the model (to be machined) to the area of the raw stock. Figure 5.17 illustrates various geometries that are considered as the subject for performance evaluation of the proposed TSP-based area-filling strategy.

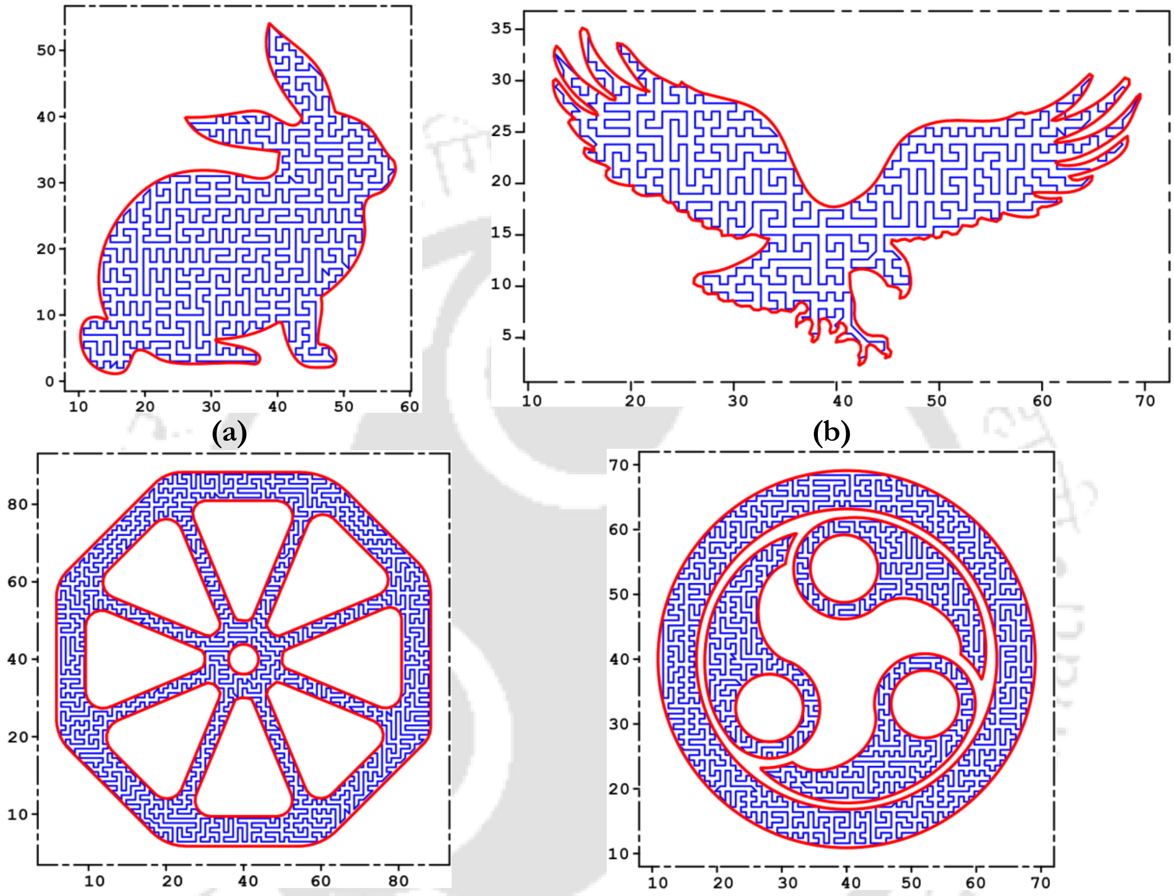

(a) (b)

(c) (d)

Fig. 5.17: Test geometries for performance evaluation of TSP-Based toolpath strategy (a) Geometry 1, (b) Geometry 2, (c) Geometry 3, and Geometry (4)

The results, illustrated in Fig. 5.18, show a negative correlation of deposition efficiency with the step-over distance; this agrees with previous studies on path planning for material deposition in AM [167]. The negative correlation between η and s can be attributed to the additional material that has to be deposited to compensate for the increase in step-over value so as to avoid voids in the deposition and ensure complete fill. For the case of stock machining, η maintains a constant value.

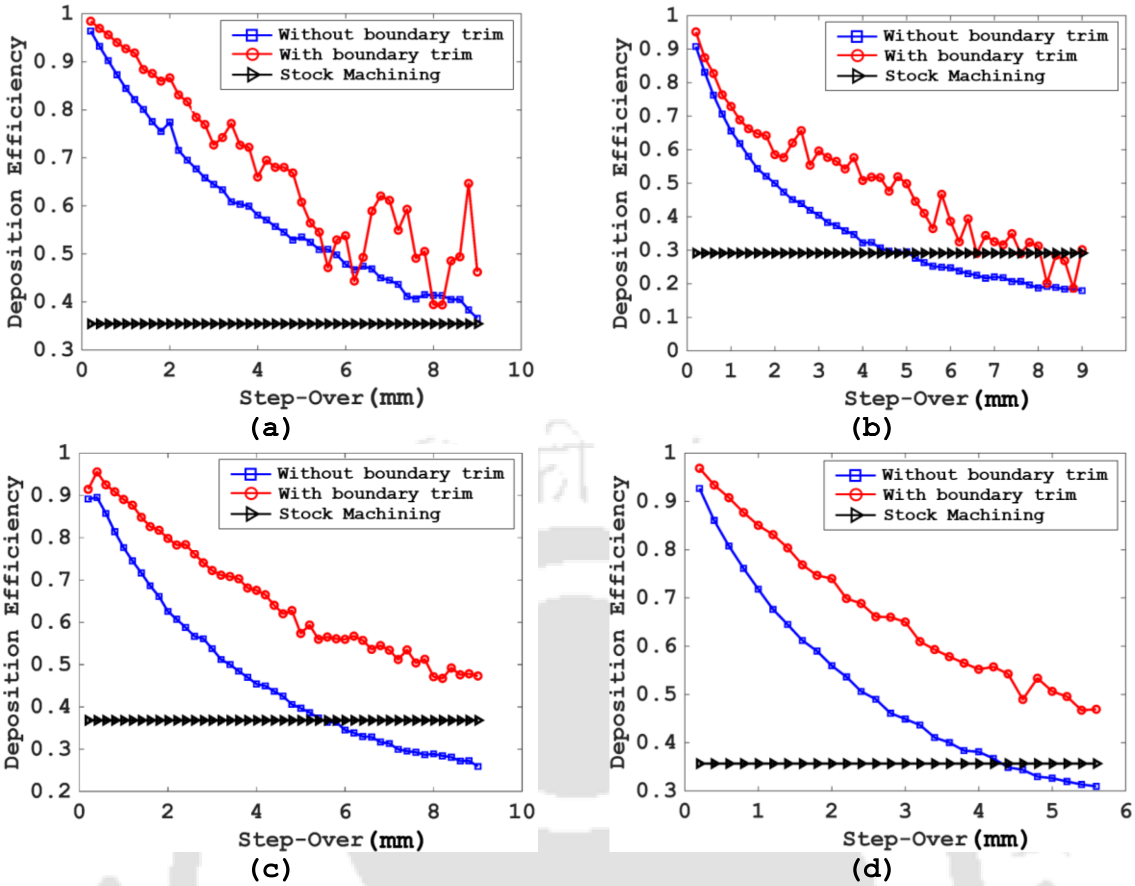

Fig. 5.18: Negative correlation between the material deposition efficiency and the step-over for (a) Geometry 1, (b) Geometry 2, (c) Geometry 3, and (d) Geometry 4

5.6.2 Effect of Direction Bias on Number of Turns

The number of turns $'N'$ in any given toolpath significantly affects the overall process efficiency and product quality [156,281–284]. Increasing step-over (for the contour geometries illustrated in Fig. 5.17) decreases the number of turns in a toolpath. However, this reduction in the number of turns is made at the expense of deposition efficiency. One primary advantage of a TSP-based algorithm is the ability to manipulate grid points such that the resulting toolpath provides a minimal number of turns while preserving high deposition efficiency, as illustrated in Fig. 5.19. Figure 5.19 illustrates a nearly constant efficiency curve with a decreasing number of turns as the distance between grid points is reduced. The numbers on the abscissa (ranging in decreasing order from 1 to 0.3) represent a multiplication (reduction) factor for the width of a unit cell in a rectangular grid, which starts with a value equal to the step-over and decreases gradually, moving away from the origin. This multiplication factor is represented by α for circular grids; a decrease in α forces the toolpath to prefer the azimuth direction to travel over the radial direction.

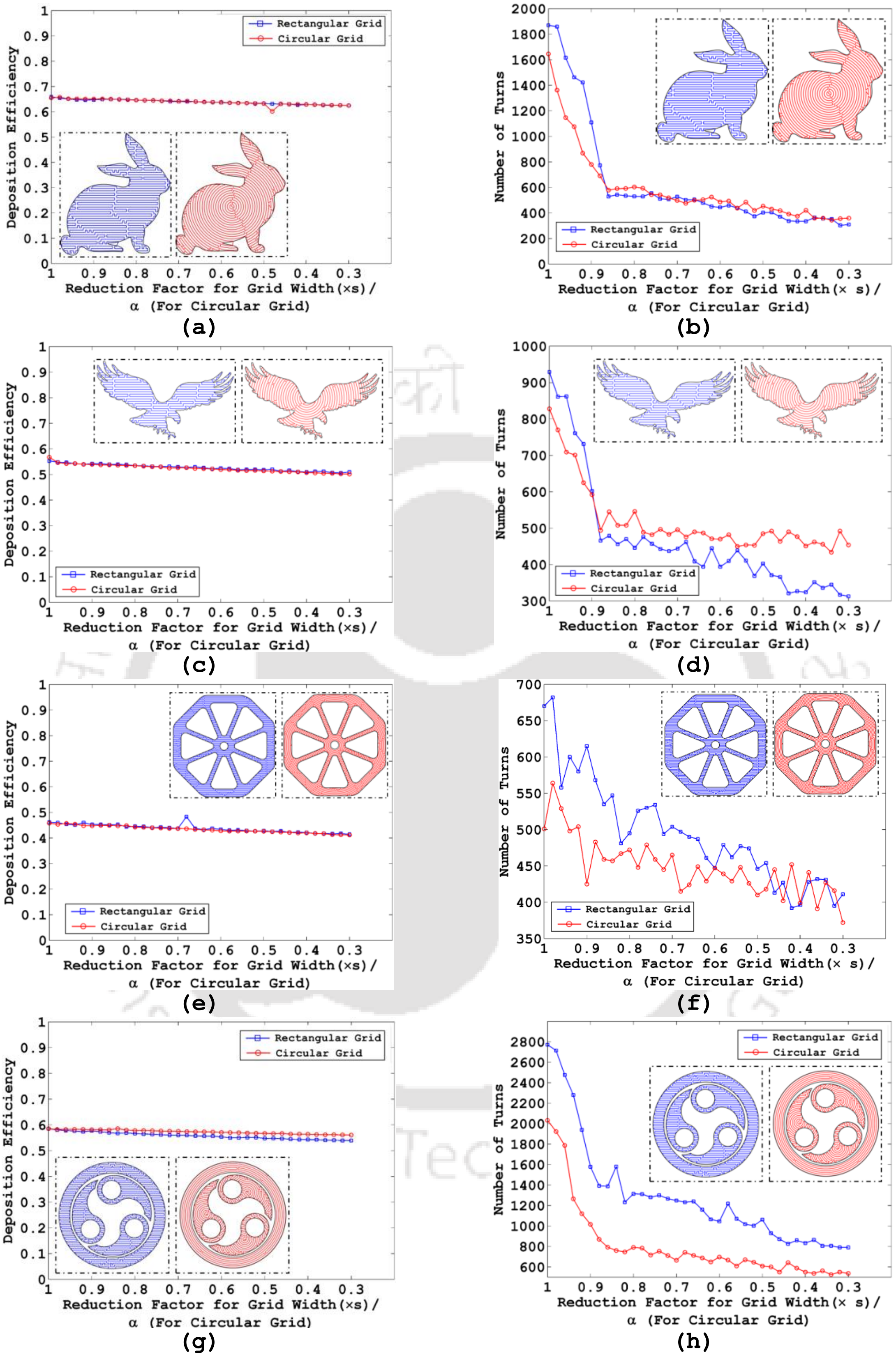

Fig. 5.19: Constant deposition efficiency for geometries (a) 1, (c) 2, (e) 3, and (g) 4 and (b) decreasing number of turns with decreasing grid width (for rectangular grid) or $'\alpha'$ (for circular grid) for geometries (b) 1, (d) 2, (f) 3, and (h) 4

It can be observed from these plots that the decrease in 'Number of Turns' with a reduction in grid width, initially, is very high; however, the curve tends to flatten towards the end. Therefore, it can be inferred from Fig. 5.19 that, for the case of rectangular and circular grids configured to favor horizontal and azimuthal directions, a significant reduction in the number of turns can be achieved with reasonably high values of reduction factors. Furthermore, reducing the distance between two neighboring grid points in the aforementioned favored directions through a selection of lower multiplication factors beyond a specified value yields little to no change in N.

Observing the plot of the geometry of the hexagonal wheel with narrow spokes (Fig. 5.19(f)), a large variation in the number of turns is evident. A possible explanation can be derived from the relative position of the grid points within the spokes. Figure 5.20(a) represents the grid point position at a reduction factor of $0.60s$; observing the first and second spoke, marked by spoke lengths (S_{L1}) and (S_{L2}), respectively, it can be seen that the number of turns in the first spoke is more than that in the second. As for the second case with a reduction factor of $0.58s$, as illustrated in Fig. 5.20(b) opposite is observed, i.e., the number of turns in the first spoke is less than in the second.

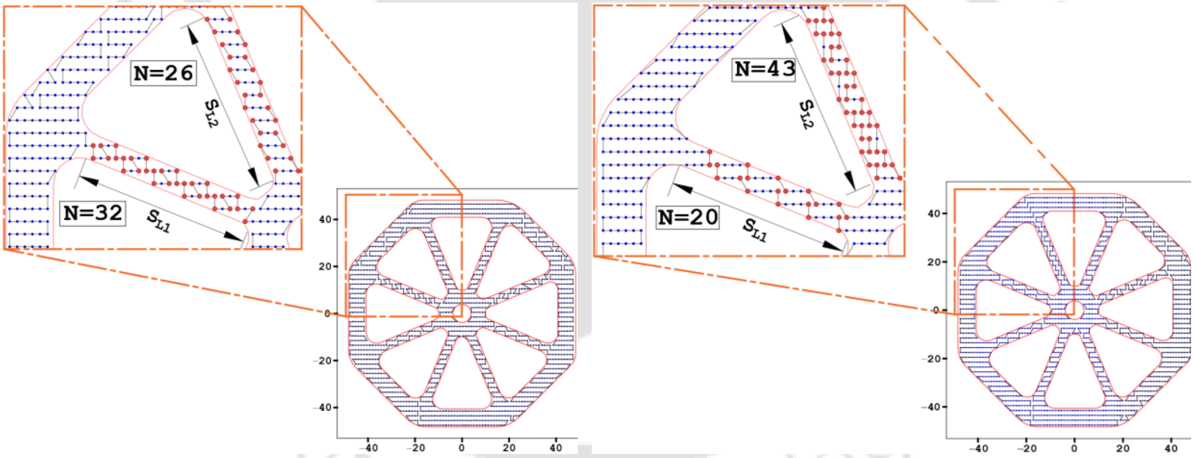

(a) **(b)**

Fig. 5.20: Variation in the local number of turns observed in the narrow regions of the plot with grid point positioned at (a) 0.60 × step-over and (b) 0.58 × step-over

From this observation, it can be inferred that the positioning of the grid points in the narrow regions (such as that of the spoke), to a large extent, dictates the total number of turns in a toolpath. Often, the grid points in these narrow regions are so positioned that even with a decreased spacing between two consecutive grid points, the number of turns (globally speaking) increases.

5.6.3 Discontinuity/ Lifts in Toolpath

So far, the discussion points to the continuous nature of the toolpath. Even though it is desirable to have a toolpath with no lifts (retraction) as it provides better print properties with reduced print times, in certain cases, it is difficult to achieve. Figure 5.21 points to a few of these cases. It is apparent from the toolpath, as illustrated in Fig. 5.21, that, in certain (very specific) locations, the positioned grid points force the traveling salesman algorithm to extend the toolpath beyond the geometric contour of the layer. This problem of toolpath extending beyond the specified geometric contour is exacerbated for the geometries with several narrow feature profiles placed very close to each other, as illustrated in Fig. 5.21(d) (near the wingtips of the eagle). Thus, tool retraction in these locations becomes imperative to avoid any post-processing time and cost.

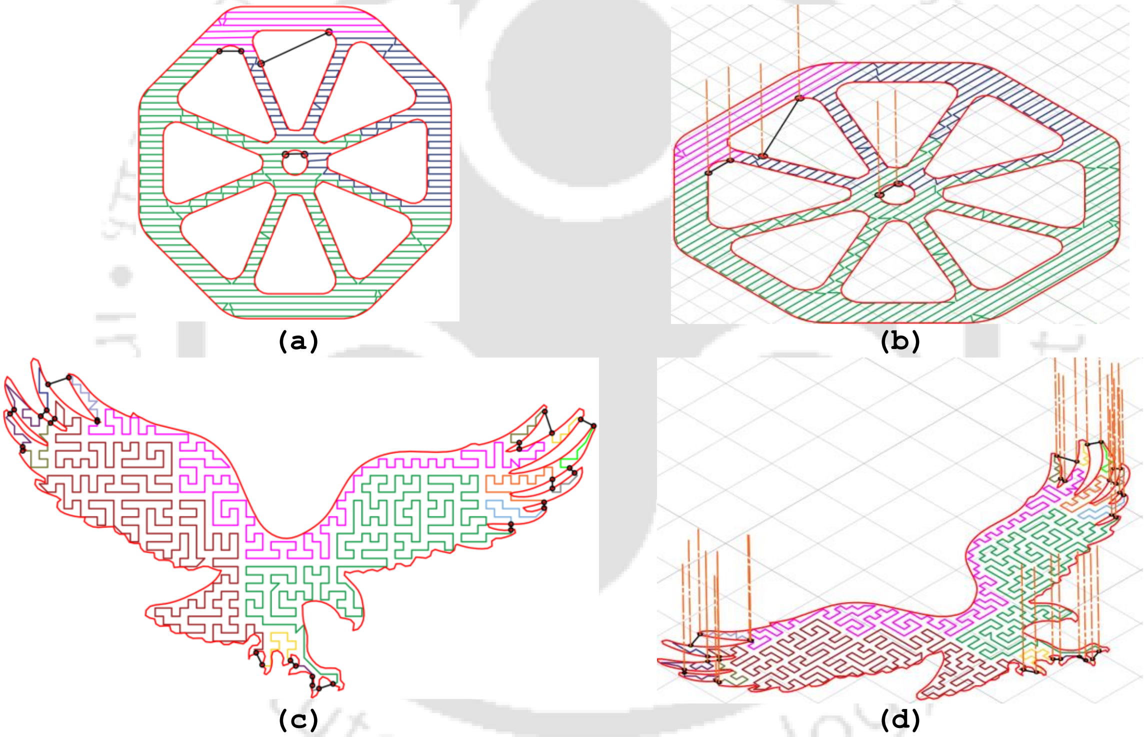

Fig. 5.21: Toolpath with tool retraction points highlighted in red illustrating (a, b) 6 retractions and (c, d) 34 retractions (switch on/ offs)

5.7 Implementation of TSP-based Toolpath Strategy

The proposed toolpath strategy was successfully implemented on an FFF-based printer and through Cold Metal Transfer (CMT)-based WAAM. The results, as illustrated in Fig. 5.22 and Fig. 5.23, conclusively validate the effectiveness of the toolpath in fabricating complex geometries with high deposition efficiency and print resolution. For the case of FDM, the prints with the rectangular grid point array (Fig. 5.22 (a) and Fig. 5.22(b)) show a reduced number of turns with a bias to horizontal direction as the cell width decreases (from Fig. 5.22(a) to Fig. 5.22(b)). Figure

5.22(c) and Fig. 5.22(d) illustrate the prints obtained for the case of a circular grid point array. By appropriately selecting the value of α and β one can bias the toolpath in either radial (Fig. 5.22 (c)) or azimuthal direction (Fig. 5.22 (d)).

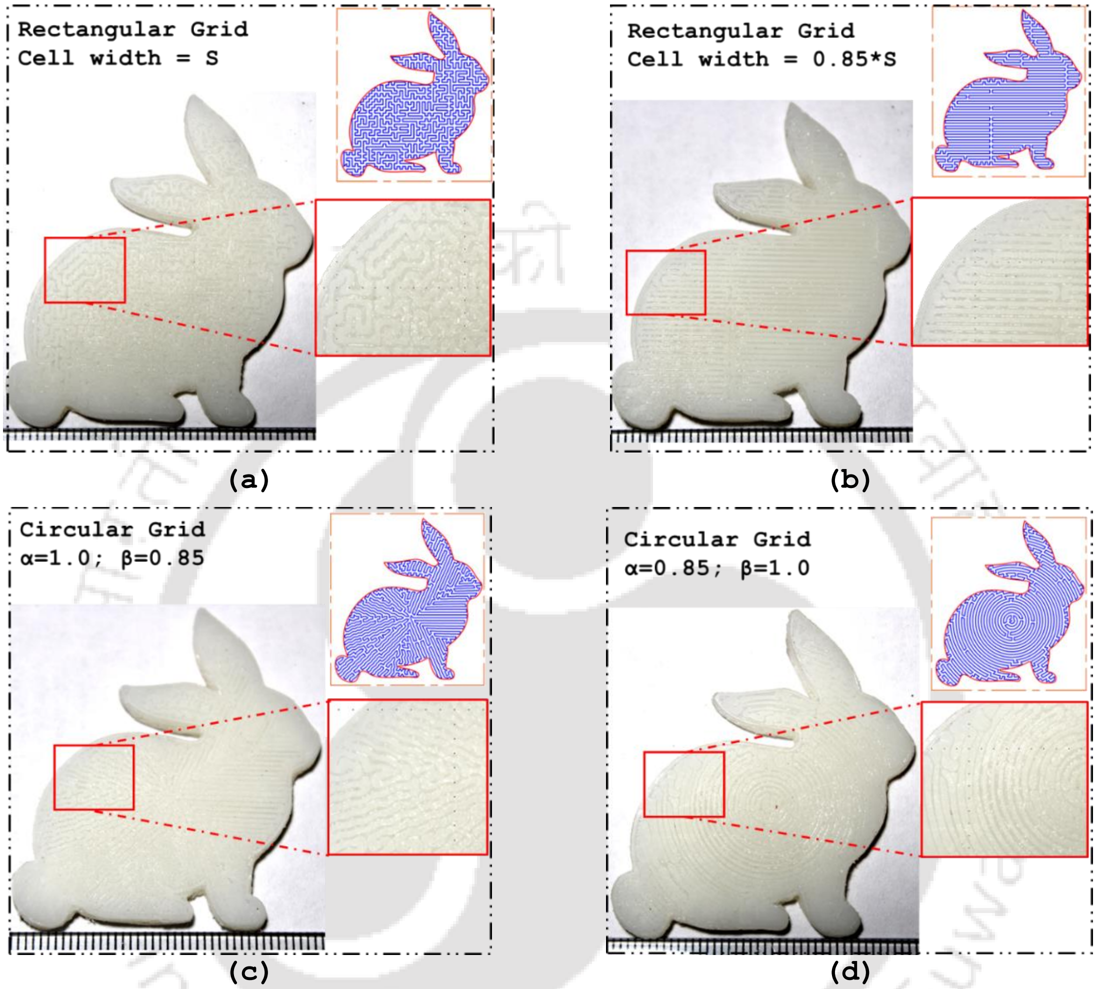

Fig. 5.22: Implementation of the TSP-based toolpath scheme on an FFF-based printer, with prints (a) and (c) following the toolpath presented in Fig. 5.7(a) and (d), respectively, and prints (c) and (d) following the toolpath presented in Fig. 5.9(b) and (d), respectively

Figure 5.23 shows the deposition through WAAM, where the first row of images shows the toolpath followed, the second row shows the samples deposited through WAAM, and the third and final row shows the part after face milling. All the depositions were carried out under identical conditions with a fixed value of stepover of 2.33 mm.

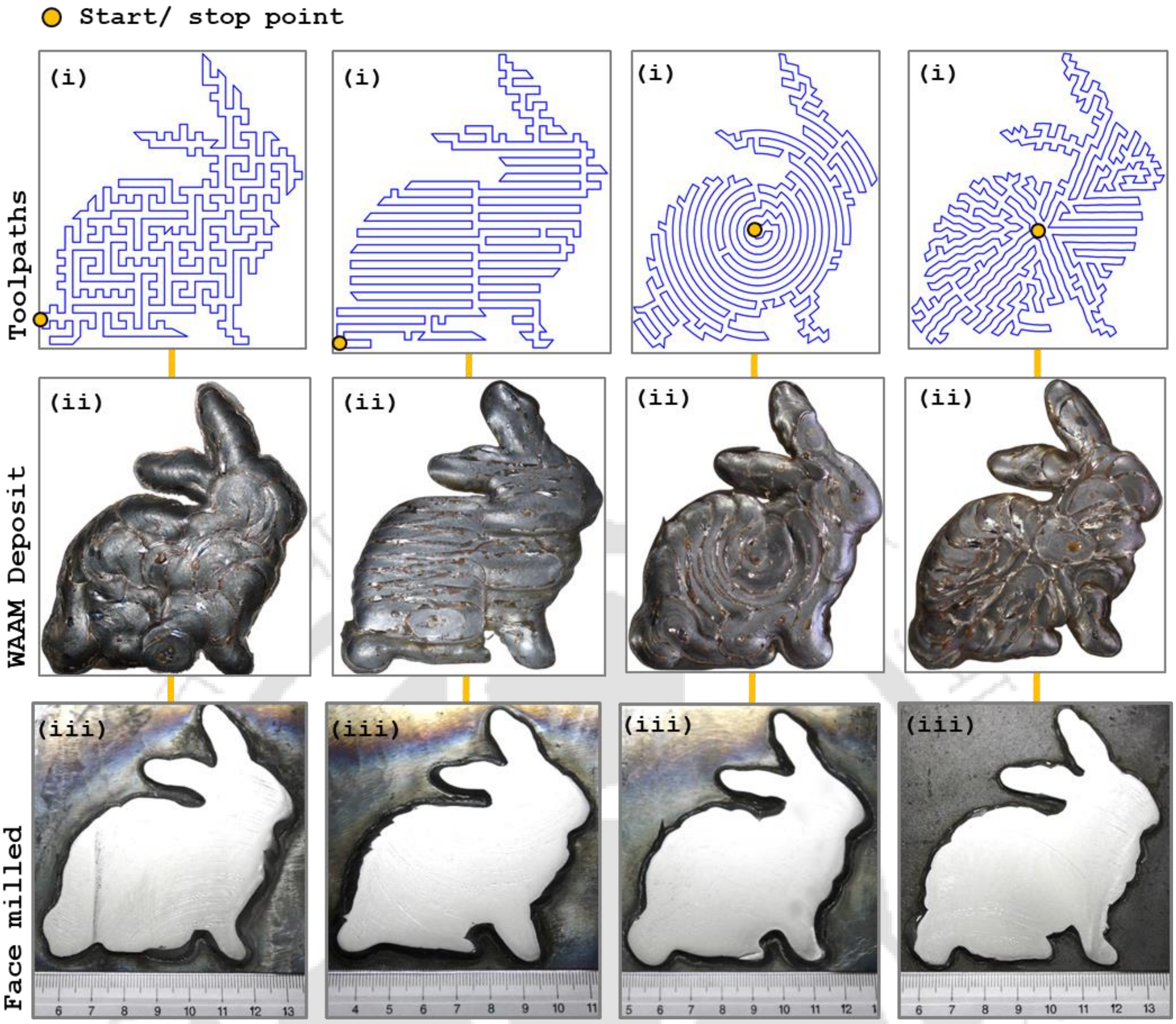

(a) Rectangular Grid W = s

(b) Rectangular Grid W = 0.85*s

(c) Circular Grid α=0.85; β=1.0

(d) Circular Grid α=1.0; β=0.85

Fig. 5.23: Implementation of the TSP-based toolpath scheme on WAAM deposits for rectangular grid favoring (a) no unique direction, (b) horizontal direction and circular grid favoring (c) azimuthal, and (d) radial directions

5.8 Summary

This work presents a Travelling Salesman Problem (TSP) based area-filling strategy for toolpath generation in Additive Manufacturing (AM). Several crucial aspects of a TSP-based toolpath are explored in this work, most prominently the effect of grid point placement relative to each other as well as the geometric boundary. The following are key highlights from this work.

- By appropriately positioning the grid points, the toolpath could be forced to favor one direction over the other. The resulting toolpath was not only efficient in the material deposition but was able to significantly reduce the number of turns.

- An advantage of a TSP-based toolpath is its continuous closed-loop nature. This avoids multiple ON and OFF states of the laser (analogous to tool retraction) during material deposition. Continuous deposition of material prevents the process instabilities that typically occur when the state of the fusion source transitions from ON to OFF or vice-versa.
- The TSP-based toolpath, in general, offers a higher number of turns as compared with the standard rastering toolpath; however, the study presents a possible solution to reduce the number of turns via appropriate digitization techniques. This allows the user to avail other advantages of a TSP-based toolpath, such as a minimal number of retracts, common start/ stop points, and user-preferred direction of deposition.
- The suggested TSP-based toolpath offers a common start and end point of deposition. Also, this common endpoint can be selected by the user. This feature ensures a localized defect at the start-stop location, which can be easily addressed during post-processing.

Chapter 6

Generation of Continuous and Sparse Space Filling Toolpath with Tailored Density

Functionally Graded Materials are prevalent in nature; Fig. 6.1 schematically shows an example of two such materials, i.e., bone (Fig. 6.1(a)) and cellulose fibers of a bamboo plant (Fig. 6.1(b)). The variation in part density in both of these examples is evident as one traverses from outside to inside. Fabricating such structures through AM can be accomplished via suitable toolpath planning. These toolpaths can be designed such that the stepover between two consecutive beads varies, consequently varying the 'packing' of the material to reflect the variation in part density. It is noteworthy to mention the variation in part density is a consequence of the toolpath and not the material property.

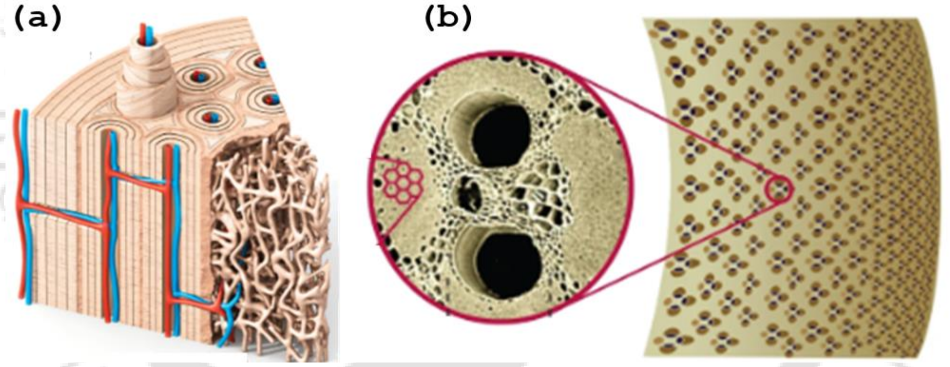

Fig. 6.1: Gradient structures found in nature, schematic representation of (a) bone and (b) bamboo. Reproduced with permission from [285], copyright(2014), Springer Nature Limited.

Fabrication of Functionally Graded Materials(FGMs) is a strong suit of AM. As presented previously in Chapter 1 Section 1.6.2, several methods of strategic material deposition can be found in the literature that can achieve a gradation of part density. In this work, an algorithm using a TSP-based solver is proposed that generates a continuous toolpath in accordance with a user-defined gradient. The Lin Kernighan heuristic-based TSP solver, described previously in Chapter 5, is used to create a continuous, closed-loop, and density-graded toolpath while retaining the ability to bias the deposition direction. Three force-based methods of digitization, namely rectangular, circular, and contour adaptive, are proposed in this work. Each of these methods initializes from a structured or an unstructured grid, where the grid points are assumed to be connected with either linear (rectangular digitization) or a combination of linear and torsional springs (circular and contour adaptive digitization). Enforcing an equilibrium amongst the spring forces and appropriately selecting the ideal spring length, the necessary configuration of grid points can be generated for a desired toolpath.

The density of grid points (consequently, part density) can be varied through the user-defined input function or an image-based density map imposed on the ideal spring length over the contour domain. As a case study, the proposed toolpath was implemented for printing a bone with density prescribed through a CT scan image stack. The printed part's CT scan qualitatively establishes the toolpath's conformity to the user-specified density gradient.

6.1 Methodology

Figure 6.2 outlines the general algorithm of the proposed toolpath. This algorithm, originally developed for the generation of unstructured simplex mesh, was adopted and appropriately modified from the works of Persson *et al.* [286] to implement toolpath planning for FGMs.

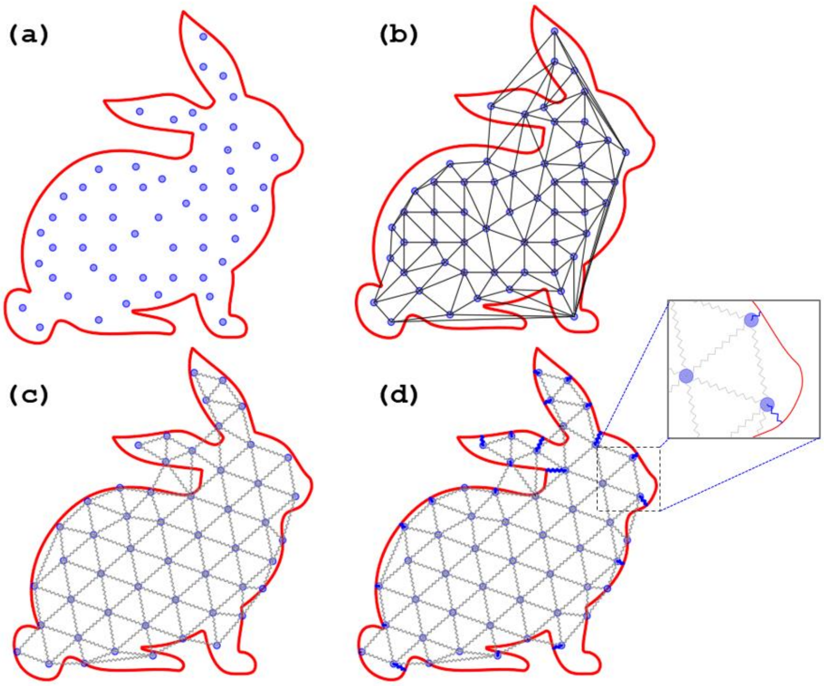

Fig. 6.2: Force-based algorithm for digitization (a) set of points randomly distributed within the contour (b) triangulated points (c) sides of triangles represented as spring in equilateral configuration and (d) points adjacent to the boundary connected to the nearest point on the contour using (blue) springs

Essentially, the algorithm consists of a set of points distributed (randomly or in the form of a structured grid) within a given contour (as illustrated in Fig. 6.2(a)), which can be triangulated using the Delaunay Triangulation algorithm, as shown in Fig. 6.2(b). The edges of these triangulated points can be considered as springs that push the nodes apart, such that the resulting triangle formed by any given set of points is equilateral, as illustrated in Fig. 6.2(c). The grid points that are immediately adjacent to the contour are connected with similar springs with the nearest point on the contour, as illustrated in Fig. 6.2(d).

6.1.1 Generation of a Square Grid

Consider a case where a square grid, which features equal stepover, is to be generated using the force-based algorithm as outlined above. For the generation of such a grid, as illustrated in Fig. 6.3, the points have to be so positioned such that some points of the initial grid assume a position corresponding to the corner points (on the opposite ends of the two diagonals) while others are the side points of a square.

Let $\hat{l}$ be a unit vector in the direction of spring force for a given point in consideration, say A (marked as red in Fig. 6.3(a)). Similarly, unit vector $\hat{v}$ points to one of the two orthogonal directions (horizontal or vertical) of the square grid. In order to achieve a square grid, the points which are immediate neighbors of A must adjust themselves such that either they assume the position of a 'diagonal point' (domain marked grey) or a 'side point' (domain marked white), as illustrated in Fig. 6.3. For sorting the points as 'diagonal' or 'side' points, the following argument can be considered.

$$\vec{l} = (x_B - x_A) \cdot \hat{\imath} - (y_B - y_A) \cdot \hat{\jmath} \tag{6.1}$$

$$\hat{l} = \frac{\vec{l}}{|\vec{l}|} \tag{6.2}$$

$$\gamma = \cos^{-1}\left(\hat{v} \cdot \hat{l}\right) \tag{6.3}$$

where x_B and y_B are the coordinates of one of the neighbor points (say) B to the point of consideration A, x_A and y_A are the coordinates of the point in consideration. The unit vector ($\hat{v}$) and ($\hat{v}'$), defined at A, represents the horizontal and vertical direction of a rectangular grid. For a grid point to be considered a diagonal point following criteria must be satisfied.

$$\nu_2 < |\gamma| < \nu_1 \tag{6.4}$$

$\nu_1$and ν_2, defined from the horizontal ($\hat{v}$), represents the lower and upper bound of the angle, the domain within which marks the region considered for a grid point to be diagonal a point. The above-mentioned test is carried out for all the neighboring points to the point of consideration. Having categorized the position of a given point into a diagonal (a grey region point) and a side point(a white region), the following criteria are used to enforce a rectangular grid.

1. The optimal spring length (l_0), to be achieved through force balance, corresponding to the diagonal point with A is considered $\sqrt{2}s$, where s is the stepover.
2. The optimal spring length (l_0), to be achieved through force balance, corresponding to the side point with A is considered as s
3. The objective of the algorithm is to update the locations of grid points within the contour such that the resulting spring forces, as illustrated in equation 6.5, achieve equilibrium

$$\vec{f_l}(l, l_0) = \begin{cases} k(l_0 - l) & \text{if} \quad (l < l_0) \\ 0 & \text{if} \quad (l > l_0) \end{cases} \tag{6.5}$$

4. The force calculation is carried out iteratively using the forward Euler method, expressed in equation 6.6, where the new point coordinate (P_{n+1}) is derived from its previous state (P_n) and the force function ($\vec{f_l}$). The system of connected springs is advanced one step at a time (Δt) by first considering a single point (schematically represented in red in Fig. 6.3) and looping through all its neighboring points as obtained through Delaunay Triangulation schematically represented in blue in Fig. 6.3). Table 6.1 briefly summarizes the algorithm.

$$P_{n+1} = P_n + \Delta t \vec{f_l} \tag{6.6}$$

Enforcing the above spring length criteria and force balance ensures a rectangular grid within a specified tolerance.

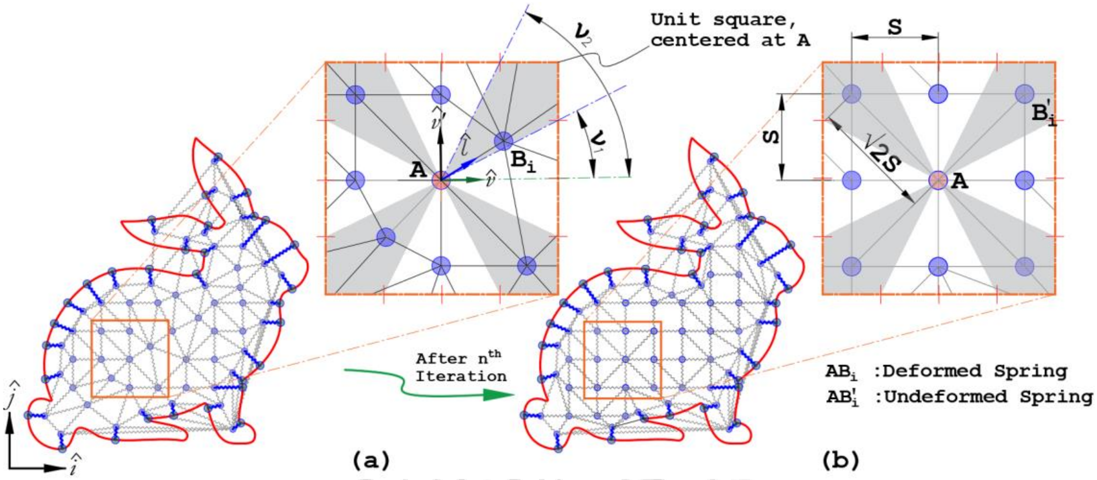

Fig. 6.3: Points inside the contour after (a) Delaunay triangulation, here, ν_1 and ν_2 are chosen as $\tan^{-1}(1/2)$ and $\tan^{-1}(2)$, respectively, and (b) implementation of the square grid algorithm

Table 6.1: Algorithm for generation of a rectangular grid using conditions of force balance

```
while (True)
  If convergence criteria == True:
     Break
  Else
    for all 'P' within contour
    1. Consider a grid point (say) $A_i(x_{A_i}, y_{A_i})$: $A_i \in P$, where $P = [x \quad y]_{n\times 2}$
    2. Define vector $\vec{F_i}$ such that $\vec{F_i} \in \vec{F}$, where $\vec{F_i}$ is the net force on a point $A_i$ due to all
       springs attached to it.
    3. Get $\xi_{Ai}$ the closest point on the boundary $(\Gamma)$ to point $A_i$

          If $l = distance(A_i, \xi_{Ai}) < d_{min}$
             Compute $\vec{f}_{Boundary}(l, l_0)_{A_i}$ on $A_i$ due to $\xi_{Ai}$
             Update $F_i = F_i + \vec{f}_{Boundary}(l, l_0)_{A_i \xi_{Ai}}$
      for all '$B_i$' within B
    4. Identify a vector $(\overrightarrow{A_i B_i})$ between $A_i$ and the neighboring grid point
       (say)$B_i(x_{B_i}, y_{B_i})$: $B_i \in B$ and $B \subset P$ where $B = [x_{B_i} \quad y_{B_i}]_{m\times 2}$. 'm' is the number of
       points connected to $A_i$, as a result of DT. The direction of $\overrightarrow{A_i B_i}$ is denoted by a unit
       vector (say) $\hat{l}$.
    5. Define $\gamma = \cos^{-1}(\hat{v} \cdot \hat{l})$

       if $\nu_1 < |\gamma| < \nu_2$
           $l_0 = \sqrt{2}S$
       else
           $l_0 = S$
           Compute $\vec{f}_{Linear}(l, l_0)_{A_i B_i}$ on $A_i$ due to $B_i$
           Update $\vec{F_i} = \vec{F_i} + \vec{f}_{Linear}(l, l_0)_{A_i B_i}$
    6. Update point coordinates of $P$ to $P' = [x' \quad y']_{m\times 2}$ such that $P' = P + \Delta t\vec{F}$.
7. Run TSP solver on $P'$
```

6.1.2 Generation of a Circular Grid

A circular grid can be achieved through an additional consideration of a torsional spring acting alongside linear springs. A grid is circular if it exhibits the following properties.

1. The distance between two consecutive circular tracks (T_n and T_{n+1}), as shown in Fig. 6.4, upon which grid points are placed, is equal to the stepover (s).
2. The distance between two adjacent grid points on a given circular track is equal to stepover.
3. The line segment joining two adjacent points on the same contour should be perpendicular to the radial direction ($\hat{r}$).

The directions ($\hat{v}$) and ($\hat{v}'$) of the rectangular grid now correspond to ($\hat{R}$) and ($\hat{\emptyset}$) respectively, which are defined from the input center position of the circular grid. The 'zone of influence' for the torsional spring is schematically shown in Fig. 6.4. The 'zone of influence' is primarily based on the proximity of a given grid point to its respective circular track ($T_1, T_2, T_3 \dots T_n$).

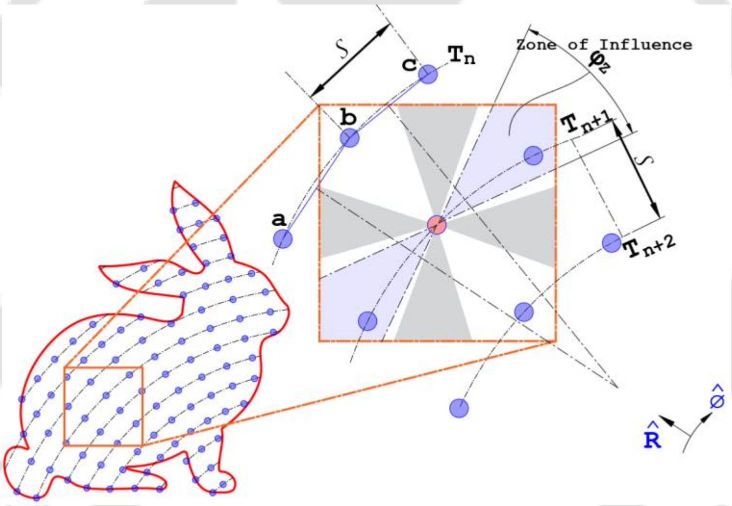

Fig. 6.4: Generation of circular grids; the domain within the contour is marked with circular concentric tracks ($T_1, T_2, T_3 \dots T_n$) with a user-defined center. These tracks are subsequently discretized with grid points

Consider the grid point $'A'$, marked in red in Fig. 6.5. The line segment AB, formed by joining the neighboring grid points (lying within the zone of influence for A), makes an angle θ with the radius of the track T_n centered at O, and contains the point M, as illustrated in Fig. 6.5(a). Under such a grid point configuration, the torsional spring is said to be in a deformed state. The spring force from the deformed torsional spring adjusts the line segment AB (Fig. 6.5(a)) to CD (Fig. 6.5 (b)) such that the angle θ and δ is $90°$ and $0°$, respectively. The torsional spring can be assumed to be anchored at M in Fig. 6.5, with its two ends attached to A and O. τ_d and τ_n are the angles between the free (connecting segments) ends of the torsional spring under deformation and its natural rest state, respectively, as illustrated in Fig. 6.5(a) and (b).

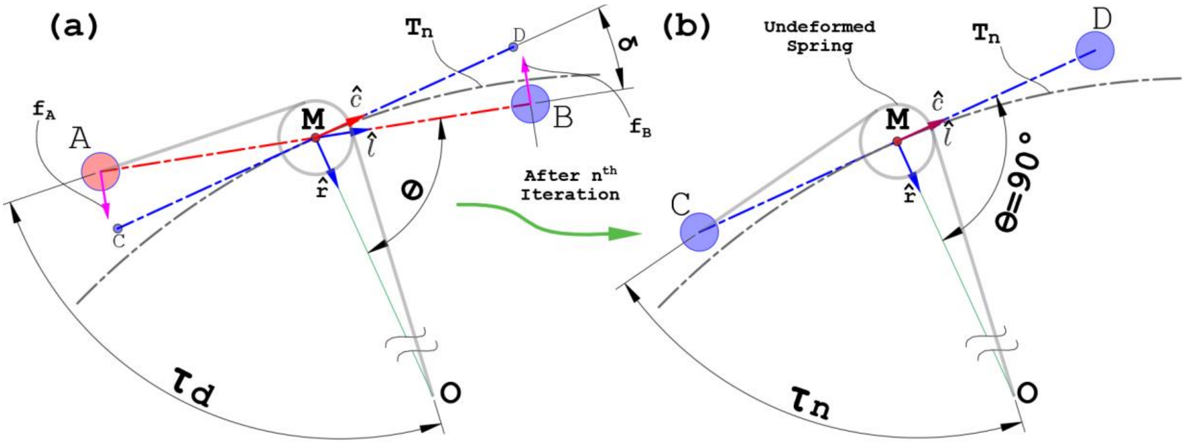

Fig. 6.5: The presence of a torsional spring, represented by a solid gray line, orients the line segment AB perpendicular to the track radius

Let $\hat{r}$ be a unit vector pointing towards the center from the midpoint of line segment AB. The angle θ formed between unit vectors $\hat{l}$ and $\hat{r}$, representing directions along the line segment (AB, in Fig. 6.5) and the radial direction of the circular track T_n, respectively, is expressed by equation 6.7. Consider a unit vector $\hat{c}$, which is perpendicular to $\hat{r}$ and oriented in the general direction as $\hat{l}$. An angle δ is defined between the unit vectors $\hat{c}$ and $\hat{l}$, mathematically expressed by equation 6.7. The torsional spring, ideally, applies a force at point A on the line segment $\overrightarrow{AB}$ such that an angular deflection, about point M, of magnitude δ orients $\overrightarrow{AB}$ to $\overrightarrow{CD}$, as shown in Fig. 6.5(b). The torque on $\overrightarrow{AB}$ consists of two parallel forces, one acting on A and the other on B; both are equal and opposite to each other but are mutually perpendicular to AB.

$$\delta = \theta - \pi/2 \quad \text{where } \theta = \cos^{-1}(\hat{r} \cdot \hat{l}\,) \tag{6.7}$$

If the value of δ is smaller than a user-defined critical value (δ_c), i.e., $|\delta| < \delta_c$ then, the grid points are considered within the zone of influence of the torsional spring. While the value of δ_c is user input, currently, it is arbitrarily compared with a value of $\pi/9$ for quantifying the zone of influence. The torsional spring exerts a torque T_{AB} on line segment AB for which magnitude is given by equation 6.8.

$$|T_{AB}| = k_t \cdot \delta \tag{6.8}$$

This torque moment is replaced by an equivalent force-couple f_A and f_B acting on points A and B, respectively, as shown in Fig. 6.5(a). Equating the moment due to force-couple to the moment due to an imaginary torsional spring, expressed in equation 6.9, gives us the value of force acting on point A due to the torsional spring between points A and O.

$$|T_{AB}| = 2 \cdot f_t(\delta) \cdot \frac{l}{2} \tag{6.9}$$

From equation 6.8 and 6.9

$$f_t(\delta) = \frac{k_t \cdot \delta}{l} \tag{6.10}$$

The magnitude of the force on points A and B is expressed in equation 6.10, where l is the length of line segment AB and k_t is the torsion spring constant. The forward Euler method of integration, as described for linear spring forces, over an incremental time step of Δt is implemented for the calculation of updated point position due to torsional spring force ($\vec{f_t}$). For a line segment formed by joining the grid point in consideration (A) to its neighboring point (B) ($\overrightarrow{AB}$ in Fig. 6.5), represented by the unit vector $\hat{l}$, two possibilities determine the direction of torsional force. First, as shown in Fig. 6.6(a) and (d), point A must be pulled inwards towards the center O. This turns $\overrightarrow{AB}$ counter-clockwise for Fig. 6.6(a) and clockwise for Fig. 6.6(d), thereby achieving the desired orientation $\overrightarrow{CD}$. Second, as shown in Fig. 6.6(b) and (c), point A must be pushed outwards away from the center O. This turns $\overrightarrow{AB}$ clockwise for Fig. 6.6(b) and counter-clockwise for Fig. 6.6(c) thereby achieving the desired orientation $\overrightarrow{CD}$. The unit vector $\hat{d}$, defined at point A, represents the direction of pull/ push (toward and away) relative to point O. Therefore, additional force in $\hat{d}$ direction is added to equation 6.5 for aligning the grid towards a center point. The force on a point due to a neighboring point on the same contour is given by.

$$\vec{f_l}(l, l_0, \delta) = \begin{cases} -k(l_0 - l)\,\hat{l} + \dfrac{k_t \cdot \delta}{l}\,\hat{d}, & \text{if} \quad (l < l_0) \\ 0\,\hat{l} + \dfrac{k_t \cdot \delta}{l}\,\hat{d}, & \text{if} \quad (l > l_0) \end{cases} \tag{6.11}$$

Table 6.2 outlines the algorithm for obtaining the magnitude and the direction of the torsional spring force.

Table 6.2: Algorithm for generation of a circular grid using conditions of force balance

```
while (True):
  If convergence criteria == True:
      Break
    Else
  for all $'P'$ within contour
    1. Consider a grid point (say) $A_i(x_{A_i}, y_{A_i})$: $A_i \in P$, where $P = [x \quad y]_{n\times 2}$
    2. Define vector $\vec{F_i}$ such that $\vec{F_i} \in \vec{F}$, where $\vec{F_i}$ is the net force on a point $A_i$ due to all springs attached to it
    3. Get $\xi_{Ai}$ the closest point on boundary($\Gamma$) to point $A_i$
          If   $l = distance(A_i, \xi_{Ai}\ ) < d_{min}$:
               Compute $\vec{f}_{Boundary}(l, l_0)_{A_i}$ on $A_i$ due to $\xi_{Ai}$
               Update $\vec{F_i} = \vec{F_i} + \vec{f}_{Boundary}(l, l_0)_{A_i \xi_{Ai}}$
    for all $'B_i'$ within B
    4. Identify a vector $(\overrightarrow{A_i B_i})$ between $A_i$ and the neighboring grid point (say)$B_i(x_{B_i}, y_{B_i})$: $B_i \in B$ and $B \subset P$ where $B = [x_{B_i} \quad y_{B_i}]_{m\times 2}$. $'m'$ is the number of points connected to $A_i$, as a result of DT. The direction of $\overrightarrow{A_i B_i}$ is denoted by a unit vector (say) $\hat{l}$.
    5. Repeat step 5 of Table 1 for calculating and storing $\vec{f}_{Linear}(l, l_0)_{A_i B_i}$ on $A_i$ due to $B_i$ as a result of the rectangular grid into the vector $\vec{F}$. Take $\hat{v}$ as $\overrightarrow{A_i O}$
    6. Define $\hat{r} = \frac{\overrightarrow{OM}}{|\overrightarrow{OM}|}$, where $M = \left[\frac{(x_{A_i}+x_{B_i})}{2}, \frac{(y_{A_i}+y_{B_i})}{2}\right]$ and $\theta$ as $\cos^{-1}(\hat{r}\cdot\hat{l})$
    7. Define $\delta$, such that $\delta = \theta - 90°$
       if $|\delta| < \delta_c$

       Define $\hat{l'}: \hat{l}\cdot\hat{l'} = 0$ and $\hat{z}: \hat{z} = \hat{l}\times\hat{l'}$ and $\hat{z} > 0$

       Define $C_1 = sign(\delta)$ and $C_2 = sign\ (\hat{r}\cdot\hat{l'})$
       (sign function outputs 1 if $(\delta) > 0$ and outputs $-1$ if $(\delta) < 0$)

       $N$ = input $[C_1 \quad C_2]$
           switch $N$
              case $[-1 \quad 1]$
                  $\hat{d} = \hat{l}$       // Force on $A$ towards $O$, shown in Fig. 6.5(a)
              case $[1 \quad 1]$
                  $\hat{d} = -\hat{l}$      // Force on $A$ away from $O$, shown in Fig. 6.5(b)
              case $[1 \quad -1]$
                  $\hat{d} = \hat{l}$       // Force on $A$ away from $O$, shown in Fig. 6.5(c)
              case $[-1 \quad -1]$
                  $\hat{d} = -\hat{l}$      // Force on $A$ towards $O$, shown in Fig. 6.5(d)
            Compute $\vec{f}_{Torsional}(l, l_0)_{A_i B_i}$ on $A_i$ due to $B_i$ as a result of torsional spring

            Update $\vec{F_i} = \vec{F_i} + \vec{f}_{Torsional}(l, l_0)_{A_i B_i}$
    8. Update point coordinates of $P$ to $P' = [x' \quad y']_{m\times 2}$ such that $P' = P + \Delta t\vec{F}$.
9. Run TSP solver on $P' = [x' \quad y']_{m\times 2}$
```

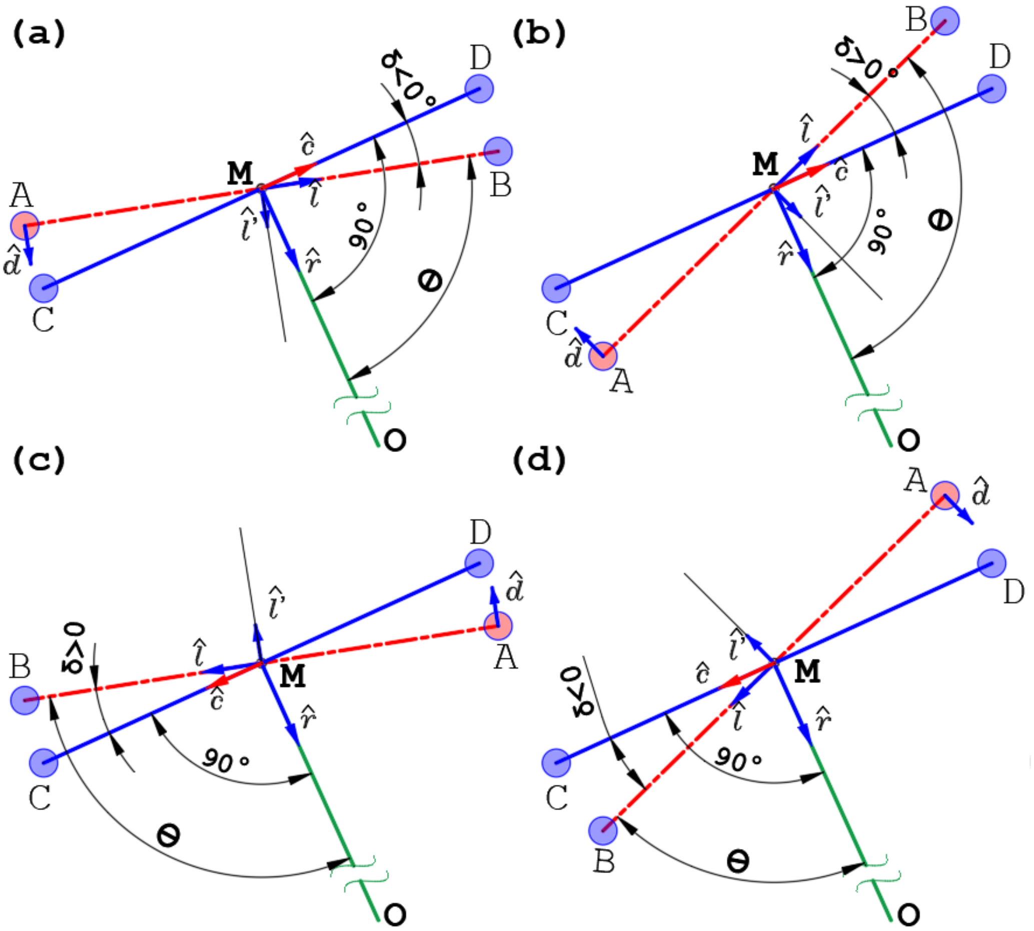

Fig. 6.6: Method of sorting possible configurations of current grid points relative to their desired configuration for determining the direction of application of force on the 'point in consideration' (a)$\delta < 0 \,\&\, \hat{r} \cdot \widehat{l'} > 0$ (b) $\delta > 0 \,\&\, \hat{r} \cdot \widehat{l'} > 0$ (c) $\delta > 0 \,\&\, \hat{r} \cdot \widehat{l'} < 0$ and (d) $\delta < 0 \,\&\, \hat{r} \cdot \widehat{l'} < 0$

6.1.3 Generation of an Adaptive Grid

Adaptive grid results in an area-filling toolpath that mimics the contour boundary. This toolpath can be considered more or less a continuous equivalent of the common contour-parallel or contour offset infill. Implementing a TSP-based solver to generate such toolpaths results in minimal lifts with a common start-end point, thus more advantageous over similar area-filling strategies. Furthermore, as proposed here, a force-based digitization algorithm offers an added ability to fabricate parts with graded density while maintaining a general contour-adaptive property.

In most aspects, the generation of the adaptive grid follows the same algorithm as that of the circular grid. The deviation in the algorithm from circular to adaptive emerges from the implementation of a grid-point-specific track center (O_n). As discussed in section 6.1.2, for a circular grid, the radial direction ($\hat{r}$) corresponds to the fixed user-defined track center (O).

However, for the adaptive grid, the radial direction ($\hat{r}$) varies in accordance with the 'current' grid point in consideration. The track center (O_n) for the current grid point (A) corresponds to the nearest point on the contour (C) to the midpoint of the line joining circular grid points pair, as illustrated in Fig. 6.7. Consequently, as the algorithm loops through every grid point (updating A), the track center updates, thus updating the radial vector ($\hat{r}$). This forces the resulting array of grid points to be conformal to the outer contour (C).

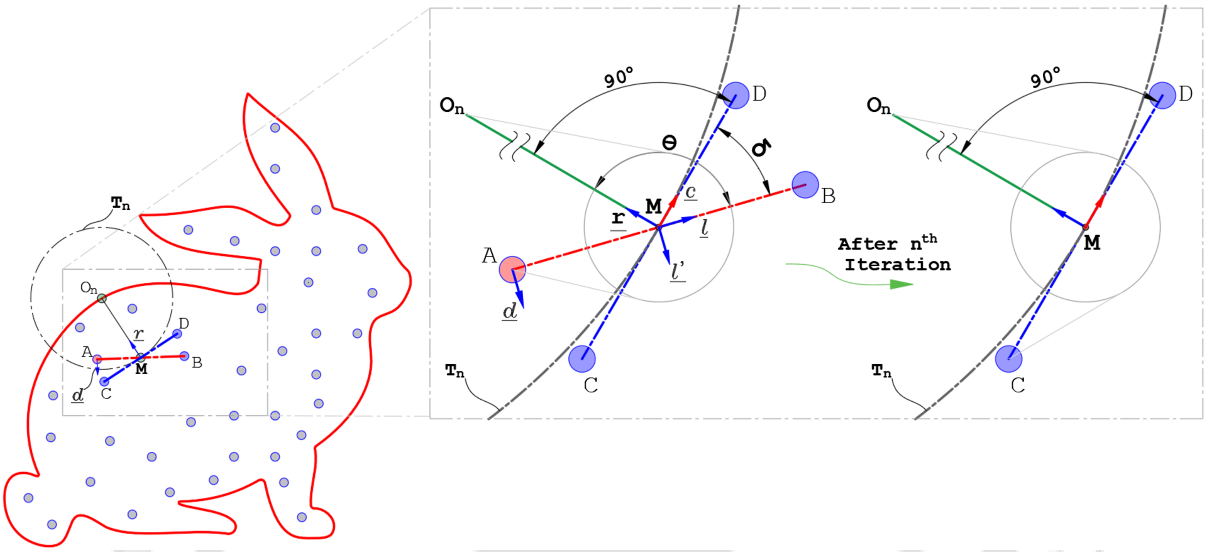

Fig. 6.7: Generation of contour adaptive grid through the selection of grid-point-specific track center

It can be observed that as the grid point in consideration (A) changes, the basis vectors ($\hat{l}$, $\hat{\emptyset}$, and $\hat{R}$) update themselves, thus resulting in an adaptive grid. The following Table 6.3 highlights the key aspects of the implemented algorithm.

Table 6.3: Algorithm for generation of a contour-adaptive grid using conditions of force balance

```
while (True):
  If convergence criteria == True:
     Break
  Else:
   for all $'P'$ within contour
   1. Consider a grid point (say) $A_i(x_{A_i}, y_{A_i})$: $A_i \in P$, where $P = [x \quad y]_{n\times 2}$
   2. Define vector $\vec{F_i}$ such that $\vec{F_i} \in \vec{F}$, where $\vec{F_i}$ is the net force on a point $A_i$ due to all springs attached to it
   3. Get $\xi_{Ai}$ the closest point on boundary($\Gamma$) to point $A_i$
         If $l = distance(A_i, \xi_{Ai}) < d_{min}$:
            Compute $\vec{f}_{Boundary}(l, l_0)_{A_i}$ on $A_i$ due to $\xi_{Ai}$
            Update $F_i = F_i + \vec{f}_{Boundary}(l, l_0)_{A_i \xi_{Ai}}$
   for all $'B_i'$ within B
   4. Identify a vector $(\overrightarrow{A_i B_i})$ between $A_i$ and the neighboring grid point (say)$B_i(x_{B_i}, y_{B_i})$: $B_i \in B$ and $B \subset P$ where $B = [x_{B_i} \quad y_{B_i}]_{m\times 2}$. $'m'$ is the number of neighboring points connected to $A_i$, as a result of DT. The direction of $\overrightarrow{A_i B_i}$ is denoted by a unit vector (say) $\hat{l}$.
   5. Take $\xi_{Ai}$ as the center point $O$
   6. Repeat step 5 of Table 1 for calculating and storing $\vec{f}_{Linear}(l, l_0)_{A_i B_i}$ on $A_i$ due to $B_i$ as a result of the rectangular grid into the vector $\vec{F}$. Take $\hat{v}$ as $\overrightarrow{A_i O}$
   7. Repeat steps 7 of Table 2 for calculating and storing $\vec{f}_{Torsional}(l, l_0)_{A_i B_i}$ on $A_i$ due to $B_i$ as a result of the circular grid into vector $\vec{F}$.
 8. Run TSP solver on $P' = [x' \quad y']_{m\times 2}$
```

6.2 Add/ Delete Points

The array of grid points within a contour can have either an initial user-defined unstructured or a structured configuration. The unstructured configuration implies a random fixed collection of points, whereas a set of grid points following a rectangular, circular, or hexagonal motif is termed a structured configuration. Irrespective of the starting configuration, upon implementation of a force-based algorithm to obtain a structured configuration, the digitization of the space may be non-uniform. The non-uniformity primarily results from a fixed number of grid points transforming from one configuration to the other, leaving either voids or overcrowding of the grid points. Figure 6.8 shows a rectangular array of grid points transforming into a circular array of non-uniform 'local' density.

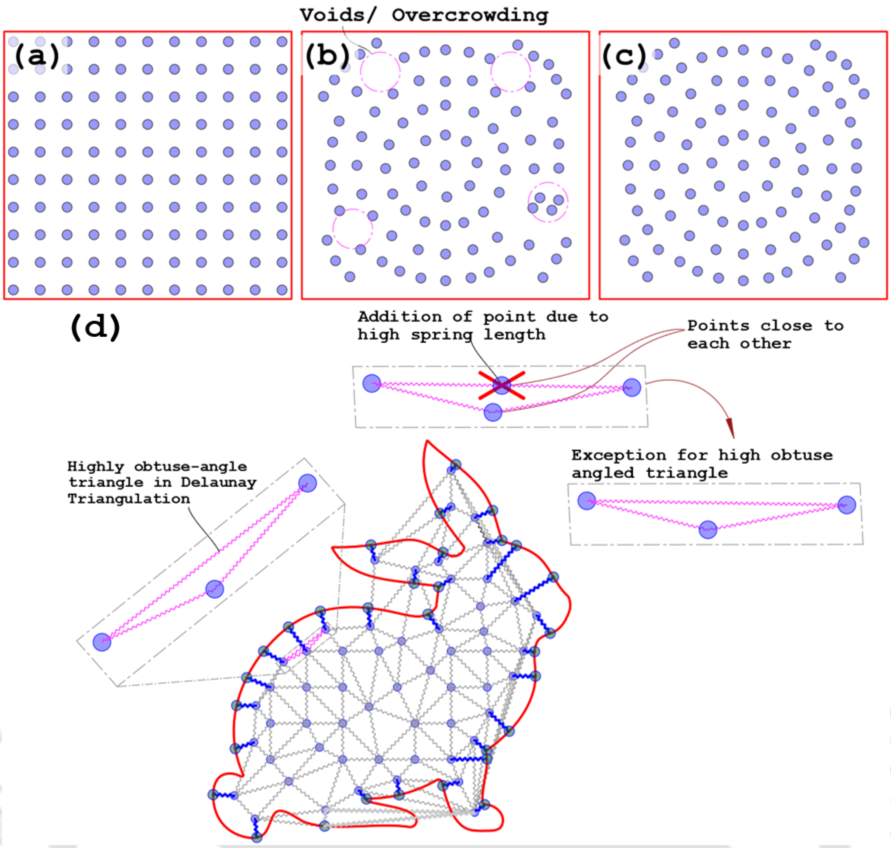

Fig. 6.8: (a)Rectangular input grid transforming into a circular grid may lead to (b) voids or overcrowding, (c) uniformity of grid points achieved through add/ delete point criteria, and (d) exception for the boundary case for the add/ delete criteria

The algorithm implements a check on the spring length (l) after every n^{th} iteration (user-defined). If the spring length exceeds 1.3 times its own value, in the subsequent iteration, a new grid point is added at its center. Conversely, a reduction in spring length below $0.6S$, deletes a point from the spring pair in the subsequent iteration.

An exception has to be made for the grid point lying immediately adjacent to the boundary, which, when triangulated, may produce highly obtuse triangles, as shown in Fig. 6.8(d). In such cases, an additional point on the side opposite to the obtuse angle will result in the newly added point being very close to the point associated with the obtuse angle. Thus, an additional constraint is enforced on the grid points neighboring the boundary, i.e., for highly obtuse-angled ($> 160°$) triangles, no consideration is made for adding the grid points.

6.3 Direction Favouring Toolpath

Direction favoring is a unique aspect of the proposed toolpath, wherein the deposition direction (or scanning) can be biased by prioritizing one travel direction over another, as shown in Fig. 6.11. This is achieved through control variables α and β. Each of the three digitization methods, i.e., rectangular, circular, and adaptive, through appropriate selection of control variables, can be designed so that the number of points along a given basis vector is more than its orthogonal counterpart. Consider Fig. 6.9 (a); a unit cell ($S = 1$) is placed at the point of consideration A, and the space within the unit cell is categorized into regions of side and diagonal points, represented with white and grey regions, respectively, as discussed in section 6.1.1. These regions are quantified through angles ν_1 and ν_2. The control variables α and β are associated with $\hat{v}$ and $\widehat{v'}$ directions of travel, respectively. A value of (say) 0.5 for α allows for a direction favoring in $\hat{v}$ by essentially reducing the stepover from S to ${}^{S}/_{2}$ along $\hat{v}$, as shown in Fig. 6.9(b). Conversely, a value of (say) 0.5 for β allows for direction favoring in $\widehat{v'}$, as shown in Fig. 6.9(c).

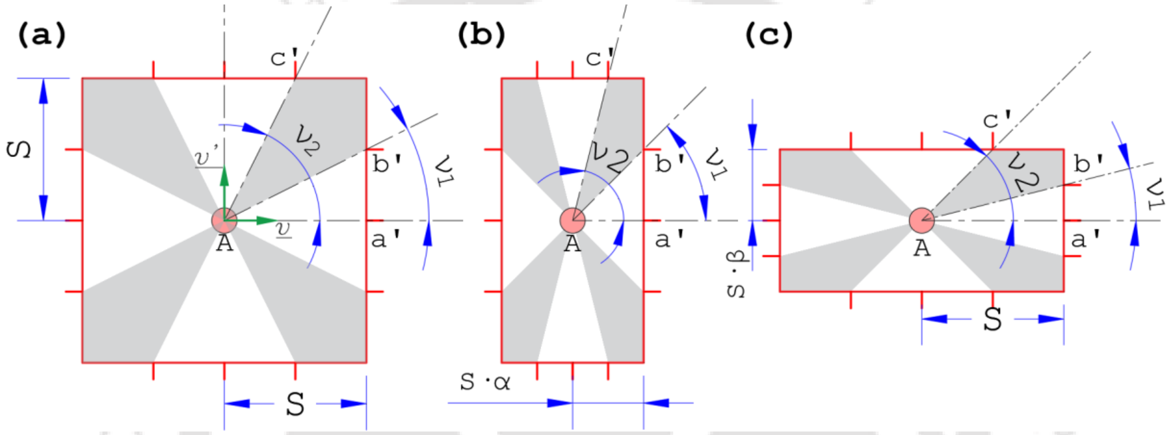

Fig. 6.9: (a) Equal stepover in all directions for a non-direction-favoring toolpath, (b) reduced stepover along (b) cell length for horizontal, and (c) cell width for vertical direction favoring

However, introducing these control variables to alter the unit cell changes the span of grey and white regions; thus, the angles ν_1 and ν_2 must be updated accordingly. Equation 6.12 expresses the updated angles ν_1 and ν_2 in terms of control variables α and β relative to an altered unit cell with unequal stepover values.

$$\nu_1 \rightarrow \tan^{-1}\left(\frac{\beta}{\alpha}\tan\nu_1\right) \text{ and } \nu_2 \rightarrow \tan^{-1}\left(\frac{\beta}{\alpha}\tan\nu_2\right) \tag{6.12}$$

The conditional statement for a point to be considered a diagonal point in the unit cell, as expressed in equation 6.4, is updated through equation 6.12 to accommodate the control variables for grid favoring. It is to be noted that the spring lengths corresponding to $\hat{v}$, $\widehat{v'}$, and the diagonal points are multiplied by α, β and $\sqrt{\alpha^2 + \beta^2}$, respectively.

A similar approach can be implemented for the case of circular and adaptive grids, wherein the control variables α and β are associated with azimuth ($\hat{\phi}$) and radial ($\hat{R}$) directions, respectively.

Figure 6.10 shows the digitized contour where the grid points are biased in either of the basis directions.

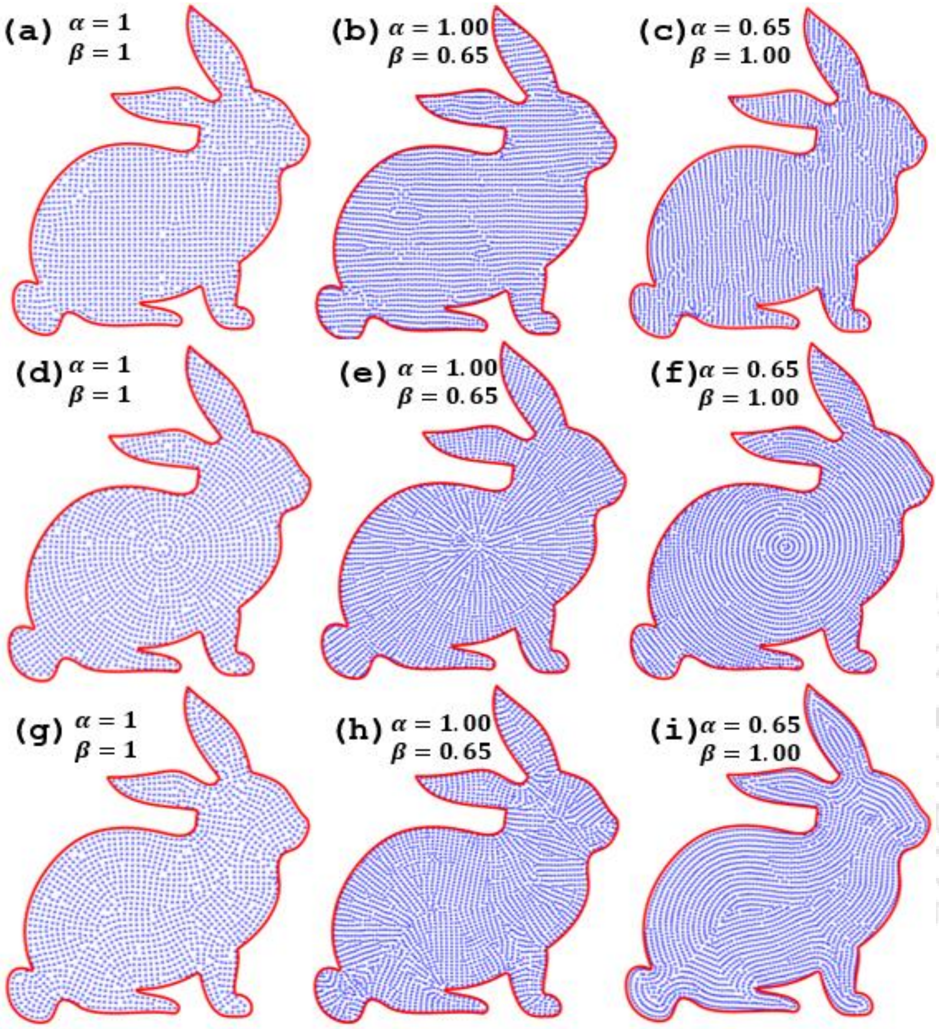

Fig. 6.10: Digitized space within the contour corresponding to (a) rectangular no favoring, (b) rectangular horizontal, (c) rectangular vertical, (d) circular no favoring, (e) circular-radial, (f) circular-azimuthal, (g) adaptive no favoring, (h) contour-orthogonal, and (f) contour-parallel favoring

An advantage of the direction-favoring property of the proposed toolpath strategy is its ability to reduce the number of turns (N) in a toolpath, as is evident from Fig. 6.11. A reduction in the number of turns is often associated with uniformity of material deposition as a consequence of the 'jerk-free' motion of the travel head, especially observed at the corners (or sharp turns) of a toolpath.

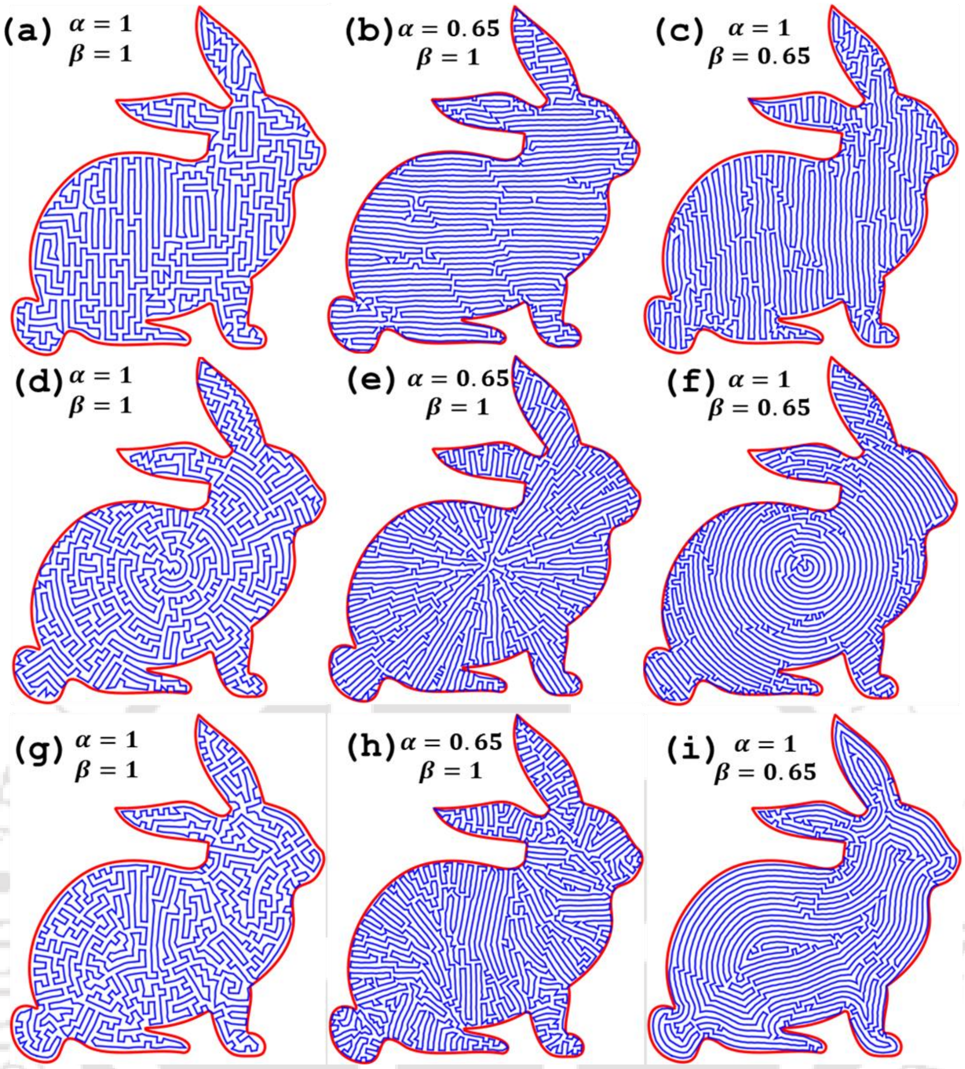

Fig. 6.11: TSP-based toolpath for (a) rectangular no favoring ($N = 720$), (b) rectangular horizontal($N = 532$), (c) rectangular vertical($N = 601$), (d) circular no favoring($N = 832$), (e) circular-radial($N = 781$), (f) circular-azimuthal($N = 647$), (g) adaptive no favoring($N = 926$), (h) contour-orthogonal($N = 829$), and (f) contour-parallel favoring ($N = 446$)

6.4 Toolpath for Gradient Density

In the discussions so far, the optimal length of the spring l_0, as described in section 6.1.1, is constant irrespective of the location of the grid point within the contour. This, upon implementation of the force-based algorithm, results in digitized space with uniform density of the grid points. A gradient in density can be achieved by varying l_0 (consequently stepover s) as a function of 2D space within the contour ($\mathbb{R}^2$). The input arguments for a gradient density are; a governing density function $d(\mathbb{R}^2)$ and an initial stepover value (s). The initial stepover value is specified by the user and corresponds to l_0 at maximum density. The density function $d(\mathbb{R}^2)$ outputs a range of $(0, 1]$, with lower and upper limits corresponding to minimum and maximum relative densities, respectively. Thus, the density function $d(\mathbb{R}^2)$ acts as a scaling factor to the initial stepover s to output spring length l_0, expressed through equation 6.13.

$$l_0(\mathbb{R}^2) = \frac{s}{d(\mathbb{R}^2)} \tag{6.13}$$

Figure 6.12 shows illustrative examples of gradient toolpaths for rectangular, circular, and adaptive digitizations with and without direction favoring. The gradient in the toolpath (for $s = 1$) is expressed through equation 6.14

$$d(x) = 1 - \left({}^{0.5x}/_{100}\right) \tag{6.14}$$

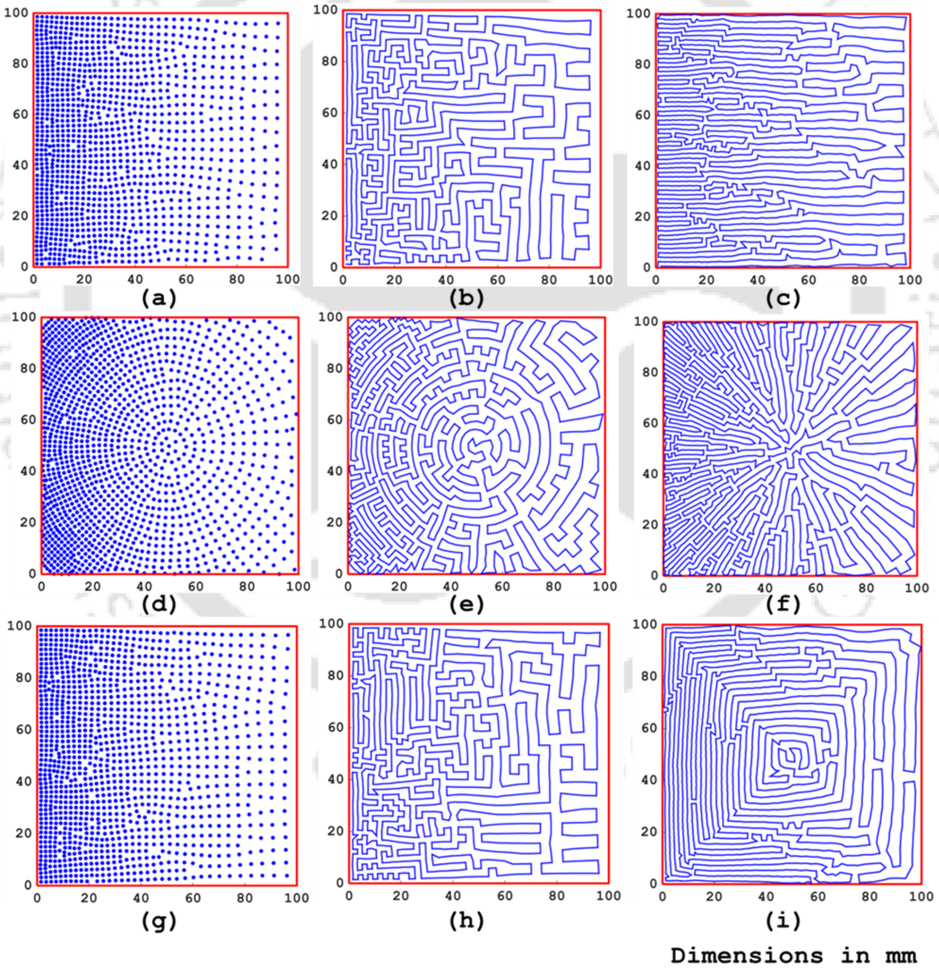

Fig. 6.12: Digitization with gradient toolpath for (a-b) rectangular grid, (c) rectangular-horizontal biased, (d-e) circular grid, (f) circular-radial biased, (g-h) adaptive, and (i) adaptive contour parallel toolpaths

6.4.1 Density-based Digitization from Image

The digitization of the domain within the contour can also be achieved through an image-based density map. The gradient in the toolpath corresponds to the image intensity of the user-input grayscale image. Consider, for example, Fig. 6.13; the white and the dark regions of the density map corresponding to the maximum and minimum material densities, respectively. In order to establish the gradient of digitization, the input image maps to the part density, where the regions with the smallest and highest intensity values correspond to the minimum and maximum part densities, respectively. The boundaries of the input image can also be extracted through 'thresholding,' where the user sets the upper and lower bounds of the grayscale image. The 'gray level' above and below the upper and the lower bounds is set to one and zero, respectively. The grid points can acquire one of three configurations, rectangular, circular, or adaptive (as outlined in sections 6.1.1, 6.1.2, and 6.1.3) while preserving the density distribution as dictated by the density map. Furthermore, the direction-favoring method, as outlined in section 6.3, can be applied to bias the toolpath in one or the other direction.

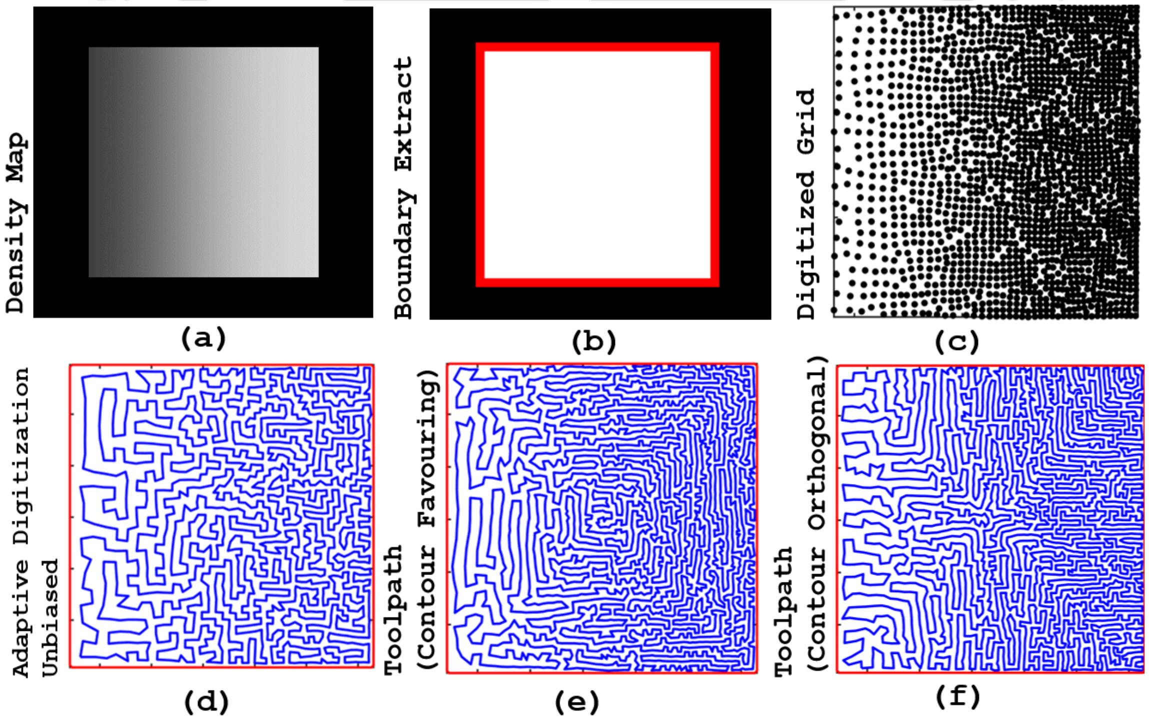

Fig. 6.13: Density gradation of toolpath prescribed by the user-input density map

6.5 Convergence Criteria

A limit on the movement of the grid points corresponding to the spring forces is used to prevent an infinite loop in the algorithm. The stopping criteria can be set by the user, or the program terminates with default values if no input is received. The grid points can be monitored for the following.

1. The maximum value of movement for a given grid point in each iteration.
2. The average movement of the collective digitized grid in each iteration.
3. Number of iterations.

Another method that produces minimal noise in the convergence graph is to monitor the rolling average of the grid movement for a given iteration. For instance, if the change in the average movement of the grid points in the current iteration is less than a preset value of the previous iteration, then convergence is said to be achieved. The user can also interrupt the iterations upon qualitative inspection of the digitized grid point after a specific number of iterations.

6.6 Results and Discussion

The proposed toolpath was implemented on an FFF-based 3D printer, and each of the digitization methods was explored. The image-based and quantitative analysis of the toolpath was performed to establish the conformance of the toolpath to the input function.

6.6.1 Toolpath Length

Consider a square contour with the gradient toolpath, as shown in Fig. 6.14. The input function varies linearly in positive $'x'$ direction and is expressed as: $d(x) = 1 - \left({}^{0.5x}/_{50}\right)$. The density function implies a fully dense part at the extreme left ($d(0) = 1$) and a 50 percent infill at the extreme right ($d(50) = 0.5$). In order to establish the validity of the variation, the generated toolpath is sectioned into 20 discrete segments (or blocks) along the positive $'x'$ direction. The length of the toolpath contained within each segment is measured and is shown in Fig. 6.14(a). This process is repeated for every category of digitization (rectangular, circular, and adaptive) with and without direction favoring (for the sake of brevity, Fig. 6.14(a)outlines the processes for rectangular toolpath without direction favoring only). Considering a unit bead width, the toolpath length for each category of digitization is normalized by the maximum value to obtain relative part density. The maximum deviation from the intended part density occurs on the far right of the square contour, as is evident from Fig. 6.14(b-c). However, globally speaking, the part density follows the same trend as the input function. The toolpath was obtained after 150 iterations.

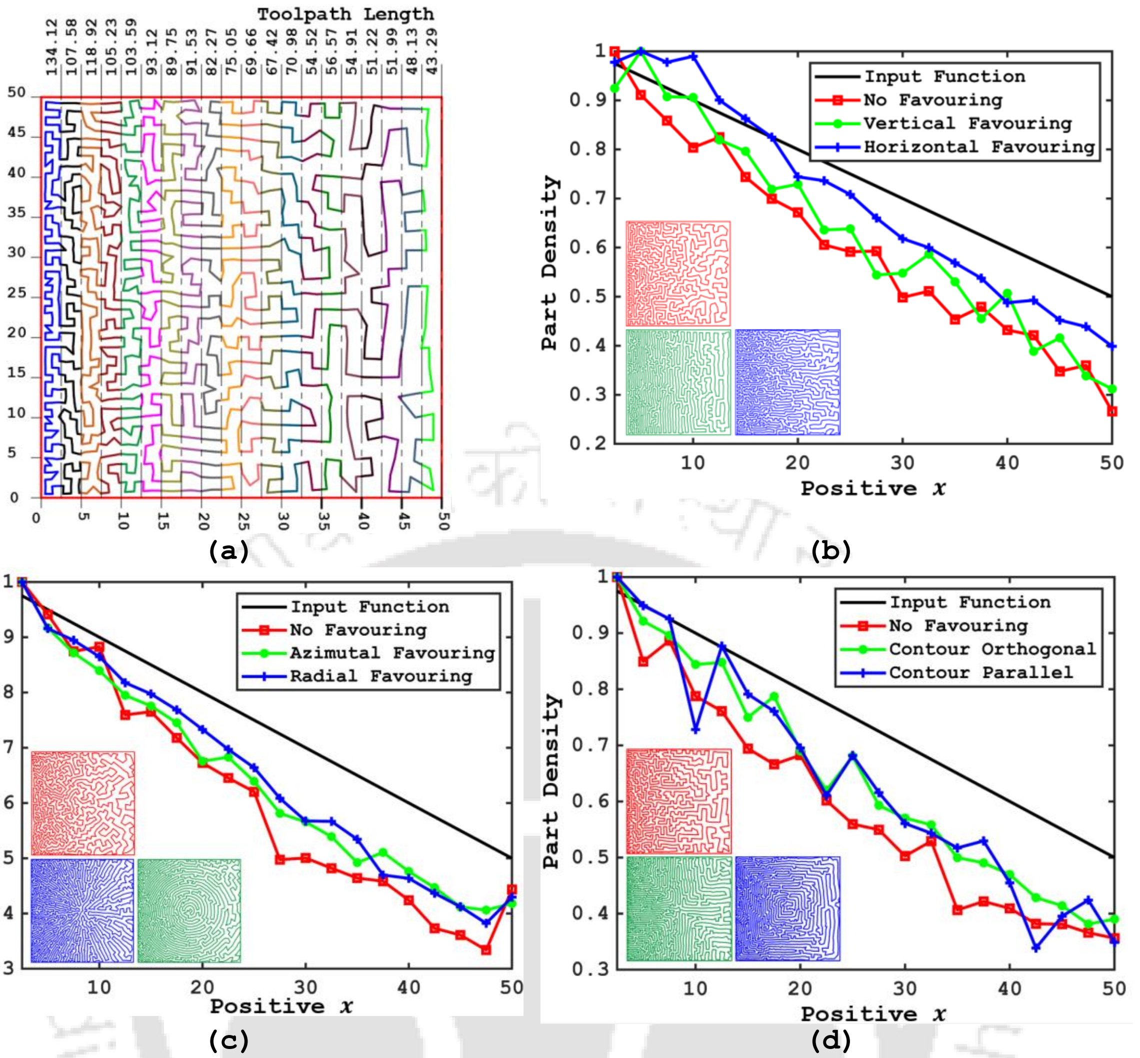

Fig. 6.14: (a)Process of segmenting toolpaths into blocks and relative part density obtained (after 150 iterations) for the case of (a) rectangular, (b) circular, and (c) adaptive digitized grids

Another observation made for the case of toolpath length within each segment suggests that irrespective of the method of digitization, the toolpath length for non-favoring cases is lower than the direction-favoring counterpart, as illustrated in Fig. 6.15. This can be primarily attributed to the additional grid points introduced during digitization leading to a higher toolpath length.

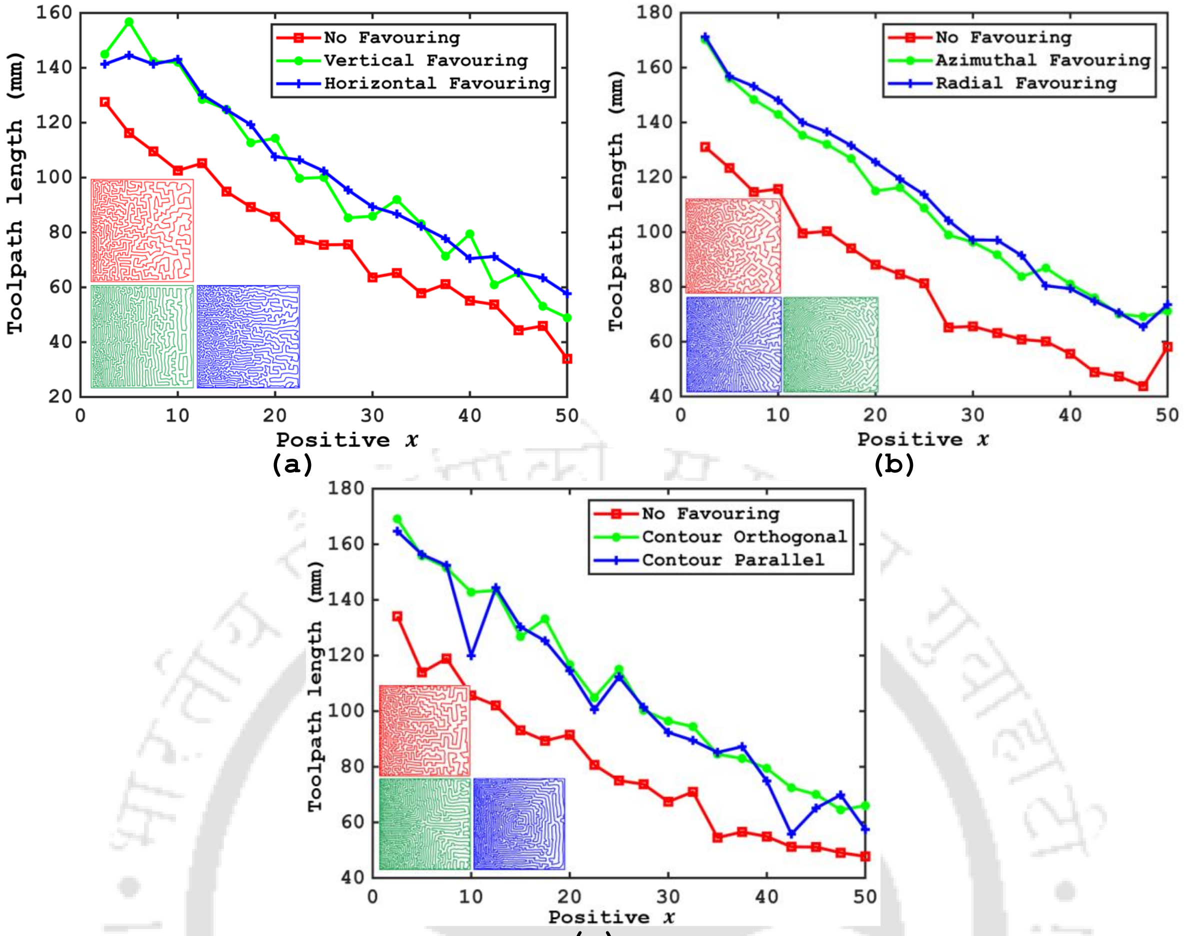

(a) (b) (c)

Fig. 6.15: Toolpath length observed within each segment for (a)rectangular, (b)circular, and (c) adaptive methods of digitization

6.6.2 Image-based Gradation Analysis

In this method, the spatially graded toolpath is first saved as a grayscale image with a specified resolution, where the image intensity varies from zero to 255. This image is further processed using a block mean method. The intensity values in the grayscale image contain, say r and c number of rows and columns, respectively, where each element of the matrix holds an intensity value of the pixel at that location. This intensity matrix is sectioned into smaller sub-matrices or bins with a user-specified number of rows (r_{avg}) and columns(c_{avg}). The elements in the intensity matrix are then replaced by the average values of these sub-matrices. The resulting matrix, termed the 'block mean' matrix, represents the variation in global part density as a collection of a specified number of bins. Furthermore, the elements of the block mean matrix are normalized with maximum value to arrive at the relative part density, varying between zero and one. Fig. 6.16 shows an illustrative example, where Fig. 6.16(a) shows the gradient toolpath, and Fig. 6.16(b) is its grayscale image of size $r = 106$Px and $c = 1663$Px. A bin, marked yellow in Fig. 6.16(c), labeled as $'a'$ of size

$r_{avg} = 53$Px and $c_{avg} = 54$Px, represents the domain over which the intensity values are averaged to obtain Fig. 6.16(d). Thus, for Fig. 6.16(d), a collection of uniform intensity bins, two along the width and thirty along the length, represents the global variation in density along the toolpath. Furthermore, a selection of even smaller bin sizes, Fig. 6.16(e-g), would produce a sharper distinction of the toolpath with the space that it fills. Figure 6.17 shows the case for uniform infill, where each of the three digitization categories produced fully dense toolpaths with a stepover of 0.4 mm.

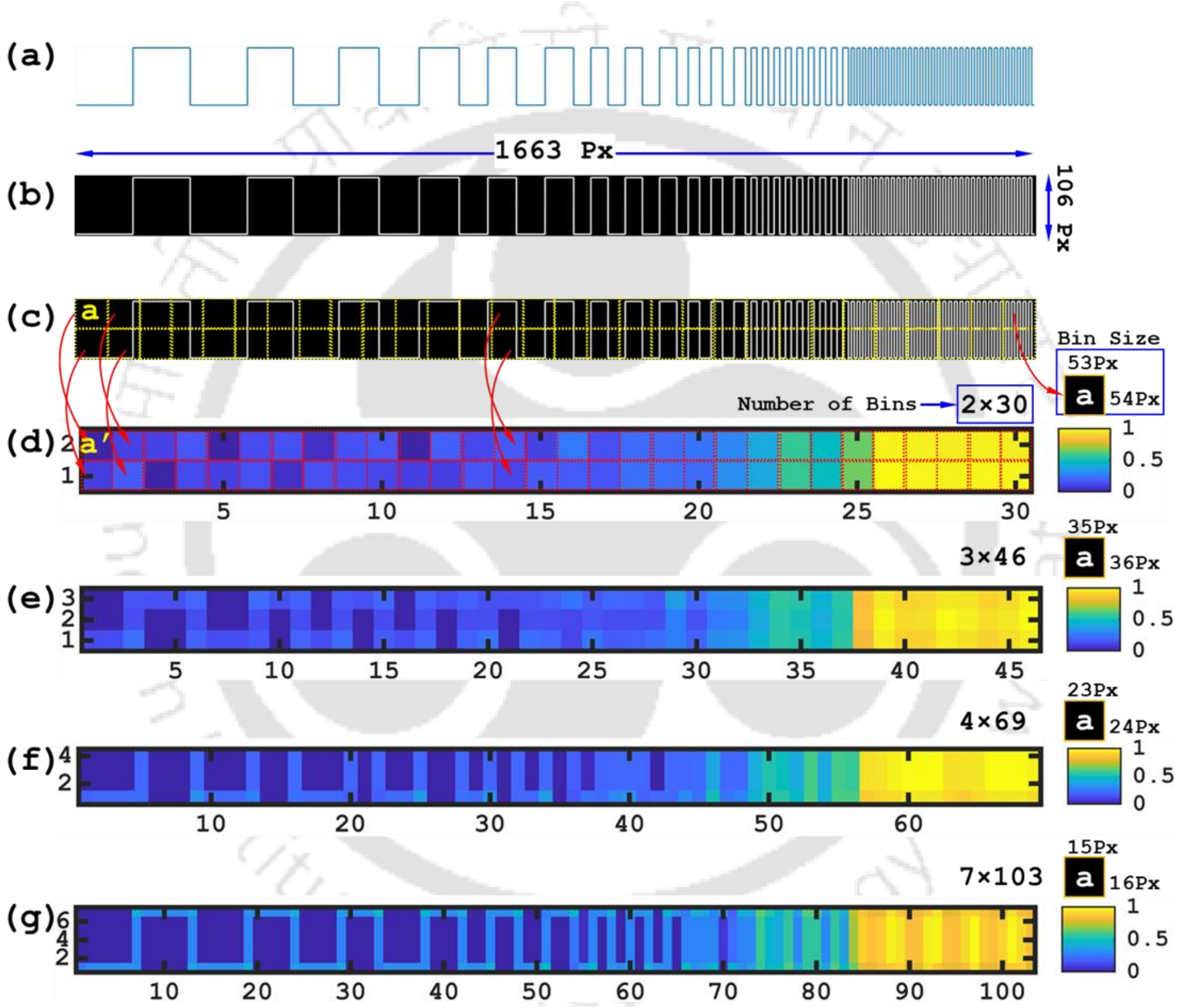

Fig. 6.16: (a) Example toolpath (b) grayscale image of the toolpath (c) bin size over which averaging is carried out for (d), and representation of variation in density as a collection of (e)138, (f) 276, (g) 721 bins

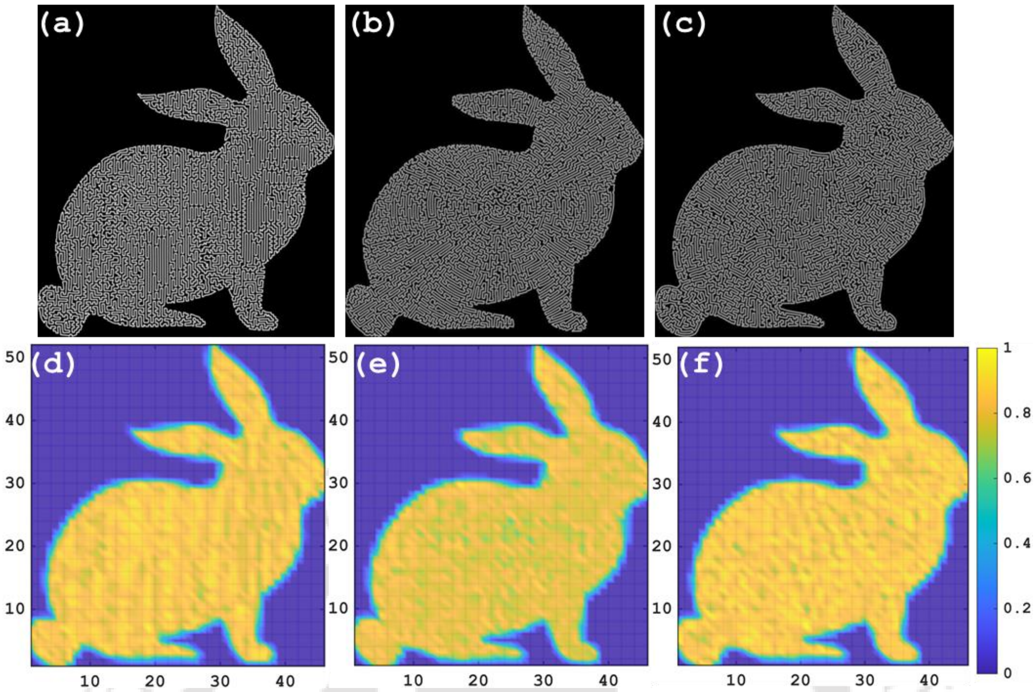

Fig. 6.17: (a-c)Grayscale image of uniform density toolpaths (obtained after 350 iterations) and their (d-f) corresponding density distribution for (a) and (d) rectangular, (b) and (e) circular, and (c) and (f) adaptive grid

A graded toolpath, with an input function given by equation 6.15, was also fabricated. Figure 6.18 shows the ideal gradation to be generated by equation 6.15 within the contour bounds.

$$d(x,y) = \frac{1}{\sqrt{2\pi}} e^{\frac{1}{2}\left(\left(\frac{(x-25)}{18}\right)^2 - \left(\frac{(y-21)}{18}\right)^2\right)*2.5} \tag{6.15}$$

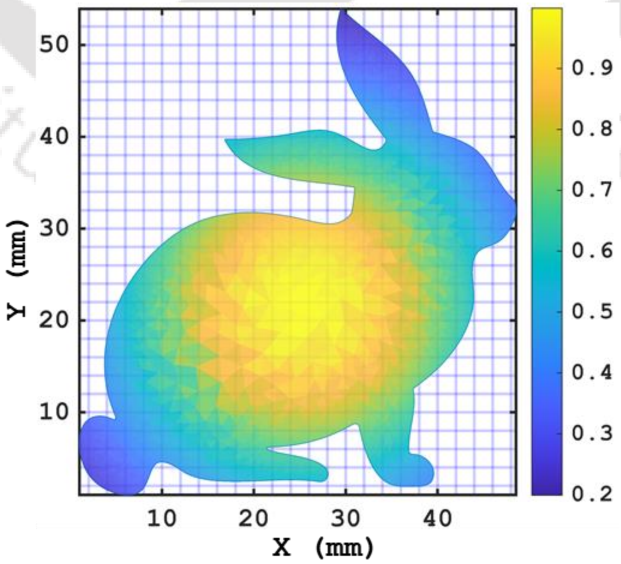

Fig. 6.18: Ideal density gradient within the contour, corresponding to the input function expressed through equation 6.15

Figure 6.19 shows the grayscale image of the toolpaths corresponding to equation 6.15 for each of the three proposed toolpath varieties, i.e., rectangular, circular, and adaptive with and without direction favoring. The intensity distribution of the toolpaths, as shown in Fig. 6.20, further suggests that the proposed algorithm closely follows the density gradation as specified by the input function. The direction-favoring aspect of the proposed toolpath, as outlined in section 6.3, preserves the user-specified density gradation. These toolpaths were also implemented on an FFF-based 3D printer; the results are shown in Fig. 6.21. In the case of directional toolpaths, within each category, the image shows a more tightly packed infill as compared to their non-direction-favoring counterparts. This observation is also reflected in the observed weights of the printed parts, as shown in Table 6.4.

Table 6.4: Weight of printed parts for each category of digitization

Toopath	Weight (g)
Rectangular (No favoring)	3.95
Rectangular (Horizontal favoring)	5.75
Rectangular (Vertical favoring)	5.59
Circular (No favoring)	4.69
Circular (Radial favoring)	5.96
Circular (Azimuthal favoring)	5.76
Adaptive (No favoring)	4.65
Adaptive (Contour orthogonal)	6.07
Adaptive (Contour parallel)	5.70

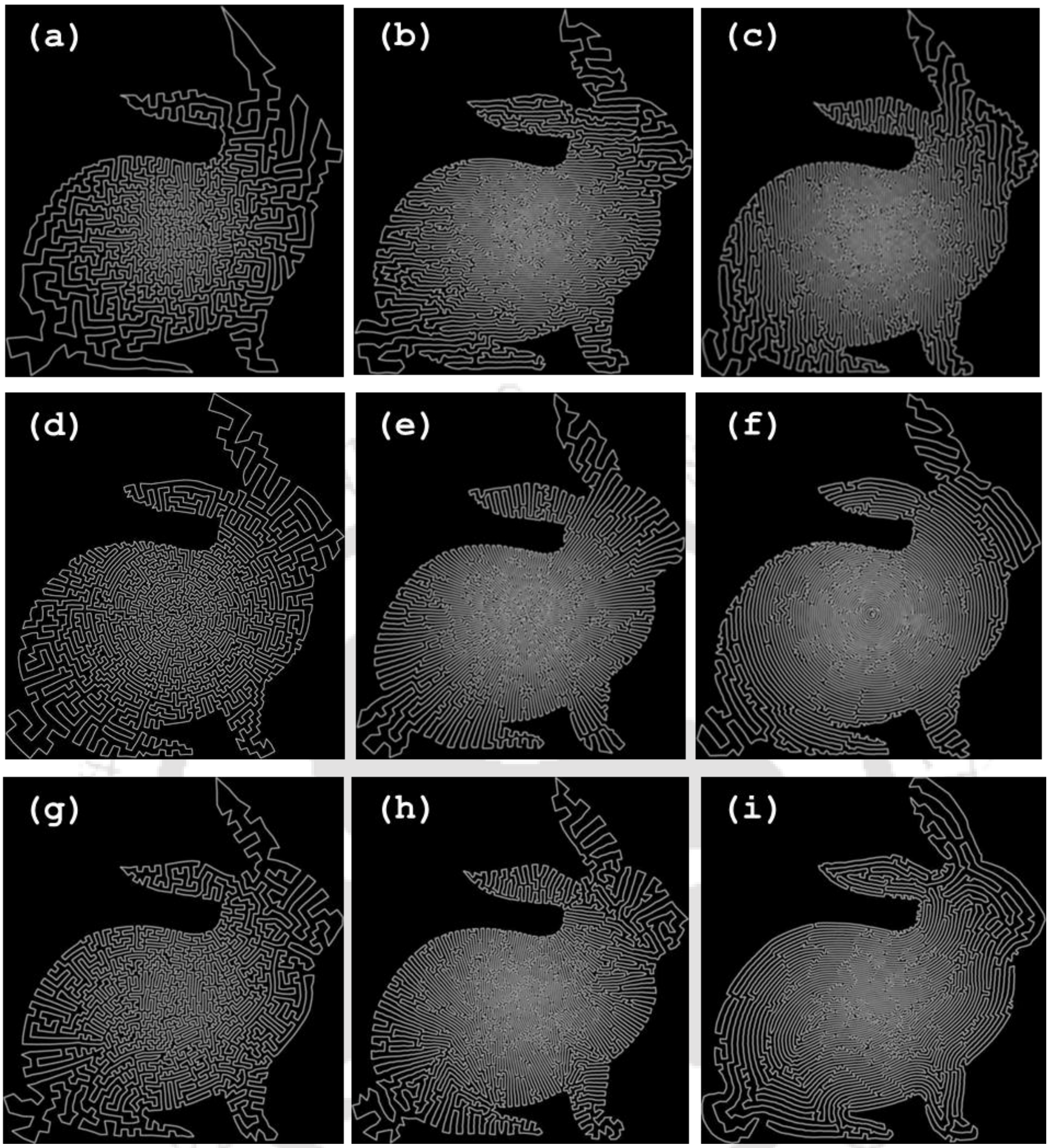

Fig. 6.19: Grayscale image of the graded-density toolpath following equation 6.15 for rectangular toolpath with (a) no direction favoring, (b) horizontal favoring, (c) vertical favoring; circular toolpath with (d) no direction favoring, (e) radial favoring, (f) azimuthal favoring, and adaptive toolpath with (g) no direction favoring, (h)contour-orthogonal, and (i) contour-parallel direction favoring

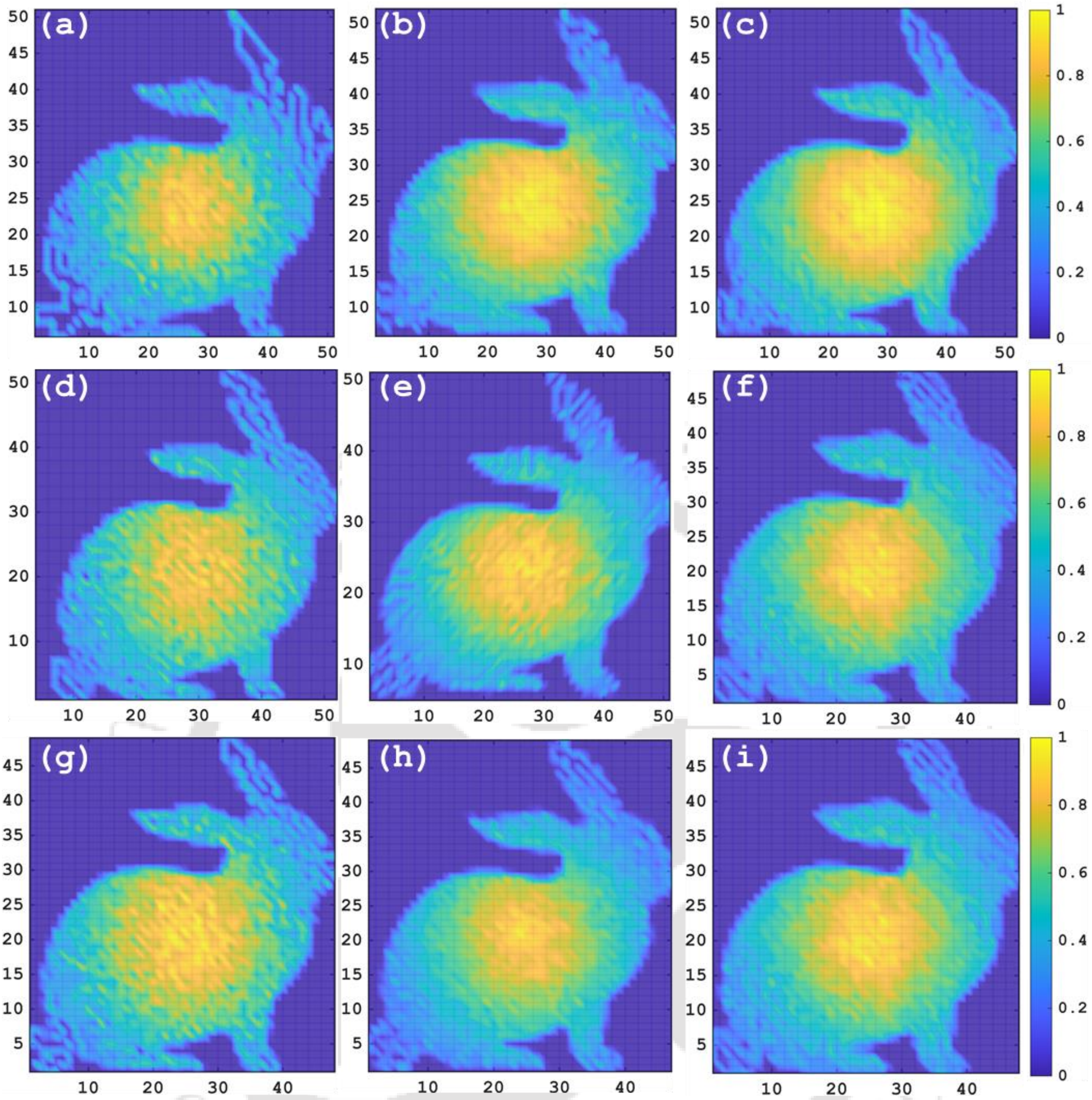

Fig. 6.20: Density distribution of the graded toolpath following equation 6.15 for rectangular toolpath with (a) no direction favoring, (b) horizontal favoring, (c) vertical favoring; circular toolpath with (d) no direction favoring, (e) radial favoring, (f) azimuthal favoring, and adaptive toolpath with (g) no direction favoring, (h)contour-orthogonal, and (i) contour-parallel direction favoring

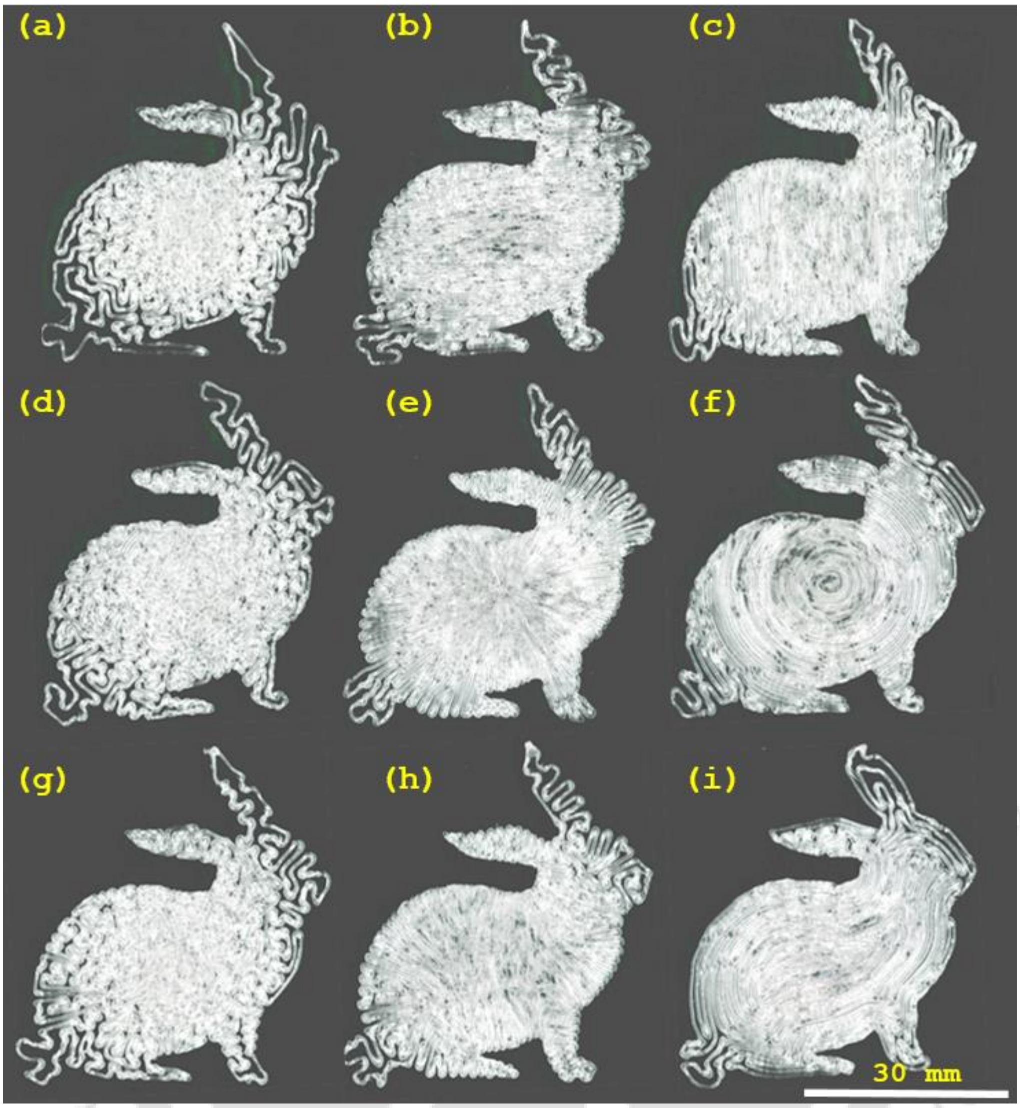

Fig. 6.21: 3D printed parts using gradient toolpaths illustrated in Fig. 6.18 (a) rectangular no-favoring, (b) rectangular-horizontal, (c) rectangular-vertical, (d) circular no-favoring, (e) circular-radial, (f) circular-azimuthal, (g)adaptive no-favoring, (h) adaptive-contour orthogonal, and (i) adaptive-contour parallel

6.6.3 Gradient Infill through Density Map

An example of a gradient fill is the porous structure of a bone. The proposed toolpath, with a density map as the input function, can be used for the fabrication of such structures. The density map can be obtained from a CT scan or MR imaging, which then serves as the governing function for achieving density gradient in the toolpath. Figure 6.22 illustrates the methodology for fabricating such structures, where first, the density map from the CT scan image stack is taken as input; correspondingly, the gradient toolpath is generated. The process repeats for each layer, taking a density map from the CT scan image stack and prescribing gradient to the toolpath for the current layer; subsequently, a combined (all layers) machine-interpretable Gcode file is generated. Figure 6.22 schematically illustrates this sequence for toolpath generation. It can be observed from Fig. 6.22 that the toolpath closely resembles the density map, which is subsequently reflected in the infill. The white and black regions correspond to high and low densities, respectively. Furthermore, the density is higher at the outer contour (cortical region) and sparse inside (cancellous region). Also, for instance, at layer 60, the inside region of high density (marked red in Fig. 6.22, labeled 'A' and 'B') is preserved during deposition (marked red and labeled 'C' in Fig. 6.22). A CT Scan of the FDM-printed part was performed to qualitatively establish the conformity of the infill to density map obtained through the CT Scan image stack. The results, as illustrated in Fig. 6.22, show strong conformity of the infill to the density map. A high density was observed around the edges of the part, which corresponds to the cortical (high density) part of the bone, and a low density inside, corresponding to the cancellous (spongy) part. The open-source image datasets used in this experiment were from the Laboratory of Human Anatomy and Embryology, University of Brussels (ULB), Belgium[287].

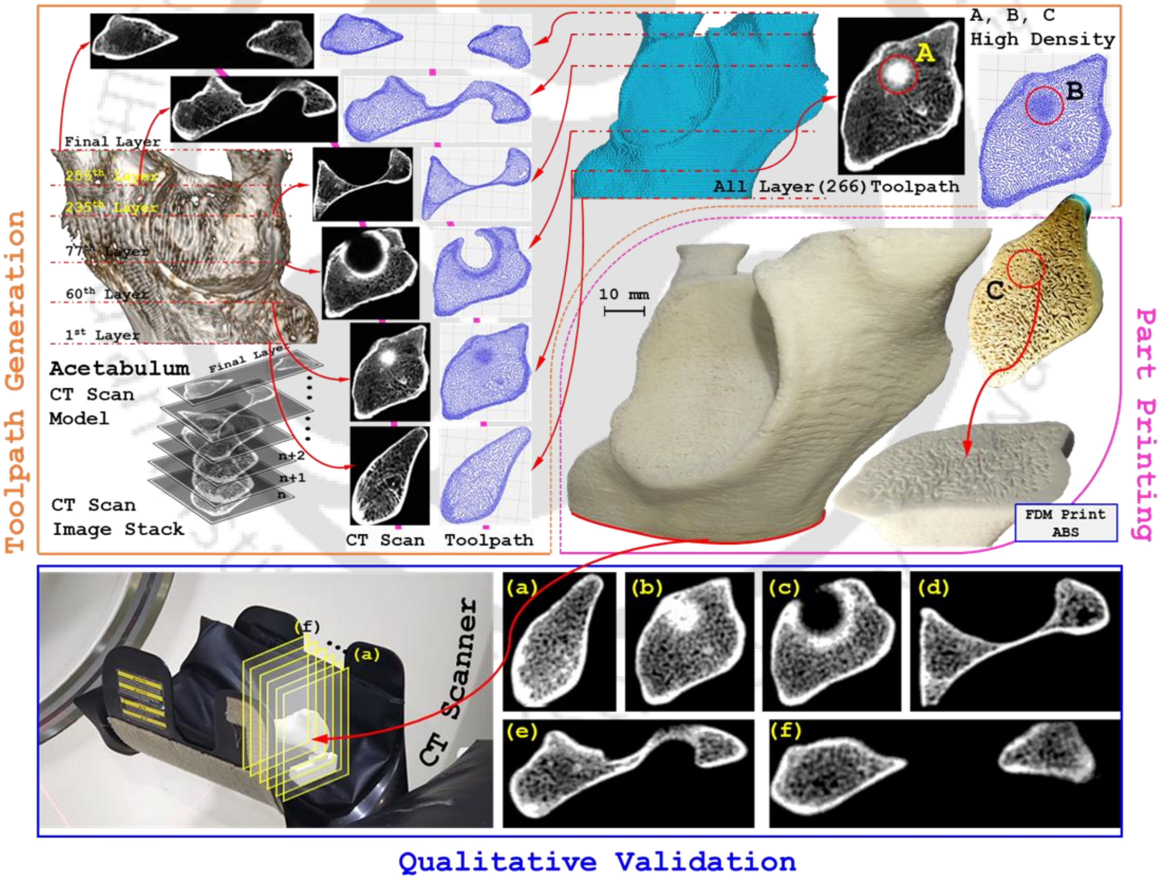

Fig. 6.22: Process sequence for generating gradient toolpath in accordance with CT scan image stack, regions marked 'A,' 'B,' and 'C' shows an example of a 'local' high-density infill in CT Scan, generated toolpath and printed part, respectively

6.7 Summary

Through the utilization of a heuristic-based TSP solver, a methodology for generating gradient-density AM parts is proposed. The algorithm digitizes the domain within a contour into a set of spring-connected points, which can be positioned to obtain either a rectangular, circular, or contour adaptive grid. While the rectangular configuration of the grid points can be achieved through linear springs, additional consideration of torsional spring is required for circular and contour-adaptive digitization. Within each of these three digitization methods, through variation in stepover values along basis vector directions, the toolpath can be biased to favor one direction of travel over the other, thus reducing the number of turns.

The gradient in the toolpath can be accommodated through a user-defined density function or a density map that varies the ideal spring length (stepover). The algorithm was implemented for each of the three methods of digitization for producing gradient toolpaths with and without direction favoring. Through quantitative analysis of toolpath length and image-based analysis, the conformity of the part density to the user-input function (or density map) was established. While the toolpath length was higher for direction-favoring toolpaths as compared to unbiased ones, both, within the limits of a prescribed number of iterations of spring force calculation, followed the input density function. As a case study, using the density map from a CT scan image stack, a region of bone from the acetabulum of the pelvis was printed on an FFF-based 3D printer.

Chapter 7

Conclusions and Future Scope

7.1 Summary

This work, in essence, covers three distinct aspects of the DED process, namely, feedstock handling, machine tool development through the integration of sub-systems with retrofits, and finally toolpath planning for part fabrication. The following sections summarize the crucial findings from each of these three aspects of the presented study. Subsequently, a short conclusion of the thesis is presented which is followed by the future scope.

7.1.1 Non-pneumatic Feedstock Handling

In order to address the limitations associated with pneumatic feedstock handling in DED and to allow for the use of electron beams in powder-feed-based metal additive manufacturing, a non-pneumatic system was developed. The development was carried out by first modeling the granular flow through the designed nozzle components, incorporating design changes based on the simulation results, followed by the fabrication of a functional prototype. The following are the key highlights of this study.

- Through parameter sensitivity analysis, it was ascertained that DEM models for centrifugal spreaders were highly susceptible to the *Coefficient of Static Friction(COSF)* values. Consequently, an apparatus for its accurate evaluation was developed. The apparatus was used for the evaluation of COSF values for several commonly used AM powders against a stainless steel substrate.
- The proposed powder metering unit, featuring a helical-grooved shaft rotating inside a cylindrical encasement, was able to deliver consistent powder flow to the powder delivery nozzle. The initial design of powder metering through an auger showed pulsed powder discharge and, therefore, was not utilized here.
- For the case of centrifugal spreaders under the specified condition of operation, the parameters associated with restricted granular flow conditions, such as higher values of coefficient of static friction and rolling resistance, promote uniformity in spatial distribution. However, this uniformity in spatial distribution is achieved at the expense of temporal uniformity.

- For the selection of a centrifugal spreader design, a two-stage distributor should be preferred over a single-stage distributor for achieving uniformity in the spatial distribution of powder particles around the fusion source. This ensures the omnidirectional capabilities of the nozzle.
- The percentage difference between the simulated and observed values of spatial distribution is high for the case of a two-stage distributor disk. This can be partially attributed to the negligence of the surface properties of the distributor disk. These surface properties, in addition to surface roughness, include machining marks and surface damage. Also, inconsistencies in the part dimensions introduced during the fabrication of the centrifugal disk are likely to have contributed to the discrepancy between the simulated and observed results.
- The granular stream from the continuous coaxial nozzle, with the spatial distribution obtained through a centrifugal spreader, was uniform, conical, and convergent in nature; however, a high focal spot diameter was observed. For reduction in the powder stream's focal spot, a longer cone is proposed, or the use of a discrete coaxial nozzle is suggested for an even smaller spot size.
- The continuous coaxial was studied for the effects of nozzle tilt, which showed a severe distortion in the focal spot for a small value of nozzle inclination. Therefore, machine kinematics should be so chosen to maintain the powder delivery nozzle vertically during deposition.

7.1.2 Development of Hybrid Machine Tool

The machine tool developed as part of this study features a Tormach 3-axis CNC machine (PCNC 1100) and a separate 1kW IPG Photonics laser unit. The interfacing between them was performed by mounting the laser optical head to the CNC spindle, and through repurposing the coolant control of the CNC machine, the laser emission was triggered ON/OFF. The following are the key takeaways from this study.

- The laser unit was interfaced with the CNC using auxiliary electrical arrangements. These auxiliary arrangements include an Ethernet Smooth Stepper (ESS) card with a Mach3® environment for generating control signals that can trigger designated pins of the laser unit that enable beam emissions.
- The power to the laser unit was controlled using a frequency-to-voltage converter that uses an M03 (conventionally used for spindle-on), followed by specifying spindle RPM to set

the laser power. This input, which, in the case of a CNC, is designed to be read by a *Variable Frequency Drive (VFD),* was given to the frequency-to-voltage converter that sets the power to the laser accordingly.

- Mounting arrangements with provisions to adjust the powder stream's focal point relative to the laser beam were also designed and fabricated. These mounts ensure the concentricity of the powder stream relative to the laser beam and the coincidence of the powder stream's focal point with the melt pool.
- The laser optics were mounted to the housing of the CNC spindle while ensuring a small angle of inclination from the CNC bed. This is generally a recommended practice to avoid damage to the laser source.
- Several case studies were performed that demonstrated the viability of the developed hybrid machine tool in fabricating complex parts and substrate coatings.

7.1.3 Utilization of TSP Algorithm for Toolpath Planning

Toolpath planning is a crucial part of Additive Manufacturing. It significantly affects almost every aspect of part fabrication, from part properties and dimensional accuracy to print cost and time. The toolpath generation process starts by first digitizing the layer being processed, i.e., given a geometric contour, a series of grid points (analogous to cities) within the boundary is generated. After digitization, the deposition head sequentially traverses these grid points, as dictated by a *Travelling Salesman Problem (TSP)*-solver, filling the entire area with no voids (or porosity).

7.1.3.1 Toolpath Planning for Uniform Density Part

The proposed path planning method is capable of orienting the toolpath such that the deposited track (or the scan lines) favors one direction of motion over the other. However, the part density remains constant over the domain bounded by the contour. Following are a few key conclusions from the study.

- Considering the grid points obtained through digitization analogous to cities to be visited by a traveling salesman, a heuristic-based TSP solver can be used to generate a toolpath that is continuous and closed-loop.
- The configuration of these grid points within the boundary can take rectangular or circular forms, which alters the direction of deposition while preserving the properties of the Hamiltonian curve. Furthermore, the distance between two successive grid points, along with the number of grid points in a given direction, can be modified to bias the toolpath

in one direction of travel over the other. This can be used for the reduction in the number of turns in a toolpath that offers a selection of 'user-preferred' directions of deposition.

- An advantage of a TSP-based toolpath is its continuous closed-loop nature. This avoids multiple ON and OFF states of the laser (analogous to tool retraction) during material deposition. Continuous deposition of material prevents the process instabilities that typically occur when the state of the laser transitions from ON to OFF or vice-versa.
- Due to the closed-loop (common start-stop point) nature of the toolpath, the defects associated with process instabilities at the beginning and end of the deposition can be localized to a user-preferred region within the plane of deposition. This region can be user-selected such that it is easily addressed during post-processing.

7.1.3.2 Toolpath Planning for Gradient Density Part

The utilization of a TSP-based toolpath, as described above, can also be used for generating a continuous toolpath for the fabrication of density-based functionally graded parts. The following are a few key conclusions from the study.

- The digitization of the space to achieve a gradient in density is accomplished by considering a set of spring-connected points, which can be positioned to obtain either a rectangular, circular, or contour adaptive grid.
- While the rectangular grid can be obtained through linear springs, circular or contour-adaptive digitization can be achieved through a combination of linear and torsional springs acting on a set of grid points.
- Within each of the three digitization methods, through variation in stepover values along basis vector directions, the toolpath can be biased to favor one direction of travel over the other, thus reducing the number of turns. This reduction in the number of turns is accomplished with minimal influence on the conformity of the toolpath to the user-specified part density.
- The gradient in the toolpath can be accommodated through a user-defined density function or a density map that varies the ideal spring length (stepover) of the digitized contour domain.
- The quantitative analysis of toolpath length and qualitative image-based analysis of the gradient toolpath reveals a strong conformity of the part density to the user input function (or density map).

- In order to establish the viability of the proposed toolpath, as a case study, a region of bone from the acetabulum of the pelvis was printed on an FFF-based 3D printer. The input for the gradient in the toolpath was obtained from the images in a CT scan image stack of the bone.

7.2 Conclusion

Additive Manufacturing (AM) has found applications in several domains, and as the progress in AM continues, new avenues for its growth will open up. The most significant advantage of AM over other traditional manufacturing processes is the design freedom offered to its users. This design freedom encapsulates geometric complexity and material selection. While the fabrication of geometrically complex parts is feasible through sequential layer-by-layer deposition, material complexity is achieved through the use of multi-material input for each layer throughout the part printing in AM. This allows for the fabrication of parts with added complexity, introduced through a user-defined gradient in part density (through toolpath planning), part properties (through multi-material input), and(or) a combination of both.

While the possibilities in AM are immense, it is through the exploration of novel ideas its full capabilities can be realized, and limitations can be addressed. This work, in essence, was a humble attempt at such an exploration. The gravity-based, non-pneumatic system provided a possible alternative to pneumatic feedstock handling. The proposed non-pneumatic system offered simplicity in design where the apparatus is easy to fabricate with functional prototypes easily produced through FDM and SLA-based 3D printers and can be retrofitted to any laser welding head, thus providing additive manufacturing capabilities. The toolpath strategies were synthesized keeping in view the ability to generate continuous deposition curves for both uniform and gradient part density, to prevent defects associated with process instabilities during the start and stop of the deposition processes.

Although the work presented here attempts to be detailed in its approach, several new possibilities for research lie within the bounds of the presented ideas. A selection of such research opportunities is outlined as future scope in the following section.

7.3 Scope for Future Work

The work presented here offers several avenues for further exploration of the DED process. Some of these possible avenues are listed below.

- Although, as mentioned previously, the developed feedstock handling system is capable of multi-material input, however, its exploration in this work is minimal. Fig. 7.1(a) shows a mild steel sample coated with a mixture of SS316L and Alumina powder. This preliminary study points to the possibility that such a system can be further explored for the fabrication of material-based FGMs and composites (as shown in Fig. 7.1(b)) and the coating of surfaces.

- The design of the discrete coaxial nozzle can be altered such that it can change the focal length of the powder stream during deposition. Such a system, as shown in Fig. 7.1(d), can then be coupled with the laser and the CNC unit in a feedback control to allow for the compensation of variation in deposited bead height. Also, such a design will make the powder handling unit more versatile, such that it can be mounted on several laser welding heads while easily accounting for their difference in focal length. This versatility and the modular nature of the powder feed device can be further explored.
- The two-stage centrifugal disk design can be further optimized by analyzing the effect of blade length and blade curvature (as shown in Fig. 7.1(c)) on the spatial uniformity of the distributed granular media. Other design selections, such as the slope of the disk surface and the material of the disk, can be studied from a process optimization point of view.
- In order to reduce the discrepancy between the modeled and observed values in a DEM simulation, a material calibration can be performed. During material calibration, the input values of COSF, CORF, and COR in the DEM environment can be adjusted such that the studied response, as predicted by the simulation, matches the experimental results. This aspect of material calibration can be further investigated to accurately capture the surface properties of the equipment used in a DEM.
- A longer conical channel for powder delivery and an appropriate design of a shield gas supply system can reduce the spot size of the powder stream for a continuous coaxial nozzle. Further experimentation and prototyping are needed to analyze the interaction between the powder stream and the shield gases.
- Given the non-pneumatic nature of the proposed powder handling unit, the laser/EB-based metal deposition within a vacuum chamber can be performed. Such a system can be investigated with regard to melt-pool protection against oxidation.
- Implementation of the TSP toolpath for multi-material deposition can be further explored.

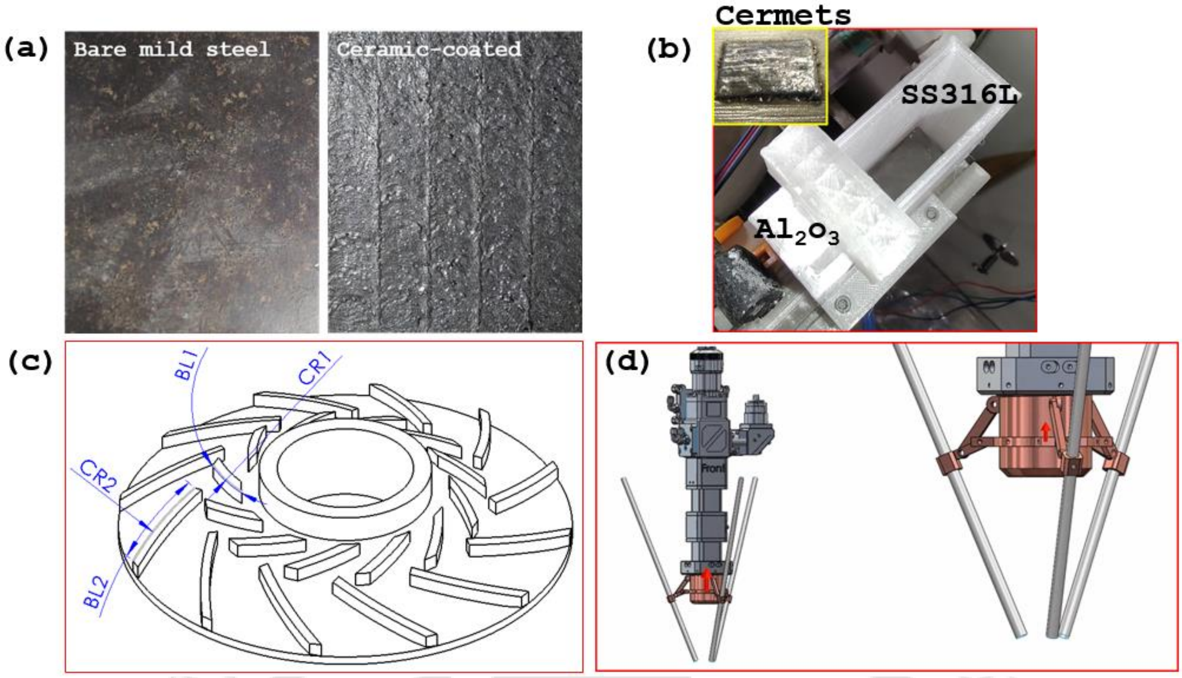

Fig. 7.1: Preliminary study on (a) ceramic coating of the mild steel substrate, (b) fabrication of ceramic-metal composites, (c) design parameter that can be considered for distributor disk optimization, and (d) variable focal length powder delivery nozzle

Appendix 1

Study of Auxiliary Arrangements for Attaining Omnidirectionality in Additive Manufacturing Machine Tools

A1.1 Introduction

Methods and mechanisms of material deposition in AM is an important considerations to achieve parts with uniform and sound mechanical properties. Even though a lot of work has been done in this regard, this study brings out yet another important (but mostly neglected) aspect of layer-by-layer material deposition, termed "Omnidirectionality." The term omnidirectional indicates an equal sensitivity of the deposition process in all directions. An omnidirectional antenna, for example, will send or receive signals equally well in all directions. In the context of AM, omnidirectionality implies invariance of material and geometric properties regardless of the travel direction. Omnidirectionality, more often than not, is a property of the setup/ 3D printer; however, a few AM processes are inherently omnidirectional, while others are made so by appropriate arrangement. This work highlights such arrangements and their necessity in a 3D printer (or printing process) design.

From a software point of view, AM follows a generic workflow. A CAD model with continuous features and facets is approximated using a series of connected triangles, resulting in an STL (Standard Tessellation/ Triangulation Language) file. An error-free STL file is sliced into multiple layers, each containing contour information of the part at any given cross-section. This contour information is then sent to the print head (commonly in the form of G-Codes), which traces these contours for each layer while ensuring the bonding of the freshly deposited layer with the previously deposited one. Several processes have evolved out of this layer-by-layer approach; a generic classification, as suggested by ASTM, based on the increasing order of ease of achieving omnidirectionality, is shown in Fig. A1.1.

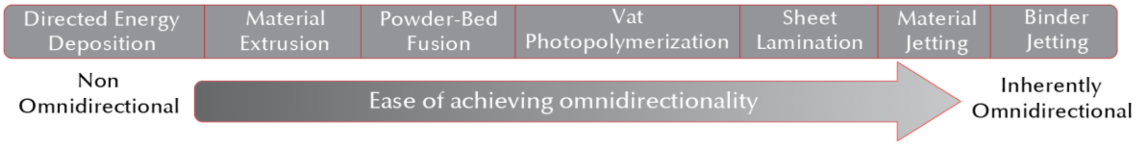

Fig. A1.1: AM processes in increasing order of ease of achieving omnidirectionality

The following sections individually discuss each of these processes and a few of their variants in the context of omnidirectionality. However, their generic and detailed description can be found in Ref [288,289]. At this point in the discussion, it is important to draw a distinction between 'Isotropy' and 'Omnidirectionality.' Isotropy underlines uniformity in part properties irrespective of the part orientation and the location of measurement. Omnidirectionality, on the other hand, is associated with the machine tool. An omnidirectional AM platform promotes the fabrication of isotropic parts. Conversely, anisotropy, which signifies non-uniformity in part properties, can arise from several factors, such as the layer-by-layer nature of AM, thermal gradient, solidification rate, etc. However, a non-omnidirectional deposition, which is often neglected, significantly contributes to the anisotropy of a part. Also, notice the definition of omnidirectionality, as presented here, is confined to the plane of deposition, unlike isotropy, which extends to three dimensions.

A1.2 Omnidirectionality

Consider the process of part fabrication using a Tungsten Inert Gas (TIG) cladding setup, schematically illustrated in Fig. A1.2. The TIG torch is constrained in the X-Y plane and is free to move vertically in the Z direction. The build platform in case 1, as illustrated in Fig. A1.2(a), supports linear travel along the 'X' and 'Y' axis whereas, in case 2, shown in Fig. A1.2(b), linear X-Y movement along with substrate rotation about the 'Z' axis is also added. Observing the orientation of the filler wire relative to the electric arc for case 1 reveals the following. For the first leg of the travel (along +X, from a to b), with the shown starting position, the filler wire maintains a front-feed orientation. For the second leg (along +Y, from b to c), the orientation changes to side-feed followed by back-feed for the third leg (along –X, from c to d), and finally, it reverts to side-feed again (along -Y, from d to a). This same cycle repeats for the next layer of deposition. As for case 2, the substrate motion can be decomposed into a combination of linear and rotational movements. The filler wire starts with a linear travel (along +X) in a front-feed orientation; as the TIG torch approaches the corner marked 'b,' the substrate turns clockwise (highlighted in red arrow) by 90°. This sequence of linear travel followed by a rotation of the substrate at the corners is followed for every corner of the rectangular track, thus ensuring the front-feed orientation of the filler wire throughout the deposition.

In case 1, the variation in feed orientation induces variation in the dimensions of the deposited track. For example, the bead area at the sectional plane marked A-A, where the filler wire maintains a side-feed orientation, will be smaller than the bead area at B-B [101]. Through introducing an additional (rotational) 'degree of freedom' in case 2, the setup turns omnidirectional in nature as the travel direction adjusts itself such that the front-feed orientation of the filler wire is preserved throughout the build. Consequently, the deposition carried out from the second setup (case 2) results in more uniform and geometrically accurate tracks.

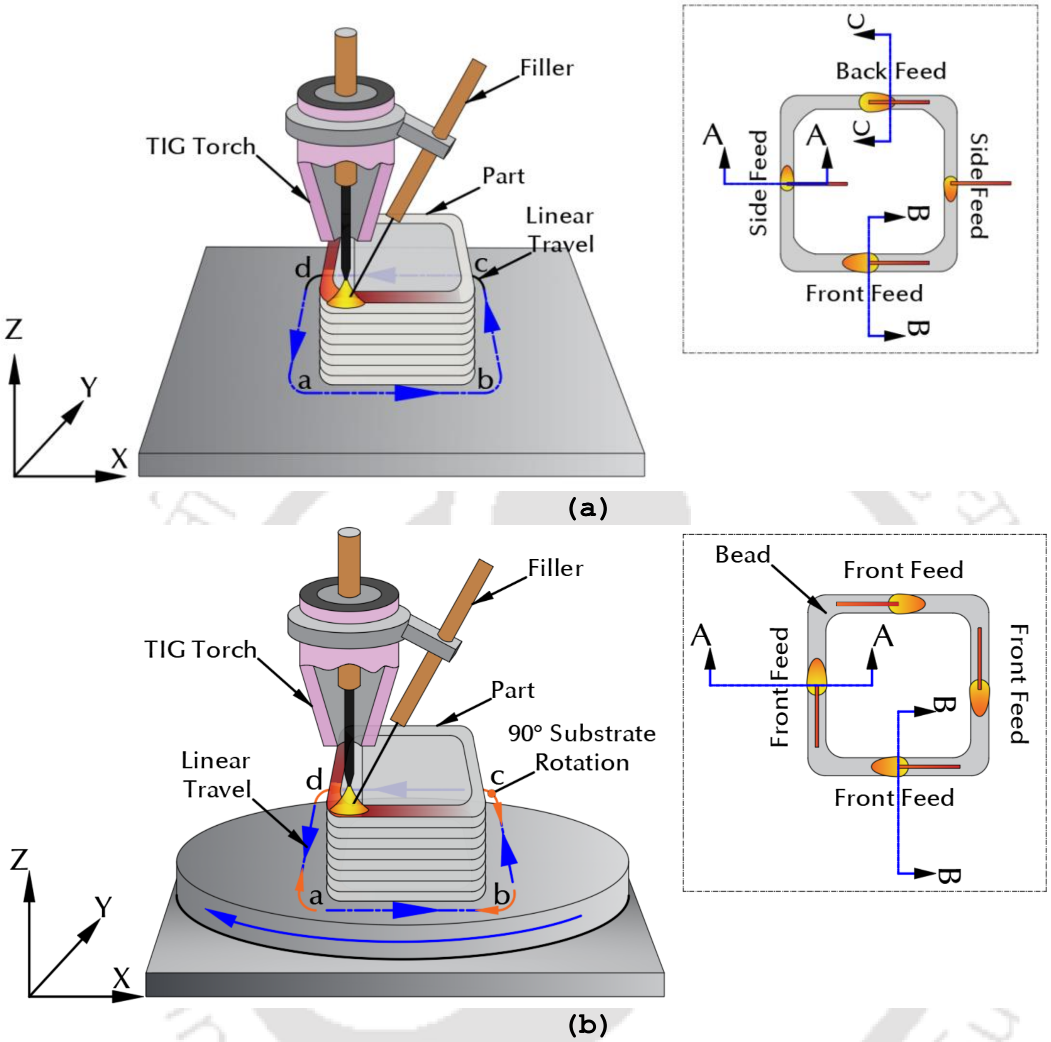

Fig. A1.2: Part fabrication using TIG welding setup with (a) linear movement in the X-Y plane and (b) linear movement in X-Y, along with rotation about Z. Adapted with permission from [101], copyright(2019) Taylor and Francis

Apart from the undesired geometric variation outlined above, a non-omnidirectional setup presents a variety of other accompanying issues. Some of these issues are illustrated in Fig. A1.3. Serration, as illustrated in Fig. A1.3(a), occurs during the back-feed orientation of the filler wire. As the arc progresses forward, the trailing filler rod digs in the freshly (and soft due to heat retention) deposited bead, leading to the formation of a groove-like feature [290]. Fig. A1.3(b) depicts the deviation of the deposited bead from the desired location of the deposition. As the filler wire, during deposition, switches from one orientation to another, the deposited track offsets from the initially selected location. This problem of track offset is exacerbated in parts with complex geometry, and unlike over-deposit (deposition of excess material), it is difficult to address through machining post-deposit [33]. Yet another issue associated with non-omnidirectionality is that of non-uniform substrate dilution, as illustrated in Fig. A1.3(c)[120]. The heat input from the arc is jointly consumed by the filler wire and the substrate. One factor that affects the substrate melt area and its location is the position of the filler wire relative to the fusion source. In the first illustration of Fig. A1.3(c), the filler wire is positioned to the left of the fusion source; therefore, more substrate melting is observed on the right. In the second illustration of Fig. A1.3(c), the position of the filler wire and, consequently, that of the substrate melt location is reversed. It is to be noted that often, the substrate melting takes place regardless of the filler orientation; the degree of melting, however, varies.

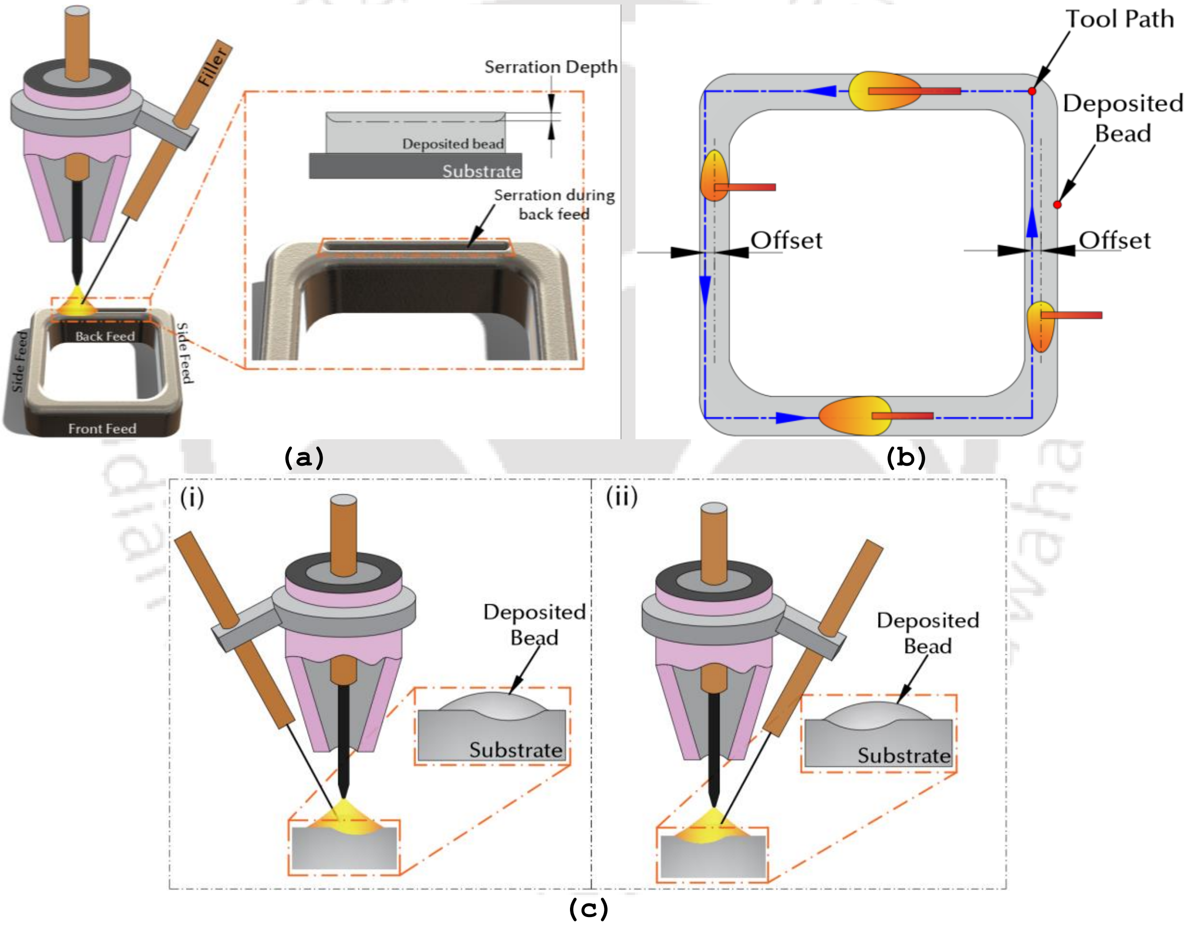

Fig. A1.3: Issues in TIG-based DED primarily emanating from non-omnidirectional behavior of the setup (a) serrations in the deposit, (b) deviation of the deposited bead from actual tool path, and (c) variation in substrate dilution due to partial obstruction. Adapted with permission from [290], copyright(2005) Elsevier

Through the discussion so far, it is apparent that omnidirectionality is a key ingredient in any robust and reliable AM platform. Overlooking this important property of the AM setup can induce a host of issues in the printed parts, which often compromises the part's service life and performance. The discussion presented above is specific to the case of DED using TIG welding as the method of deposition. A more formal definition, which establishes a criterion for an AM process to be omnidirectional, is as follows. (Later in the discussion, the TIG setup, as presented above, will be analyzed against the established definition of omnidirectionality.)

The directional sensitivity in the AM processes arises from the inconsistency between the spatial orientation of three vectors relative to each other, viz, the source of fusion (or joining) $\boldsymbol{V_S}$, the direction of the feedstock delivery $\boldsymbol{V_F}$, and the travel direction $\boldsymbol{V_D}$. These three vectors, termed 'Orientation Vectors,' are illustrated in Fig. A1.4. A distinction is made between AM processes that require a pre-placed feedstock as opposed to ones that require feedstock delivery. For example, Vat Photopolymerization, Sheet Lamination, Powder-Bed Fusion, and Binder Jetting fall under the category of pre-placed feedstock. On the other hand, Directed Energy Deposition (DED), Fused Deposition Modelling (FDM), and Material-Jetting exhibit feedstock delivery on the print bed (or the substrate) concurrent to contour tracing. For pre-placed feedstock $\boldsymbol{V_F}$ can be assumed zero, as illustrated in Fig. A1.4(b).

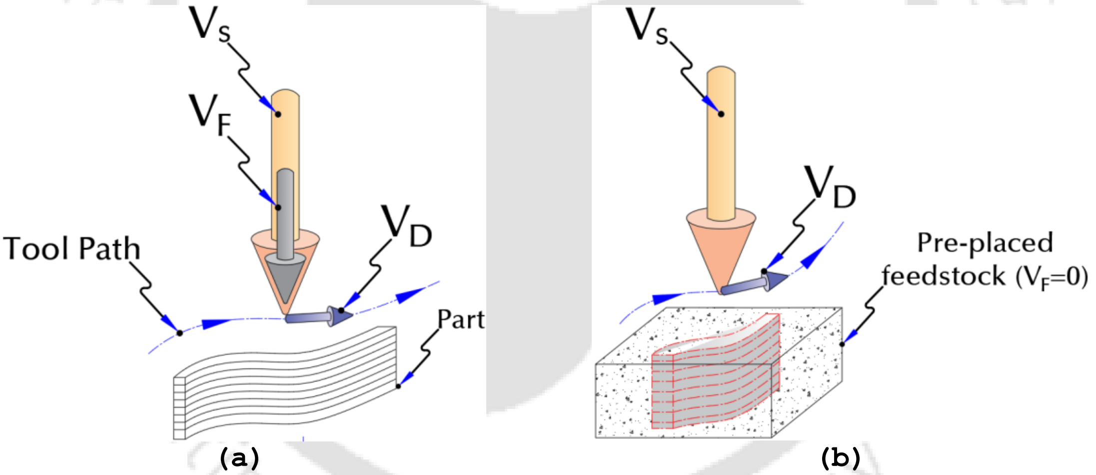

Fig. A1.4: Feedstock Vector (VF), Deposition Vector (VD), and Source of Fusion Vector (Vs) for (a) feedstock delivery and (b) pre-placed feedstock AM processes

The condition for inherent omnidirectionality, based on the relative position of the three orientation vectors in feedstock-feed-based AM processes, can be symbolically defined as $\boldsymbol{V_S} \parallel \boldsymbol{V_F}$, $\boldsymbol{V_D} \perp \boldsymbol{V_F}$ and $\boldsymbol{V_D} \perp \boldsymbol{V_S}$. In other words, to be inherently omnidirectional, the fusion source should be kept parallel to the direction of feedstock delivery, and the direction of travel (of the substrate or deposition head) should be maintained perpendicular to both; the feedstock delivery, as well as the fusion source vector, as illustrated in Fig. A1.4(a). For pre-placed feedstock processes, since $\boldsymbol{V_F}$ is zero, the condition of inherent omnidirectionality implies the source of fusion is perpendicular to the travel direction ($\boldsymbol{V_S} \perp \boldsymbol{V_D}$) throughout the build. Some of the AM processes require additional constraints to ensure omnidirectionality; these processes will be discussed in their respective sections. Figure A1.5 illustrates a few cases of non-omnidirectional nature.

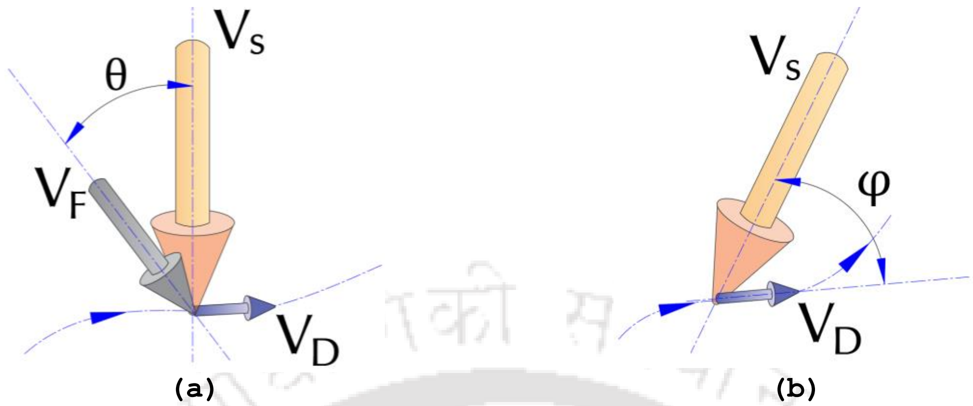

Fig. A1.5: Few examples of non-omnidirectional nature due to inclination of (a) feedstock with fusion source and (b) fusion source and travel direction

This work will address each of the AM processes(listed in Fig. A1.1) and some of their variants in terms of their omnidirectional (or lack thereof) nature. The processes will be evaluated against the condition for omnidirectionality established above. It has been observed that some of the AM processes are inherently omnidirectional, whereas some require an appropriate arrangement for ensuring omnidirectionality. These arrangements and various methods of ensuring omnidirectionality in a variety of AM processes are also discussed throughout the article in detail.

A1.3 Directed Energy Deposition

For the Directed Energy Deposition (DED)-based AM processes, the feedstock is fed instantaneously along the vector $\boldsymbol{V_F}$ into the molten pool created by the fusion source. Hence, the relative position of the vector $\boldsymbol{V_S}$, $\boldsymbol{V_F}$ and $\boldsymbol{V_D}$ may vary when following a non-linear trajectory in the X-Y plane. A few common variants of DED are discussed in terms of omnidirectionality in the following sections.

In the case of Metal Inert Gas (MIG) cladding, the feedstock enters the molten pool coaxially, hence the relative position between $\boldsymbol{V_S}$, $\boldsymbol{V_F}$ and $\boldsymbol{V_D}$ is consistent ($\boldsymbol{V_S} \parallel \boldsymbol{V_F}, \boldsymbol{V_D} \perp \boldsymbol{V_F}$ and $\boldsymbol{V_D} \perp \boldsymbol{V_S}$ refer to Fig. A1.6(a)). This effectively yields a uniform deposition condition regardless of the contour trajectory. However, the condition is not the same for *Tungsten Inert Gas (TIG)* (see Fig. A1.6(b)), Plasma, Laser, or *Electron Beam (EB)* cladding for depositing the material. In such DED processes, the relative position between $\boldsymbol{V_F}$ and $\boldsymbol{V_D}$ may vary because of variations in the travel direction ($\boldsymbol{V_D}$) in the X-Y plane. Therefore, these AM processes are not inherently omnidirectional.

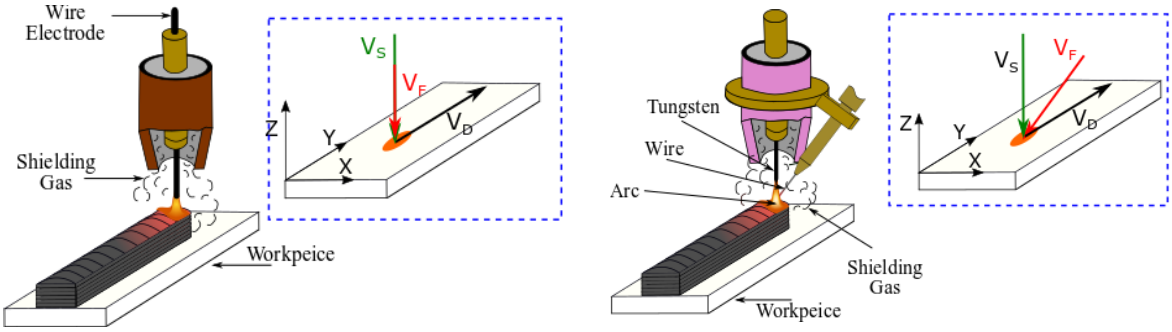

(a) (b)

Fig. A1.6: Directional sensitivity in DED-based AM processes example of (a) omnidirectional MIG cladding (b) non-omnidirectional TIG Cladding. Reproduced with permission from [101], copyright(2019), Taylor and Francis

A1.3.1 Methods of Achieving Omnidirectionality in DED

In the first method, the feedstock and fusion source are both coaxial, as shown in Fig. A1.7(a); here, the relative position between $\boldsymbol{V_S}$, $\boldsymbol{V_F}$ and $\boldsymbol{V_D}$ will be consistent to $\boldsymbol{V_S} \parallel \boldsymbol{V_F}$, $\boldsymbol{V_D} \perp \boldsymbol{V_F}$ and $\boldsymbol{V_D} \perp \boldsymbol{V_S}$ irrespective of travel direction. Among the several cladding processes, only the MIG cladding process falls into this category (see Fig. A1.6(a)). Other methods of achieving omnidirectionality are either feedstock surrounding the coaxial fusion source or fusion source surrounding the coaxial feedstock supply, as shown in Fig. A1.7 (b) and (c), respectively. One can observe that in these cases, the relative position between $\boldsymbol{V_S}$, $\boldsymbol{V_F}$ and $\boldsymbol{V_D}$ will remain consistent independent of travel direction. Furthermore, in another method, an arrangement can be built such that feedstock or substrate dynamically adjusts the orientation vectors $\boldsymbol{V_F}$ or $\boldsymbol{V_D}$ to keep the relative position between $\boldsymbol{V_S}$, $\boldsymbol{V_F}$ and $\boldsymbol{V_D}$ consistent (see Fig. A1.7(d)) throughout the build. All these methods can be divided into four generic categories as given below:

Coaxial feedstock and fusion source (refer to Fig. A1.7(a))
Coaxial fusion source surrounded by feedstock (refer to Fig. A1.7(b))
Coaxial feedstock surrounded by fusion source (refer to Fig. A1.7(c))
Dynamically adjusting feedstock-delivery or deposition direction (refer to Fig. A1.7(d))

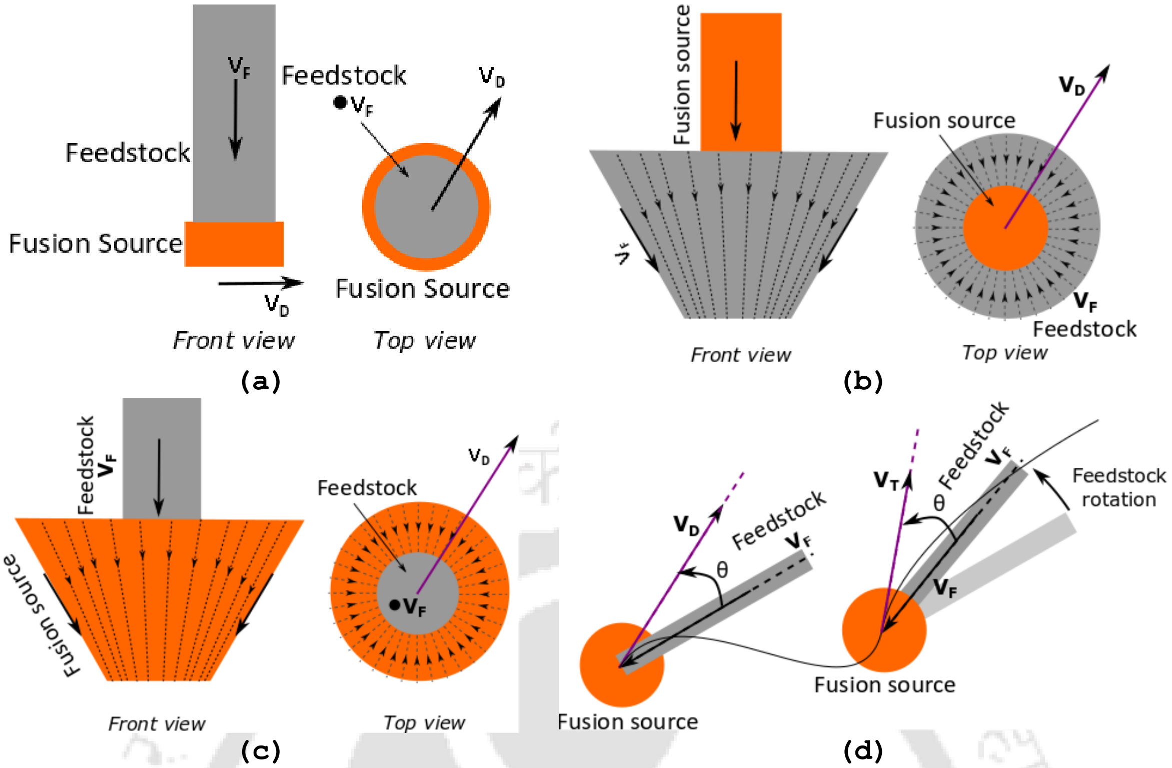

Fig. A1.7: Principle of different methods of obtaining omnidirectionality in DED-based metal AM: (a) coaxial feedstock and fusion source, (b) coaxial fusion source and surrounded by feedstock, (c) coaxial feedstock and surrounded by fusion source, and (d) dynamically adjusting the feedstock-delivery direction

According to the type of cladding process, one or more methods mentioned above can be applied to obtain an omnidirectional AM platform.

A1.3.1.1 Omnidirectional TIG/Plasma Cladding

In the conventional TIG/Plasma cladding process, the fusion source is located at the center, and the feedstock is fed laterally in the molten pool. Methods II, III & IV (section A1.3.1) can be implemented to achieve omnidirectionality in this cladding process.

A1.3.1.1.1 Method II: Coaxial Fusion Source Surrounded by Feedstock

In the TIG/Plasma cladding processes, commonly, the feedstock is in the form of only a wire/strip and not in the form of powder. Unlike powders, it is not possible to uniformly distribute the wire/strip form of the feedstock into a conical envelope, as illustrated in Fig.A1.7 (b). Therefore, multiple wires/strips surrounding the arc/plasma should be fed into the molten pool at different angles. Three feedstocks spaced $120°$ can be assumed to be a reasonable approximation to keep the relative position between $\boldsymbol{V_S}$, $\boldsymbol{V_F}$ and $\boldsymbol{V_D}$ consistent. A schematic representation of such an omnidirectional TIG/Plasma cladding process has been illustrated in Fig. A1.8. The feasibility of fabricating such a system has been reported in the work of Voice *et al.* [291]. Authors have proposed to use different material compositions for different wires; however, they did not address the omnidirectionality of the process.

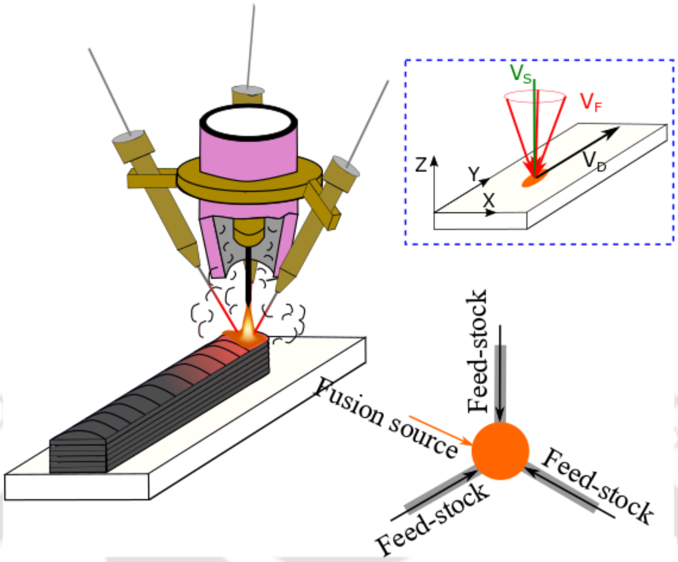

Fig. A1.8: Method-II for Omnidirectional TIG/Plasma Cladding

A1.3.1.1.2 Method III: Coaxial Feedstock Surrounded by Fusion Source

As per method III, to restore omnidirectionality, the feedstock should be fed coaxially, surrounded by an energy source. TIG and Plasma cladding processes with a hollow electrode and a centrally fed wire, as shown in Fig .A1.9 (a) & (b), fall under this category. For TIG and Plasma cladding, such inventions are reported in the work of Morgan *et al.* [292] and Hooper *et al.* [293], respectively. However, no such commercial system was found in the literature survey.

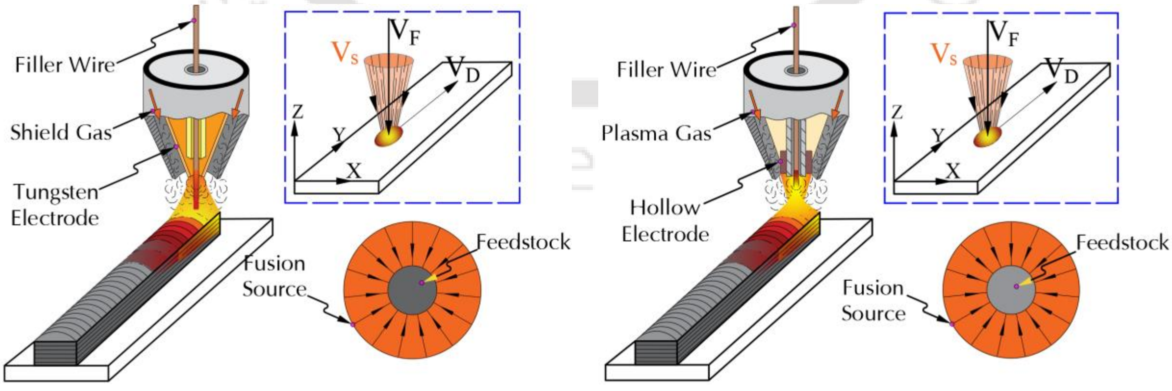

(a) (b)

Fig. A1.9: Hollow cathode with coaxial wire feeding for an omnidirectional (a) TIG and (b) plasma cladding

It is also possible to use multiple fusion energy sources surrounding the coaxially fed feedstock (similar to method III) for TIG/Plasma cladding. It can be achieved by placing multiple fusion energy sources symmetrically around a centrally-fed wire perpendicular to the substrate surface.

A1.3.1.1.3 Method-IV: Dynamically Adjusting Feedstock or Deposition Direction

In the conventional TIG/Plasma cladding process, the torch is vertical, which means the fusion source ($\boldsymbol{V_S}$) is vertical (along the Z-axis) and is fixed. Therefore, omnidirectionality can also be achieved just by maintaining a constant relative position between the feedstock-delivery direction vector ($\boldsymbol{V_F}$) and travel direction vector ($\boldsymbol{V_D}$). For this purpose, there should be a mechanism to provide the relative motion between the workpiece and the feedstock, which is possible in two ways:

(a) Dynamically orient the workpiece to regulate the deposition direction (Fig. A1.10 (a)).

(b) Dynamically orient the feedstock to adjust the feedstock-delivery direction (Fig. A1.10 (b)).

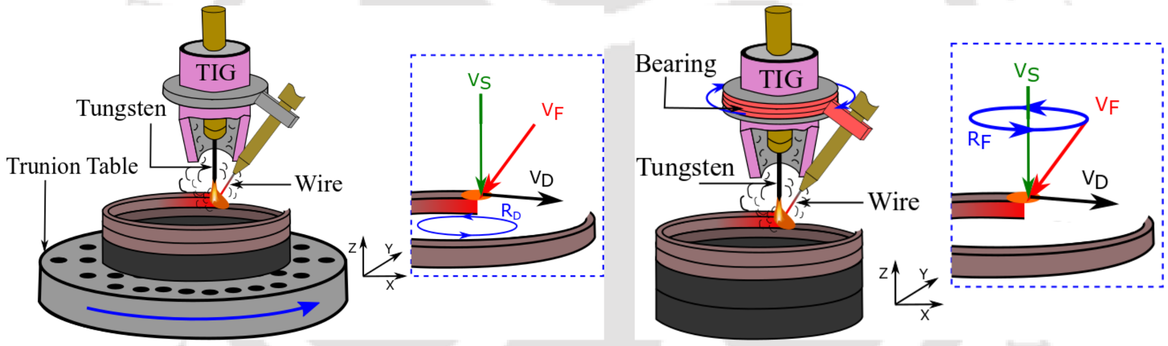

(a) (b)

Fig. A1.10: Achieving omnidirectionality through the dynamic orientation of (a) workpiece, and (b) feedstock delivery

(a) Dynamically orienting the workpiece to regulate the deposition direction

Various DED-based AM systems use a 3/4/5-axis CNC machine for depositing the material on a desirable path. If $\boldsymbol{V_s}$ is fixed and attached with a vertical axis (see Fig. A1.10 (a)) and $\boldsymbol{V_F}$ maintains an angle of constant inclination with $\boldsymbol{V_S}$. Then, $\boldsymbol{V_D}$ must orient itself in such a way that the resulting deposition maintains consistency in the spatial orientation of $\boldsymbol{V_S}$, $\boldsymbol{V_F}$, and $\boldsymbol{V_D}$ throughout the build. In a multi-axis deposition bed such as a 5-axis CNC machine, a rotating table (C-axis, rotation about Z-axis) is available, which can be used to position the deposition vector $\boldsymbol{V_D}$ in the desired manner. An illustrative example of this method has been demonstrated through a schematic diagram in Fig. A1.10(a); such an experimental setup has been developed by Kapil *et al.* [101].

(b) Dynamically orienting the feedstock to regulate the feedstock-delivery direction

By rotating the wire feeder through an appropriate mechanism, consistency in the spatial orientation of $\boldsymbol{V_S}$, $\boldsymbol{V_F}$, and $\boldsymbol{V_D}$ can be achieved. Fig. A1.10(b) shows a rotating wire feeder, which is changing its position according to the change in the moving direction of the torch to keep a consistent wire feed direction (front feeding here). A mounting unit has to be designed and manufactured for this method, which can be retrofitted on the existing torch of the power source.

A1.3.1.2 Omnidirectional Laser Cladding

In this section, a laser beam will be considered as a heat source, while the feedstock can be in the form of wire, powder, or a combination of both. Generally, for the wire form of feedstock, the method of its feed into the melt pool is similar to the one discussed in section A1.3.1 (for the case of TIG/Plasma cladding); however, when using powder as feedstock, specially designed nozzles are used. The use of a laser beam over an electric arc is advantageous for precise deposition as it can be focused to a small diameter using appropriate optics. The position of the feedstock relative to the heat source, as discussed previously, can be lateral (at an angle) or coaxial. Methods II, III & IV (refer to section A1.3) can be implemented to achieve omnidirectionality in laser cladding. These methods are discussed in detail in the following sections.

A1.3.1.2.1 Method II: Coaxial Fusion Source Surrounded by Feedstock

For wires, developing a conical envelope of feedstock surrounding the fusion source was a limitation. Powders, on the other hand, can be fluidized using an inert gas, and such an envelope can be created [104,116,141]. The nozzle design, shown schematically in Fig. A1.11(a), consists of two concentric cones spaced apart by a predetermined value. These concentric cones form an annular outlet through which a convergent stream of powder feedstock is produced. Ideally, the focal spot of the powder stream should be less than or equal to the dimension of the melt pool. Also, the depth of focus (distance up to which the powder stream remains convergent) should be extended to achieve high catchment efficiency during the build.

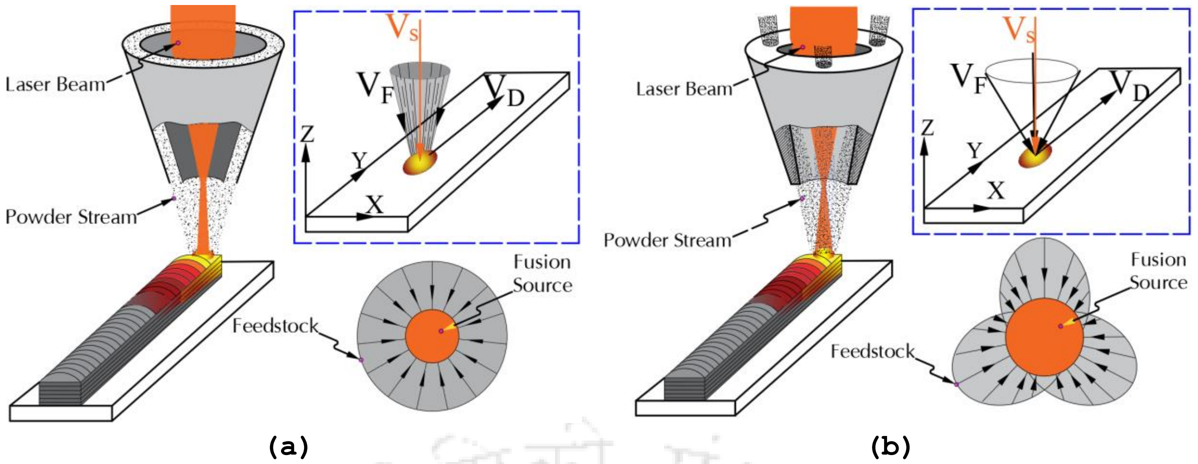

Fig. A1.11: Omnidirectional laser cladding using coaxial feedstock and fusion source with (a) continuous outer feedstock with central fusion source, and (b) discrete channels of feedstock with central fusion source

Multi-channel powder flow with a coaxial laser beam, schematically shown in Fig. A1.11 (b), has been developed and studied by several researchers [42,110,111]. This variant of the coaxial nozzle, often termed a 'Discrete coaxial nozzle,' provides the freedom to vary process parameters (such as mass flow rate, flow velocity, etc.) for each individual powder stream. One advantage of such a nozzle design is the ability to deliver different types of feedstock material simultaneously into the melt pool and create Functionally Graded Materials (FGMs) [27,28,294,295].

A1.3.1.2.2 Method-III: Coaxial Feedstock Surrounded by Fusion Source

Achieving omnidirectionality through the central powder feed and annular laser beam, as illustrated in Fig. A1.12(a), has been explored by quite a few researchers [114,296]. Even though such a setup has been shown to possess higher powder catchment efficiency [114], it is generally not preferred due to the involvement of a complex optical system. The laser beam emerging from the cavity is hollowed using a series of mirrors and prisms (called Axicons), and the resulting laser beam intensity distribution accommodates a central feed of powder.

Another advantage of using such a setup is the aspect ratio of the deposited clad. Generally, with Gaussian laser beams, the deposited clad layer shows a detachment from the substrate at the edges and high dilution at the center [116]. Therefore, a Gaussian laser beam is widely preferred for cutting as it can maintain a narrow kerf. With annular laser beams (TEM 01 + TEM 10), sufficient melting occurs at the edges of the substrate with minimal dilution at the center.

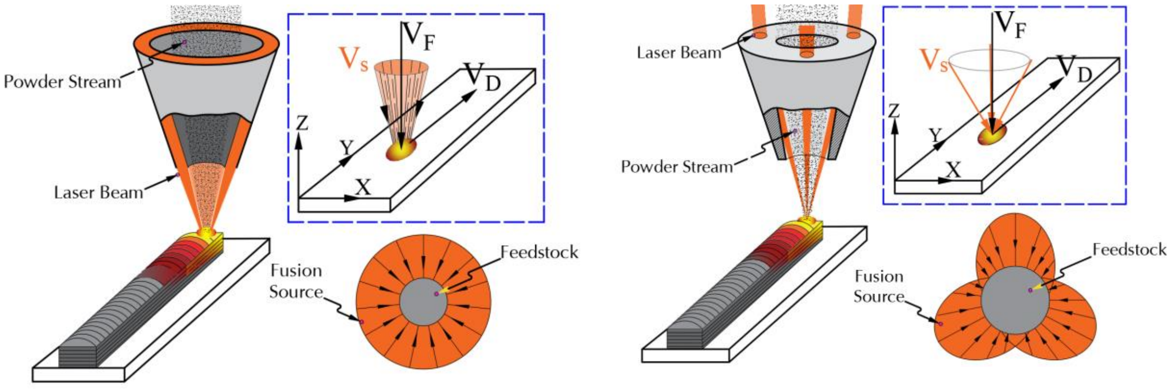

(a) (b)

Fig. A1.12: Omnidirectional laser cladding using coaxial feedstock and fusion source with (a) continuous outer fusion source with central feedstock, and (b) discrete outer fusion source with central feedstock

A similar setup (feedstock surrounding the fusion source), with a simpler build, is illustrated in Fig. A1.12 (b). Here, it can be observed that instead of having an annular-shaped beam intensity profile, three separate laser beams, each delivered through an optical fiber, are used. These three beams are inclined relative to vertical in such a way that the convergence point of the laser beams matches the focal point of the powder stream. Such a system has been developed by Pajukoski *et al.* [297]. However, instead of using three separate laser beams, the laser head splits a single laser beam into three beams using suitable optics.

A1.3.1.2.3 Method-IV: Dynamically Adjusting Feedstock-delivery or Deposition Direction

In this method, as discussed previously, a consistent orientation between the feedstock-delivery direction vector $\boldsymbol{V_F}$ and travel direction vector $\boldsymbol{V_D}$ has to be maintained during the build. The two methods proposed earlier (in section A1.3.1, Method IV (a, b)) require dynamic (on the fly) adjustment of either the material feed or the substrate direction to achieve omnidirectionality. It must be noted that even though such a setup is feasible for wire as feedstock, its use with powders has not been studied so far. Also, it can be observed that as the powder feedstock is suspended in a stream of inert gas, rapid changes in feed direction could lead to a decreased catchment efficiency. This is because the rapid changes in feed orientation are more likely to disrupt the powder flow characteristics, giving rise to a spray-like pattern rather than a convergent one.

A1.3.1.3 Omnidirectionality in Electron Beam Cladding

In Electron Beam (EB) systems, electrons are generated and accelerated using high potential difference (≈60-100 kV) towards the substrate. Upon impacting the substrate, a melt pool is generated into which feedstock material can be injected. A separate focusing and deflecting coil is used to converge and scan EB over a given area, respectively. A vacuum environment (≈10-4 Torr.) is required for successful material processing using EBs. Since most of the powder feedstock handling systems use a pneumatic method, wires are used as feedstocks in EB systems; the following are some of the methods adopted for achieving omnidirectionality in EB cladding.

EB systems, due to the inclination between feedstock and fusion source, are non-omnidirectional in nature. In order to achieve omnidirectionality in EB systems, methods II, III, and IV from the previous discussion (section A1.3.1) can be implemented.

A1.3.1.3.1 Method II: Coaxial Fusion Source Surrounded by Feedstock

(a) Use of coaxial gravity feed nozzles

Due to the pneumatic powder feedstock handling system, all commercially available cladding setups are restricted to the use of either lasers or electric arcs [298] as a heat source. In order to maintain a vacuum environment while using powder feedstock, it is essential to develop non-pneumatic-based systems for EB cladding. A few researchers [76,77] have explored such systems in the context of a laser-based Directed Energy Deposition. These systems are gravity-based, thus eliminating the requirement of inert carrier gas for feedstock handling. Even though these systems maintain concentricity between feedstock and fusion source to achieve omnidirectionality, they have not been tested for the case of EBs.

A1.3.1.3.2 Method III: Coaxial Feedstock Surrounded by Fusion Source

(a) High-frequency oscillating EBs with central feedstock delivery

Centrally fed feedstock surrounded by multiple, equally spaced oscillating EBs, schematically shown in Fig. A1.13, results in a heat intensity distribution similar to an annular laser beam profile (as discussed in section A1.3.1, Method III). Such high frequencies, capable of mimicking an annular heat intensity distribution without any additional setup (as in the case of lasers, which require axicons), are possible in the case of EBs as varying electromagnetic fields are used for beam deflection. Contrary to a galvanometer-based arrangement for lasers, which feature tilting mirrors for laser scanning, EBs generate a scan pattern by simply deflecting the beam trajectory through an appropriate application of electromagnetic fields. Mirrors, due to their high mass, possess inertia, which delays the response time system, whereas, in the case of EBs, there are no moving parts, resulting in a very responsive apparatus. Consequently, an arrangement can be devised, as illustrated in Fig. A1.13, which takes advantage of the high responsiveness of EBs and generates an annular heat intensity distribution to achieve omnidirectionality. It is important to note that the beam profile of two oscillating EBs at high frequency is expected to act similarly to an annular laser beam profile. However, it can also be argued that a similar, perhaps more robust setup can be conceived with three EBs spaced 120° parts oscillating at high frequency. Thus, further studies in this regard are imperative to conclusively establish the heat intensity distribution around the central feedstock and to arrive at an optimum setup. However, the answer to an optimum setup is most likely to depend on the frequency and amplitude of oscillation for each individual EB.

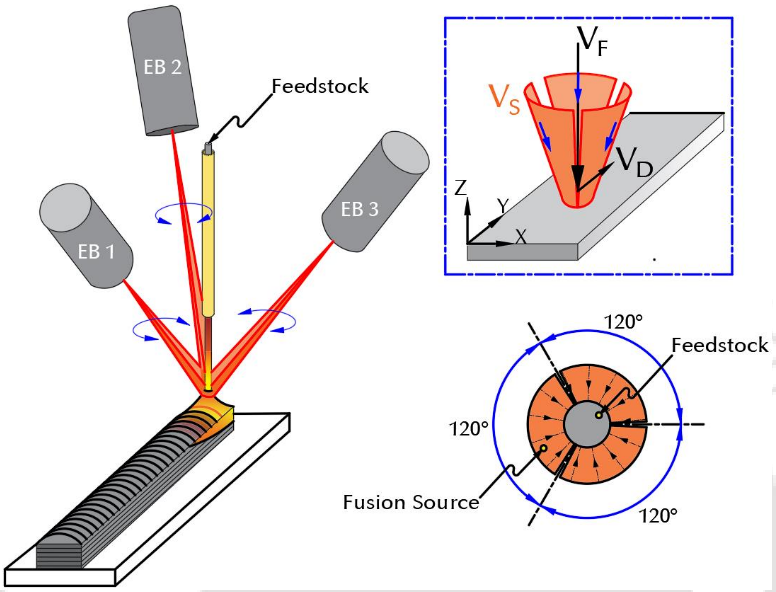

Fig. A1.13: High-frequency oscillating EBs with central feedstock-delivery

(b) Use of hollow cathode electron beam

This method of achieving omnidirectionality in EB cladding requires the use of a special type of EB gun termed a Plasma-Cathode Electron Gun (PCEG*)* [299]*,* schematically shown in Fig. A1.14. In comparison to conventional EB guns, which rely on the hot filament to extract electrons, PCEG first creates plasma within a hollow cathode from which electrons are extracted and subsequently accelerated. This hollow cathode allows the feedstock to be kept central to the fusion source without the requirement of multiple EBs to achieve omnidirectionality.

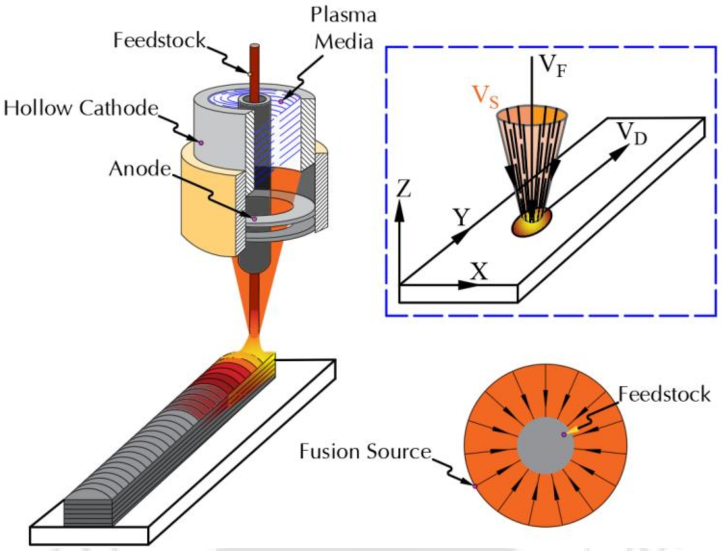

Fig. A1.14: Hollow cathode electron beam gun with coaxial wire feed

A1.3.1.3.3 Method-IV: Dynamically Adjusting Feedstock or Deposition Direction

(a) Dynamically orienting the workpiece to regulate the deposition direction

Dynamic adjustment of the substrate to maintain omnidirectionality, as described in Section 1.3.1, Method IV(a), is adopted for EBs also. Rotation of the substrate to maintain the consistency between the orientation vectors has been successfully commercialized by Sciaky Inc.[300]. The following table (Table A1.1) summarizes all the methods of achieving omnidirectionality discussed so far in the context of DED.

Table A1.1: Methods of achieving omnidirectionality in Directed Energy Deposition: Summary

Sl. No.	**Feedstock and Fusion source**	**Method of achieving omnidirectionality**	**Description of Auxiliary arrangement**	**Ref**	**Detailed Description (Section Ref)**
1.	Wire with Electric Arc/ Plasma	Unified fusion source and feedstock (MIG Welding)	No auxiliary unit is required **(Inherently Omnidirectional)**	[101]	A1.3.1.1
		Coaxial fusion source surrounded by feedstock	Multiple wires, uniformly spaced, feed concentric to the heat source	[291]	A1.3.1.1.1 Method II
		Coaxial feedstock surrounded by fusion source	Hollow tungsten electrode	[292]	A1.3.1.1.2 Method III
		Dynamic adjustment of orientation (**V_F** or (and) **V_D**) vectors	Rotation of substrate	[101]	A1.3.1.1.3 Method IV (a)
			Rotation of feedstock	[101]	A1.3.1.1.3 Method IV (b)
2.	Wire with Laser	Central feedstock surrounded by fusion source	Generation of an annular laser beam profile using axicons	[296]	A1.3.1.2.1 Method III
			Multiple convergent laser beams	[114]	A1.3.1.2.2 Method III
			Rotation of substrate	-	A1.3.1.2.3

		Dynamic adjustment of orientation ($\mathbf{V_F}$ or (and) $\mathbf{V_D}$) vectors	Rotation of feedstock	-	Method-IV
3.	Wire with EB	Coaxial feedstock surrounded by fusion source	High frequency of oscillation of multiple electron beams	-	A1.3.1.3.1 Method III (a)
			Hollow cathode electron beam	[299]	A1.3.1.3.2 Method III (b)
		Dynamic adjustment of orientation ($\mathbf{V_F}$ or (and) $\mathbf{V_D}$) vectors	Rotation of substrate	[300]	A1.3.1.3.3 Method IV
			Rotation of feedstock	-	
4.	Powder with Laser	Coaxial feedstock surrounded by fusion source	Generation of an annular laser beam profile using axicons	[114]	A1.3.1.2.1 Method III
			Multiple convergent laser beams	[114,297]	A1.3.1.2.1 Method III
		Coaxial fusion source surrounded by feedstock	Generation of convergent and coaxial power envelop through a continuous coaxial nozzle	[104,116,141]	A1.3.1.2.2 Method II
			Multiple (usually, but not restricted to 3) powder streams uniformly spaced around the fusion source. (Discrete coaxial nozzle)	[42,110,111]	A1.3.1.2.2 Method III
		Dynamic adjustment of orientation ($\mathbf{V_F}$ or (and) $\mathbf{V_D}$) vectors	Rotation of substrate	-	A1.3.1.2.3 Method IV
			Rotation of feedstock	-	
5.	Powder with EB	Coaxial fusion source surrounded by feedstock	Non-pneumatic coaxial feedstock delivery unit	-	A1.3.1.3.1 Method II

A1.4 Material Extrusion

The extrusion-based AM processes are typically identified by a nozzle (or extruder) through which material under pressure is forced out and deposited on the print bed. Fused Filament Fabrication(FFF), more commonly known as Fused Deposition Modeling (FDM), is a common extrusion-based AM technology for polymers and plastics. FDM is generally assumed to be omnidirectional in nature as the material is extruded through a circular orifice, resulting in uniform track dimensions. Concrete printing, however, requires special arrangements to ensure omnidirectionality. In either case, the source of fusion is carried by the feedstock. In the case of polymer FDM, heat energy carried by the heated polymer is the source of fusion, whereas, for concrete, it is the chemical reaction taking place within the feedstock.

AM, through material extrusion in the field of construction, has unique challenges associated with it. Unlike polymer FDM, square outlet nozzles are preferred over circular ones. This ensures ease in the stacking of layers (especially for large-scale construction) and prevents porosity, as illustrated in Fig. A1.15 [301].

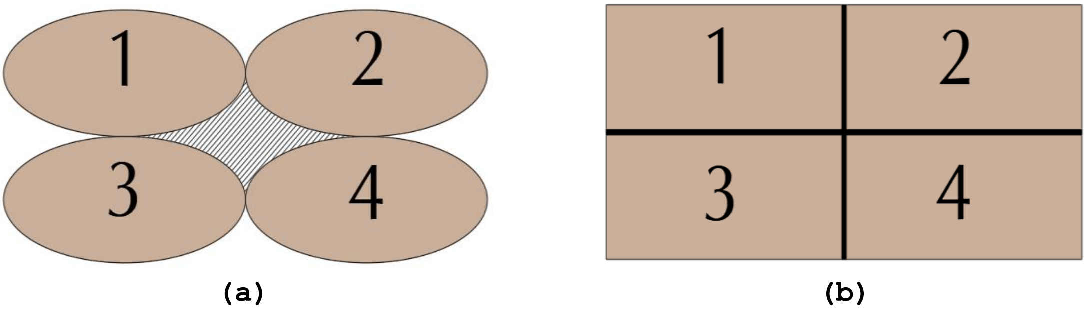

Fig. A1.15: Material extrusion carried out through (a) circular nozzle and (b) rectangular nozzle (the shaded portion in (a) represents porosity due to the elliptical geometry of the track). Adapted with permission from [301], copyright(2018) Elsevier.

The rectangular nozzle also provides a wider area of contact for stacked layers, thus improving resistance to the deformation of uncured layers under self-weight. Also, a track from the rectangular nozzle shows high compressive strength, better surface finish, improved load distribution, and stable build properties [302].

Figure A1.16(a) shows a print bed for a rectangular nozzle, 'a,' 'b,' and 'c' show the relative track dimensions when the print head is moved along its length, width, and diagonal, respectively. This highlights the non-omnidirectional nature of the nozzle. Tracks deposited without any consideration of geometric uniformity often lead to twisted tracks, especially around the corners, as illustrated in Fig. A1.16(b) [281]. These tracks lead to porous and dimensionally inaccurate builds.

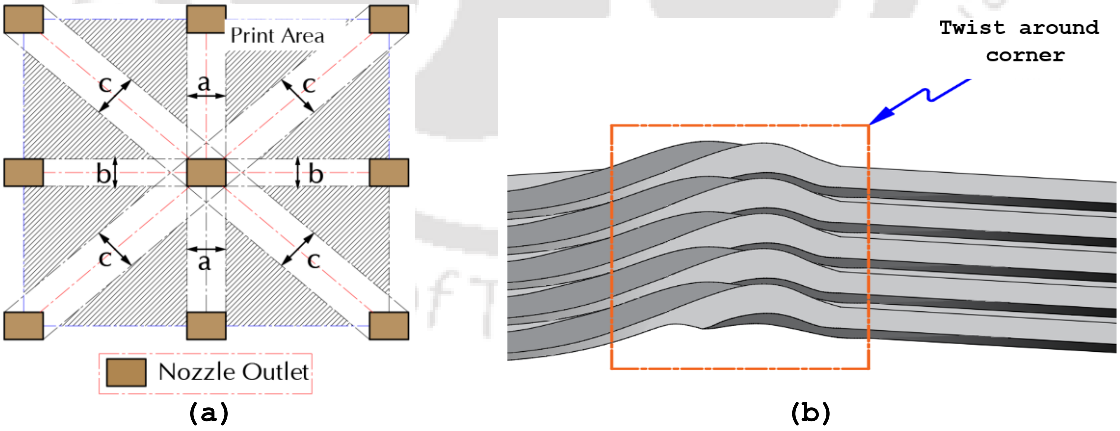

Fig. A1.16: (a) Print bed for a rectangular deposition nozzle and (b) twist in deposited tracks around the corner. Adapted with permission from [281], copyright (2016) Taylor and Francis Group

Check for inherent omnidirectionality

From the above discussion, it can be inferred that FDM processes for polymer printing can be considered inherently omnidirectional as the condition $\boldsymbol{V_S} \parallel \boldsymbol{V_F}, \boldsymbol{V_F} \perp \boldsymbol{V_D}$, and $\boldsymbol{V_D} \perp \boldsymbol{V_S}$ is satisfied. In the case of concrete, however, attributing to the use of square (or rectangular) nozzles, the additional constraint of tangency between nozzle orientation and tool path needs to be imposed to ensure omnidirectionality. This additional constraint requires special arrangements (outlined below), which signifies that the process is not inherently omnidirectional.

A1.4.1 Method-IV: Dynamically Adjusting Feedstock-delivery or Deposition Direction

(a) Dynamically orienting the workpiece to regulate the deposition direction

Similar to TIG/ Plasma cladding (Section A1.3.1.1.3, Method-IV (a)), in this method, the deposition (or extrusion) head is held vertical and stationary while the substrate orients itself such that a geometrically uniform track is deposited. This method requires a rotation of the print bed, which, even though feasible, can become cumbersome for large-area construction. Also, as the print progresses, due to an increase in the weight of the platform (from added layers), a delay in response of the system to directional changes can increase the computational complexity during process planning. These factors contribute to a limited build volume and mass.

(b) Dynamically orienting the feedstock to regulate the feedstock-delivery direction

In this method of achieving omnidirectionality in extrusion-based concrete printing, the deposition head is rotated about a vertical axis such that nozzle orientation remains tangent to the tool path, as illustrated in Fig. A1.17 [281]. This ensures a constant orientation of the feed nozzle relative to the deposition direction, thus achieving omnidirectionality of the machine tool.

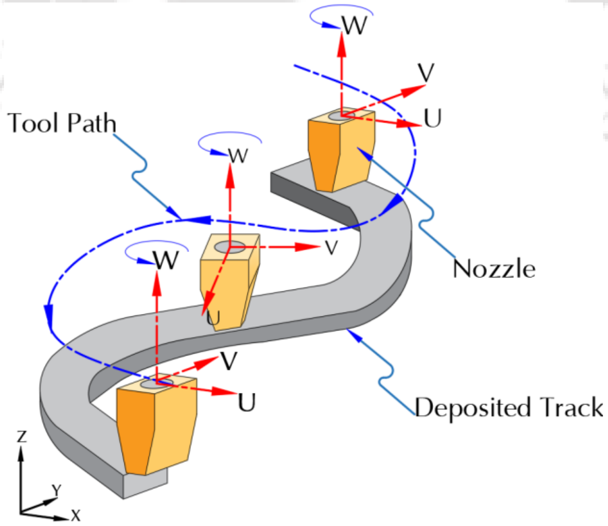

Fig. A1.17: Rotation of deposition nozzle to achieve omnidirectionality and prevent track twisting. Adapted with permission from [281], copyright (2016) Taylor and Francis Group

A1.5 Vat Photopolymerization

Vat photopolymerization (or Stereolithography) employs a UV laser (310-355 nm) to selectively harden the photocurable resin and build the desired geometry layer-by-layer. Most Stereolithography systems use galvanometers to deflect the incoming laser beam onto the photo-resin. A laser beam striking the build surface at an inclination to the vertical results in an elliptical spot rather than a circular one, schematically shown in Fig. A1.18. This beam distortion inadvertently changes processing parameters during part fabrication, thus producing non-homogeneous as-built parts. Given the fact galvanometers are used to scan the layer geometry in most SLA systems, beam correction becomes essential to ensure omnidirectionality.

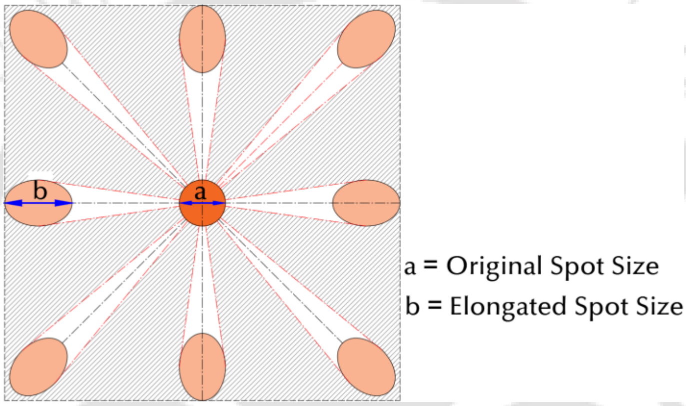

Fig. A1.18: Laser scan field with spot profile at various locations without any corrective measures

Check for Inherent Omnidirectionality

From the above discussion, it can be inferred that VAT photopolymerization is a pre-placed feedstock-based process, where energy beam $\boldsymbol{V_S}$ does not remain perpendicular to the travel direction $\boldsymbol{V_D}$ throughout the build. Thus, the process is not inherently omnidirectional. Ensuring omnidirectionality in VAT photopolymerization, to a large extent, relies on beam correction of the fusion source. Several methods of beam correction exist in the literature [303–306]. The following discussion elaborates on some of the most popular ones. In succession to our previous discussion, the method of 'fusion source beam correction' to ensure omnidirectionality is labeled as 'Method V' here.

A1.5.1 Method-V: Fusion Source Beam Correction

(a) Galvanometric Scanning Systems with F-theta lens

Deflecting a laser beam using a pair of galvo-mirrors to trace the required geometry allows for working in raster and (or) vector mode. Raster implies a collection of individual dots to make up an image, whereas vector suggests a collection of lines. Since a Galvanometric Scanning System (GSS) restricts the motion of the workpiece (in XY plane) and the laser head (unlike flying optics), high scanning speeds (1000 mm/min) can be obtained [307,308].

$F-\theta$ lenses are an essential component of any GSS-based design. They ensure a flat scan field (as illustrated in Fig. A1.19), a small spot diameter at the focal plane, and circular and uniform spot shape anywhere in the scan field (as shown in Fig. A1.20).

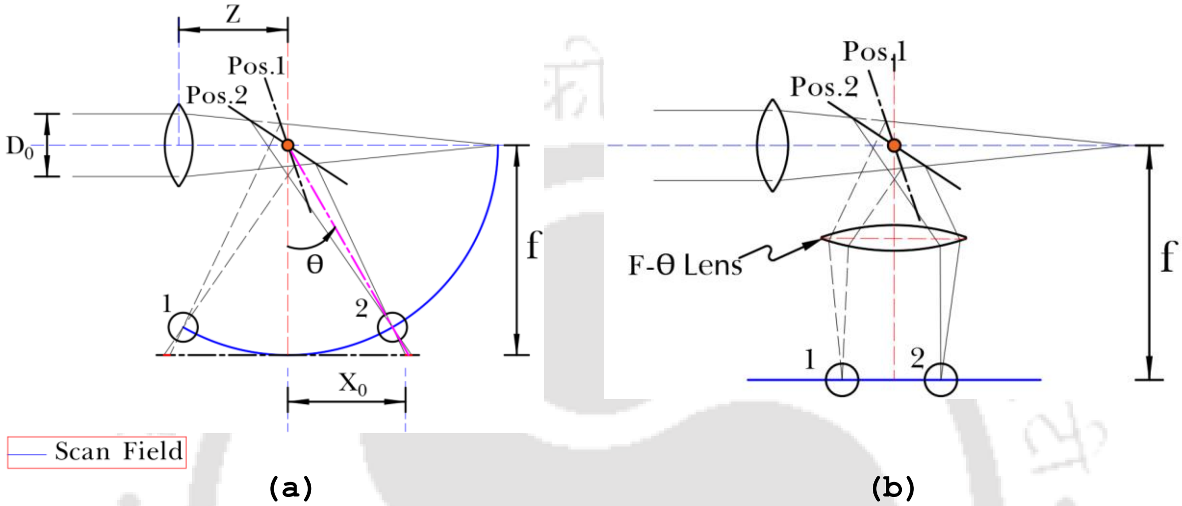

Fig. A1.19: Application of F- θ lens to convert (a) a non-planar scan field to (b) a planar scan field. Adapted from [309], copyright (1978) Optical society of America

Matsuda *et al.*[309], through simple mathematical expressions, presents a general overview of beam distortion in a tilting mirror-type scanning system. These expressions highlight several participating factors that distort the beam during a scan. Ideally, the beam location from a central tilt axis, also termed 'image height' (X), is directly proportional to the scanning angle (θ), and is mathematically expressed as

$$X = f \cdot \theta \tag{A1}$$

However, for a real scanning system without any provision for beam correction, the locus of the focused beam traces an arc (solid blue line in Fig. A1.19 (a)) centered around the tilt axis (highlighted by an orange dot). The image height X_0 is such a case is expressed as

$$X_0 = f \cdot \tan\theta \tag{A2}$$

Using expressions (A1) and (A2), the percentage beam distortion (δ) is expressed as

$$\delta = \frac{X_0 - X}{X} \times 100 \tag{A3}$$

$$\delta = \frac{\tan\theta - \theta}{\theta} \times 100 \tag{A4}$$

The time derivative of the image height (X) results in beam distortion arising from the scanning of the laser beam (or scanning velocity distortion ($\dot{\delta}$)).

$$\dot{\delta} = \frac{\frac{1}{cos^2\theta}\cdot(f\cdot\omega) - f\cdot\omega}{f\cdot\omega} \times 100 \tag{A5}$$

$$= \left(\frac{1}{cos^2\theta} - 1\right) \times 100 \tag{A6}$$

The distorted beam diameter (d) as a function of the angle of tilt (θ), linear distances (f, Z)(schematically represented in Fig. A1.19), and collimated beam diameter (D_0) is expressed as

$$d \approx \frac{f}{f+Z}\cdot D_0 \cdot \left(\frac{1}{cos^2\theta} - 1\right) \tag{A7}$$

At $\theta = 0$, the beam diameter approaches a theoretical condition of 'diffraction-limited.' The $F - \theta$ lenses are prominently used to correct $\frac{1}{cos^2\theta}$ distortion incurred due to scanning velocity and the distortion in beam diameter [309]. Some of these beam corrections are schematically illustrated in Fig. A1.18. Apart from $F - \theta$ lenses other optical methods of beam correction can also be found the literature [310,311].

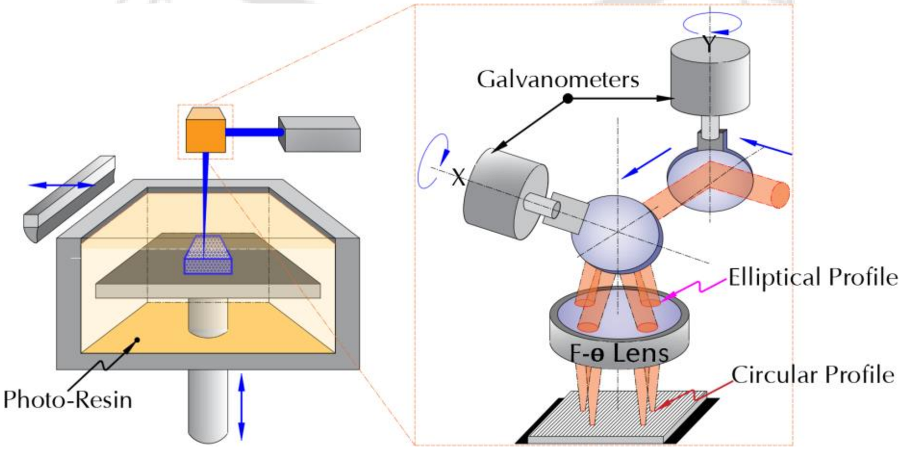

Fig. A1.20: Application of $F - \theta$ lens for the generation of a circular spot profile from an inclined laser beam

From an omnidirectional standpoint, the laser beam converging on the pre-placed feedstock after the F-theta lens remains perpendicular to the travel/ scanning direction throughout the build, thus, restoring omnidirectionality.

(b) Use of flying optics

Unlike galvanometers, which use mirrors to deflect the energy beam, in flying optics, the laser head is mounted on a computer-controlled X-Y platform. The CNC motion of the platform results in the motion of the laser head. The planar (X-Y) motion of laser head to scan layer geometry is generally avoided in Stereolithography due to their slow scan speeds. Increasing laser spot size can counteract this problem but at the expense of print resolution. However, in most cases, flying optics-based systems, schematically illustrated in Fig. A1.21[312,313], are omnidirectional in nature as they maintain perpendicularity between the laser beam and the scanned contour. This ensures a flat scan field and a circular beam profile.

CNC motion inherently possesses accelerations; however, its impact on part properties has not been extensively studied in the literature. It must be noted that these accelerations can influence process parameters (such as scan speed and exposure time) during the build, thus, inducing property variations. The severity of these variations remains a question of further research.

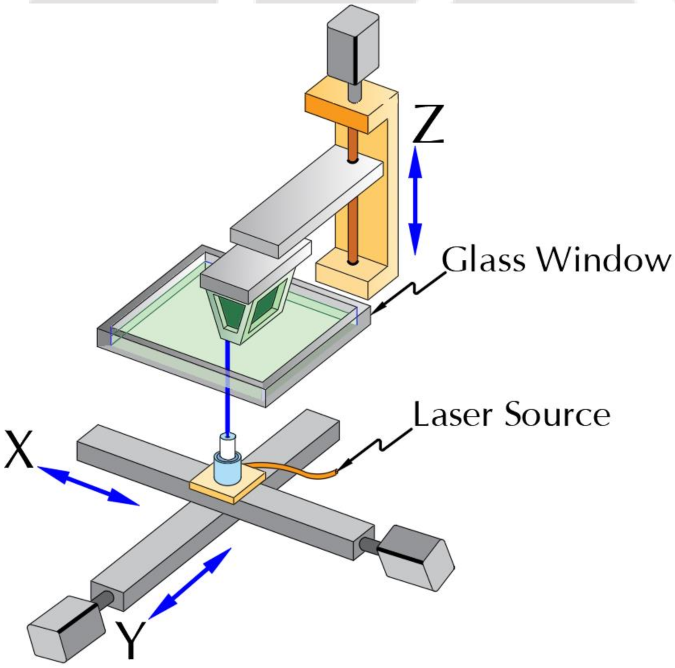

Fig. A1.21: Flying optics-based stereolithography apparatus *(c) Irradiating a layer at a time*

Digital Light Projection (DLP) based systems use Digital Mirror Device (DMD) to selectively (based on layer geometry) project UV light on photocurable resin for part fabrication, schematically illustrated in Fig. A1.22. DMD comprises an array of micro-mirrors that can be individually manipulated to project the light as per the layer geometry currently being processed. The density of micro-mirrors (or pixels) governs the resolution of fabricated parts. Fig. A1.22 schematically shows a DLP-based Stereolithography system where light is projected from the bottom of the vat, and part is fabricated upside down. A similar setup with upright part fabrication is also reported in the literature [11].

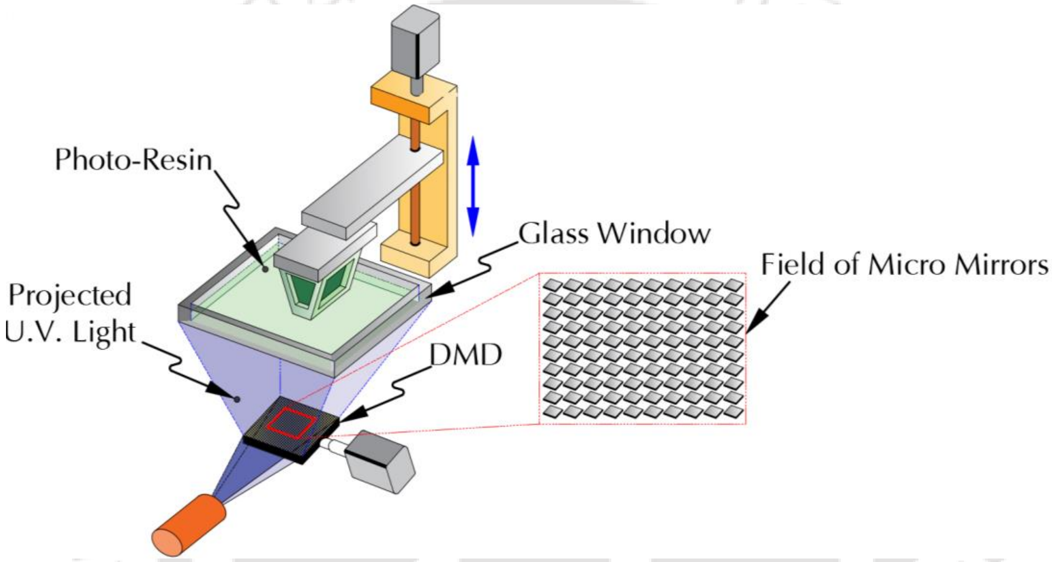

Fig. A1.22: DLP-based Stereolithography system

Several mask-based techniques for Stereolithography can also be found in the literature [314,315]; Fig. A1.23 schematically shows one developed by Bertsch *et al.* [316]. UV Light from the source (1) is projected onto a computer-controlled Liquid Crystal Display (LCD*)* screen (3). The LCD screen comprises liquid crystals, which can either be opaque or transparent to the projected light, thus acting as a mask for the photopolymer. The state of these crystals (opaque or transparent) can be varied, corresponding to the geometry of the layer currently being processed, hence called a dynamic mask. A mirror inclined at 45°, as shown in Fig. A1.23 (projecting mirror(6)), projects the incoming light onto the photopolymer, thus irradiating a layer at a time.

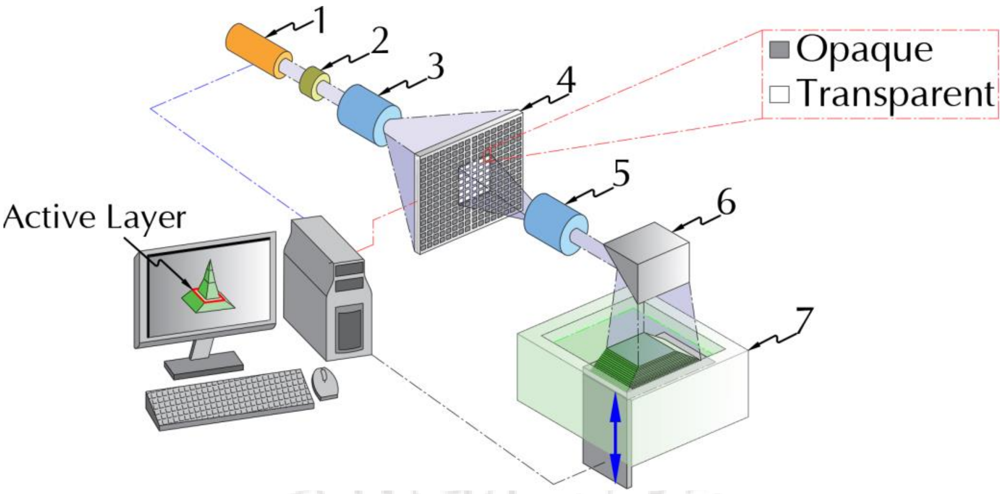

Fig. A1.23: Mask-based Stereolithography. 1-U.V. Light; 2-Shutter; 3-Beam Expander; 4- LCD Screen (Dynamic Mask); 5-Beam Reducer, 6-Projecting Mirror, and 7-Vat with photopolymer

DLP and mask-based systems address the challenge of omnidirectionality by curing each layer in one single irradiation, unlike scanning. This eliminates the necessity of beam correction for obtaining a circular spot profile as the projected light is kept perpendicular to the pre-placed feedstock.

A1.6 Sheet Lamination

Sheet lamination is an AM process that employs pre-placed feedstock. Shaping the feedstock corresponding to the layer geometry can be carried out by multiple means. For example, in the case of paper feedstock, layer geometry is carved out either by a mechanical knife or by a laser. In the case of metals, an end mill is more commonly used. Also, the source of fusion for various sheet-based processes is different. In the case of metals, ultrasonic vibrations for frictional heating and solid-state joining are commonly used, whereas, for polymers, heat-sensitive chemical adhesion is preferred. Fig. A1.24 shows a case of metal sheet lamination where the *Friction Stir Welding (FSW)* process is employed for layer joining.

Check for inherent omnidirectionality for metal feedstock

Sheet lamination AM for metals falls under the category of inherently omnidirectional as the feedstock is pre-placed, and the fusion source remains perpendicular to the travel direction throughout the build.

Check for inherent omnidirectionality for polymer (or paper feedstock)

In the case of a polymer, similar to concrete printing, an additional tangency constraint needs to be imposed to ensure omnidirectionality. Apart from polymers, other feedstock types that can be considered under a similar perspective are paper, cardboard, matboard, wood veneer, foam, leather, etc. [317]. Implementing this additional constraint requires special arrangements and thus makes the process inherently non-omnidirectional. In addition to Method-IV, discussed previously, the use of an energy beam (labeled as Method-VI) can act as a viable method to ensure omnidirectionality in the context of sheet lamination. These two methods are listed below.

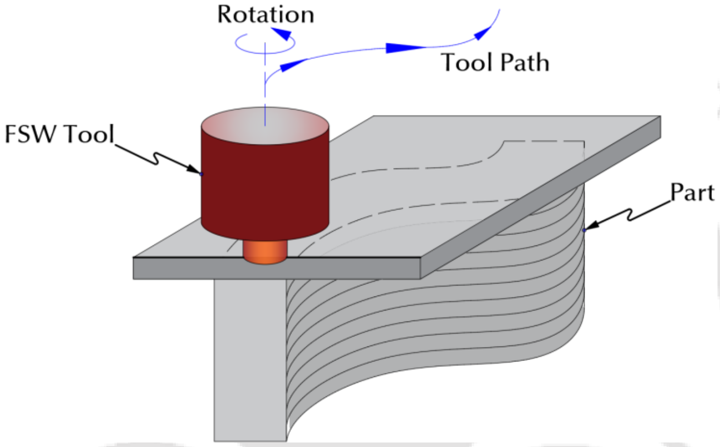

Fig. A1.24: Use of FSW of solid-state joining of layers

A1.6.1 Method-IV: Dynamically Adjusting Cutting Edge Orientation or Cutting Direction

The use of a mechanical knife for cutting layer geometry in sheet-based AM processes has been featured in a few older models [318]. Cutting knives have a single cutting edge, unlike end mills. This requires the cutting edge to be always oriented parallel to the travel direction, as illustrated in Fig. A1.25. Without proper orientation, the cutting head is more likely to tear the paper instead of shearing it, thus limiting the accuracy of the as-built part.

(a) Dynamically orienting the workpiece to regulate the cutting direction

Similar to previous discussions (Section A1.3.1), the method of dynamic substrate orientation to achieve omnidirectionality can be implemented in the case of sheet lamination as well. Through the rotation of the substrate, the orientation of the cutting knife can be regulated such that the cutting edge remains parallel to the travel direction. However, the literature on such systems is very scarce.

(b) Dynamically orienting the cutting head to regulate the cutting-edge orientation

To keep the cutting edge facing towards the travel direction for a given tool path, the rotation of the cutting tool is a popular design choice to achieve omnidirectionality, as illustrated in Fig. A1.25. This method finds widespread application in pattern cutting using a drag knife.

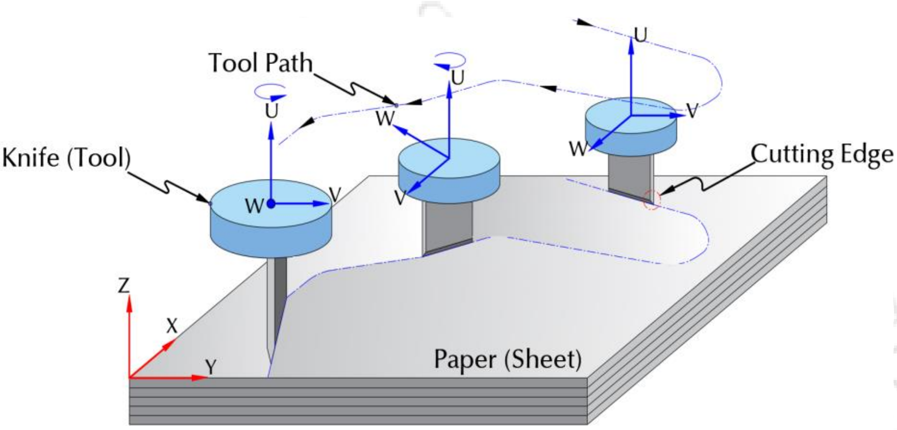

Fig. A1.25: Use of mechanical knife for cutting layer contour on paper/ polymer

A1.6.2 Method V: Use of an Energy Beam

Replacement of a mechanical knife with an energy beam such as a laser is an alternate method of ensuring omnidirectionality in paper or polymer-based sheet lamination. The use of a laser in conjunction with either the F-theta lens or flying optics (discussed in Section A1.5.1) for beam correction can produce parts with precision [319].

A1.7 Powder Bed Fusion

Check for inherent omnidirectionality

In several aspects, *Powder Bed Fusion (PBF)* is similar to Vat Photopolymerization; for example, both utilize pre-placed feedstock and a scanning laser beam as a fusion source. The feedstock in PBF is pre-placed in the X-Y plane, hence $\boldsymbol{V_F} = 0$; however, the relative position between the fusion source $\boldsymbol{V_S}$ and travel direction $\boldsymbol{V_D}$ is not always perpendicular; therefore, this process is not inherently omnidirectional. Method V (a) and (b), discussed previously in the context of VAT photopolymerization (Section A1.5), can be implemented to restore omnidirectionality in PBF processes.

A1.7.1 Method-V: Fusion Source Beam Correction

(a) Galvanometric Scanning Systems with F-theta lens

The use of a galvanometer for scanning layer contour has been discussed in the previous section (Section A1.5). It has been observed that the distortion of the beam is the PBF process due to scanning systems, which can incur significant errors in built parts [320]. A laser beam inclination of 45° reduces power density by 30% and increases interaction time by 40% at the original travel speed [320]. Results by Tang *et al.*[321] shows a deviation of the dimensions of the as-built part by as much as 21% of the original ones as a consequence of an improper scanning system. This deviation was primarily due to the rotating mirror-based scanning system. The use of an F-theta lens, schematically shown in Fig. A1.26, provides a solution for the beam distortion by ensuring a circular spot profile and a flat scan field.

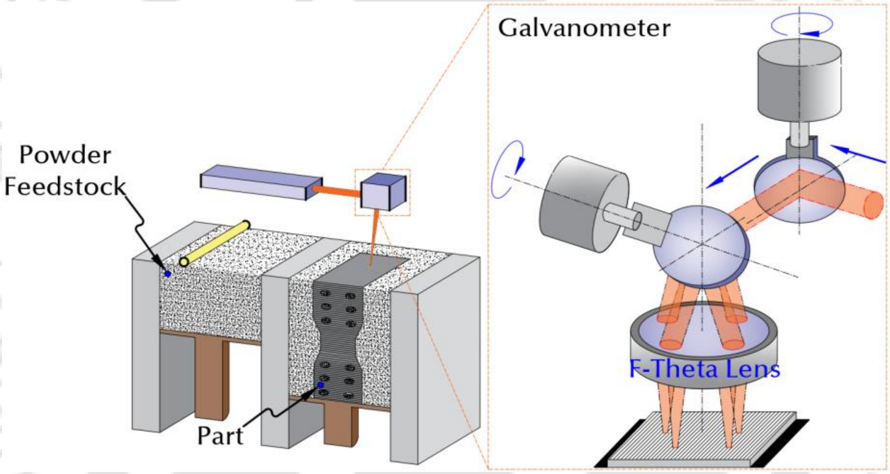

Fig. A1.26: Use of F-Theta lens for ensuring omnidirectionality in Powder Bed Fusion

(b) Use of flying optics

The use of flying optics is not very popular in laser scanning systems due to their high inertia and slow scanning speeds. However, flying optics-based PBF is inherently omnidirectional in nature as they keep the fusion source perpendicular to the travel direction on a pre-placed feedstock throughout the build [322].

A1.8 Material Jetting

Check for inherent omnidirectionality

Most material jetting systems use feedstock (in powder or liquid droplet form) delivered to the build area through a nozzle [323]. The feedstock thus remains parallel to the deposition head and perpendicular to the travel direction. The source of fusion also remains perpendicular to the direction of travel throughout the build. Therefore, it can be concluded that the condition for inherent omnidirectionality ($\boldsymbol{V_S} \parallel \boldsymbol{V_F}, \boldsymbol{V_F} \perp \boldsymbol{V_D}$ and $\boldsymbol{V_D} \perp \boldsymbol{V_S}$) is satisfied, and the process is inherently omnidirectional.

An interesting case of cold spray, which is a type of Material Jetting AM process, is schematically illustrated in Fig. A1.27. This process employs highly accelerated powder particles impinging the substrate to form a metallurgical bond for building parts layer-by-layer. The high kinetic energy carried by the particles is the fusion source in the process. A particle can impact the substrate normally (i.e., perpendicular to the substrate) or at an arbitrary angle, which would result in a decreased powder catchment efficiency. In other words, the more tightly the process adheres to the condition of omnidirectionality, the more efficient it is [324,325].

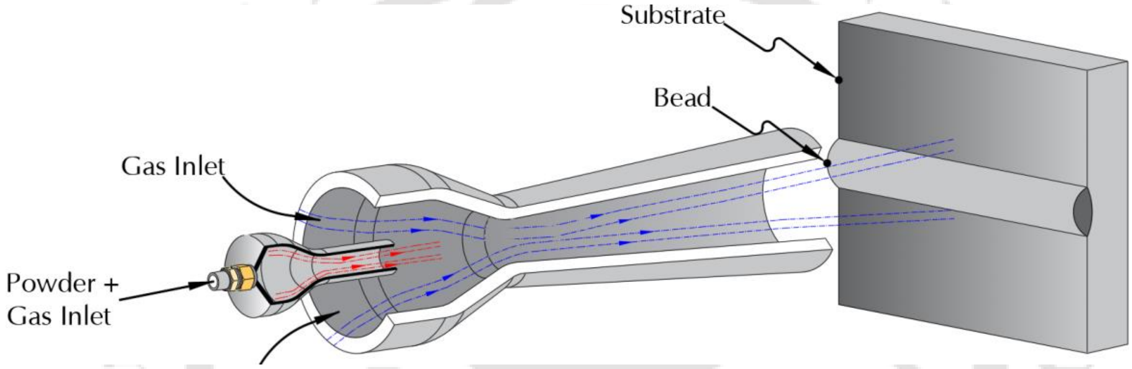

Fig. A1.27: Cold spray deposition process.

A1.9 Binder Jetting

Check for inherent omnidirectionality

Similar to material jetting, binder jetting-based AM processes are inherently omnidirectional. A binder is selectively deposited on the powder bed, which adhesively joins the particles together and builds the geometry layer-by-layer [326–328]. The process keeps the fusion source (which is chemical adhesion) perpendicular to the travel direction throughout the build, and since the feedstock is pre-placed on the print bed, the process falls under the category of inherently omnidirectional.

A1.10 Key Considerations in Method Selection and Ongoing Challenges

The selection of an appropriate method to achieve omnidirectionality for any given AM process requires careful consideration of various factors. More often than not, the selection criteria mostly involve establishing a balanced tradeoff between various desired outputs. For example, in method V, the use of flying optics for beam correction in VAT photopolymerization and PBF provides a robust solution to achieve omnidirectionality; however, it does so at the expense of print time. On the other hand, the use of Galvanometeric Scanning Systems (GSS) with the F-theta lens provides higher print speeds; however, they are limited to a smaller print area. Increasing the print area for a GSS-based system will require more fusion sources operating in sync with each other.

In methods II and III, which suggest maintaining concentricity between feedstock and fusion source, either by surrounding the fusion source with feedstock or vice-versa, an important consideration could be the cost and ease of fabrication. Fabricating a coaxial nozzle with a central fusion source is considerably more cost-effective than three individual laser beams surrounding the feedstock. This cost-effectiveness is even more apparent in the case of EBs. From a 'setup compactness' perspective, generating an annular laser beam with axicons provides a better solution than three separate individual laser beams converging at the plane of deposition. Similarly, the argument can be extended for the case of EBs and TIG/Plasmas cladding, i.e., compared with multiple EBs or filler wires, the use of a hollow electrode offers a better solution. However, the 'ease of fabrication' for such setups, which employ components that are commercially not very common, remains a question of further study.

Method IV suggests a dynamic adjustment of orientation vectors. Orienting the deposition direction through the rotation of the substrate can get increasingly cumbersome as the build progresses, especially in the case of concrete extrusion. With the addition of each layer, the build platform acquires more mass, which restricts rapid and quick correction in the path of deposition. Also, the larger the print bed, the slower the response time, an important factor to be considered during process planning. On the other hand, adjusting the feedstock-delivery direction requires an additional setup, which communicates with the rest of the CNC machine. This additional setup can compromise the total range of travel and print space. Table A1.2 summarizes the important considerations in various methods of achieving omnidirectionality by comparing the advantages and limitations of each.

While the methods discussed so far have been proven by several researchers to be effective in their own right, no 'one' particular method provides a universal solution. Having discussed several of these methods, the field of developing accurate, precise, and omnidirectional AM platforms is wide open for further investigations. This study restricts itself to the plane of deposition; however, several challenges exist in achieving omnidirectionality, which is inclusive of the build direction. For instance, in the case of powder-based DED, it is imperative that the increment in the Z-axis closely matches the deposited bead height. Adhering closely to this criterion ensures the focal plane of the powder stream matches the location of the melt pool for optimum deposition conditions. Deviation from this criterion beyond a specified range (termed passive stability [329]) promotes non-uniform deposition along the Z-axis (build direction). Thus making the AM platform inefficient and the part fabrication costly. Several researchers have explored this challenge, and the solution is often presented in the form of closed-loop feedback control, which monitors the bead height in situ and conveys necessary modifications to the process controller [330,331]. Other AM processes, such as Fused Filament Fabrication (FFF), have also been explored in the light of feedback control to ensure part uniformity [332].

Yet another challenge that is prominent in DED and other similar processes employing CNC motion for precise part fabrication is that of excessive material deposition at the corners. During part fabrication, as the deposition head traces the contour geometry and the area fill, it is subjected to high accelerations (and retardation) at sharp corners. Having a constant feedstock delivery rate, while the deposition/travel speed varies, produces track with over or under-deposited material, thus inducing dimensional inaccuracies. A feedback control similar to the one described previously stands out as a popular solution. Regulating travel/deposition speed or feedstock delivery rate to compensate for CNC accelerations, thus producing uniform deposits, has been explored in the past [156,333]. Even though a lot of studies have been carried out in the past to ensure an omnidirectional AM setup, the field still remains open for further studies.

Table A1.2: Classification of AM processes based on various methods employed to ensure omnidirectionality

Sub Method	Applicable AM Process	Advantages	Limitations
Method I: Coaxial feedstock and fusion source			
Coaxial and feedstock and fusion source	MIG Cladding	No extra setup required	Limited to MIG Cladding
Method II: Coaxial fusion source surrounded by feedstock			
Discrete coaxial power-feed nozzle	Laser Cladding	Easy fabrication, economical, and compact Supports nozzle tilt for increased 'DOF.'[104]	Relatively low catchment efficiency [334]
Continuous coaxial powder feed nozzle	Laser Cladding	Easy fabrication, economical, and compact Increased catchment efficiency	Does not support nozzle tilt
Three filler wires, equally spaced, fed simultaneously	Laser Cladding TIG/Plasma Cladding	Easy fabrication and economical	Not compact, reduced print area
Non-pneumatic powder feed nozzle	EB Cladding	Easy fabrication and economical	Limited literature necessitating further study
Method III: Coaxial feedstock surrounded by fusion source			

Use of axicons for annular heat intensity distribution	Laser Cladding	Compact and economical fabrication High catchment efficiency [114]	Difficult to fabricate
Three convergent, equally spaced fusion sources surrounding the feedstock	Laser Cladding EB Cladding	Easy fabrication High catchment efficiency [114,117]	Expensive setup Large footprint
Use of hollow cathode	EB Cladding TIG/Plasma Cladding	Compact setup thus, promoting large print area Economical as compared to multibeam systems	Difficult to fabricate
Multiple (equally spaced) high-frequency oscillating EBs surrounding a feedstock	EB Cladding	Relatively easy fabrication	Expensive setup Large footprint
Method IV: Dynamically adjusting feedstock-delivery or deposition direction			
Dynamic orientation of deposition direction	EB Cladding TIG/Plasma Cladding Material Extrusion (Concrete)	Easy and compact fabrication with no additional setup required No loss of print area due to any auxiliary arrangement	Slow response time, especially with higher print mass Suitable for smaller print area
Dynamic orientation of the feedstock-delivery direction	EB Cladding TIG/Plasma Cladding Material Extrusion (Concrete)	Quick response time Applicable to a larger print area	Additional setup required to facilitate dynamic orientation Complex process planning
Dynamic orientation of the substrate	Paper/ polymer-based sheet lamination with mechanical knife	No additional components required	Difficult to integrate with other essential units, such as feedstock delivery and collection units.
Dynamic orientation of cutting head	Paper/ polymer-based sheet lamination with mechanical knife	Easy and economical fabrication Easy integration with other essential units with the setup	Requires additional setup
Method V: Fusion source beam correction			
Galvanometric Scanning System (GSS) with F-theta lens	Powder bed fusion SLA	High print speeds	Complex fabrication Relatively expensive Small print area
Use of flying optics	Powder bed fusion SLA	Large print area Easy and economical fabrication	Slow print speeds
Irradiating a layer at a time	DLP based SLA	High print speed Easy fabrication	Small print area Relatively expensive Only applicable to SLA
Method VI: Use of Energy Beam			
Replacement of cutting tool (single-edge knife) with a laser that has F-theta lens correction	Paper/ polymer-based sheet lamination with mechanical knife	High speed of operation	Expensive fabrication Smaller print area
Use of flying optics	Paper/ polymer-based sheet lamination with mechanical knife	Easy and economical fabrication Large print area	Slow speed of operation

A1.11 Summary

Omnidirectionality is an important consideration in AM, which implies invariance in the material and geometric properties of the as-built parts across various AM platforms. The processes of Binder and Material Jetting are inherently omnidirectional; other processes, however, require additional considerations. Table A1.3 categorizes various AM processes based on omnidirectionality. The use of F-theta lenses, layer irradiations, and flying optics are suitable for achieving omnidirectionality in VAT photopolymerization. Powder Bed Fusion, which is similar to VAT photopolymerization in the context of omnidirectionality, employs F-theta lenses and flying optics.

Table A1.3: AM processes categorized based on the property of omnidirectionality

Inherently Omnidirectional	Inherently Non-Omnidirectional
Binder Jetting	Powder bed fusion
Material Jetting	Scanning Vat Photopolymerization
Sheet lamination of Metals	Sheet lamination employing a mechanical knife for cross-section tracing (used for polymers, paper, cardboard, matboard, wood, veneer, foam, leather, etc.)
Material extrusion employing deposition nozzle with circular orifice	Material extrusion employing a deposition nozzle with a square orifice (concrete printing)
MIG cladding-based DED	Directed Energy Deposition (TIG, Plasma, Laser, and Electron Beam)

Sheet lamination-based processes, even though they are mostly omnidirectional, however, some variants require an additional constraint to achieve omnidirectionality. In a very similar fashion, FDM is omnidirectional; however, concrete printing (which falls under the same category as FDM) requires a tangency constraint between the deposition head and the tool path to ensure omnidirectionality. Rotation of cutting and deposition head in sheet lamination (knife-based) and concrete printing, respectively, are employed for addressing the additional tangency constraint.

The majority of DED-based processes rely on achieving the concentricity of the feedstock and fusion source to establish omnidirectionality. Other methods include dynamic adjustment of the feedstock feed direction or travel direction to consistently maintain the relative position of the feedstock, fusion source, and travel direction vectors. Identifying the optimal method to achieve omnidirectionality in a cladding head depends on the economic aspects, the complexity of the part, and the accuracy of the system. A few commercial systems and their preference for achieving omnidirectionality in various AM platforms are summarized in Table A1.4.

Table A1.4: Commercial AM systems and their methods of achieving omnidirectionality

Sl. No	Ref	Make	Inherently Omnidirectional	Method of Achieving Omnidirectionality
Vat Photopolymerization				
1.	[335]	3d Systems	Pre-placed Feedstock & $\because \boldsymbol{V_S} \perp \boldsymbol{V_D} \therefore$ No	Use of F-theta lens
2.	[312]	Autostrade E-Dart	Pre-placed Feedstock & $\because \boldsymbol{V_S} \perp \boldsymbol{V_D} \therefore$ No	Use of flying optics
3.	[336]	EnvisionTec	Pre-placed Feedstock & $\because \boldsymbol{V_S} \perp \boldsymbol{V_D} \therefore$ No	Layer irradiation at a time
Material Jetting				
4.	[337]	GE Aviation	$\because \boldsymbol{V_S} \parallel \boldsymbol{V_F}, \boldsymbol{V_F} \perp \boldsymbol{V_D}, \boldsymbol{V_D} \perp \boldsymbol{V_S} \therefore$ Yes	-
5.	[338]	Stratasys	$\because \boldsymbol{V_S} \parallel \boldsymbol{V_F}, \boldsymbol{V_F} \perp \boldsymbol{V_D}, \boldsymbol{V_D} \perp \boldsymbol{V_S} \therefore$ Yes	-
Binder Jetting				
6.	[339]	ExOne	$\because \boldsymbol{V_S} \parallel \boldsymbol{V_F}, \boldsymbol{V_F} \perp \boldsymbol{V_D}, \boldsymbol{V_D} \perp \boldsymbol{V_S} \therefore$ Yes	-
7.	[340]	HP Metal Jet	$\because \boldsymbol{V_S} \parallel \boldsymbol{V_F}, \boldsymbol{V_F} \perp \boldsymbol{V_D}, \boldsymbol{V_D} \perp \boldsymbol{V_S} \therefore$ Yes	-
Material Extrusion				
8.	[341]	WinSun Co.Ltd	Square nozzle for concrete printing$\therefore$ Yes	Rotation of deposition head
9.	[342]	Desktop Metal	Circular nozzle for metal printing $\therefore$ Yes	-
Sheet Lamination				
10.	[343]	Fabrisonic LLC	Pre-placed Feedstock $\because \boldsymbol{V_S} \perp \boldsymbol{V_D} \therefore$ Yes	-
Powder-Bed Fusion				
11.	[322]	Xact Metal	Pre-placed Feedstock & $\because \boldsymbol{V_S} \perp \boldsymbol{V_D} \therefore$ No	Use of Flying Optics
12.	[344]	Renishaw	Pre-placed Feedstock & $\because \boldsymbol{V_S} \perp \boldsymbol{V_D} \therefore$ No	Use of F-theta Lens
13.	[345]	EoS GmbH	Pre-placed Feedstock & $\because \boldsymbol{V_S} \perp \boldsymbol{V_D} \therefore$ No	Use of F-theta Lens
Directed Energy Deposition				
14.	[346]	Sciaky Inc.	$\because \boldsymbol{V_S} \nparallel \boldsymbol{V_F}, \boldsymbol{V_F} \perp \boldsymbol{V_D}, \boldsymbol{V_D} \perp \boldsymbol{V_S} \therefore$ No	Rotation of substrate
15.	[347]	DMG Mori	$\because \boldsymbol{V_S} \nparallel \boldsymbol{V_F}, \boldsymbol{V_F} \perp \boldsymbol{V_D}, \boldsymbol{V_D} \perp \boldsymbol{V_S} \therefore$ No	Use of continuous and discrete coaxial nozzles
16.	[348]	Additec	$\because \boldsymbol{V_S} \nparallel \boldsymbol{V_F}, \boldsymbol{V_F} \perp \boldsymbol{V_D}, \boldsymbol{V_D} \perp \boldsymbol{V_S} \therefore$ No	Use of annular laser beam
17.	[349]	Gefertec	$\because \boldsymbol{V_S} \parallel \boldsymbol{V_F}, \boldsymbol{V_F} \perp \boldsymbol{V_D}, \boldsymbol{V_D} \perp \boldsymbol{V_S} \therefore$ Yes	-

Symbols:⊥: Perpendicular to; ∥: Parallel to; ⊥ **Not perpendicular to;** ∦: Not parallel to

Appendix 2

The Elemental Composition Test Samples for Evaluation of Static Friction Coefficient

The commonly used powders in additive manufacturing were considered as test samples for the evaluation of the coefficient of static friction. These test samples were prepared and tested as described in Chapter 2. The following Table A2.1 lists the composition of selected powder samples as obtained from the literature.

Table A2.1: Elemental composition of the powder material used as test samples

Metal Powder	Elemental composition (wt%)	Ref
IN 718	C(≤0.08), Si(≤0.35), Mn(≤0.35), Cr(17.0-21.0), Mo(2.8-2.3), Al(0.2-0.8), Cu(≤0.3), Co(≤1.0), Ti(~0.65-1.15), P(≤0.015), S(≤0.015), Nb(4.75-5.5), Mg(≤0.01),), Ni(50.0-55.0.), Fe(Bal.)	[350]
IN 625	C(≤0.01), Si(≤0.5), Mn(≤0.5), Cr(20.0-23.0), Mo(8-10), Al(≤0.4), Cu(≤0.07), Co(≤1.0), Ti(≤0.4), P(≤0.015), S(≤0.015), Nb(3.15-4.15), Fe(≤5.0), Ni(Bal.)	[351]
AISI 1040	Mn(0.60-0.90), C(0.370-0.440), S(≤0.05), P(≤0.040), Fe(98.6-99.00)	[352]
H13	Cr(≤5.2), Mo(≤1.5), V(≤1.0), Si(≤1.0), C(≤0.35) , Mn(≤0.3) , O(≤0.05) , N(≤0.04) , Fe(Bal.)	[353]
AlSi10Mg	Mn(≤0.45), Si(9.0-11.0), Ni(≤0.05), Zn(≤0.1), Sn(≤0.05) , Pb(≤0.05), Mg(0.5-0.45), Cu(≤0.1), Ti(≤0.15), Fe(≤0.55), Al(Bal),	[354]
S7	C(0.45-0.55), Mn(0.20-0.80), Si(0.20-1.0), Cr(3.0-5.0), Mo(1.30-1.80), V(0.20-0.30), Cu(≤0.0.25), P(≤0.03), S(≤0.03), Fe(Bal.)	[355]
18Ni300	C(≤0.03), Si(≤0.03), Ni(~17.0), Cr(≤0.5), Mo(~5.2), Al(≤0.05), Cu(≤0.5), Co(~8.5), Ti(~0.6), Fe(Bal.)	[356]
SS316L	C(≤0.09), Si(≤1.0), Mn(≤2.0), Cr(16.0-18.0), Mo(2.0-3.0) , Fe(Bal.)	[357]
D2	C(1.4-1.6), Cr(11.0-13.0), Ni(≤0.3), Mo(0.7-1.2), Si(≤0.6), V(≤1.1), Fe(Bal.)	[358]

Engineering Drawing of Non-pneumatic Powder Delivery Nozzle

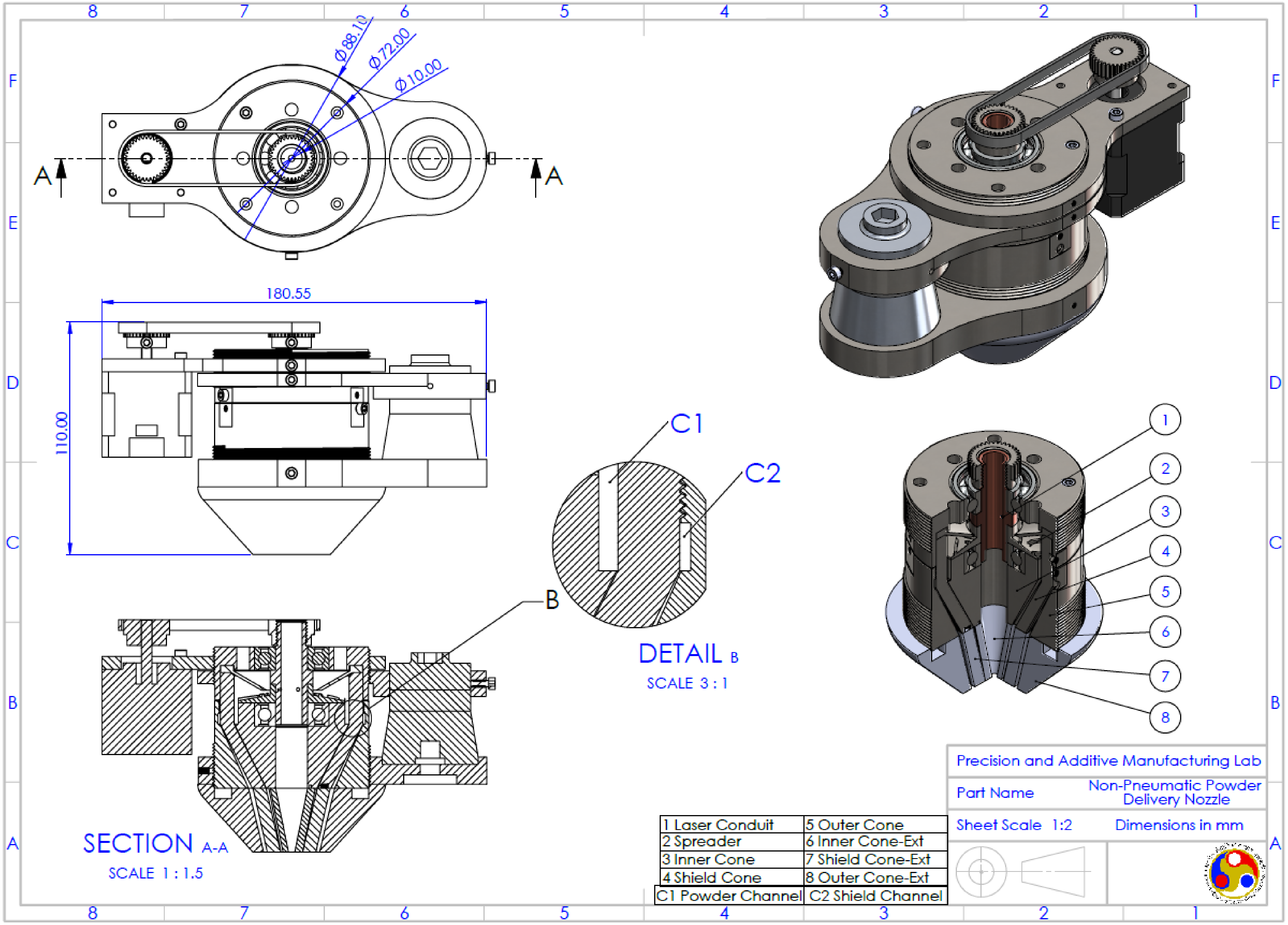

1 Laser Conduit	5 Outer Cone
2 Spreader	6 Inner Cone-Ext
3 Inner Cone	7 Shield Cone-Ext
4 Shield Cone	8 Outer Cone-Ext
C1 Powder Channel	C2 Shield Channel

Precision and Additive Manufacturing Lab

Part Name Non-Pneumatic Powder Delivery Nozzle

Sheet Scale 1:2 Dimensions in mm

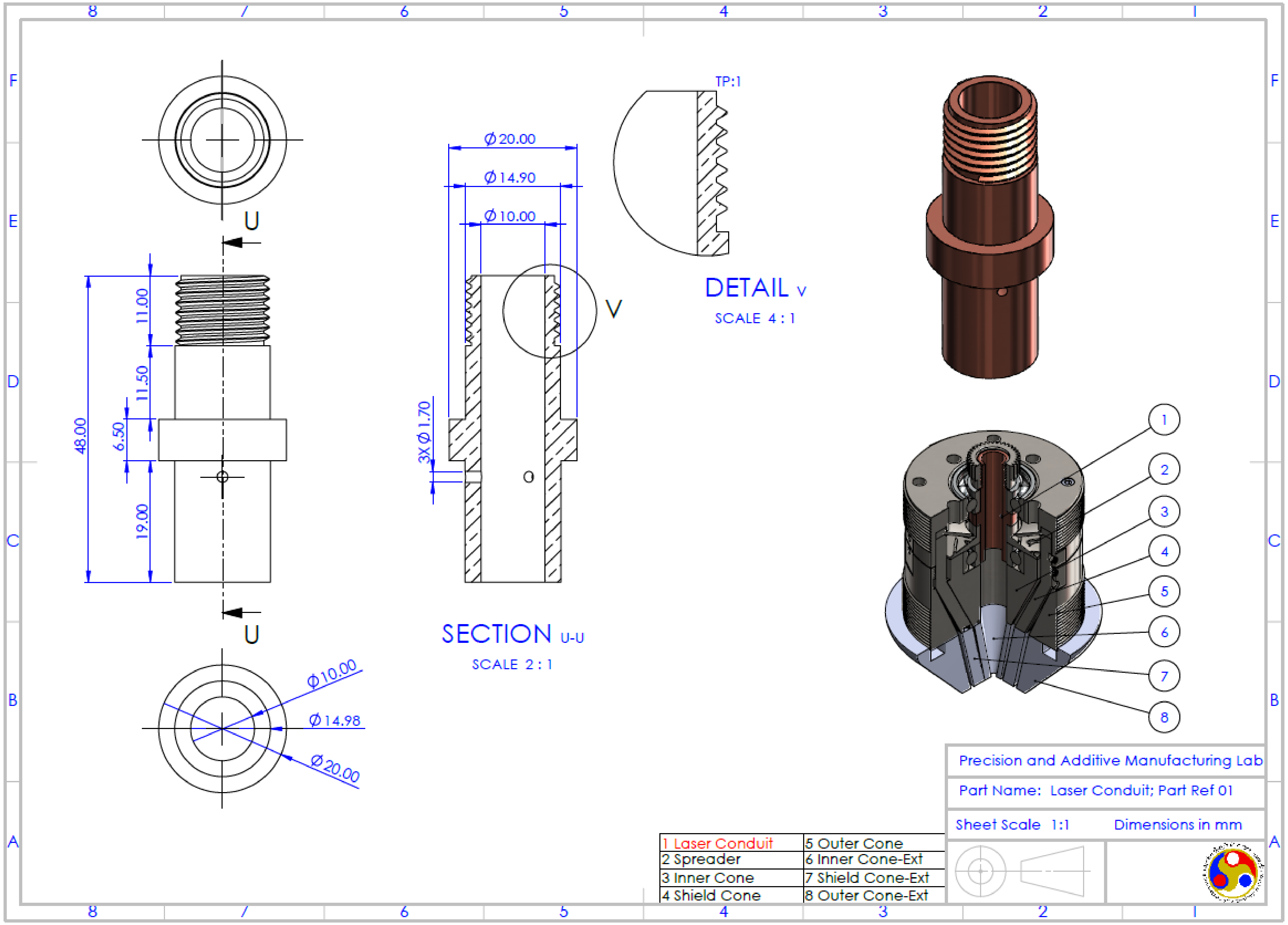

Precision and Additive Manufacturing Lab

Part Name: Laser Conduit; Part Ref 01

Sheet Scale 1:1 Dimensions in mm

1 Laser Conduit	5 Outer Cone
2 Spreader	6 Inner Cone-Ext
3 Inner Cone	7 Shield Cone-Ext
4 Shield Cone	8 Outer Cone-Ext

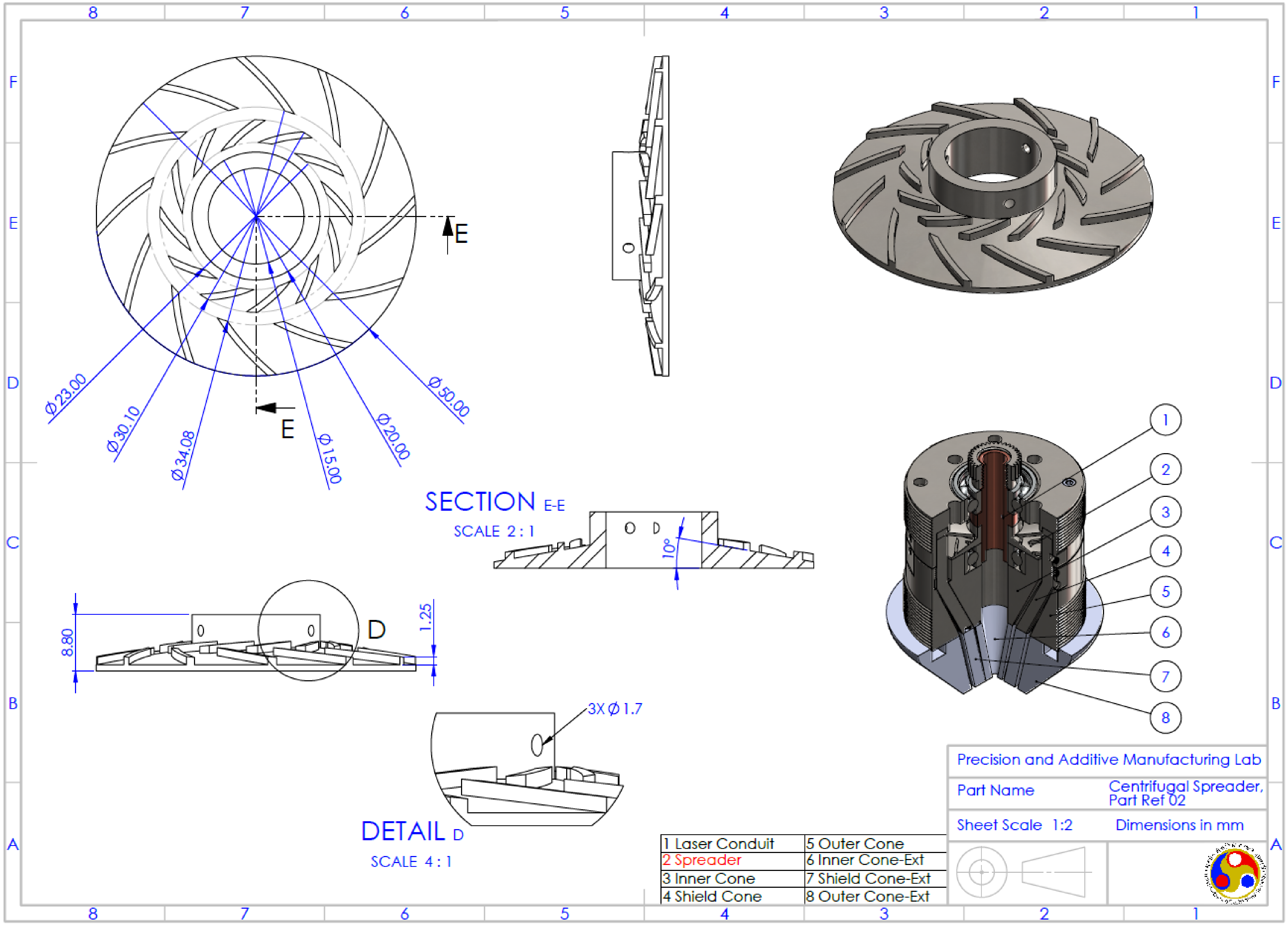

1 Laser Conduit	5 Outer Cone
2 Spreader	6 Inner Cone-Ext
3 Inner Cone	7 Shield Cone-Ext
4 Shield Cone	8 Outer Cone-Ext

Precision and Additive Manufacturing Lab

Part Name Centrifugal Spreader, Part Ref 02

Sheet Scale 1:2 Dimensions in mm

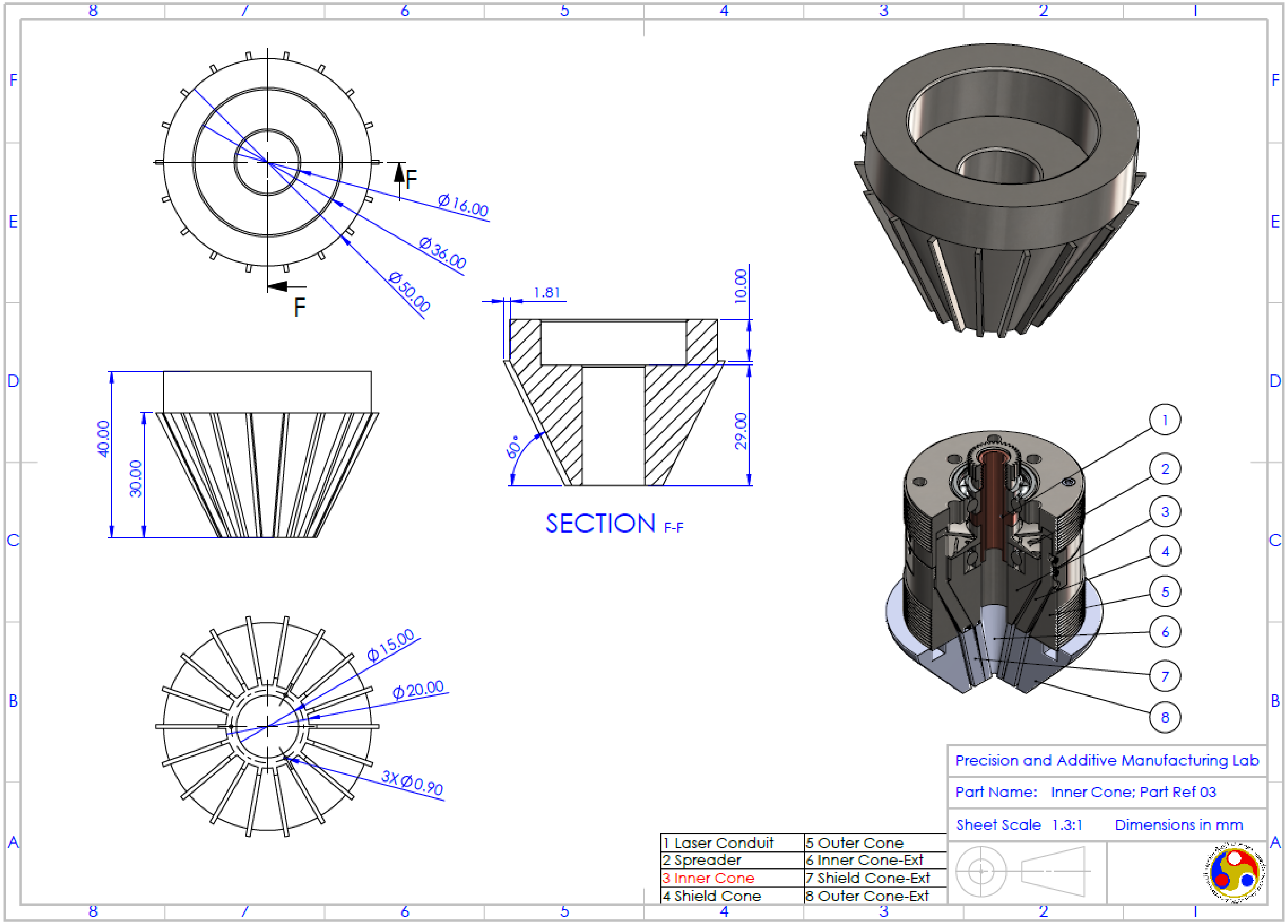

1 Laser Conduit	5 Outer Cone
2 Spreader	6 Inner Cone-Ext
3 Inner Cone	7 Shield Cone-Ext
4 Shield Cone	8 Outer Cone-Ext

Precision and Additive Manufacturing Lab

Part Name: Inner Cone; Part Ref 03

Sheet Scale 1.3:1 Dimensions in mm

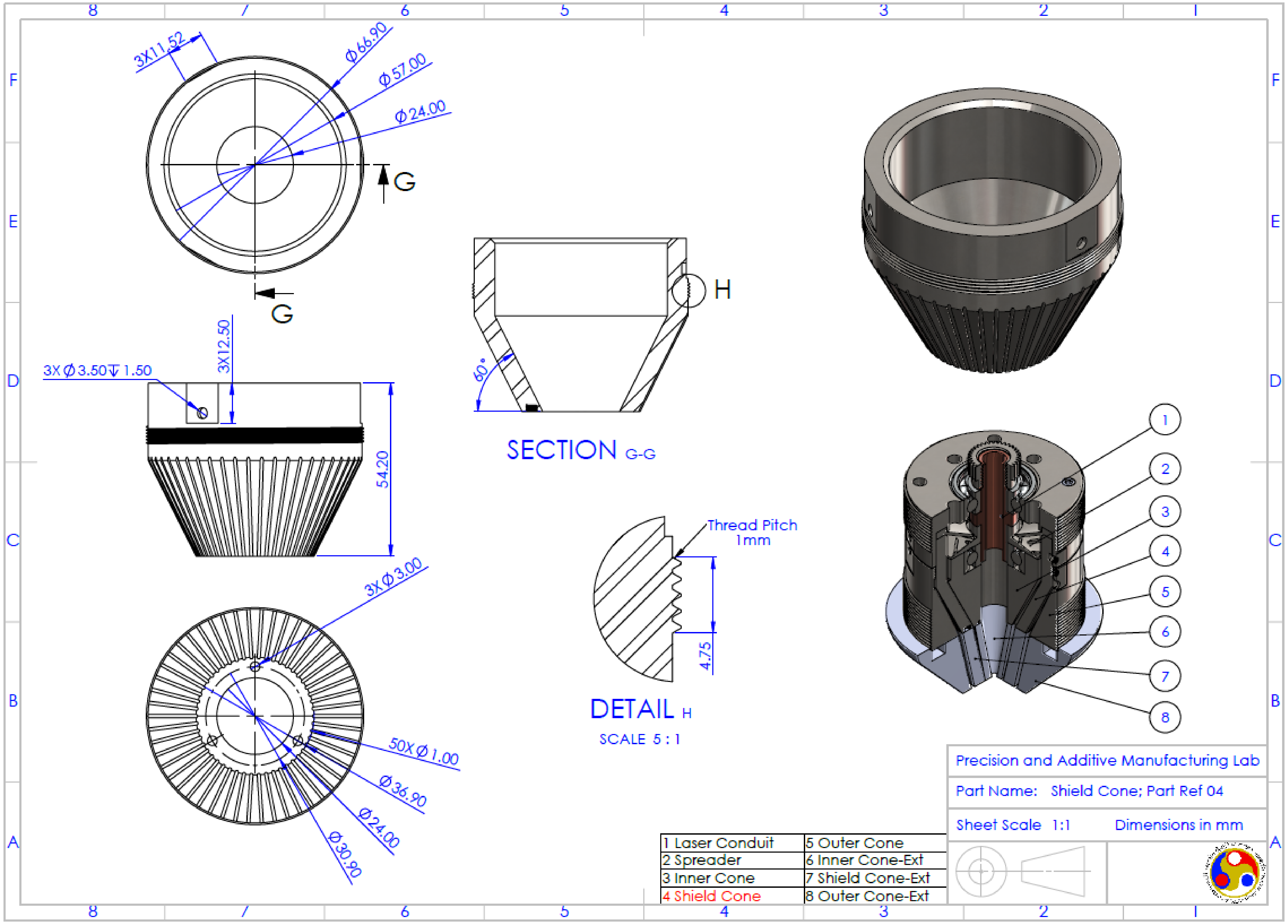

1 Laser Conduit	5 Outer Cone
2 Spreader	6 Inner Cone-Ext
3 Inner Cone	7 Shield Cone-Ext
4 Shield Cone	8 Outer Cone-Ext

Precision and Additive Manufacturing Lab

Part Name: Shield Cone; Part Ref 04

Sheet Scale 1:1 Dimensions in mm

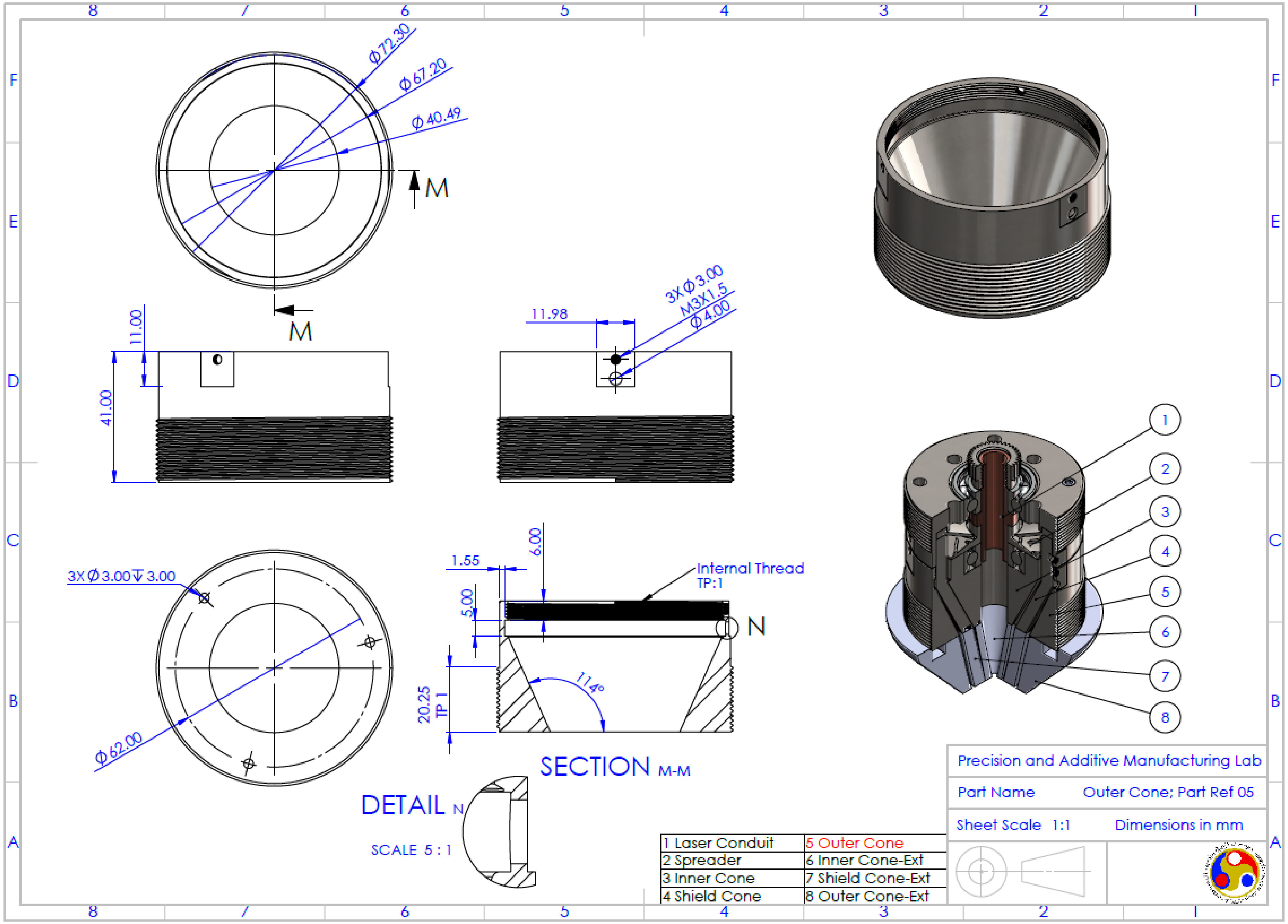

1 Laser Conduit	5 Outer Cone
2 Spreader	6 Inner Cone-Ext
3 Inner Cone	7 Shield Cone-Ext
4 Shield Cone	8 Outer Cone-Ext

Precision and Additive Manufacturing Lab

Part Name Outer Cone; Part Ref 05

Sheet Scale 1:1 Dimensions in mm

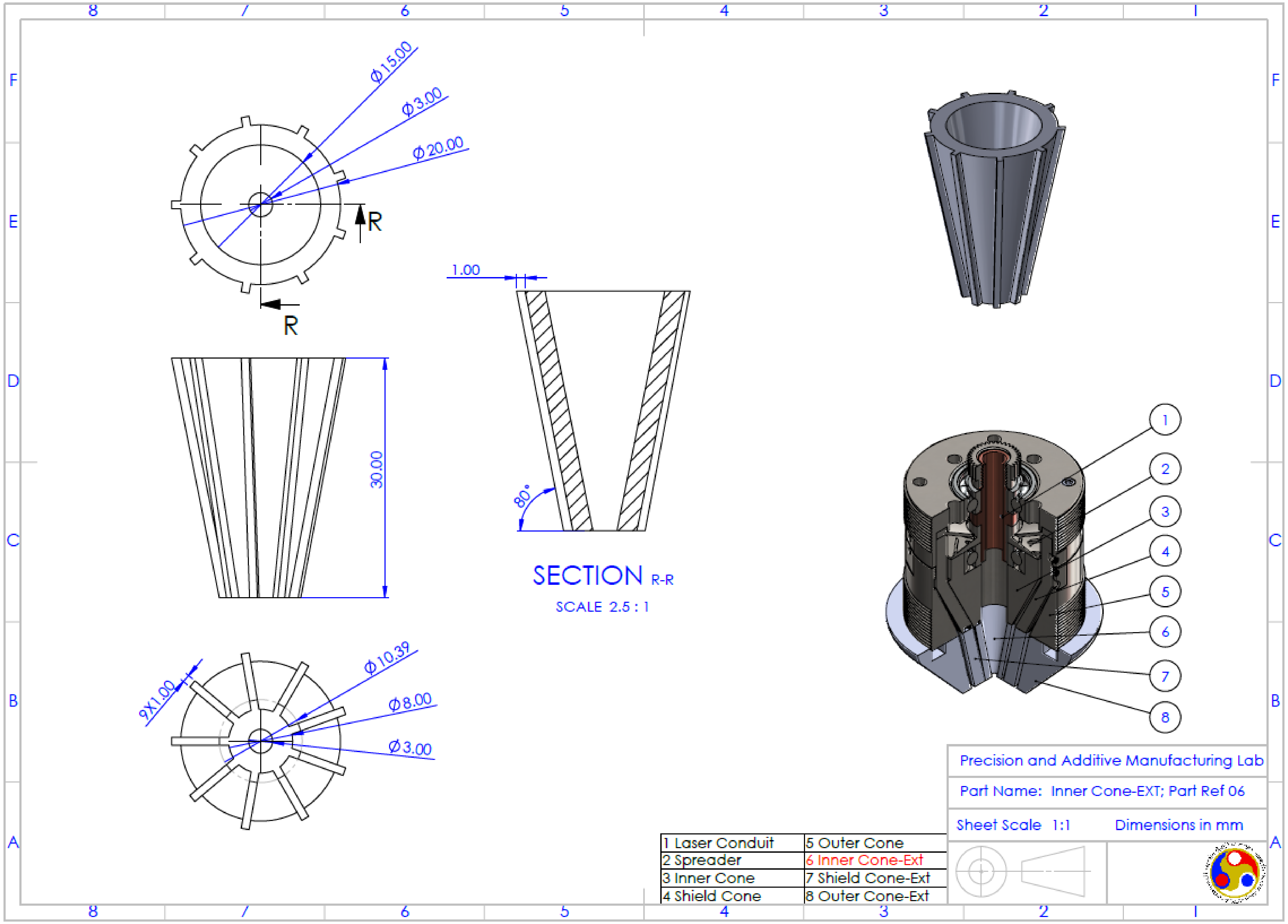

1 Laser Conduit	5 Outer Cone
2 Spreader	6 Inner Cone-Ext
3 Inner Cone	7 Shield Cone-Ext
4 Shield Cone	8 Outer Cone-Ext

Precision and Additive Manufacturing Lab

Part Name: Inner Cone-EXT; Part Ref 06

Sheet Scale 1:1 Dimensions in mm

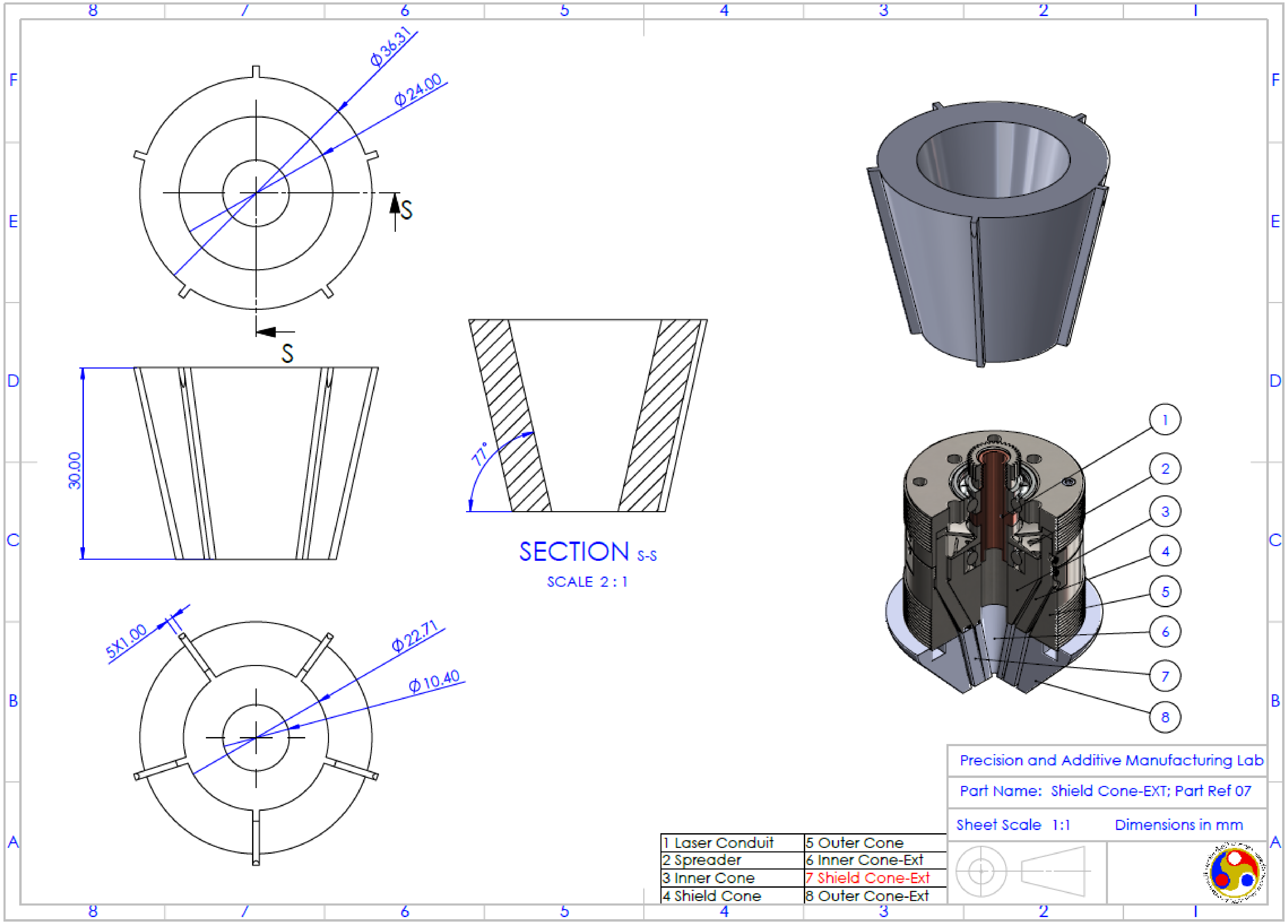

1 Laser Conduit	5 Outer Cone
2 Spreader	6 Inner Cone-Ext
3 Inner Cone	7 Shield Cone-Ext
4 Shield Cone	8 Outer Cone-Ext

Precision and Additive Manufacturing Lab

Part Name: Shield Cone-EXT; Part Ref 07

Sheet Scale 1:1 Dimensions in mm

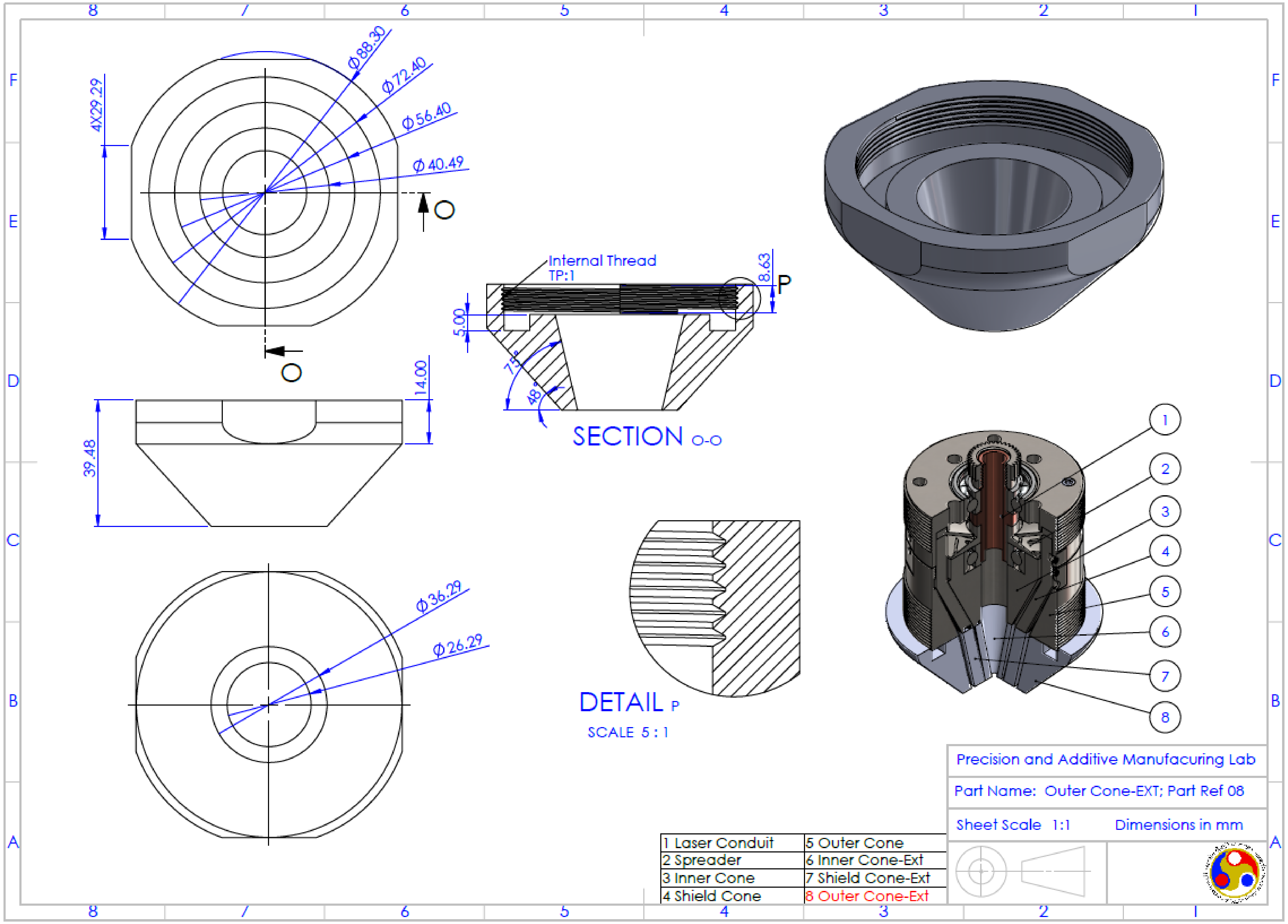

1 Laser Conduit	5 Outer Cone
2 Spreader	6 Inner Cone-Ext
3 Inner Cone	7 Shield Cone-Ext
4 Shield Cone	8 Outer Cone-Ext

Precision and Additive Manufacuring Lab

Part Name: Outer Cone-EXT; Part Ref 08

Sheet Scale 1:1 Dimensions in mm

References

[1] M. Foust, D. Thomsen, R. Stickles, C. Cooper, W. Dodds, Development of the GE Aviation Low Emissions TAPS Combustor for Next Generation Aircraft Engines, in: 50th AIAA Aerosp. Sci. Meet. Incl. New Horizons Forum Aerosp. Expo., American Institute of Aeronautics and Astronautics, Reston, Virigina, 2012. https://doi.org/10.2514/6.2012-936.

[2] L.E. Murr, S.M. Gaytan, F. Medina, H. Lopez, E. Martinez, B.I. MacHado, D.H. Hernandez, L. Martinez, M.I. Lopez, R.B. Wicker, J. Bracke, Next-generation biomedical implants using additive manufacturing of complex cellular and functional mesh arrays, Philos. Trans. R. Soc. A Math. Phys. Eng. Sci. 368 (2010) 1999–2032. https://doi.org/10.1098/rsta.2010.0010.

[3] C. Atwood, M. Griffith, L. Harwell, E. Schlienger, M. Ensz, J. Smugeresky, T. Romero, D. Greene, D. Reckaway, Laser engineered net shaping (LENS^{TM}): A tool for direct fabrication of metal parts, Int. Congr. Appl. Lasers Electro-Optics 1 (1998) E1–E7. https://doi.org/10.2351/1.5059147.

[4] A. Kratky, Production of Hard Metal Alloys, US Pat. 2076952, 1937.

[5] I. Harter, Method of Forming Structures Wholly of Fusion Deposited Weld Metal, (1942) US2299747 A.

[6] Additive Manufacturing State of the Industry Reports | Wohlers Associates, (2020). https://wohlersassociates.com/state-of-the-industry-reports.html (accessed May 11, 2020).

[7] J. Horvath, A Brief History of 3D Printing. In: Mastering 3D Printing, 2014. https://doi.org/10.4324/9781315776798-2.

[8] J. Blindheim, Ø. Grong, U.R. Aakenes, T. Welo, M. Steinert, Hybrid Metal Extrusion & Bonding (HYB) - A new technology for solid-state additive manufacturing of aluminium components, Procedia Manuf. 26 (2018) 782–789. https://doi.org/10.1016/j.promfg.2018.07.092.

[9] A. Bournias-Varotsis, R.J. Friel, R.A. Harris, D.S. Engstrøm, Ultrasonic Additive Manufacturing as a form-then-bond process for embedding electronic circuitry into a metal matrix, J. Manuf. Process. 32 (2018) 664–675. https://doi.org/10.1016/j.jmapro.2018.03.027.

[10] S. Yin, P. Cavaliere, B. Aldwell, R. Jenkins, H. Liao, W. Li, R. Lupoi, Cold spray additive manufacturing and repair: Fundamentals and applications, Addit. Manuf. 21 (2018) 628–650. https://doi.org/10.1016/j.addma.2018.04.017.

[11] Deep dive: Bound Metal Deposition | Desktop Metal, (n.d.).

https://www.desktopmetal.com/article/deep-dive-bound-metal-deposition/ (accessed May 21, 2019).

[12] Deep dive: Bound Metal Deposition^{TM} | Desktop Metal, (n.d.). https://www.desktopmetal.com/article/deep-dive-bound-metal-deposition/ (accessed March 22, 2020).

[13] iro3d - metal 3D printer, (n.d.). http://iro3d.com/ (accessed February 15, 2020).

[14] J.-M. Jouvard, D.F. Grevey, F. Lemoine, A.B. Vannes, Continuous wave Nd : YAG laser cladding modeling : a physical study of track creation during low power processing, (1997) 43–50.

[15] J. Volpp, H.S. Prasad, A. Kaplan, Behavior of heated powder particles on solid surfaces, Procedia Manuf. 25 (2018) 365–374. https://doi.org/10.1016/j.promfg.2018.06.105.

[16] S.M. Thompson, L. Bian, N. Shamsaei, A. Yadollahi, An overview of Direct Laser Deposition for additive manufacturing; Part I: Transport phenomena, modeling and diagnostics, Addit. Manuf. 8 (2015) 36–62. https://doi.org/10.1016/j.addma.2015.07.001.

[17] N. Shamsaei, A. Yadollahi, L. Bian, S.M. Thompson, An overview of Direct Laser Deposition for additive manufacturing; Part II: Mechanical behavior, process parameter optimization and control, Addit. Manuf. 8 (2015) 12–35. https://doi.org/10.1016/j.addma.2015.07.002.

[18] R. Vilar, Laser Powder Deposition, Compr. Mater. Process. 10 (2014) 163–216. https://doi.org/10.1016/B978-0-08-096532-1.01005-0.

[19] L. Xue, J.-Y. Chen, M.U. Islam, J. Pritchard, D. Manente, S. Rush, Laser consolidation of Ni-base IN-738 superalloy for repairing gas turbine blades, 30 (2018) D30–D39. https://doi.org/10.2351/1.5059473.

[20] J.H. Yao, Q.L. Zhang, F.Z. Kong, Laser remanufacturing to improve the erosion and corrosion resistance of metal components, Laser Surf. Modif. Alloy. Corros. Eros. Resist. (2012) 320–354. https://doi.org/10.1016/B978-0-85709-015-7.50009-9.

[21] A. Dass, A. Moridi, State of the art in directed energy deposition: From additive manufacturing to materials design, Coatings 9 (2019) 1–26. https://doi.org/10.3390/COATINGS9070418.

[22] A. Bandyopadhyay, B. V. Krishna, W. Xue, S. Bose, Application of Laser Engineered Net Shaping (LENS) to manufacture porous and functionally graded structures for load bearing implants, J. Mater. Sci. Mater. Med. 20 (2009). https://doi.org/10.1007/s10856-008-3478-2.

[23] A. Saboori, A. Aversa, G. Marchese, S. Biamino, M. Lombardi, P. Fino, Application of

directed energy deposition-based additive manufacturing in repair, Appl. Sci. 9 (2019). https://doi.org/10.3390/app9163316.

[24] F.G. Arcella, F.H. Froes, Components from Powder Using Laser Forming, Jom 52 (2000) 28–30.

[25] D.G. Ahn, Applications of laser assisted metal rapid tooling process to manufacture of molding & forming tools - state of the art, Int. J. Precis. Eng. Manuf. 12 (2011) 925–938. https://doi.org/10.1007/s12541-011-0125-5.

[26] J. Choi, J. Koch, The Direct Metal Deposition of H13 Tool Steel for 3-D Components, JOM (1997) 55–59. https://link.springer.com/content/pdf/10.1007%2FBF02914687.pdf.

[27] Y. Liu, C. Liu, W. Liu, Y. Ma, C. Zhang, Q. Cai, B. Liu, Microstructure and properties of Ti/Al lightweight graded material by direct laser deposition, Mater. Sci. Technol. (United Kingdom) 34 (2018) 945–951. https://doi.org/10.1080/02670836.2017.1412042.

[28] R.M. Mahamood, E.T. Akinlabi, Laser metal deposition of functionally graded Ti6Al4V/TiC, Mater. Des. 84 (2015) 402–410. https://doi.org/10.1016/j.matdes.2015.06.135.

[29] A.N. Jinoop, C.P. Paul, K.S. Bindra, Laser-assisted directed energy deposition of nickel super alloys: A review, Proc. Inst. Mech. Eng. Part L J. Mater. Des. Appl. 233 (2019) 2376–2400. https://doi.org/10.1177/1464420719852658.

[30] G. Totaro, F. De Nicola, P. Caramuta, Local buckling modelling of anisogrid lattice structures with hexagonal cells: An experimental verification, Compos. Struct. 106 (2013) 734–741. https://doi.org/10.1016/j.compstruct.2013.07.031.

[31] M. Li, C. Lai, Q. Zheng, B. Han, H. Wu, H. Fan, Design and mechanical properties of hierarchical isogrid structures validated by 3D printing technique, Mater. Des. 168 (2019) 107664. https://doi.org/10.1016/j.matdes.2019.107664.

[32] S. Kapil, F. Legesse, P. Kulkarni, P. Joshi, A. Desai, K.P. Karunakaran, Hybrid-layered manufacturing using tungsten inert gas cladding, Prog. Addit. Manuf. 1 (2016) 79–91. https://doi.org/10.1007/s40964-016-0005-8.

[33] S. Kapil, P.M. Kulkarni, K.P. Karunakaran, P. Joshi, Development and Characterization of Functionally Graded Materials Using Hybrid Layered Manufacturing, All India Manuf. Technol. Des. Res. Conf. (AIMTDR 2014) December 5 (2014) 1–6.

[34] T.A. Rodrigues, V. Duarte, R.M. Miranda, T.G. Santos, J.P. Oliveira, Current Status and Perspectives on Wire and Arc Additive Manufacturing (WAAM), Materials (Basel). 12 (2019) 1121. https://doi.org/10.3390/ma12071121.

[35] T. DebRoy, H.L. Wei, J.S. Zuback, T. Mukherjee, J.W. Elmer, J.O. Milewski, A.M. Beese,

A. Wilson-Heid, A. De, W. Zhang, Additive manufacturing of metallic components – Process, structure and properties, Prog. Mater. Sci. 92 (2018) 112–224. https://doi.org/10.1016/j.pmatsci.2017.10.001.

[36] K. Mahmood, an Investigation Into Laser Deposition of Machining Chips and Characteristics of the Final Clad, (2012).

[37] M. Dalaee, F. Cheaitani, A. Arabi-Hashemi, C. Rohrer, B. Weisse, C. Leinenbach, K. Wegener, Feasibility study in combined direct metal deposition (DMD) and plasma transfer arc welding (PTA) additive manufacturing, Int. J. Adv. Manuf. Technol. 106 (2020) 4375–4389. https://doi.org/10.1007/s00170-019-04917-2.

[38] D. Ding, Z. Pan, D. Cuiuri, H. Li, Wire-feed additive manufacturing of metal components: technologies, developments and future interests, Int. J. Adv. Manuf. Technol. 81 (2015) 465–481. https://doi.org/10.1007/s00170-015-7077-3.

[39] A.G. Demir, Micro laser metal wire deposition for additive manufacturing of thin-walled structures, Opt. Lasers Eng. 100 (2018) 9–17. https://doi.org/10.1016/j.optlaseng.2017.07.003.

[40] W.U.H. Syed, A.J. Pinkerton, L. Li, A comparative study of wire feeding and powder feeding in direct diode laser deposition for rapid prototyping, Appl. Surf. Sci. 247 (2005) 268–276. https://doi.org/10.1016/j.apsusc.2005.01.138.

[41] T.E. Abioye, J. Folkes, A.T. Clare, A parametric study of Inconel 625 wire laser deposition, J. Mater. Process. Technol. 213 (2013) 2145–2151. https://doi.org/10.1016/j.jmatprotec.2013.06.007.

[42] S. Zekovic, R. Dwivedi, R. Kovacevic, Numerical simulation and experimental investigation of gas–powder flow from radially symmetrical nozzles in laser-based direct metal deposition, Int. J. Mach. Tools Manuf. 47 (2007) 112–123. https://doi.org/10.1016/j.ijmachtools.2006.02.004.

[43] M. Rombouts, G. Maes, W. Hendrix, E. Delarbre, F. Motmans, Surface finish after laser metal deposition, Phys. Procedia 41 (2013) 810–814. https://doi.org/10.1016/j.phpro.2013.03.152.

[44] M. Motta, A.G. Demir, B. Previtali, High-speed imaging and process characterization of coaxial laser metal wire deposition, Addit. Manuf. 22 (2018) 497–507. https://doi.org/10.1016/j.addma.2018.05.043.

[45] E. Louvis, P. Fox, C.J. Sutcliffe, Selective laser melting of aluminium components, J. Mater. Process. Technol. 211 (2011) 275–284. https://doi.org/10.1016/j.jmatprotec.2010.09.019.

[46] D. Gu, Y. Shen, S. Fang, J. Xiao, Metallurgical mechanisms in direct laser sintering of Cu-

CuSn-CuP mixed powder, J. Alloys Compd. 438 (2007) 184–189. https://doi.org/10.1016/j.jallcom.2006.08.040.

[47] A. Simchi, F. Petzoldt, H. Pohl, On the development of direct metal laser sintering for rapid tooling, J. Mater. Process. Technol. 141 (2003) 319–328. https://doi.org/10.1016/S0924-0136(03)00283-8.

[48] J.C. Haley, J.M. Schoenung, E.J. Lavernia, Observations of particle-melt pool impact events in directed energy deposition, Addit. Manuf. 22 (2018) 368–374. https://doi.org/10.1016/j.addma.2018.04.028.

[49] A.J. Pinkerton, L. Li, The significance of deposition point standoff variations in multiple-layer coaxial laser cladding (coaxial cladding standoff effects), Int. J. Mach. Tools Manuf. 44 (2004) 573–584. https://doi.org/10.1016/j.ijmachtools.2004.01.001.

[50] H. Dobbelstein, M. Thiele, E.L. Gurevich, E.P. George, A. Ostendorf, Direct metal deposition of refractory high entropy alloy MoNbTaW, Phys. Procedia 83 (2016) 624–633. https://doi.org/10.1016/j.phpro.2016.08.065.

[51] H.H. Zhu, J.Y.H. Fuh, L. Lu, Formation of Fe-Cu metal parts using direct laser sintering, Proc. Inst. Mech. Eng. Part C J. Mech. Eng. Sci. 217 (2003) 139–147. https://doi.org/10.1243/095440603762554686.

[52] C.N. Kuo, C.K. Chua, P.C. Peng, Y.W. Chen, S.L. Sing, S. Huang, Y.L. Su, Microstructure evolution and mechanical property response via 3D printing parameter development of Al–Sc alloy, Virtual Phys. Prototyp. 15 (2020) 120–129. https://doi.org/10.1080/17452759.2019.1698967.

[53] K.L. Terrassa, J.C. Haley, B.E. MacDonald, J.M. Schoenung, Reuse of powder feedstock for directed energy deposition, Powder Technol. 338 (2018) 819–829. https://doi.org/10.1016/j.powtec.2018.07.065.

[54] C. Kong, P. Carroll, P. Brown, R. Scudamore, The effect of average powder particle size on deposition efficiency, deposit height and surface roughness in the direct metal laser deposition process, (n.d.).

[55] R.M. Clayton, The use of elemental powder mixes in laser-based additive manufacturing, Masters Theses (2013). http://scholarsmine.mst.edu/masters_theses/7194.

[56] O.M. Ivasishin, Cost effective BE PM of Ti alloys in transportation application, Key Eng Mat 188 (2000) 55. https://doi.org/10.4028/www.scientific.net/KEM.188.55.

[57] W. Ul, H.A.Q. Syed, COMBINED DEPOSITION METAL AND POWDER FOR LASER DIRECT MANUFACTURING A thesis submitted to The University of Manchester for the degree of COPYRIGHT, (2006).

[58] W.U.H. Syed, A.J. Pinkerton, L. Li, Combined wire and powder feeding laser direct metal deposition for rapid prototyping, in: Int. Congr. Appl. Lasers Electro-Optics, Laser Institute of America, 2004: p. 609. https://doi.org/10.2351/1.5060287.

[59] F. Wang, J. Mei, X. Wu, Microstructure study of direct laser fabricated compositionally graded ti alloys using simultaneous feed of powder and wire, in: Int. Congr. Appl. Lasers Electro-Optics, Laser Institute of America, 2005: p. 607. https://doi.org/10.2351/1.5060509.

[60] W.U.H. Syed, A.J. Pinkerton, L. Li, A comparative study of wire feeding and powder feeding in direct diode laser deposition for rapid prototyping, Appl. Surf. Sci. 247 (2005) 268–276. https://doi.org/10.1016/j.apsusc.2005.01.138.

[61] K. Mahmood, W.U.H. Syed, A.J. Pinkerton, Innovative reconsolidation of carbon steel machining swarf by laser metal deposition, Opt. Lasers Eng. 49 (2011) 240–247. https://doi.org/10.1016/j.optlaseng.2010.09.014.

[62] A. V. Kumar, A. Dutta, J.E. Fay, Electrophotographic printing of part and binder powders, Rapid Prototyp. J. 10 (2004) 7–13. https://doi.org/10.1108/13552540410512480.

[63] S. Yang, J.R.G. Evans, Metering and dispensing of powder; the quest for new solid freeforming techniques, Powder Technol. 178 (2007) 56–72. https://doi.org/10.1016/j.powtec.2007.04.004.

[64] J.M. Ottino, K. D.V., Mixing and segregation of granular materials, Annu. Rev. Fuild Mech. 32 (2000) 55–91.

[65] J. Bridgwater, Mixing of powders and granular materials by mechanical means - A perspective, Particuology 10 (2012) 397–427. https://doi.org/10.1016/j.partic.2012.06.002.

[66] I. Bauman, D. Ćurić, M. Boban, Mixing of solids in different mixing devices, Sadhana - Acad. Proc. Eng. Sci. 33 (2008) 721–731. https://doi.org/10.1007/s12046-008-0030-5.

[67] L. Pernenkil, C.L. Cooney, A review on the continuous blending of powders, Chem. Eng. Sci. 61 (2006) 720–742. https://doi.org/10.1016/j.ces.2005.06.016.

[68] G.F. Zimmer, The Mechanical Handling of Material, Crosby Lockwood and Son, 1905.

[69] Q. Jinping, S. Baoshan, F. Yanhong, H. Hezhi, Dependence of solids conveying on screw axial vibration in single screw extruders, J. Appl. Polym. Sci. 102 (2006) 2998–3007. https://doi.org/10.1002/app.24658.

[70] W.M. Steen, V.M. Weerasinghe, Screw powder feeders, 4726715, 1988.

[71] A.D. Iams, M.Z. Gao, A. Shetty, T.A. Palmer, Influence of particle size on powder rheology and effects on mass flow during directed energy deposition additive manufacturing, Powder

Technol. 396 (2022) 316–326. https://doi.org/10.1016/j.powtec.2021.10.059.

[72] L.R. Jepson, J.J. Beaman, D.L. Bourell, K.L. Wood, Multi-Material Selective Laser Sintering : Empirical Studies and Hardware Development, NSF Des. Manuf. Grantees Conf. (2000) 2–5.

[73] C. Guo, W. Ge, F. Lin, Dual-Material Electron Beam Selective Melting: Hardware Development and Validation Studies, Engineering 1 (2015) 124–130. https://doi.org/10.15302/j-eng-2015013.

[74] G. Winkler, Analysing the vibrating conveyor, Int. J. Mech. Sci. 20 (1978) 561–570. https://doi.org/10.1016/0020-7403(78)90014-0.

[75] P. Dunst, P. Bornmann, T. Hemsel, W. Sextro, Vibration-Assisted Handling of Dry Fine Powders, Actuators 7 (2018) 18. https://doi.org/10.3390/act7020018.

[76] V. Thayalan, R.G. Landers, Regulation of powder mass flow rate in gravity-fed powder feeder systems, J. Manuf. Process. 8 (2006) 121–132. https://doi.org/10.1016/S1526-6125(06)80007-1.

[77] H. Pan, T. Sparks, Y.D. Thakar, F. Liou, The Investigation of Gravity-Driven Metal Powder Flow in Coaxial Nozzle for Laser-Aided Direct Metal Deposition Process, J. Manuf. Sci. Eng. 128 (2006) 541. https://doi.org/10.1115/1.2162588.

[78] C.A. Alvarez, E. de Moraes Franklin, Intermittent gravity-driven flow of grains through narrow pipes, Phys. A Stat. Mech. Its Appl. 465 (2017) 725–741. https://doi.org/10.1016/j.physa.2016.08.071.

[79] I. Zuriguel, Invited review: Clogging of granular materials in bottlenecks, Pap. Phys. 6 (2014) 1–13. https://doi.org/10.4279/pip.060014.

[80] I. Zuriguel, A. Garcimartín, D. Maza, L.A. Pugnaloni, J.M. Pastor, Jamming during the discharge of granular matter from a silo, Phys. Rev. E - Stat. Nonlinear, Soft Matter Phys. 71 (2005) 1–9. https://doi.org/10.1103/PhysRevE.71.051303.

[81] R.A. Heaton, R.G. Davey, Dispensing rate control mechanism, US Pat. 3329396, 1967.

[82] J.W.F. John, H.K. Parker, S.W. Brookshier, Powder-Delivery Apparatus for Laser-Cladding, US Pat. 20120199564 A1, 2012. https://doi.org/10.1016/j.(73).

[83] F.P. Jeantette, D.M. Keicher, J.A. Romera, L.P. Schanwald, Method and system for producing complex shape objects, US006046426, 4, Apr. 2000, n.d.

[84] S. Akio, I. Yoshinori, N. Steffen, S. Siegfried, Powder Metal Cladding Nozzle, US Pat. 7626136 B2, 2009. https://doi.org/10.1038/incomms1464.

[85] J.-P. Douche, J.-C. Coulon, P. Bouttier, Device for metering pulverulent materials, US Pat. 5104230, 1992. https://doi.org/US005485919A.

[86] N.B. Koebler, Characterization and Optimization of a Powder Feed Nozzle for High Deposition Laser Cladding, Penn State McNair J. 17 (2010) 175–187. http://forms.gradsch.psu.edu/diversity/mcnair/mcnair_jrnl2010/files/Koebler.pdf.

[87] A.F. Theodore, C. Glen, Method and Apparatus for Measuring and Dispensing Predetermined Equal Amounts of Powdered Material, US Pat. 3656518, 1972. https://doi.org/10.1016/j.(73).

[88] G. Arun, K. Heinrich, S. Helmut, Device and process for drawing off very small quantities of powder, US Pat. 4350049, 1982.

[89] W. Chen, M. Hou, K. Lu, Z. Jiang, L. Lam, Granular flows through vertical pipes controlled by an electric field, Phys. Rev. E - Stat. Physics, Plasmas, Fluids, Relat. Interdiscip. Top. 64, 061305 (2001). https://doi.org/10.1103/PhysRevE.64.061305.

[90] W. Balachandran, The study of the performance of an electrostatic valve used for bulk transport of particulate materials, IEEE Trans. Ind. Appl. 33 (1997) 871–878. https://doi.org/10.1109/28.605726.

[91] M. Ghadiri, C.M. Martin, P.A. Arteaga, U. Tüzün, B. Formisani, Evaluation of the single contact electrical clamping force, Chem. Eng. Sci. 61 (2006) 2290–2300. https://doi.org/10.1016/j.ces.2005.05.009.

[92] C.M. Martin, M. Ghadiri, U. Tüzün, B. Formisani, Effect of the electrical clamping forces on the mechanics of particulate solids, Powder Technol. 65 (1991) 37–49. https://doi.org/10.1016/0032-5910(91)80167-H.

[93] G.M. Colver, An interparticle force model for ac-dc electric fields in powders, Powder Technol. 112 (2000) 126–136. https://doi.org/10.1016/S0032-5910(99)00313-7.

[94] G.B. Moslehi, S.A. Self, Electromechanics of Precipitated Particulate Layers, IEEE Trans. Ind. Appl. IA-20 (1984) 1598–1606. https://doi.org/10.1109/TIA.1984.4504647.

[95] A. V. Kumar, Solid free form fabrication using powder deposition, US Pat. 6066285, 2000.

[96] J.B. Olansen, P.F. Dunn, V.J. Novick, Dispensing particles under atmospheric and vacuum conditions using an electrostatic device, J. Appl. Phys. 66 (1989) 6098–6109. https://doi.org/10.1063/1.343591.

[97] J. Lin, W.M. Steen, Design characteristics and development of a nozzle for coaxial laser cladding, J. Laser Appl. 10 (1998) 55–63. https://doi.org/10.2351/1.521821.

[98] A. Lamikiz, I. Tabernero, E. Ukar, S. Martinez, L. N. Lopez de Lacalle, Current Designs of Coaxial Nozzles for Laser Cladding, Recent Patents Mech. Eng. 4 (2012) 29–36. https://doi.org/10.2174/2212797611104010029.

[99] M. Dias Da Silva, K. Partes, T. Seefeld, F. Vollertsen, Comparison of coaxial and off-axis

nozzle configurations in one step process laser cladding on aluminum substrate, J. Mater. Process. Technol. 212 (2012) 2514–2519. https://doi.org/10.1016/j.jmatprotec.2012.06.011.

[100] Y. Li, H. Yang, X. Lin, W. Huang, J. Li, Y. Zhou, The influences of processing parameters on forming characterizations during laser rapid forming, Mater. Sci. Eng. A 360 (2003) 18–25. https://doi.org/10.1016/S0921-5093(03)00435-0.

[101] S. Kapil, P. Kulkarni, P. Joshi, S. Negi, K.P. Karunakaran, Retrofitment of a CNC machine for omni-directional tungsten inert gas cladding, Virtual Phys. Prototyp. 2759 (2018). https://doi.org/10.1080/17452759.2018.1552484.

[102] P.R. Castro, M.O. Edesa, A.A. Gurrutxaga, A.L. Mentxaka, Optimization of the efficiency of the laser metal deposition process applied to high hardness coatings by the analysis of different types of coaxial nozzles, Dyna Ing. e Ind. Spain (2018) 1–10.

[103] G.J. Harris, M. Brandt, Powder Delivery Nozzle, Int. Pub. WO2007022567 AI, 2007.

[104] J.L. Arrizubieta, I. Tabernero, J. Exequiel Ruiz, A. Lamikiz, S. Martinez, E. Ukar, Continuous coaxial nozzle design for LMD based on numerical simulation, Phys. Procedia 56 (2014) 429–438. https://doi.org/10.1016/j.phpro.2014.08.146.

[105] H. Ju, Z.J. Zhang, C.X. Lin, Z.J. Liu, H.L. Jiang, Design optimization and experimental study of coaxial powder-feeding nozzle in the laser cladding process, IOP Conf. Ser. Mater. Sci. Eng. 474 (2019). https://doi.org/10.1088/1757-899X/474/1/012008.

[106] W.P. Ronald, H.L. Omer, Laser cladding device with an improved nozzle, US Pat 20130319325A1, 2017. https://doi.org/10.1037/t24245-000.

[107] Y. Hu, Coaxial nozzle design for laser cladding welding process, US Pat. 20050056628 A1, 2005. https://doi.org/10.1016/j.(73).

[108] S. Nam, H. Cho, C. Kim, Y.-M. Kim, Effect of Process Parameters on Deposition Properties of Functionally Graded STS 316/Fe Manufactured by Laser Direct Metal Deposition, Metals (Basel). 8 (2018) 607. https://doi.org/10.3390/met8080607.

[109] M. Cortina, J.I. Arrizubieta, J.E. Ruiz, A. Lamikiz, E. Ukar, Design and Manufacturing of a Protective Nozzle for Highly Reactive Materials Processing via Laser Material Deposition, Procedia CIRP 68 (2018) 387–392. https://doi.org/10.1016/j.procir.2017.12.100.

[110] J. Wu, P. Zhao, H. Wei, Q. Lin, Y. Zhang, Development of powder distribution model of discontinuous coaxial powder stream in laser direct metal deposition, Powder Technol. 340 (2018) 449–458. https://doi.org/10.1016/j.powtec.2018.09.032.

[111] H. Tan, W. Shang, F. Zhang, A.T. Clare, X. Lin, J. Chen, W. Huang, Process mechanisms based on powder flow spatial distribution in direct metal deposition, J. Mater. Process.

Technol. 254 (2018) 361–372. https://doi.org/10.1016/j.jmatprotec.2017.11.026.

[112] V. Kovalenko, J. Yao, Q. Zhang, M. Anyakin, X. Hu, R. Zhuk, Development of Multichannel Gas-powder Feeding System Coaxial with Laser Beam, Procedia CIRP 42 (2016) 96–100. https://doi.org/10.1016/j.procir.2016.02.197.

[113] C. Zhong, N. Pirch, A. Gasser, R. Poprawe, J. Schleifenbaum, The Influence of the Powder Stream on High-Deposition-Rate Laser Metal Deposition with Inconel 718, Metals (Basel). 7 (2017) 443. https://doi.org/10.3390/met7100443.

[114] A. Jeromen, A. Kuznetsov, E. Govekar, M. Kondo, M. Kotar, Annular laser beam based direct metal deposition, Procedia CIRP 74 (2018) 222–227. https://doi.org/10.1016/j.procir.2018.08.099.

[115] H.K. Lee, Effects of the cladding parameters on the deposition efficiency in pulsed Nd:YAG laser cladding, J. Mater. Process. Technol. 202 (2008) 321–327. https://doi.org/10.1016/j.jmatprotec.2007.09.024.

[116] U. de Oliveira, V. Ocelík, J.T.M. De Hosson, Analysis of coaxial laser cladding processing conditions, Surf. Coatings Technol. 197 (2005) 127–136. https://doi.org/10.1016/j.surfcoat.2004.06.029.

[117] A. Kuznetsov, A. Jeromen, G. Levy, M. Fujishima, E. Govekar, Annular laser beam cladding process feasibility study, Phys. Procedia 83 (2016) 647–656. https://doi.org/10.1016/j.phpro.2016.08.067.

[118] F. Mazzucato, S. Tusacciu, M. Lai, S. Biamino, M. Lombardi, A. Valente, Monitoring Approach to Evaluate the Performances of a New Deposition Nozzle Solution for DED Systems, Technologies 5 (2017) 29. https://doi.org/10.3390/technologies5020029.

[119] W. Wang, L. L, High-Quality High-Material-Usage Multiple-Layer Laser Deposition of Nickel Alloys Using Sonic or Ultrasonic Vibration Powder Feeding, Proc. Inst. Mech. Eng. Part B J. Eng. Manuf. 225 (2011) 130–139. https://doi.org/10.1177/09544054JEM2128.

[120] D.M. Goodarzi, J. Pekkarinen, A. Salminen, Effect of process parameters in laser cladding on substrate melted areas and the substrate melted shape, J. Laser Appl. 27 (2015) S29201. https://doi.org/10.2351/1.4906376.

[121] K. Shah, H. Khurshid, I. ul Haq, S. Anwar, S.A. Shah, Numerical modelling of pulsed and continuous wave direct laser deposition of Ti-6Al-4V and Inconel 718, Int. J. Adv. Manuf. Technol. 95 (2018) 847–860. https://doi.org/10.1007/s00170-017-1224-y.

[122] Y. Kakinuma, M. Mori, Y. Oda, T. Mori, M. Kashihara, A. Hansel, M. Fujishima, Influence of metal powder characteristics on product quality with directed energy deposition of Inconel 625, CIRP Ann. - Manuf. Technol. 65 (2016) 209–212.

https://doi.org/10.1016/j.cirp.2016.04.058.

[123] Z. Wang, T.A. Palmer, A.M. Beese, Effect of processing parameters on microstructure and tensile properties of austenitic stainless steel 304L made by directed energy deposition additive manufacturing, Acta Mater. 110 (2016) 226–235. https://doi.org/10.1016/j.actamat.2016.03.019.

[124] W. Wang, A.J. Pinkerton, L. Li, A gas-free powder delivery system for 100% deposition efficiency in Direct Laser Deposition, ICALEO 2008 - 27th Int. Congr. Appl. Lasers Electro-Optics, Congr. Proc. 801 (2008) 415–423. https://doi.org/10.2351/1.5061341.

[125] J.B. Knight, C.G. Fandrich, C. Ning Lau, H.M. Jaeger, S.R. Nagel, Density relaxation in a vibration, Phys. Rev. E 51 (1995).

[126] S. Chianrabutra, B.G. Mellor, S. Yang, A Dry Powder Material Delivery Device for Multiple Material Additive Manufacturing, Proc. Solid Free. Fabr. Symp. (2014) 36–48. https://sffsymposium.engr.utexas.edu/sites/default/files/2014-005-Chianrabutra.pdf.

[127] X. Zhang, C. Wei, Y.-H. Chueh, L. Li, An Integrated Dual Ultrasonic Selective Powder Dispensing Platform for Three-Dimensional Printing of Multiple Material Metal/Glass Objects in Selective Laser Melting, J. Manuf. Sci. Eng. 141 (2018) 011003. https://doi.org/10.1115/1.4041427.

[128] S.J. Wolff, H. Wu, N. Parab, C. Zhao, K.F. Ehmann, T. Sun, J. Cao, In-situ high-speed X-ray imaging of piezo-driven directed energy deposition additive manufacturing, Sci. Rep. 9 (2019) 1–14. https://doi.org/10.1038/s41598-018-36678-5.

[129] C. Zhong, T. Biermann, A. Gasser, R. Poprawe, Experimental study of effects of main process parameters on porosity, track geometry, deposition rate, and powder efficiency for high deposition rate laser metal deposition, J. Laser Appl. 27 (2015) 042003. https://doi.org/10.2351/1.4923335.

[130] J.C. Haley, J.M. Schoenung, E.J. Lavernia, Observations of particle-melt pool impact events in directed energy deposition, Addit. Manuf. 22 (2018) 368–374. https://doi.org/10.1016/j.addma.2018.04.028.

[131] H. Tan, F. Zhang, R. Wen, J. Chen, W. Huang, Experiment study of powder flow feed behavior of laser solid forming, Opt. Lasers Eng. 50 (2012) 391–398. https://doi.org/10.1016/j.optlaseng.2011.10.017.

[132] J. Volpp, Impact of fume particles in the keyhole vapour, Appl. Phys. A Mater. Sci. Process. 125 (2019) 1–7. https://doi.org/10.1007/s00339-018-2346-2.

[133] Y. Yang, X. Li, Experimental and analytical study of ultrasonic micro powder feeding, J. Phys. D. Appl. Phys. 36 (2003) 1349–1354. https://doi.org/10.1088/0022-

3727/36/11/316.

[134] S. Matsusaka, K. Yamamoto, H. Masuda, Micro-feeding of a fine powder using a vibrating capillary tube, Adv. Powder Technol. 7 (1996) 141–151. https://doi.org/10.1016/S0921-8831(08)60509-9.

[135] X. Lu, S. Yang, J.R.G. Evans, Studies on ultrasonic microfeeding of fine powders, J. Phys. D. Appl. Phys. 39 (2006) 2444–2453. https://doi.org/10.1088/0022-3727/39/11/020.

[136] S. Yang, J.R.G. Evans, Acoustic initiation of powder flow in capillaries, Chem. Eng. Sci. 60 (2005) 413–421. https://doi.org/10.1016/j.ces.2004.07.124.

[137] C. Wei, H. Gu, X. Zhang, Y. hui Chueh, L. Li, Hybrid ultrasonic and mini-motor vibration-induced irregularly shaped powder delivery for multiple materials additive manufacturing, Addit. Manuf. 33 (2020) 101138. https://doi.org/10.1016/j.addma.2020.101138.

[138] D. Corbin, A. Nassar, E.W. Reutzel, Effect of directed energy deposition processing parameters on laser deposited Inconel ® 718 : External morphology, (2017). https://doi.org/10.2351/1.4977476.

[139] J. Lin, W.M. Steen, Powder flow and catchment during coaxial laser cladding, Lasers Mater. Process. 3097 (2010) 517–528. https://doi.org/10.1117/12.281111.

[140] A.J. Pinkerton, An analytical model of beam attenuation and powder heating during coaxial laser direct metal deposition, J. Phys. D. Appl. Phys. 40 (2007) 7323–7334. https://doi.org/10.1088/0022-3727/40/23/012.

[141] I. Tabernero, A. Lamikiz, E. Ukar, L.N. López De Lacalle, C. Angulo, G. Urbikain, Numerical simulation and experimental validation of powder flux distribution in coaxial laser cladding, J. Mater. Process. Technol. 210 (2010) 2125–2134. https://doi.org/10.1016/j.jmatprotec.2010.07.036.

[142] V. Kovalenko, J. Yao, Q. Zhang, M. Anyakin, X. Hu, R. Zhuk, Development of Multichannel Gas-powder Feeding System Coaxial with Laser Beam, Procedia CIRP 42 (2016) 96–100. https://doi.org/10.1016/j.procir.2016.02.197.

[143] R. Koike, R. Ashida, K. Yamazaki, Y. Kakinuma, T. Aoyama, Graphical evaluation method for void distribution in direct energy deposition, Procedia Manuf. 6 (2016) 105–112. https://doi.org/10.1016/j.promfg.2016.11.014.

[144] F.M. Sciammarella, B.S. Najafabadi, Processing Parameter DOE for 316L Using Directed Energy Deposition, (2018). https://doi.org/10.3390/jmmp2030061.

[145] J.C. Heigel, P. Michaleris, E.W. Reutzel, Thermo-mechanical model development and validation of directed energy deposition additive manufacturing of Ti-6Al-4V, Addit. Manuf. 5 (2015) 9–19. https://doi.org/10.1016/j.addma.2014.10.003.

[146] A.J. Pinkerton, L. Li, Multiple-layer laser deposition of steel components using gas- and water-atomised powders: The differences and the mechanisms leading to them, Appl. Surf. Sci. 247 (2005) 175–181. https://doi.org/10.1016/j.apsusc.2005.01.083.

[147] J. Jiang, Y. Ma, Path planning strategies to optimize accuracy, quality, build time and material use in additive manufacturing: A review, Micromachines 11 (2020). https://doi.org/10.3390/MI11070633.

[148] X. Qu, B. Stucker, Raster milling tool-path generation from STL files, Rapid Prototyp. J. 12 (2006) 4–11. https://doi.org/10.1108/13552540610637219.

[149] H. Ramaswami, R.S. Shaw, S. Anand, Selection of optimal set of cutting tools for machining of polygonal pockets with islands, Int. J. Adv. Manuf. Technol. 53 (2011) 963–977. https://doi.org/10.1007/s00170-010-2909-7.

[150] F. Ren, Y. Sun, D. Guo, Combined reparameterization-based spiral toolpath generation for five-axis sculptured surface machining, Int. J. Adv. Manuf. Technol. 40 (2009) 760–768. https://doi.org/10.1007/s00170-008-1385-9.

[151] M. Dolen, U. Yaman, New morphological methods to generate two-dimensional curve offsets, Int. J. Adv. Manuf. Technol. 71 (2014) 1687–1700. https://doi.org/10.1007/s00170-013-5595-4.

[152] S. Kapil, P. Joshi, H.V. Yagani, D. Rana, P.M. Kulkarni, R. Kumar, K.P. Karunakaran, Optimal space filling for additive manufacturing, Rapid Prototyp. J. 22 (2016) 660–675. https://doi.org/10.1108/RPJ-03-2015-0034.

[153] Y. Lu, S. Wu, Y. Gan, T. Huang, C. Yang, L. Junjie, J. Lin, Study on the microstructure, mechanical property and residual stress of SLM Inconel-718 alloy manufactured by differing island scanning strategy, Opt. Laser Technol. 75 (2015) 197–206. https://doi.org/10.1016/j.optlastec.2015.07.009.

[154] Y. Zhang, K. Chou, A parametric study of part distortions in fused deposition modelling using three-dimensional finite element analysis, Proc. Inst. Mech. Eng. Part B J. Eng. Manuf. 222 (2008) 959–967. https://doi.org/10.1243/09544054JEM990.

[155] J. Robinson, I. Ashton, P. Fox, E. Jones, C. Sutcliffe, Determination of the effect of scan strategy on residual stress in laser powder bed fusion additive manufacturing, Addit. Manuf. 23 (2018) 13–24. https://doi.org/10.1016/j.addma.2018.07.001.

[156] J.I. Arrizubieta, S. Martínez, A. Lamikiz, E. Ukar, K. Arntz, F. Klocke, Instantaneous powder flux regulation system for Laser Metal Deposition, J. Manuf. Process. 29 (2017) 242–251. https://doi.org/10.1016/j.jmapro.2017.07.018.

[157] H.H. Liu, T. Zhao, L.Y. Li, W.J. Liu, T.Q. Wang, J.F. Yue, A path planning and sharp

corner correction strategy for wire and arc additive manufacturing of solid components with polygonal cross-sections, Int. J. Adv. Manuf. Technol. 106 (2020) 4879–4889. https://doi.org/10.1007/s00170-020-04960-4.

[158] H. Giberti, L. Sbaglia, M. Urgo, A path planning algorithm for industrial processes under velocity constraints with an application to additive manufacturing, J. Manuf. Syst. 43 (2017) 160–167. https://doi.org/10.1016/j.jmsy.2017.03.003.

[159] R. Comminal, M.P. Serdeczny, D.B. Pedersen, J. Spangenberg, Motion planning and numerical simulation of material deposition at corners in extrusion additive manufacturing, Addit. Manuf. 29 (2019) 100753. https://doi.org/10.1016/j.addma.2019.06.005.

[160] G. Matache, M. Vladut, A. Paraschiv, R.M. Condruz, Edge and corner effects in selective laser melting of in 625 alloy, Manuf. Rev. 7 (2020). https://doi.org/10.1051/mfreview/2020008.

[161] J. Metelkova, C. De Formanoir, H. Haitjema, A. Witvrouw, W. Pfleging, B. Van Hooreweder, Elevated edges of metal parts produced by laser powder bed fusion : characterization and post-process correction, Proc. Spec. Interes. Gr. Meet. Adv. Precis. Addit. Manuf. (2019) 1–4.

[162] G. Ćwikła, C. Grabowik, K. Kalinowski, I. Paprocka, P. Ociepka, The influence of printing parameters on selected mechanical properties of FDM/FFF 3D-printed parts, IOP Conf. Ser. Mater. Sci. Eng. 227 (2017). https://doi.org/10.1088/1757-899X/227/1/012033.

[163] R.J. Zaldivar, D.B. Witkin, T. McLouth, D.N. Patel, K. Schmitt, J.P. Nokes, Influence of processing and orientation print effects on the mechanical and thermal behavior of 3D-Printed ULTEM ® 9085 Material, Addit. Manuf. 13 (2017) 71–80. https://doi.org/10.1016/j.addma.2016.11.007.

[164] S. Lin, L. Xia, G. Ma, S. Zhou, Y.M. Xie, A maze-like path generation scheme for fused deposition modeling, Int. J. Adv. Manuf. Technol. 104 (2019) 1509–1519. https://doi.org/10.1007/s00170-019-03986-7.

[165] X. Zhai, F. Chen, Path Planning of a Type of Porous Structures for Additive Manufacturing, CAD Comput. Aided Des. 115 (2019) 218–230. https://doi.org/10.1016/j.cad.2019.06.002.

[166] G.Q. Jin, W.D. Li, L. Gao, An adaptive process planning approach of rapid prototyping and manufacturing, Robot. Comput. Integr. Manuf. 29 (2013) 23–38. https://doi.org/10.1016/j.rcim.2012.07.001.

[167] D. Ding, Z. Pan, D. Cuiuri, H. Li, A practical path planning methodology for wire and arc additive manufacturing of thin-walled structures, Robot. Comput. Integr. Manuf. 34 (2015)

8–19. https://doi.org/10.1016/j.rcim.2015.01.003.

[168] A.R. Butz, Alternative Algorithm for Hilbert's Space-Filling Curve, IEEE Trans. Comput. C–20 (1971) 424–426. https://doi.org/10.1109/T-C.1971.223258.

[169] H. Sagan, On the geometrization of the peano curve and the arithmetization of the hilbert curve, Int. J. Math. Educ. Sci. Technol. 23 (1992) 403–411. https://doi.org/10.1080/0020739920230309.

[170] G. Breinholt, C. Schierz, Algorithm 781: Generating Hilbert's Space-Filling Curve by Recursion, ACM Trans. Math. Softw. 24 (1998) 184–189. https://doi.org/10.1145/290200.290219.

[171] A. Papacharalampopoulos, H. Bikas, P. Stavropoulos, Path planning for the infill of 3D printed parts utilizing Hilbert curves, Procedia Manuf. 21 (2018) 757–764. https://doi.org/10.1016/j.promfg.2018.02.181.

[172] X. Wang, A. Wang, Y. Li, A sequential path-planning methodology for wire and arc additive manufacturing based on a water-pouring rule, Int. J. Adv. Manuf. Technol. 103 (2019) 3813–3830. https://doi.org/10.1007/s00170-019-03706-1.

[173] M. Biegler, J. Wang, L. Kaiser, M. Rethmeier, Automated Tool-Path Generation for Rapid Manufacturing of Additive Manufacturing Directed Energy Deposition Geometries, (n.d.).

[174] T. Feldhausen, L. Heinrich, K. Saleeby, A. Burl, B. Post, E. MacDonald, C. Saldana, L. Love, Review of Computer-Aided Manufacturing (CAM) strategies for hybrid directed energy deposition, Addit. Manuf. 56 (2022). https://doi.org/10.1016/j.addma.2022.102900.

[175] N. Kladovasilakis, P. Charalampous, I. Kostavelis, D. Tzetzis, D. Tzovaras, Impact of metal additive manufacturing parameters on the powder bed fusion and direct energy deposition processes: a comprehensive review, Prog. Addit. Manuf. 6 (2021) 349–365. https://doi.org/10.1007/s40964-021-00180-8.

[176] R.S. Thanumoorthy, P. Sekar, S. Bontha, A.S.S. Balan, A study on the effect of process parameters and scan strategies on microstructure and mechanical properties of laser directed energy deposited IN718, J. Mater. Process. Technol. 319 (2023) 118096. https://doi.org/10.1016/j.jmatprotec.2023.118096.

[177] F. Soffel, D. Eisenbarth, K. Wegener, Effect of clad height, substrate thickness and scanning pattern on cantilever distortion in direct metal deposition, Int. J. Adv. Manuf. Technol. 117 (2021) 2083–2091. https://doi.org/10.1007/s00170-021-06925-7.

[178] W. Woo, D.K. Kim, E.J. Kingston, V. Luzin, F. Salvemini, M.R. Hill, Effect of interlayers and scanning strategies on through-thickness residual stress distributions in additive

manufactured ferritic-austenitic steel structure, Mater. Sci. Eng. A 744 (2019) 618–629. https://doi.org/10.1016/j.msea.2018.12.078.

[179] F. Wirth, K. Wegener, A physical modeling and predictive simulation of the laser cladding process, Addit. Manuf. 22 (2018) 307–319. https://doi.org/10.1016/j.addma.2018.05.017.

[180] J. Józwik, I. Kuric, A. Łukaszewicz, Analysis of the table motion of a 3-axis cnc milling machine tool at start-up and braking, Lect. Notes Mech. Eng. (2020) 108–117. https://doi.org/10.1007/978-3-030-40724-7_11.

[181] S.S. Makhanov, W. Anotaipaiboon, Advanced Numerical Methods to Optimize Cutting Operations of Five-Axis Milling Machines, 2015. https://doi.org/10.1007/978-3-540-71121-6.

[182] F. Wang, D.C.H. Yang, Nearly arc-length parameterized quintic-spline interpolation for precision machining, Precis. Eng. 15 (1993) 301. https://doi.org/10.1016/0141-6359(93)90176-b.

[183] Q.G. Zhang, R.B. Greenway, Development and implementation of a NURBS curve motion interpolator, Robot. Comput. Integr. Manuf. 14 (1998) 27–36. https://doi.org/10.1016/S0736-5845(97)00021-5.

[184] C.C. Lo, Real-time generation and control of cutter path for 5-axis CNC machining, Int. J. Mach. Tools Manuf. 39 (1999) 471–488. https://doi.org/10.1016/S0890-6955(98)00040-6.

[185] S.H. Suh, Y.S. Shin, Neural network modeling for tool path planning of the rough cut in complex pocket milling, J. Manuf. Syst. 15 (1996) 295–304. https://doi.org/10.1016/0278-6125(96)84192-6.

[186] Z. Lin, J. Fu, H. Shen, W. Gan, S. Yue, Tool path generation for multi-axis freeform surface finishing with the LKH TSP solver, CAD Comput. Aided Des. 69 (2015) 51–61. https://doi.org/10.1016/j.cad.2015.07.002.

[187] I. Mustafa, T.H. Kwok, Interlacing Infills for Multi-Material Fused Filament Fabrication Using Layered Depth Material Images, Micromachines 13 (2022). https://doi.org/10.3390/mi13050773.

[188] A. Nazir, O. Gokcekaya, K. Md Masum Billah, O. Ertugrul, J. Jiang, J. Sun, S. Hussain, Multi-material additive manufacturing: A systematic review of design, properties, applications, challenges, and 3D printing of materials and cellular metamaterials, Mater. Des. 226 (2023) 111661. https://doi.org/10.1016/j.matdes.2023.111661.

[189] R. Ghanavati, H. Naffakh-Moosavy, Additive manufacturing of functionally graded metallic materials: A review of experimental and numerical studies, J. Mater. Res. Technol. 13 (2021)

1628–1664. https://doi.org/10.1016/j.jmrt.2021.05.022.

[190] R. Prévost, E. Whiting, S. Lefebvre, O. Sorkine-Hornung, Make it stand: Balancing shapes for 3D fabrication, ACM Trans. Graph. 32 (2013). https://doi.org/10.1145/2461912.2461957.

[191] A. Telea, A. Jalba, Voxel-based assessment of printability of 3D shapes, Lect. Notes Comput. Sci. (Including Subser. Lect. Notes Artif. Intell. Lect. Notes Bioinformatics) 6671 LNCS (2011) 393–404. https://doi.org/10.1007/978-3-642-21569-8_34.

[192] O. Stava, J. Vanek, B. Benes, N. Carr, R. Měch, Stress relief: Improving structural strength of 3D printable objects, ACM Trans. Graph. 31 (2012). https://doi.org/10.1145/2185520.2185544.

[193] J. Martínez, J. Dumas, S. Lefebvre, Procedural voronoi foams for additive manufacturing, ACM Trans. Graph. 35 (2016). https://doi.org/10.1145/2897824.2925922.

[194] S.R.G. Bates, I.R. Farrow, R.S. Trask, Compressive behaviour of 3D printed thermoplastic polyurethane honeycombs with graded densities, Mater. Des. 162 (2019) 130–142. https://doi.org/10.1016/j.matdes.2018.11.019.

[195] S.Y. Choy, C.N. Sun, K.F. Leong, J. Wei, Compressive properties of functionally graded lattice structures manufactured by selective laser melting, Mater. Des. 131 (2017) 112–120. https://doi.org/10.1016/j.matdes.2017.06.006.

[196] J. Wu, N. Aage, R. Westermann, O. Sigmund, Infill Optimization for Additive Manufacturing-Approaching Bone-Like Porous Structures, IEEE Trans. Vis. Comput. Graph. 24 (2018) 1127–1140. https://doi.org/10.1109/TVCG.2017.2655523.

[197] J. Wu, Continuous optimization of adaptive quadtree structures, CAD Comput. Aided Des. 102 (2018) 72–82. https://doi.org/10.1016/j.cad.2018.04.008.

[198] C. Liu, Z. Du, Y. Zhu, W. Zhang, X. Zhang, X. Guo, Optimal design of shell-graded-infill structures by a hybrid MMC-MMV approach, Comput. Methods Appl. Mech. Eng. 369 (2020) 113187. https://doi.org/10.1016/j.cma.2020.113187.

[199] S.R. Mohan, S.N. Khaderi, S. Simhambhatla, 3D Printing of Components with Tailored Properties through Hilbert Curve Filling of a Discretized Domain, 3D Print. Addit. Manuf. 7 (2020) 288–299. https://doi.org/10.1089/3dp.2020.0048.

[200] T. Kuipers, J. Wu, C.C.L. Wang, CrossFill: Foam Structures with Graded Density for Continuous Material Extrusion, CAD Comput. Aided Des. 114 (2019) 37–50. https://doi.org/10.1016/j.cad.2019.05.003.

[201] S.C. Soo, K.M. Yu, Tool-path generation for fractal curve making, Int. J. Adv. Manuf. Technol. 19 (2002) 32–48. https://doi.org/10.1007/PL00003966.

[202] W.K. Chiu, Y.C. Yeung, K.M. Yu, Toolpath generation for layer manufacturing of fractal objects, Rapid Prototyp. J. 12 (2006) 214–221. https://doi.org/10.1108/13552540610682723.

[203] E.T. Akinlabi, S.A. Akinlabi, Powder flow rate influence on laser metal deposited TiC on Ti-6A1-4V, Lect. Notes Eng. Comput. Sci. 2224 (2016) 956–960.

[204] R.M. Mahamood, E.T. Akinlabi, Effect of Powder Flow Rate on Surface Finish in Laser Additive Manufacturing Process, IOP Conf. Ser. Mater. Sci. Eng. 391 (2018). https://doi.org/10.1088/1757-899X/391/1/012005.

[205] P.R. Gradl, A. Cervone, E. Gill, Surface texture characterization for thin-wall NASA HR-1 Fe–Ni–Cr alloy using laser powder directed energy deposition (LP-DED), Adv. Ind. Manuf. Eng. 4 (2022) 100084. https://doi.org/10.1016/j.aime.2022.100084.

[206] A. Kawale, Design and Fabrication of a Feedstock Delivery System fora 3 kW Solar Gasification Reactor, University of Minnesota, 2013. https://doi.org/Retrieved from the University of Minnesota Digital Conservancy, http://hdl.handle.net/11299/160150.

[207] C.J. Coetzee, S.G. Lombard, Discrete element method modelling of a centrifugal fertiliser spreader, Biosyst. Eng. 109 (2011) 308–325. https://doi.org/10.1016/j.biosystemseng.2011.04.011.

[208] P. Van Liedekerke, E. Tijskens, E. Dintwa, F. Rioual, J. Vangeyte, H. Ramon, DEM simulations of the particle flow on a centrifugal fertilizer spreader, Powder Technol. 190 (2009) 348–360. https://doi.org/10.1016/j.powtec.2008.08.018.

[209] R.L. Parish, Review of granular applications for turfgrass, Horttechnology 16 (2006) 533–538. https://doi.org/10.21273/horttech.16.3.0533.

[210] M. McPherson, D. Beakley, Dust Collector for powdered material spreader, US Pat. 6715702B2, 1988.

[211] J.O. Wilson, Sept. 12, 1950, US Pat. 2521888, 1950.

[212] P. Van Liedekerke, E. Tijskens, H. Ramon, Discrete element simulations of the influence of fertiliser physical properties on the spread pattern from spinning disc spreaders, Biosyst. Eng. 102 (2009) 392–405. https://doi.org/10.1016/j.biosystemseng.2009.01.006.

[213] C.J. Coetzee, S.G. Lombard, Discrete element method modelling of a centrifugal fertiliser spreader, Biosyst. Eng. 109 (2011) 308–325. https://doi.org/10.1016/j.biosystemseng.2011.04.011.

[214] W. Nan, M. Pasha, T. Bonakdar, A. Lopez, U. Zafar, S. Nadimi, M. Ghadiri, Jamming during particle spreading in additive manufacturing, Powder Technol. 338 (2018) 253–262. https://doi.org/10.1016/j.powtec.2018.07.030.

[215] L. Wang, A. Yu, E. Li, H. Shen, Z. Zhou, Effects of spreader geometry on powder spreading process in powder bed additive manufacturing, Powder Technol. 384 (2021) 211–222. https://doi.org/10.1016/j.powtec.2021.02.022.

[216] J. Zhang, Y. Tan, T. Bao, Y. Xu, X. Xiao, S. Jiang, Discrete element simulation of the effect of roller-spreading parameters on powder-bed density in additive manufacturing, Materials (Basel). 13 (2020). https://doi.org/10.3390/ma13102285.

[217] S.R. Schwartz, D.C. Richardson, P. Michel, An implementation of the soft-sphere discrete element method in a high-performance parallel gravity tree-code, Granul. Matter 14 (2012) 363–380. https://doi.org/10.1007/s10035-012-0346-z.

[218] N.G. Deen, M. Van Sint Annaland, M.A. Van der Hoef, J.A.M. Kuipers, Review of discrete particle modeling of fluidized beds, Chem. Eng. Sci. 62 (2007) 28–44. https://doi.org/10.1016/j.ces.2006.08.014.

[219] C. Wassgren, J.S. Curtis, The application of computational modeling to pharmaceutical materials science, MRS Bull. 31 (2006) 900–904. https://doi.org/10.1557/mrs2006.210.

[220] C. Wassgren (Purdue University), DEM Modeling : Lecture 06 Introduction to Soft-Particle DEM Normal Contact Force Models . Part I Introduction to Soft-Particle DEM, Lect. Notes (n.d.) 1–37.

[221] J. Horabik, M. Molenda, Parameters and contact models for DEM simulations of agricultural granular materials: A review, Biosyst. Eng. 147 (2016) 206–225. https://doi.org/10.1016/j.biosystemseng.2016.02.017.

[222] R.D. Mindlin, H. Deresiewicz, Elastic Spheres in Contact Under Varying Oblique Forces, J. Appl. Mech. 20 (2021) 327–344. https://doi.org/10.1115/1.4010702.

[223] D. Elata, J.G. Berryman, Contact force-displacement laws and the mechanical behavior of random packs of identical spheres, Mech. Mater. 24 (1996) 229–240. https://doi.org/10.1016/S0167-6636(96)00034-8.

[224] C. Thornton, S.J. Cummins, P.W. Cleary, An investigation of the comparative behaviour of alternative contact force models during inelastic collisions, Powder Technol. 233 (2013) 30–46. https://doi.org/10.1016/j.powtec.2012.08.012.

[225] D.M. Rathbone, An Advanced Elastic-Plastic Contact Model for Discrete Element Method, Imperial College London, 2017.

[226] DEM Solutions Ltd, Theory Reference Guide, Version 2.6, (2014). https://www.edemsimulation.com/content/uploads/2016/08/EDEM2.6_theory_reference_guide.pdf.

[227] S.P. Section, B. Railways, T. Centre, S. Physics, Surface energy and the contact of elastic

solids, Proc. R. Soc. London. A. Math. Phys. Sci. 324 (1971) 301–313. https://doi.org/10.1098/rspa.1971.0141.

[228] C.M. Wensrich, A. Katterfeld, Rolling friction as a technique for modelling particle shape in DEM, Powder Technol. 217 (2012) 409–417. https://doi.org/10.1016/j.powtec.2011.10.057.

[229] S. Geer, M.L. Bernhardt-Barry, E.J. Garboczi, J. Whiting, A. Donmez, A more efficient method for calibrating discrete element method parameters for simulations of metallic powder used in additive manufacturing, Granul. Matter 20 (2018) 1–17. https://doi.org/10.1007/s10035-018-0848-4.

[230] A. Hafez, Q. Liu, T. Finkbeiner, R.A. Alouhali, T.E. Moellendick, J.C. Santamarina, The effect of particle shape on discharge and clogging, Sci. Rep. 11 (2021) 1–11. https://doi.org/10.1038/s41598-021-82744-w.

[231] A. Khazeni, Z. Mansourpour, Influence of non-spherical shape approximation on DEM simulation accuracy by multi-sphere method, Powder Technol. 332 (2018) 265–278. https://doi.org/10.1016/j.powtec.2018.03.030.

[232] M. Mullier, U. Tüzün, O.R. Walton, A single-particle friction cell for measuring contact frictional properties of granular materials, Powder Technol. 65 (1991) 61–74. https://doi.org/10.1016/0032-5910(91)80169-J.

[233] J. Wang, M. Zhang, L. Feng, H. Yang, Y. Wu, G. Yue, The behaviors of particle-wall collision for non-spherical particles: Experimental investigation, Powder Technol. 363 (2020) 187–194. https://doi.org/10.1016/j.powtec.2019.12.041.

[234] V. Gunaraj, N. Murugan, Application of response surface methodology for predicting weld bead quality in submerged arc welding of pipes, J. Mater. Process. Technol. 88 (1999) 266–275. https://doi.org/10.1016/S0924-0136(98)00405-1.

[235] R. Furukawa, Y. Shiosaka, K. Kadota, K. Takagaki, T. Noguchi, A. Shimosaka, Y. Shirakawa, Size-induced segregation during pharmaceutical particle die filling assessed by response surface methodology using discrete element method, J. Drug Deliv. Sci. Technol. 35 (2016) 284–293. https://doi.org/10.1016/j.jddst.2016.08.004.

[236] Z. Chen, G. Wang, D. Xue, Q. Bi, Simulation and optimization of gyratory crusher performance based on the discrete element method, Powder Technol. 376 (2020) 93–103. https://doi.org/10.1016/j.powtec.2020.07.034.

[237] L. Zhao, H. Zhou, L. Xu, S. Song, C. Zhang, Q. Yu, Parameter calibration of coconut bran substrate simulation model based on discrete element and response surface methodology, Powder Technol. 395 (2022) 183–194. https://doi.org/10.1016/j.powtec.2021.09.065.

[238] Z. Zuo, S. Gong, G. Xie, J. Zhang, Sensitivity analysis of process parameters for granular mixing in an intensive mixer using response surface methodology, Powder Technol. 384 (2021) 51–61. https://doi.org/10.1016/j.powtec.2021.01.076.

[239] W. Rong, Y. Feng, P. Schwarz, T. Yurata, P. Witt, B. Li, T. Song, J. Zhou, Sensitivity analysis of particle contact parameters for DEM simulation in a rotating drum using response surface methodology, Powder Technol. 362 (2020) 604–614. https://doi.org/10.1016/j.powtec.2019.12.004.

[240] R. Xia, B. Li, X. Wang, T. Li, Z. Yang, Measurement and calibration of the discrete element parameters of wet bulk coal, Meas. J. Int. Meas. Confed. 142 (2019) 84–95. https://doi.org/10.1016/j.measurement.2019.04.069.

[241] S.L.C. Ferreira, R.E. Bruns, H.S. Ferreira, G.D. Matos, J.M. David, G.C. Brandão, E.G.P. da Silva, L.A. Portugal, P.S. dos Reis, A.S. Souza, W.N.L. dos Santos, Box-Behnken design: An alternative for the optimization of analytical methods, Anal. Chim. Acta 597 (2007) 179–186. https://doi.org/10.1016/j.aca.2007.07.011.

[242] M.A. Bezerra, R.E. Santelli, E.P. Oliveira, L.S. Villar, L.A. Escaleira, Response surface methodology (RSM) as a tool for optimization in analytical chemistry, Talanta 76 (2008) 965–977. https://doi.org/10.1016/j.talanta.2008.05.019.

[243] S. Mack, P. Langston, C. Webb, T. York, Experimental validation of polyhedral discrete element model, Powder Technol. 214 (2011) 431–442. https://doi.org/10.1016/j.powtec.2011.08.043.

[244] D. Wang, M. Servin, T. Berglund, K.O. Mickelsson, S. Rönnbäck, Parametrization and validation of a nonsmooth discrete element method for simulating flows of iron ore green pellets, Powder Technol. 283 (2015) 475–487. https://doi.org/10.1016/j.powtec.2015.05.040.

[245] Stat-Ease » v11 » Adequate Precision, (n.d.). https://www.statease.com/docs/v11/navigation/adequate-precision/ (accessed July 25, 2022).

[246] Stat-Ease » v11 » Anova: Adjusted R-Squared, (n.d.). https://www.statease.com/docs/v11/navigation/anova-adj-r-squared/ (accessed July 25, 2022).

[247] V.S. Bitragunta, Performance metrics for powder feeder systems in additive manufacturing Presented to the Graduate Faculty of the In Partial Fulfillment of the Requirements for the Degree, Missouri university of science and technology, 2015.

[248] P. Tang, V.M. Puri, Methods for minimizing segregation: A review, Part. Sci. Technol. 22

(2004) 321–337. https://doi.org/10.1080/02726350490501420.

[249] D. Yao, J. Wang, M. Li, T. Zhao, Y. Cai, X. An, R. Zou, H. Zhang, H. Fu, X. Yang, Q. Zou, Segregation of 316L stainless steel powder during spreading in selective laser melting based additive manufacturing, Powder Technol. 397 (2022) 117096. https://doi.org/10.1016/j.powtec.2021.117096.

[250] W. Li, J. Zhang, X. Zhang, F. Liou, Effect of optimizing particle size on directed energy deposition of Functionally Graded Material with blown Pre-Mixed Multi-Powder, Manuf. Lett. 13 (2017) 39–43. https://doi.org/10.1016/j.mfglet.2017.07.001.

[251] B. Nau, A. Roderburg, F. Klocke, Ramp-up of hybrid manufacturing technologies, CIRP J. Manuf. Sci. Technol. 4 (2011) 313–316. https://doi.org/10.1016/j.cirpj.2011.04.003.

[252] K.P. Karunakaran, S. Suryakumar, V. Pushpa, S. Akula, Retrofitment of a CNC machine for hybrid layered manufacturing, Int. J. Adv. Manuf. Technol. 45 (2009) 690–703. https://doi.org/10.1007/s00170-009-2002-2.

[253] C.M. Lee, D.H. Kim, J.T. Baek, E.J. Kim, Laser assisted milling device: A review, Int. J. Precis. Eng. Manuf. - Green Technol. 3 (2016) 199–208. https://doi.org/10.1007/s40684-016-0027-1.

[254] J. Jones, P. McNutt, R. Tosi, C. Perry, D. Wimpenny, Remanufacture of turbine blades by laser cladding, machining and in-process scanning in a single machine, 23rd Annu. Int. Solid Free. Fabr. Symp. - An Addit. Manuf. Conf. SFF 2012 (2012) 821–827.

[255] F. Klocke, H. Wirtz, W. Meiners, Direct manufacturing of metal prototypes and prototype tools, Proc. SFF Symp. (1996) 141–148.

[256] J. Nagel, K. Liou, W. Frank, Hybrid Manufacturing System Design and Development, Manuf. Syst. IntechOpen (2012) 223--224.

[257] T. Himmer, A. Techel, S. Nowotny, E. Beyer, Recent developments in metal laminated tooling by multiple laser processing, Rapid Prototyp. J. 9 (2003) 24–29. https://doi.org/10.1108/13552540310455629.

[258] A. Calleja, G. Urbikain, H. González, I. Cerrillo, R. Polvorosa, A. Lamikiz, Inconel®718 superalloy machinability evaluation after laser cladding additive manufacturing process, Int. J. Adv. Manuf. Technol. 97 (2018) 2873–2885. https://doi.org/10.1007/s00170-018-2169-5.

[259] R. Li, W. Yuan, H. Yue, Y. Zhu, Study on microstructure and properties of Fe-based amorphous composite coating by high-speed laser cladding, Opt. Laser Technol. 146 (2022) 107574. https://doi.org/10.1016/j.optlastec.2021.107574.

[260] YLM and YLR, up to 1.5 kW | IPG Photonics, (n.d.).

https://www.ipgphotonics.com/en/products/lasers/mid-power-cw-fiber-lasers/1-micron/ylm-and-ylr#[ylr-wc-1-4-kw] (accessed June 13, 2022).

[261] K.P. Karunakaran, S. Suryakumar, V. Pushpa, S. Akula, Low cost integration of additive and subtractive processes for hybrid layered manufacturing, Robot. Comput. Integr. Manuf. 26 (2010) 490–499. https://doi.org/10.1016/j.rcim.2010.03.008.

[262] Tormach PCNC 1100 Series 3 Mill Documents, (n.d.). https://tormach.com/support/mill/pcnc-1100-series-3-documents (accessed June 17, 2022).

[263] F. Kaji, H. Nguyen-huu, J.A. Narayanan, M. Zimny, E. Toyserkani, Intermittent adaptive trajectory planning for geometric defect correction in large-scale robotic laser directed energy deposition based additive manufacturing, J. Intell. Manuf. (2023). https://doi.org/10.1007/s10845-023-02194-1.

[264] A. Zapata, A. Benda, M. Spreitler, X.F. Zhao, C. Bernauer, H. Yoshioka, M.F. Zaeh, A model-based approach to reduce kinematics-related overfill in robot-guided Laser Directed Energy Deposition, CIRP J. Manuf. Sci. Technol. 45 (2023) 200–209. https://doi.org/10.1016/j.cirpj.2023.06.014.

[265] Z. Hu, X. Qin, T. Shao, H. Liu, Understanding and overcoming of abnormity at start and end of the weld bead in additive manufacturing with GMAW, Int. J. Adv. Manuf. Technol. 95 (2018) 2357–2368. https://doi.org/10.1007/s00170-017-1392-9.

[266] J. Xiong, Z. Yin, W. Zhang, Forming appearance control of arc striking and extinguishing area in multi-layer single-pass GMAW-based additive manufacturing, Int. J. Adv. Manuf. Technol. 87 (2016) 579–586. https://doi.org/10.1007/s00170-016-8543-2.

[267] HELSGAUN K., An effective implementation of the Lin-Kernighan traveling salesman heuristic, Eur. J. Oper. Res. 126 (1998) 106–130. https://doi.org/https://doi.org/10.1016/S0377-2217(99)00284-2.

[268] Traveling Salesman Problem, (n.d.). http://www.math.uwaterloo.ca/tsp/index.html (accessed April 3, 2022).

[269] C.A. Silva, J.M. Souza, T.A. Runkler, R. Palm, J.M. Sa da Costa, Scheduling in manufacturing systems using the ant colonies optimization algorithm, V Port. Conf. Autom. Control (2002).

[270] J. Lenstra, A. Rinnooy Kan, Some Simple Applications of the Travelling Salesman Problem, J. Oper. Res. Soc. 26 (1975) 717–733. https://doi.org/https://doi.org/10.1057/jors.1975.151.

[271] C. Osterman, C. Rego, The Satellite List and New Data Structures for Symmetric Traveling

Salesman Problems, 2003.

[272] N.L.J. Ulder, E.H.L. Aarts, H. Bandelt, P.J.M. Van Laarhoven, E. Pesch, Genetic Local Search Algorithms for the Traveling Salesman Problem, in: In International Conference on Parallel Problem Solving from Nature,Springer, Berlin, Heidelberg, n.d.: pp. 109–116.

[273] The Shapely User Manual — Shapely 1.8.1.post1 documentation, (n.d.). https://shapely.readthedocs.io/en/stable/manual.html (accessed April 3, 2022).

[274] Y. an Jin, Y. He, J. zhong Fu, W. feng Gan, Z. wei Lin, Optimization of tool-path generation for material extrusion-based additive manufacturing technology, Addit. Manuf. 1 (2014) 32–47. https://doi.org/10.1016/j.addma.2014.08.004.

[275] D. Jafari, T.H.J. Vaneker, I. Gibson, Wire and arc additive manufacturing: Opportunities and challenges to control the quality and accuracy of manufactured parts, Mater. Des. 202 (2021) 109471. https://doi.org/10.1016/j.matdes.2021.109471.

[276] T. Hauser, A. Da Silva, R.T. Reisch, J. Volpp, T. Kamps, A.F.H. Kaplan, Fluctuation effects in Wire Arc Additive Manufacturing of aluminium analysed by high-speed imaging, J. Manuf. Process. 56 (2020) 1088–1098. https://doi.org/10.1016/j.jmapro.2020.05.030.

[277] M. Köhler, L. Sun, J. Hensel, S. Pallaspuro, J. Kömi, K. Dilger, Z. Zhang, Comparative study of deposition patterns for DED-Arc additive manufacturing of Al-4046, Mater. Des. 210 (2021). https://doi.org/10.1016/j.matdes.2021.110122.

[278] Y. Yehorov, L.J. da Silva, A. Scotti, Balancing WAAM production costs and wall surface quality through parameter selection: A case study of an Al-Mg5 alloy multilayer-non-oscillated single pass wall, J. Manuf. Mater. Process. 3 (2019). https://doi.org/10.3390/jmmp3020032.

[279] C. Zhang, C. Shen, X. Hua, F. Li, Y. Zhang, Y. Zhu, Influence of wire-arc additive manufacturing path planning strategy on the residual stress status in one single buildup layer, Int. J. Adv. Manuf. Technol. 111 (2020) 797–806. https://doi.org/10.1007/s00170-020-06178-w.

[280] Y.M. Zhang, Y. Chen, P. Li, A.T. Male, Weld deposition-based rapid prototyping: A preliminary study, J. Mater. Process. Technol. 135 (2003) 347–357. https://doi.org/10.1016/S0924-0136(02)00867-1.

[281] F. Bos, R. Wolfs, Z. Ahmed, T. Salet, Additive manufacturing of concrete in construction: potentials and challenges of 3D concrete printing, Virtual Phys. Prototyp. 11 (2016) 209–225. https://doi.org/10.1080/17452759.2016.1209867.

[282] R. Comminal, M.P. Serdeczny, D.B. Pedersen, J. Spangenberg, Motion planning and numerical simulation of material deposition at corners in extrusion additive manufacturing,

Addit. Manuf. 29 (2019) 100753. https://doi.org/10.1016/j.addma.2019.06.005.

[283] S. Bochkarev, S.L. Smith, On minimizing turns in robot coverage path planning, IEEE Int. Conf. Autom. Sci. Eng. 2016-Novem (2016) 1237–1242. https://doi.org/10.1109/COASE.2016.7743548.

[284] Z. Lin, X. Deng, J. Fu, Q. Gao, An optimisation algorithm for reducing the number of turns on space-filling curve toolpath for sculptured surface milling, Int. J. Comput. Integr. Manuf. 31 (2018) 199–209. https://doi.org/10.1080/0951192X.2017.1407453.

[285] U.G.K. Wegst, H. Bai, E. Saiz, A.P. Tomsia, R.O. Ritchie, Bioinspired structural materials, Nat. Mater. 14 (2015) 23–36. https://doi.org/10.1038/nmat4089.

[286] P.O. Persson, G. Strang, A simple mesh generator in MATLAB, SIAM Rev. 46 (2004) 329–345. https://doi.org/10.1137/S0036144503429121.

[287] Laboratory of Human Anatomy and Embryology, University of Brussels (ULB), Belgium, (n.d.). https://isbweb.org/data/vsj/iliac/.

[288] D.T. Phanm, S.S. Dimov, Rapid manufacturing, Springer-Verlag London Limited, 2001. https://doi.org/10.1007/978-1-4471-0703-3.

[289] I. Gibson, D. Rosen, B. Stucker, Additive manufacturing technologies: 3D printing, rapid prototyping, and direct digital manufacturing, second edition, 2015. https://doi.org/10.1007/978-1-4939-2113-3.

[290] W. Ul Haq Syed, L. Li, Effects of wire feeding direction and location in multiple layer diode laser direct metal deposition, Elsevier 248 (2005) 518–524. https://www.sciencedirect.com/science/article/pii/S0169433205004344 (accessed January 30, 2020).

[291] W.E. Voice, D.J. Jarvis, N.J.E. Adkins, Multi - Wire Feeder Method and System for Alloy Sample Formation and Additive Manufacturing, US Pat.9902018, 2018.

[292] G.E. Morgan, G.E. Dyer, Electrode Carrying Wire for GTAW Welding, US Pat. 4924053, 1990.

[293] F.M. Hooper, Plasma arc torch with coaxial wire feed, US Pat. 63658657B1, 2002.

[294] L.D. Bobbio, B. Bocklund, R. Otis, J.P. Borgonia, R.P. Dillon, A.A. Shapiro, B. McEnerney, Z.K. Liu, A.M. Beese, Characterization of a functionally graded material of Ti-6Al-4V to 304L stainless steel with an intermediate V section, J. Alloys Compd. 742 (2018) 1031–1036. https://doi.org/10.1016/j.jallcom.2018.01.156.

[295] C. Schneider-Maunoury, L. Weiss, P. Acquier, D. Boisselier, P. Laheurte, Functionally graded Ti6Al4V-Mo alloy manufactured with DED-CLAD®process, Addit. Manuf. 17 (2017) 55–66. https://doi.org/10.1016/j.addma.2017.07.008.

[296] O. Pütsch, J. Stollenwerk, M. Kogel-Hollacher, M. Traub, Annular beam shaping system for advanced 3D laser brazing, Adv. Opt. Technol. 1 (2012) 397–402. https://doi.org/10.1515/aot-2012-0040.

[297] H. Pajukoski, J. Näkki, S. Thieme, J. Tuominen, S. Nowotny, P. Vuoristo, High performance corrosion resistant coatings by novel coaxial cold- and hot-wire laser cladding methods, J. Laser Appl. 28 (2016) 012011. https://doi.org/10.2351/1.4936988.

[298] G.M. Robert, N.J. Summit, N.H. Ontario, Y.M. Donald, Collimated electric arc-powder deposition process, US Pat. 3016447, 1962. https://doi.org/10.1145/178951.178972.

[299] V. Burdovitsin, E. Oks, Hollow-cathode plasma electron gun for beam generation at forepump gas pressure, Rev. Sci. Instrum. 70 (1999) 2975–2978. https://doi.org/10.1063/1.1149856.

[300] Wirefeed Additive Manufacturing vs. Powder Methods | Sciaky, (n.d.). http://www.sciaky.com/additive-manufacturing/wire-am-vs-powder-am (accessed May 31, 2019).

[301] A. Perrot, D. Rangeard, E. Courteille, 3D printing of earth-based materials: Processing aspects, Constr. Build. Mater. 172 (2018) 670–676. https://doi.org/10.1016/j.conbuildmat.2018.04.017.

[302] P. Shakor, S. Nejadi, G. Paul, A study into the effect of different nozzles shapes and fibre-reinforcement in 3D printed mortar, Materials (Basel). 12 (2019). https://doi.org/10.3390/MA12101708.

[303] J. Huang, Q. Qin, J. Wang, H. Fang, Two Dimensional Laser Galvanometer Scanning Technology for Additive Manufacturing, Int. J. Mater. Mech. Manuf. 6 (2018) 332–336. https://doi.org/10.18178/ijmmm.2018.6.5.402.

[304] C. C.K., K.F. Leong, L. C.S., Rapid Prototyping, Second, World Scientific, 2003.

[305] M.P. Lee, G.J.T. Cooper, T. Hinkley, G.M. Gibson, M.J. Padgett, L. Cronin, Development of a 3D printer using scanning projection stereolithography, Sci. Rep. 5 (2015). https://doi.org/10.1038/srep09875.

[306] F. W Liou, Rapid Prototyping and Engineering Applications, 2008.

[307] N. Alharbi, R. Osman, D. Wismeijer, Effects of build direction on the mechanical properties of 3D-printed complete coverage interim dental restorations, J. Prosthet. Dent. 115 (2016) 760–767. https://doi.org/10.1016/j.prosdent.2015.12.002.

[308] H.W. Choi, J.Y. Yoon, Composite polymer joining by laser combined hybrid laser process, Adv. Mater. Res. 875–877 (2014) 1362–1366. https://doi.org/10.4028/www.scientific.net/AMR.875-877.1362.

[309] T. Matsuda, F. Abe, H. Takahashi, 4.4 Laser Printer Scanning System with a Parabollic Mirror, IEEE J. Quantum Electron. 13 (1977) 826. https://doi.org/10.1109/JQE.1977.1069470.

[310] Y. Li, J. Katz, Asymmetric distribution of the scanned field of a rotating reflective polygon, Appl. Opt. 36 (1997) 342. https://doi.org/10.1364/ao.36.000342.

[311] K.O.G. Varughese, K. Siva Rama Krishna, Flattening the field of postobjective scanners by optimum choice and positioning of polygons, Appl. Opt. 32 (1993) 1104–1108. https://doi.org/10.1364/AO.32.001104.

[312] Y.M. Huang, S. Kuriyama, C.P. Jiang, Fundamental study and theoretical analysis in a constrained-surface stereolithography system, Int. J. Adv. Manuf. Technol. 24 (2004) 361–369. https://doi.org/10.1007/s00170-003-1627-9.

[313] Y.M. Huang, H.Y. Lan, Path planning effect for the accuracy of rapid prototyping system, Int. J. Adv. Manuf. Technol. 30 (2006) 233–246. https://doi.org/10.1007/s00170-005-0085-y.

[314] X. Zhang, B. Zhou, Y. Zeng, P. Gu, Model layout optimization for solid ground curing rapid prototyping processes, Robot. Comput. Integr. Manuf. 18 (2002) 41–51. https://doi.org/10.1016/S0736-5845(01)00022-9.

[315] P.M. Lambert, E.A. Campaigne, C.B. Williams, Design considerations for mask projection microstereolithography systems, 24th Int. SFF Symp. - An Addit. Manuf. Conf. SFF 2013 (2013) 111–130.

[316] A. Bertsch, S. Zissi, J.Y. Jézéquel, S. Corbel, J.C. André, Microstereophotolithography using a liquid crystal display as dynamic mask-generator, Microsyst. Technol. 3 (1997) 42–47. https://doi.org/10.1007/s005420050053.

[317] A. Jacob, Automating cutting of composites, Reinf. Plast. 52 (2008) 20–24. https://doi.org/10.1016/S0034-3617(08)70211-X.

[318] S. Morita, K. Sugiyam, Sheet lamination modelling method, US Pat. 6056843, n.d.

[319] M. Feygin, B. Hsieh, Laminated object manufacturing: A simpler process, Proc. 2nd Solid Free. Fabr. Symp. 0 (1991) 123–130. http://sffsymposium.engr.utexas.edu/Manuscripts/1991/1991-16-Feygin.pdf%5Cnhttp://sffsymposium.engr.utexas.edu/1991TOC.

[320] W.A. Ayoola, W.J. Suder, S.W. Williams, Effect of beam shape and spatial energy distribution on weld bead geometry in conduction welding, Opt. Laser Technol. 117 (2019) 280–287. https://doi.org/10.1016/j.optlastec.2019.04.025.

[321] Y. Tang, H.T. Loh, J.Y.H. Fuh, Y.S. Wong, L. Lu, Y. Ning, X. Wang, Accuracy analysis and

improvement for direct laser sintering, Innov. Manuf. Syst. Technol. 119260 (2004). http://dspace.mit.edu/handle/1721.1/3898.

[322] Xact Metal: Accessible, High-Caliber 3D Metal Printing is Here., (n.d.). https://xactmetal.com/ (accessed April 21, 2020).

[323] M.W. Barclift, C.B. Williams, Examining variability in the mechanical properties of parts manufactured via polyjet direct 3D printing, InInternational Solid Free. Fabr. Symp. (2012) 876–890. https://doi.org/10.1017/CBO9781107415324.004.

[324] R. Lupoi, W. O'Neill, Powder stream characteristics in cold spray nozzles, Surf. Coatings Technol. 206 (2011) 1069–1076. https://doi.org/10.1016/j.surfcoat.2011.07.061.

[325] Y. Xie, C. Chen, M.P. Planche, S. Deng, H. Liao, Effect of spray angle on Ni particle deposition behaviour in cold spray, Surf. Eng. 34 (2018) 352–360. https://doi.org/10.1080/02670844.2017.1312221.

[326] Y. Bai, G. Wagner, C.B. Williams, Effect of particle size distribution on powder packing and sintering in binder jetting additive manufacturing of metals, J. Manuf. Sci. Eng. Trans. ASME 139 (2017) 1–6. https://doi.org/10.1115/1.4036640.

[327] B. Yun, C.B. Williams, An exploration of binder jetting of copper, Rapid Prototyp. Journa 1 (2015). https://doi.org/10.1017/CBO9781107415324.004.

[328] J.A. Gonzalez, J. Mireles, Y. Lin, R.B. Wicker, Characterization of ceramic components fabricated using binder jetting additive manufacturing technology, Ceram. Int. 42 (2016) 10559–10564. https://doi.org/10.1016/j.ceramint.2016.03.079.

[329] J.C. Haley, B. Zheng, U.S. Bertoli, A.D. Dupuy, J.M. Schoenung, E.J. Lavernia, Working distance passive stability in laser directed energy deposition additive manufacturing, Mater. Des. 161 (2019) 86–94. https://doi.org/10.1016/j.matdes.2018.11.021.

[330] C. Kledwig, H. Perfahl, M. Reisacher, F. Brückner, J. Bliedtner, C. Leyens, Analysis of melt pool characteristics and process parameters using a coaxial monitoring system during directed energy deposition in additive manufacturing, Materials (Basel). 12 (2019). https://doi.org/10.3390/ma12020308.

[331] J.I. Arrizubieta, J.E. Ruiz, S. Martinez, E. Ukar, A. Lamikiz, Intelligent nozzle design for the Laser Metal Deposition process in the Industry 4.0, Procedia Manuf. 13 (2017) 1237–1244. https://doi.org/10.1016/j.promfg.2017.09.043.

[332] C. Liu, A.C.C. Law, D. Roberson, Z. (James) Kong, Image analysis-based closed loop quality control for additive manufacturing with fused filament fabrication, J. Manuf. Syst. 51 (2019) 75–86. https://doi.org/10.1016/j.jmsy.2019.04.002.

[333] R. Comminal, M.P. Serdeczny, D.B. Pedersen, J. Spangenberg, Numerical Modeling of the

Material Deposition and Contouring, in: Proceedings of the Annual International Solid Freeform Fabrication Symposium. Laboratory for Freeform Fabrication, Austin US, 2018: pp. 1855–1864. http://dx.doi.org/10.26153/tsw/17188.

[334] C. Zhong, N. Pirch, A. Gasser, R. Poprawe, J.H. Schleifenbaum, The influence of the powder stream on high-deposition-rate laser metal deposition with inconel 718, Metals (Basel). 7 (2017). https://doi.org/10.3390/met7100443.

[335] Stereolithography (SLA) 3D Printing Overview 3D Systems, (n.d.). https://www.3dsystems.com/resources/information-guides/stereolithography/sla (accessed April 21, 2020).

[336] Perfactory Family Archives | EnvisionTEC, (n.d.). https://envisiontec.com/3d-printers/perfactory-family/ (accessed April 21, 2020).

[337] Brothers In Arms: These Robots Put A New Twist On 3D Printing - GE Reports, (n.d.). https://www.ge.com/reports/brothers-arms-robots-put-new-twist-3d-printing/ (accessed April 21, 2020).

[338] Stereolithography vs. PolyJet | Top 4 Differences | Stratasys Direct, (n.d.). https://www.stratasysdirect.com/manufacturing-services/3d-printing/differences-between-stereolithography-polyjet (accessed April 21, 2020).

[339] ExOne | Home, (n.d.). https://www.exone.com/ (accessed April 21, 2020).

[340] HP 3D Metal Jet - Commercial & Industrial Metal 3D Printer | HP® Official Site, (n.d.). https://www8.hp.com/us/en/printers/3d-printers/products/metal-jet.html (accessed April 21, 2020).

[341] Product Center-Yingchuang Building Technique （Shanghai） Co.Ltd. (WinSun), (n.d.). http://www.winsun3d.com/En/Product/pro_inner/id/1 (accessed April 21, 2020).

[342] Home | Desktop Metal, (n.d.). https://www.desktopmetal.com/ (accessed April 21, 2020).

[343] Fabrisonic LLC, (n.d.). https://fabrisonic.com/.

[344] Metal 3D printing, (n.d.). https://www.renishaw.com/en/metal-3d-printing--32084 (accessed April 21, 2020).

[345] Products & Solutions for Industrial 3D Printing | EOS GmbH, (n.d.). https://www.eos.info/en/additive-manufacturing (accessed April 21, 2020).

[346] Sciaky, Inc. | Industrial Metal 3D Printing | Arc + EB Welding, (n.d.). https://www.sciaky.com/ (accessed April 21, 2020).

[347] DMG MORI, (n.d.). https://www.dmgmori.co.jp/en/top2/ (accessed April 21, 2020).

[348] Systems – Additec Website, (n.d.). https://www.additec.net/Systems/ (accessed April 21, 2020).

[349] 3DMP process, (n.d.). https://www.gefertec.de/en/3dmp-process/ (accessed April 21, 2020).

[350] IN718 Inconel 718 Nickle Based Metal Powder for Additive Manufacturing– MSE Supplies LLC, (n.d.). https://www.msesupplies.com/products/inconel-718-nickle-based-metal-powder-for-additive-manufacturing-3d-printing?variant=32148364984378 (accessed June 14, 2022).

[351] IN625 Inconel 625 Nickle Based Metal Powder for Additive Manufacturing– MSE Supplies LLC, (n.d.). https://www.msesupplies.com/products/in625-nickle-based-metal-powder-for-additive-manufacturing-3d-printing?variant=32229906579514 (accessed June 14, 2022).

[352] AISI 1040 Carbon Steel (UNS G10400), (n.d.). https://www.azom.com/article.aspx?ArticleID=6525 (accessed June 14, 2022).

[353] Order MetcoAdd H13-A Additive Manufacturing Powder Online at myMetco, (n.d.). https://mymetco.oerlikon.com/en-us/product/metcoaddh13a (accessed June 14, 2022).

[354] AlSi10Mg Aluminum Based Metal Powder for Additive Manufacturing (3D Pr– MSE Supplies LLC, (n.d.). https://www.msesupplies.com/products/alsi10mg-aluminum-based-metal-powder-for-additive-manufacturing-3d-printing?variant=32224600424506 (accessed June 14, 2022).

[355] S7 Tool Steel - Shock-Resisting Steel (UNS T41907), (n.d.). https://www.azom.com/article.aspx?ArticleID=6248 (accessed June 14, 2022).

[356] 18Ni300 Iron Based Metal Powder for Additive Manufacturing (3D Printin– MSE Supplies LLC, (n.d.). https://www.msesupplies.com/products/18ni300-iron-based-metal-powder-for-additive-manufacturing-3d-printing (accessed June 12, 2022).

[357] 316L Iron Based Stainless Steel Metal Powder for Additive Manufacturin– MSE Supplies LLC, (n.d.). https://www.msesupplies.com/products/316l-iron-based-metal-powder-for-additive-manufacturing-3d-printing?variant=32193825833018 (accessed June 14, 2022).

[358] Metal powder in tool and high-speed steel — Metal powder | Sandvik, (n.d.). https://www.metalpowder.sandvik/en/products/metal-powder-alloys/tool-and-high-speed-steels/ (accessed June 14, 2022).

Publication Details

Journal Publications

2023 **Ambrish Singh,** Sadaival Singh, Sajan Kapil, Manas Das, "Generation of Continuous and Sparse Space Filling Toolpath with Tailored Density for Additive Manufacturing of Biomimetics," CAD Comput Aided Des| **Under Review**

2022 **Ambrish Singh**, Atul Singh Rajput, Sajan Kapil, Manas Das, "Parameter Sensitivity Analysis of Centrifugal Spreaders for Dispersing Metallic Powders and Material Property Calibration for DEM Simulation," Powder Technol. 411 (2022) 431–442, 117958, https://doi.org/10.1016/j.powtec.2022.117958.

2022 Sadaival Singh, **Ambrish Singh**, Sajan Kapil, Manas Das, "Utilization of a TSP Solver for Generating Non-Retractable, Direction Favouring Toolpath for Additive Manufacturing," Addit. Manuf. 35 (2022) 103126. https://doi.org/10.1016/j.addma.2022.103126.

2021 **Ambrish Singh**, Seema Negi, Sajan Kapil, K.P. Karunakaran, Manas Das, "A Comprehensive Study of Auxiliary Arrangements for Attaining Omnidirectionality in Additive Manufacturing" Machine Tools, J. Manuf. Sci. Eng. 143 (2021). https://doi.org/10.1115/1.4049094

2020 **Ambrish Singh**, Sajan Kapil, Manas Das, "A Comprehensive Review of the Methods and Mechanisms for Powder Feedstock Handling in Directed Energy Deposition," Addit. Manuf. 35 (2020) 101388. https://doi.org/10.1016/j.addma.2020.101388.

Patents Granted

2021 **Ambrish Singh**, Sajan Kapil, Manas Das, "A gravity-based, Gas-Free, and Omnidirectional Laser Powder Cladding Head," Indian Patent| Patent Number: IN 440581

Patents Filed

2023 **Ambrish Singh**, Sajan Kapil, Manas Das, " An apparatus for non-pneumatic powder feedstock metering and delivery through a discrete coaxial nozzle from applications in Directed Energy Deposition." | Application Number: 202331056066

Book Chapters

2021 **Ambrish Singh**, Sajan Kapil, Manas Das, "Discrete Element Analysis of Gravity-Driven Powder Flow in Coaxial Nozzles for Directed Energy Deposition", In: Bag S., Paul C.P., Baruah M. (eds) Next Generation Materials and Processing Technologies. Springer Proceedings in Materials, vol 9 (2021). Springer, Singapore. https://doi.org/10.1007/978-981-16-0182-8_24

Conference Details

2022 **Ambrish Singh**, Sajan Kapil, Manas Das, “A Non-Pneumatic Method of Powder Feedstock Handling in Laser-based Directed Energy Deposition,” 12th International conference on precision, micro, meso, and nanoengineering (COPEN-12), 08th-10th December 2022, IIT Kanpur, India,

2021 **Ambrish Singh**, Sajan Kapil, Manas Das, “An Optimized Method of Powder Feedstock Handling in Directed Energy Deposition,” 4th International Conference on “Holistic Innovation in Additive Manufacturing (HI-AM)," 1st - 2nd June 2021, The University of Waterloo, Canada in Online Mode.

Technologies and Products Developed

2023 **Ambrish Singh**, Sajan Kapil, Manas Das “ A non-pneumatic powder metering and delivery unit customizable to retrofit existing laser-based CNC platforms for additive manufacturing capabilities”| Under discussion for technology transfer to Ace Manufacturing Systems Ltd., Bangalore

Awards and Recognition

2022 **Ambrish Singh**, Sajan Kapil, Manas Das, “A Non-Pneumatic Method of Powder Feedstock Handling in Laser-based Directed Energy Deposition,” Best Poster Award| International Conference on Precision Micro, Meso, and Nano Engineering (COPEN-2022, IIT Kanpur)

2021 **Ambrish Singh**, Sajan Kapil, Manas Das, “An Optimized Method of Powder Feedstock Handling in Directed Energy Deposition,” Third Place in Oral Presentation| Network for Holistic Innovation in Additive Manufacturing (Virtual HI-AM-2021, University of Waterloo, Canada)

Overseas Assignment

Dec 2022 Invitee at RWTH Aachen for an industrial visit under IGSTC project “Multi-Axis Multi-Material Wire Arc Additive Manufacturing,” exploring fabrication of material-based FGMs through novel toolpath planning and implementation via Directed Energy Deposition

This page is intentionally left blank.